

Contributions to Antarctic Research III

Physical Sciences

ANTARCTIC OCEANOLOGY

Joseph L. Reid, *Editor*

ANTARCTIC OCEANOLOGY II: THE AUSTRALIAN-NEW ZEALAND SECTOR

Dennis E. Hayes, *Editor*

ANTARCTIC SNOW AND ICE STUDIES

Malcolm Mellor, *Editor*

ANTARCTIC SNOW AND ICE STUDIES II

A. P. Crary, *Editor*

ANTARCTIC SOILS AND SOIL FORMING PROCESSES

J. C. F. Tedrow, *Editor*

DRY VALLEY DRILLING PROJECT

L. D. McGinnis, *Editor*

GEOLOGICAL INVESTIGATIONS IN NORTHERN VICTORIA LAND

Edmund Stump, *Editor*

GEOLOGY AND PALEONTOLOGY OF THE ANTARCTIC

Jarvis B. Hadley, *Editor*

GEOLOGY OF THE CENTRAL TRANSANTARCTIC MOUNTAINS

Mort D. Turner and John F. Splettstoesser,
Editors

GEOMAGNETISM AND AERONOMY

A. H. Waynick, *Editor*

METEOROLOGICAL STUDIES AT PLATEAU STATION, ANTARCTICA

Joost A. Businger, *Editor*

OCEANOLOGY OF THE ANTARCTIC CONTINENTAL SHELF

Stanley S. Jacobs, *Editor*

STUDIES IN ANTARCTIC METEOROLOGY

Morton J. Rubin, *Editor*

UPPER ATMOSPHERE RESEARCH IN ANTARCTICA

L. J. Lanzerotti and C. G. Park, *Editors*

THE ROSS ICE SHELF: GLACIOLOGY AND GEOPHYSICS

C. R. Bentley and D. E. Hayes, *Editors*

VOLCANOES OF THE ANTARCTIC PLATE AND SOUTHERN OCEANS

W. E. LeMasurier and J. T. Thomson, *Editors*

MINERAL RESOURCES POTENTIAL OF ANTARCTICA

John F. Splettstoesser and Gisela A. M. Dreschhoff,
Editors

CONTRIBUTIONS TO ANTARCTIC RESEARCH I

David H. Elliot, *Editor*

CONTRIBUTIONS TO ANTARCTIC RESEARCH II

David H. Elliot, *Editor*

MARINE GEOLOGICAL AND GEOPHYSICAL ATLAS OF THE CIRCUM-ANTARCTIC TO 30°S

Dennis E. Hayes, *Editor*

MOLLUSCAN SYSTEMATICS AND BIOSTRATIGRAPHY

Jeffrey D. Stilwell and William J. Zinsmeister

THE ANTARCTIC PALEOENVIRONMENT:

A PERSPECTIVE ON GLOBAL CHANGE

James P. Kennett and Detlef A. Warnke,
Editors

**ANTARCTIC
RESEARCH
SERIES**

American Geophysical Union

Biological and Life Sciences

BIOLOGY OF THE ANTARCTIC SEAS

Milton O. Lee, *Editor*

BIOLOGY OF THE ANTARCTIC SEAS II

George A. Llano, *Editor*

BIOLOGY OF THE ANTARCTIC SEAS III

George A. Llano and Waldo L. Schmitt, *Editors*

BIOLOGY OF THE ANTARCTIC SEAS IV

George A. Llano and I. Eugene Wallen, *Editors*

BIOLOGY OF THE ANTARCTIC SEAS V

David L. Pawson, *Editor*

BIOLOGY OF THE ANTARCTIC SEAS VI

David L. Pawson, *Editor*

BIOLOGY OF THE ANTARCTIC SEAS VII

David L. Pawson, *Editor*

BIOLOGY OF THE ANTARCTIC SEAS VIII

David L. Pawson and Louis S. Kornicker, *Editors*

BIOLOGY OF THE ANTARCTIC SEAS IX

Louis S. Kornicker, *Editor*

BIOLOGY OF THE ANTARCTIC SEAS X

Louis S. Kornicker, *Editor*

BIOLOGY OF THE ANTARCTIC SEAS XI

Louis S. Kornicker, *Editor*

BIOLOGY OF THE ANTARCTIC SEAS XII

David L. Pawson, *Editor*

BIOLOGY OF THE ANTARCTIC SEAS XIII

Louis S. Kornicker, *Editor*

BIOLOGY OF THE ANTARCTIC SEAS XIV

Louis S. Kornicker, *Editor*

BIOLOGY OF THE ANTARCTIC SEAS XV

Louis S. Kornicker, *Editor*

BIOLOGY OF THE ANTARCTIC SEAS XVI

Louis S. Kornicker, *Editor*

BIOLOGY OF THE ANTARCTIC SEAS XVII

Louis S. Kornicker, *Editor*

BIOLOGY OF THE ANTARCTIC SEAS XVIII

Louis S. Kornicker, *Editor*

BIOLOGY OF THE ANTARCTIC SEAS XIX

Louis S. Kornicker, *Editor*

BIOLOGY OF THE ANTARCTIC SEAS XX

Louis S. Kornicker, *Editor*

BIOLOGY OF THE ANTARCTIC SEAS XXI

Louis S. Kornicker, *Editor*

ANTARCTIC TERRESTRIAL BIOLOGY

George A. Llano, *Editor*

TERRESTRIAL BIOLOGY II

Bruce Parker, *Editor*

TERRESTRIAL BIOLOGY III

Bruce Parker, *Editor*

ANTARCTIC ASCIDIACEA

Patricia Kott

ANTARCTIC BIRD STUDIES

Oliver L. Austin, Jr., *Editor*

ANTARCTIC PINNIPEDIA

William Henry Burt, *Editor*

ANTARCTIC CIRRIPEDIA

William A. Newman and Arnold Ross

BIRDS OF THE ANTARCTIC AND SUB-ANTARCTIC

George E. Watson

ENTOMOLOGY OF ANTARCTICA

J. Linsley Gressitt, *Editor*

HUMAN ADAPTABILITY TO ANTARCTIC CONDITIONS

E. K. Eric Gunderson, *Editor*

POLYCHAETA ERRANTIA OF ANTARCTICA

Olga Hartman

POLYCHAETA MYZOSTOMIDAE AND SEDENTIARIA OF ANTARCTICA

Olga Hartman

RECENT ANTARCTIC AND SUBANTARCTIC BRACHIOPODS

Merrill W. Foster

Volume 57

ANTARCTIC
RESEARCH
SERIES

Contributions to Antarctic Research III

David H. Elliot, Editor

 American Geophysical Union
Washington, D.C.
1992

CONTRIBUTIONS TO ANTARCTIC RESEARCH III

David H. Elliot, Editor

Published under the aegis of the
Board of Associate Editors, Antarctic Research Series
David H. Elliott, Chairman
John B. Anderson, Stephen Cairns,
Samuel C. Colbeck, Rodney M. Feldmann,
E. Imre Friedmann, Dennis E. Hayes,
Charles R. Stearns

Library of Congress Cataloging-in-Publication Data

(revised for volume 3)

Contributions to Antarctic research.

(Antarctic research series, ISSN 0066-4634 ; v. 57)

edited by David H. Elliott.

ISBN 0-87590-760-1 (v. 1)

ISBN 0-87590-809-8 (v. 2)

ISBN 0-87590-825-X (v. 3)

1. Antarctic regions. I. Elliot, David H. II. American Geophysical Union.

III. Series: Antarctic research series ; v. 57, etc.

G860.C58 1990

998'.9

90-1279

CIP

ISSN 0066-4634

ISBN 0-87590-825-X

Copyright 1992 by the American Geophysical Union
2000 Florida Avenue, N.W.
Washington, DC 20009

Figures, tables, and short excerpts may be reprinted in scientific books and journals if the source is properly cited.

Authorization to photocopy items for internal or personal use, or the internal or personal use of specific clients, is granted by the American Geophysical Union for libraries and other users registered with the Copyright Clearance Center (CCC) Transactional Reporting Service, provided that the base fee of \$1.00 per copy plus \$0.20 per page is paid directly to CCC, 21 Congress Street, Salem, MA 10970. 0066-4634/92/\$01.00+0.20.

This consent does not extend to other kinds of copying, such as copying for creating new collective works or for resale. The reproduction of multiple copies and the use of extracts, including figures and tables, for commercial purposes requires specific permission from AGU.

Published by
American Geophysical Union
With the aid of grant DPP-89-15494 from the
National Science Foundation

Printed in the United States of America.

CONTENTS

The Antarctic Research Series: Statement of Objectives <i>Board of Associate Editors</i>	ix
Spectral Irradiance and Bio-optical Properties in Perennially Ice-Covered Lakes of the Dry Valleys (McMurdo Sound, Antarctica) <i>M. P. Lizotte and J. C. Priscu</i>	1
Oxygen Isotope Study of the Ice Fields Surrounding the Reckling Moraine on the East Antarctic Ice Sheet <i>Gunter Faure, Pieter Grootes, David Buchanan, and Erik H. Hagen</i>	15
Scallop Shell Mineralogy and Crystalline Characteristics: Proxy Records for Interpreting Antarctic Nearshore Marine Hydrochemical Variability <i>Paul Arthur Berkman, Dennis W. Foreman, John C. Mitchell, and Robert J. Liptak</i>	27
Evidence for a Grounded Ice Sheet on the Ross Sea Continental Shelf During the Late Pleistocene and Preliminary Paleodrainage Reconstruction <i>John B. Anderson, Stephanie S. Shipp, Louis R. Bartek, and David E. Reid</i>	39
Late Quaternary Glacial History of the Northern Antarctic Peninsula's Western Continental Shelf: Evidence From the Marine Record <i>Peter G. Pope and John B. Anderson</i>	63
Pliocene-Pleistocene Seismic Stratigraphy of the Ross Sea: Evidence for Multiple Ice Sheet Grounding Episodes <i>Belén Alonso, John B. Anderson, José I. Díaz, and Louis R. Bartek</i>	93
An Analysis of Gravity Measurements on the Ross Ice Shelf, Antarctica <i>Lawrence L. Greischar, Charles R. Bentley, and Larry R. Whiting</i>	105

The Antarctic Research Series: STATEMENT OF OBJECTIVES

The Antarctic Research Series provides for the presentation of detailed scientific research results from Antarctica, particularly the results of the United States Antarctic Research Program, including monographs and long manuscripts.

The series is designed to make the results of Antarctic fieldwork available. The Antarctic Research Series encourages the collection of papers on specific geographic areas within Antarctica. In addition, many volumes focus on particular disciplines, including marine biology, oceanology, meteorology, upper atmosphere physics, terrestrial biology, geology, glaciology, human adaptability, engineering, and environmental protection.

Topical volumes in the series normally are devoted to papers in one or two disciplines. Multidisciplinary volumes, initiated in 1990 to enable more rapid publication, are open to papers from any discipline. The series can accommodate long manuscripts and utilize special formats, such as maps.

Priorities for publication are set by the Board of Associate Editors. Preference is given to research manuscripts from projects funded by U.S. agencies. Because the series serves to emphasize the U.S. Antarctic Research Program, it also performs a function similar to expedition reports of many other countries with national Antarctic research programs.

The standards of scientific excellence expected for the series are maintained by the review criteria established for the AGU publications program. Each paper is critically reviewed by two or more expert referees. A member of the Board of Associate Editors may serve as editor of a volume, or another person may be appointed. The Board works with the individual editors of each volume and with the AGU staff to assure that the objectives of the series are met, that the best possible papers are presented, and that publication is timely.

Proposals for volumes or papers offered should be sent to the Board of Associate Editors, Antarctic Research Series, at 2000 Florida Avenue, N.W., Washington, D.C. 20009. Publication of the series is partially supported by a grant from the National Science Foundation.

Board of Associate Editors
Antarctic Research Series

SPECTRAL IRRADIANCE AND BIO-OPTICAL PROPERTIES IN
PERENNIALLY ICE-COVERED LAKES OF THE DRY VALLEYS
(MCMURDO SOUND, ANTARCTICA)

M. P. LIZOTTE¹ AND J. C. PRISCU

Department of Biology, Montana State University, Bozeman, Montana 59717

Lakes of the dry valley region near McMurdo Sound, Antarctica, which are perennially ice-covered (approximately 4 m thick) and contain only microorganisms in the plankton, present unique systems for studies in hydrologic optics. Profiles of the flux and spectral distribution of photosynthetically available radiation (400–700 nm) and the optical properties of suspended particulate material were measured for Lake Bonney and Lake Fryxell. The spectral quality of light immediately beneath the ice was similar in both lakes and is comparable to previously published results for nearby Lake Hoare; irradiance was always less than $50 \mu\text{mol photons m}^{-2} \text{ s}^{-1}$. However, the concentration and vertical distribution of phytoplankton biomass (i.e., chlorophyll) differed greatly among the three lakes and was similar to the trend in light attenuation of Lake Fryxell >> Lake Hoare > Lake Bonney. The same relationship between chlorophyll and light attenuation was observed as chlorophyll concentrations increased over the growth season in Lake Bonney. The wavelengths of maximum transmission through the water columns were in the range 507–540 nm with longer wavelengths (>600 nm) attenuated most rapidly. Spectral downwelling irradiance was attenuated primarily by phytoplankton pigments at shorter wavelengths (<520 nm) and by water at longer wavelengths. An analysis of absorption due to water, phytoplankton, detritus, and, by difference, gilvin (dissolved materials) showed that water was the dominant absorber (38–75% of the total absorption coefficient) but that phytoplankton was usually the most important of the variable components (11–47%). Exceptions were the dominance of phytoplankton absorption at the chlorophyll maxima of Lake Fryxell and the importance of gilvin absorption following the seasonal introduction of glacial stream water. In terms of the relative importance of light-absorbing components, the dry valley lakes appear to be most similar to oligotrophic seas and would be defined as case 1 waters.

INTRODUCTION

The dry valleys near McMurdo sound, Antarctica, contain lakes with perennial ice cover over a liquid water column inhabited solely by microorganisms. Glacier-free land is rare in Antarctica (approximately 2% by area), with the largest contiguous area in the dry valleys of the coastal mountains near McMurdo Sound (approximately 3500 km²). Lakes and ponds are a common feature of Antarctica's dry land, but only the larger lakes at higher latitudes retain a thick ice cover (3–5 m) year-round. These unusual lakes are of particular interest to physical limnologists because they are among the least turbulent natural waters and to phytoplankton ecologists because they are among

the simplest ecosystems described (in terms of species diversity and trophic interactions). The first condition exists because of a combination of thick ice cover, low advective stream inflow, and strong vertical gradients in salinity [e.g., Angino *et al.*, 1964; Spigel *et al.*, 1991]. Phytoplankton occur in highly stratified layers [e.g., Koob and Leister, 1972; Vincent, 1981], which are typically dominated by flagellates, primarily the cryptophyte *Chroomonas lacustris*, the chrysophyte *Ochromonas* sp., and the chlorophyte *Chlamydomonas subcaudata* [Parker *et al.*, 1982; M. P. Lizotte and J. C. Priscu, unpublished data, 1992].

Growth and production of these underice phytoplankton are limited by light availability [e.g., Vincent, 1981; Parker *et al.*, 1982; Priscu *et al.*, 1987, 1990; Lizotte and Priscu, 1992]. Phytoplankton light absorption and utilization depend on the spectral quality of the photosynthetically available radiation

¹Now at BDM International, Inc., Washington, D.C. 20024.

(PAR; 400–700 nm) beneath the ice and through the water column. Spectral distribution of underice irradiance has been studied in several temperate lakes [e.g., *Bolsenga*, 1981; *Stewart and Brockett*, 1984], but the ice on the dry valley lakes is nearly an order of magnitude thicker. The spectral quality of underice light has been reported from only one Antarctic lake [*Palmisano and Simmons*, 1987]. *Palmisano and Simmons* [1987] reported that the thick ice cover of Lake Hoare (which is in the dry valleys near McMurdo Sound) produced considerable spectral narrowing with maximum transmission around 500 nm and that light attenuation through the water column was distinctly influenced by algal pigments. Other lakes in this region may have different types and concentrations of phytoplankton [*Parker et al.*, 1982], ice covers of different thicknesses and physical conditions, seasonal changes in ice condition [*Priscu*, 1991], or seasonal inputs of inorganic particulates from glacial melt streams that could yield a different spectral irradiance than that measured on a single date for Lake Hoare. Our measurements of spectral irradiance and particulate absorption spectra for Lake Bonney and Lake Fryxell indicate that all of the above factors can affect the quality of in situ irradiance, but the greatest difference between lakes is due to phytoplankton biomass.

MATERIALS AND METHODS

Site Description and Routine Sampling

Lake Bonney, Lake Hoare, and Lake Fryxell are located in the Taylor Valley (approximately 78°S, 163°E) of the dry valley region adjacent to McMurdo Sound, Antarctica. Samples were collected from the deepest site on each lake, the center of the east lobe of Lake Bonney (36 m), approximately 0.5 km west of the Canada Glacier in Lake Hoare (34 m), and the center of Lake Fryxell (18 m). In addition, water column samples were collected in a transect along both the west (stations W5, W20, W30, and N15) and the east (stations N30, E10, E20, E30, E40, and E50) lobes of Lake Bonney (as described by *Spigel et al.* [1991]). All depths were measured from the piezometric level in holes through the ice cover. Ice thickness was 4.5 m on Lake Fryxell (December 7, 1990) and Lake Hoare (December 8, 1990), was 2.9–3.3 m on the west lobe of Lake Bonney (December 6, 1990), and ranged from 3.2 to 4.2 m on the east lobe of Lake Bonney (October 1989 to January 1990, October 1990 to January 1991, and September to December 1991). Unless specified, data reported for Lake Bonney are from the east lobe. Depths

were measured from the piezometric water level in ice holes, which was 25–30 cm below the ice surface.

The ice-covered lakes of this region are classified as meromictic, even though there is no distinct mixolimnion. All the lakes we studied have freshwater ice. The water column consists of a relatively freshwater epilimnion and a saline hypolimnion divided by a chemocline with strong gradients in conductivity, nutrients, and oxygen [*Angino et al.*, 1964; *Koob and Leister*, 1972; *Vincent*, 1981; *Parker et al.*, 1982; *Priscu et al.*, 1989; *McKnight et al.*, 1991; *Sharp and Priscu*, 1990; *Spigel et al.*, 1991]. Lake Bonney has a steep salinity gradient from approximately 11 m to the anoxic hypolimnion (below 20 m in the east lobe and below 14 m in the west lobe). The salinity in Lake Fryxell increases monotonically with depth to the hypolimnion below 9 m. Lake Hoare is a freshwater reservoir dammed by the Canada Glacier, with a small anaerobic hypolimnion below 28 m. The hypolimnia of Lake Fryxell and Lake Hoare contain hydrogen sulfide and have plates of photosynthetic bacteria at the O₂-H₂S boundary. Glacial melt streams flow into all three lakes, but there are no surface outflows; the only known water loss is through ice ablation (evaporation, sublimation, and physical scouring).

Radiation Measurements

Downwelling irradiance was measured with a Biospherical Instruments MER-1000 spectroradiometer. The instrument consists of a cosine collector containing 13 photodiodes filtered for measuring total PAR (400–700 nm) and 12 discrete wavelengths (410, 441, 488, 507, 520, 540, 570, 589, 625, 656, 671, and 694 nm) with half bandwidths of 5 nm. The same instrument was used by *Palmisano and Simmons* [1987] for their studies of Lake Hoare. Calibration constants for underwater use were obtained using an immersion correction applied to air calibrations.

Spectroradiometer profiles were made in Lake Bonney at 1620 UT on November 24, at 2205 UT on December 10, and at 1240 UT and 2315 UT on January 7 and in Lake Fryxell at 1515 UT on December 7 during 1990–1991. Solar radiation is continuous and near the seasonal maximum during this period, with about a tenfold difference in flux rate between local noon and midnight [*Priscu*, 1991]. Beneath the thick ice cover the sensitivity limits of some of the sensors were reached at depths of 15–20 m. The spectroradiometer was lowered through ice holes 60–80 cm in diameter; surface (air) measurements were made before each cast.

Profiles of total underwater irradiance (PAR) were also measured with 4π sr scalar irradiance sensors,

either a Li-Cor model 193SA or a Biospherical Instruments model QSP-200. The radiometers were not calibrated together, but that is not critical for our use in estimating attenuation coefficients. These instruments were typically deployed through an ice hole 25 cm in diameter. Scalar irradiance profiles in Lake Fryxell and Lake Hoare were made on the same dates as spectroradiometer casts.

Particulate Matter Measurements

Water samples were collected with a 2.2-L Niskin bottle. Chlorophyll *a* (Chl) and phaeopigments (Phaeo) were quantified from extracts with a Turner model 111 fluorometer [Holm-Hansen *et al.*, 1965]. In 1989, triplicate samples were concentrated onto Whatman GF/F filters, frozen at -20°C for <30 days, and later macerated in 90% acetone in a Teflon-glass tissue grinder and extracted for 8–12 hours at 4°C in the dark. Sample fluorescence was calibrated against standard concentrations of purified chlorophyll *a* (Sigma Chemical); fluorescence after acidification was subtracted to correct for phaeopigment fluorescence. In 1990–1991 we changed to more porous filters (Whatman GF/C) and a simpler initial treatment (vortex for 30 s). Comparisons between filter types were made for various depths in Lake Bonney; there were no significant differences in the chlorophyll retained for most depths (Table 1) with the exception of relatively small underestimates at 8 and 10 m with GF/C filters.

The absorption spectra of suspended particulate material were determined by spectrophotometry of material collected on Whatman GF/C glass-fiber

filters [Mitchell and Kiefer, 1988]. Spectral scans from 380 to 750 nm were measured on a Perkin-Elmer model lambda-6 spectrophotometer relative to a wet blank filter. Volumes of 0.25–1.0 L were filtered to produce maximal optical densities of 0.2 units. Spectra were normalized to average optical density in the range 730–750 nm (where particulate absorption is minimal) to correct for background drift. We used the equation described by Bricaud and Stramski [1990] from the data of Mitchell and Kiefer [1988] for the path length amplification factor to derive particulate absorption coefficients from raw optical density measurements. Filters were subsequently extracted in methanol to remove algal pigments and scanned again to estimate the spectral absorption due to detritus [Kishino *et al.*, 1985]; the difference between the spectra was taken to estimate absorption due to phytoplankton.

Optical Models

Bulk attenuation coefficients for irradiance (*K*) were determined for discrete sections of water column from irradiance (*E*) at upper (*z*₁) and lower (*z*₂) depths:

$$K = [\ln E(z_1) - \ln E(z_2)]/[z_2 - z_1] \quad (1)$$

For *K* based on scalar PAR, *z*₁ and *z*₂ usually delimited 2-m sections of the water column bounding an intermediate depth where a water sample was collected. Equation (1) is based on the Lambert-Beer law, which assumes uniform distribution of optical properties between depths. The vertical distribution of pigments (Figure 1) could violate this assumption

TABLE 1. Chlorophyll Concentrations From Lake Bonney Estimated With Different Filters

Date	Depth, m	n	GF/C filter mean,* mg m ⁻³	GF/F filter mean,* mg m ⁻³	GF/C GF/F	p<†
Nov. 30, 1989	5	3	1.32(0.03)	1.42(0.08)	0.93	0.89
Dec. 7, 1989	5	5	0.99(0.04)	1.06(0.08)	0.93	0.88
	17	5	0.53(0.01)	0.55(0.02)	0.96	0.92
Nov. 15, 1991	4.5	5	2.76(0.40)	3.31(0.15)	0.83	0.97
	6	5	2.15(0.14)	1.91(0.20)	1.13	0.94
	8	5	1.31(0.13)	1.96(0.16)	0.67	0.99
	10	5	1.05(0.11)	1.24(0.04)	0.84	0.99
	12	5	0.79(0.04)	0.74(0.02)	1.07	0.96
	13	5	0.88(0.08)	0.93(0.07)	0.95	0.70
	15	5	0.63(0.05)	0.60(0.01)	1.05	0.75
	17	5	0.92(0.05)	0.86(0.07)	1.07	0.86
	20	5	0.27(0.02)	0.29(0.06)	0.95	0.50

*Values in parentheses are plus or minus standard deviations of the means.

†Probability that GF/C and GF/F results are significantly different.

over large depth intervals. However, *Gordon* [1989] suggests that estimating K for case 1 waters (where optical variance is predominantly due to phytoplankton) by the Lambert-Beer law should result in relatively small errors (5–10% depending on wavelength).

The bulk attenuation coefficient for downwelling irradiance (K_d) is dependent on absorbing and scattering factors in the water column. For K_d at the middepth of the euphotic zone (z_m), *Kirk* [1981] generated a data set that showed a relationship based on coefficients for absorbance (a) and scattering (b) with the form:

$$K_d(z_m) = (a^2 + 0.256ab)^{0.5}$$

This equation described waters with b/a ratios ranging from zero to 30, but at low b/a ratios the relationship was approximated by a linear equation:

$$K_d(z_m) = a + 0.128b \quad (2)$$

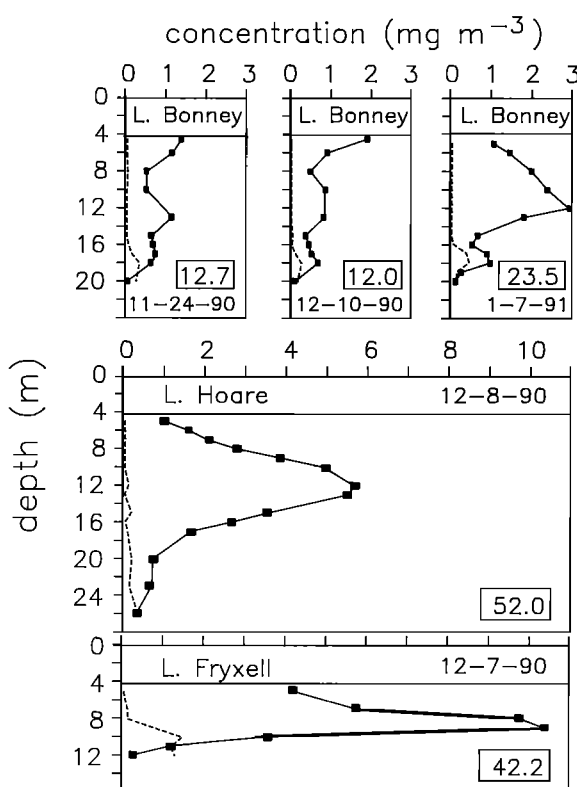


Fig. 1. Vertical profiles of chlorophyll (squares) and phaeopigment (dashed curves) concentrations. Numbers in boxes are integrated chlorophyll concentrations (milligrams per square meter) for the depths shown.

Phillips and Kirk [1984] state that further tests of these models with K_d at depths ranging from the surface to $2z_m$ showed that the equations are accurate enough to use as a first approximation at any depth. The scatter coefficient may be estimated from chlorophyll concentration using the model presented by *Morel* [1988]:

$$b(\lambda) = b_w(\lambda) + 0.3(\text{Chl})^{0.62}(550/\lambda) \quad (3)$$

where b_w is the scatter coefficient for pure water and Chl is in milligrams per cubic meter. *Morel* [1988] points out that this relationship is based on observations for case 1 waters and required a power law equation because effects due to detritus and dissolved materials tend to covary with phytoplankton biomass. We determined b for PAR at a particular depth [$b(z)$] based on the derived b spectrum [$b(\lambda)$] weighted for the measured irradiance spectrum, [$E(z, \lambda)$], as follows:

$$b(z) = [\int_{400}^{700} E(z, \lambda)b(\lambda)] / [\int_{400}^{700} E(z, \lambda)] \quad (4)$$

The linear equation from *Kirk* [1981] (equation (2)) was used to estimate $a(z)$ from measured $K_d(z)$ and modeled (by (3) and (4)) $b(z)$. The ratios of b/a from these estimates were low, ranging from 2.0 to 4.8 in Lake Bonney and 6.4 to 7.1 in Lake Fryxell, supporting our use of the linear relationship.

The total absorption coefficient can be evaluated in terms of the contribution of partial coefficients attributable to the major light-attenuating components of natural waters,

$$a = a_w + a_p + a_g$$

where the coefficients are a_w for pure water, a_p for particulates, and a_g for gelvin (colored materials in solution). The coefficient for particulate matter can be further partitioned into a coefficient for pigmented phytoplankton (a_{ph}) and detritus (a_{de}). We measured wavelength-specific values for $a_{ph}(\lambda)$ and $a_{de}(\lambda)$ and estimated $a_w(\lambda)$ on the basis of the tables of *Smith and Baker* [1981]. Integrated values of $a_w(z)$, $a_{ph}(z)$, and $a_{de}(z)$ were weighted for $E(z, \lambda)$ as with $b(z)$ in (4). Finally, a_g was estimated by difference:

$$a_g = a - a_w - a_{ph} - a_{de}$$

The bulk attenuation coefficient, K , can also be divided into partial coefficients that can be dependent on concentrations of particulate or dissolved materials:

$$K = K_c(\text{Chl} + \text{Phaeo}) + K_w + K_x$$

where Chl + Phaeo is the concentration of pigments and the coefficients include a pigment-specific term (K_c in meters squared per milligram Chl + Phaeo), a term for water (K_w in m^{-1}), and a term for other materials (K_x in m^{-1}), including gilvin and detritus. A common method for deriving K_c is to take the slope of a linear regression of K and pigment concentration. The intercept of the regression is an estimate of $K_w + K_x$. This sum can be partitioned if K_w is estimated.

The bulk attenuation coefficient for water at a given depth, $K_w(z)$, is a function of the $K_w(\lambda)$ spectrum for pure water and the irradiance spectrum entering at the surface [Baker and Frouin, 1987]. We calculated the K_w for PAR beneath the ice cover on the basis of the $K_w(\lambda)$ spectrum reported for the clearest natural waters [Smith and Baker, 1981] and our measured underice irradiance spectra. The first step was to estimate the wavelength-specific irradiance at each depth, $E(z, \lambda)$, assuming only attenuation by water:

$$E(z_2, \lambda) = E(z_1, \lambda) e^{-(z_2 - z_1)K_w(\lambda)} \quad (5)$$

Then we produced a weighted value for $K_w(z, 400\text{--}700\text{ nm})$ at a given depth as for $b(z)$ in (4). We computed $K_w(z)$ beginning with the spectral distribution for irradiance at the base of our ice holes in Lake Bonney and Lake Fryxell and from data collected by divers against the underside of the ice in Lake Hoare [Palmisano and Simmons, 1987]. All underice irradiance spectra gave similar results for K_w (underice, 400–700 nm). Compared with the K_w values previously estimated for 5–20 m in an equivalent depth of pure water [Baker and Frouin, 1987], K_w under several meters of ice was 11–20% higher. This difference would decrease to only a few percent given a path length of 100 m. The K_w for a section of the water column was estimated from modeled (equation (5)) $E(z, 400\text{--}700\text{ nm})$ for two depths using (1).

RESULTS AND DISCUSSION

Pigment Distributions

Lake Bonney, Lake Hoare, and Lake Fryxell have distinct chlorophyll profiles that differ in concentration and vertical distribution (Figure 1). Chlorophyll concentrations in Lake Bonney reached 2.9 mg m^{-3} with maxima immediately under the ice (4–6 m), at middepths (10–13 m), and at the base of the oxygenated water column (17–18 m). Lake Fryxell had up to 10.4 mg Chl m^{-3} with a peak at 9 m, just above the oxycline. Lake Hoare had a single broad peak with chlorophyll concentrations up to 5.7 mg m^{-3} at 12 m; this profile was similar to that reported by Palmisano and Simmons [1987], with a peak of 3.9

mg Chl m^{-3} at 10 m during their 1982 study of spectral irradiance. Phaeopigment concentrations were insignificant relative to chlorophyll for most of the water column, except for the deepest populations (Figure 1). In general, maximum chlorophyll concentrations followed the trend Lake Bonney < Lake Hoare < Lake Fryxell, although integrated values were greater for Lake Hoare than for the much shallower Lake Fryxell or for Lake Bonney.

It should be noted that water samples were collected with a Niskin bottle and gently mixed to produce a sample integrated over 0.75 m (the length of the sampler). Sampling smaller depth intervals may yield higher peak concentrations. However, we are confident that the vertical resolution shown by sampling every 1–3 m is an accurate representation of chlorophyll distribution in these lakes. We have verified these distributions with higher-resolution sampling techniques, including a flow-through fluorometer (25 cm resolution (J. C. Priscu, unpublished data, 1992)) and a profiling natural fluorometer (10–20 cm resolution [Lizotte and Priscu, 1991]). The only thinner pigment layers are associated with plates of photosynthetic bacteria at H_2S -O₂ boundaries in Lake Fryxell (9.5 m) and Lake Hoare (27.5 m). Analyses of pigments separated by high-performance liquid chromatography (M. P. Lizotte, unpublished data, 1992) showed that these bacteria had pigments dominated by bacteriochlorophyll *a*, which did not contribute significantly to our chlorophyll values. Pigment signatures indicated that cryptophytes dominated the phytoplankton throughout Lake Fryxell and Lake Hoare and that the underice, midwater, and deep peaks of Lake Bonney were dominated by cryptophytes, chrysophytes, and chlorophytes, respectively. Microscopic examination showed flagellates ranging in size from 4 to 25 μm .

Irradiance

Irradiance measurements beneath our ice holes showed some light contamination, but the "hole effect" became minimal at 6 m, approximately 2 m below the bottom of the ice (Figure 2). We found that irradiance measured by an instrument lowered through a hole 60 cm in diameter was higher at 4 m than could be predicted from extrapolation of deeper light measurements based on attenuation due to water and particulates. Covering the hole with a plywood disk (1 m diameter) produced a significant shadow above 6 m. Because of these hole effects, we used light measurements from 6 m or deeper for analyses of water column optical properties. Interestingly, the spectral distribution of light measured at the base of open holes in Lake Bonney and Lake Fryxell (Figure 3) did

not differ greatly from measurements made by divers beneath the ice of Lake Hoare [Palmisano and Simmons, 1987]. Presumably, hole effects through such thick ice covers are minimized because of the low angle of incidence for sunlight at this high a latitude (a daily range of 11° – 35° at the seasonal maximum on December 22), and thus all sunlight entering the ice hole is effectively filtered by several meters of ice. Depth profiles of the natural log of PAR appear to be linear, with correlation coefficients (r^2) exceeding 0.99 from 6 to 20 m in Lake Bonney (see Lizotte and Priscu [1992] for additional profiles).

Our measurements of spectral attenuation for the ice of Lake Bonney and Lake Fryxell were similar to those reported for Lake Hoare [Palmisano and Simmons, 1987]. However, because of possible hole effects, our estimates of spectral attenuation of the ice should be interpreted cautiously. Bulk attenuation coefficients for ice determined with PAR sensors lowered through 25-cm holes and suspended below refrozen ice holes were approximately 0.8 – 1.0 m^{-1} [Priscu, 1991]. It should be noted that there are no

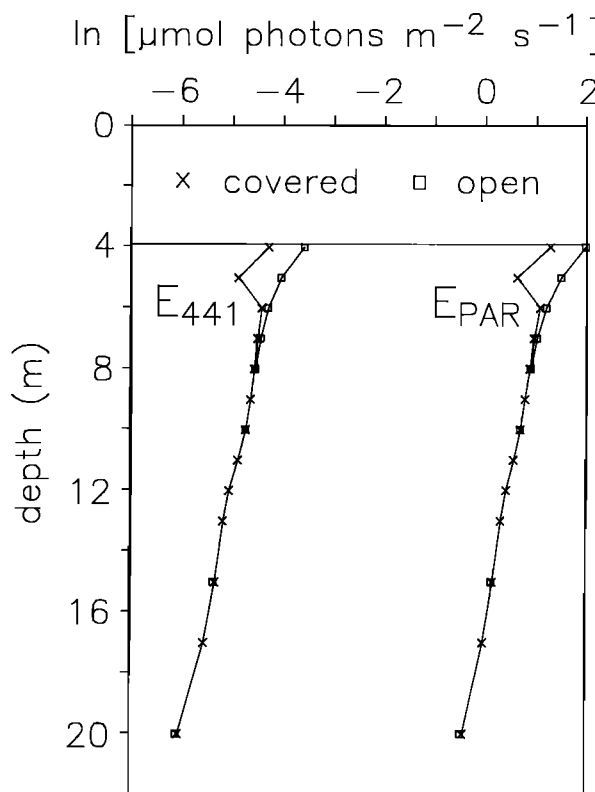


Fig. 2. Vertical profiles of irradiance (E) at 441 nm and total PAR beneath an ice hole, open and covered, in Lake Bonney.

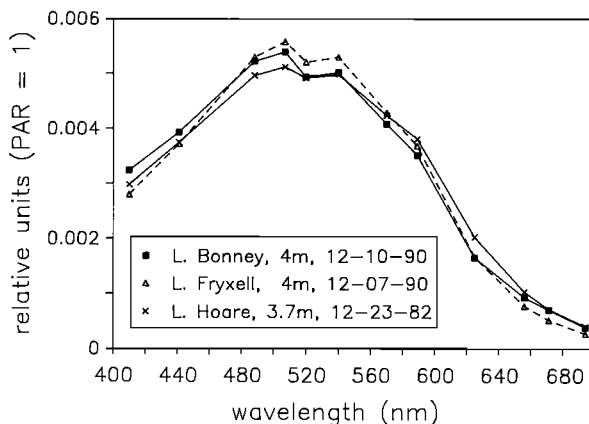


Fig. 3. Spectral downwelling irradiance normalized to total downwelling irradiance (PAR) at the base of the ice column. Measurements in Lake Bonney and Lake Fryxell were made beneath an open ice hole. Values for Lake Hoare are derived from Palmisano and Simmons [1987] for the same instrument deployed by scuba divers beneath solid ice.

known “ice algae” (analogous to that found in sea ice) to attenuate light in this freshwater ice. Irradiance beneath the ice cover in these lakes was of the order of 1–3% of incident solar irradiance and was always less than $50 \mu\text{mol photons m}^{-2} \text{s}^{-1}$.

The spectral distribution of downwelling irradiance through the water column was different between Lake Bonney and Lake Fryxell (Figures 4a–4d). Maximum transmission was measured at 507 nm for all depths in Lake Bonney during November and December and for the shallowest depth (6 m) in Lake Fryxell. Deeper waters in Lake Bonney during January and in Lake Fryxell had a maximum shifted to 540 nm, in relation to their higher chlorophyll content. The relative values and spectral characteristics of light penetration are summarized by the depth at which irradiance was 0.1% of incident levels (Figure 5). The 0.1% isolume of the least attenuated wavelength is near or below the maximum depth of photosynthesis, ranging from only a few meters below the ice in Lake Fryxell to 30 m in Lake Bonney. Wavelength-specific attenuation was much higher in Lake Fryxell than in Lake Bonney, as judged from the bulk attenuation coefficients, $K_d(\lambda)$, calculated for the 6- to 10-m section of each profile (Figure 6). The K_d spectrum measured in Lake Hoare in 1982 [Palmisano and Simmons, 1987] was intermediate between our spectra for Lake Bonney and Lake Fryxell. In Lake Bonney and Lake Hoare, red light (>600 nm) was attenuated most rapidly with depth, primarily because of water (Figure 6). Blue light (<500 nm) was also preferentially attenuated, roughly in proportion to chlorophyll concentrations.

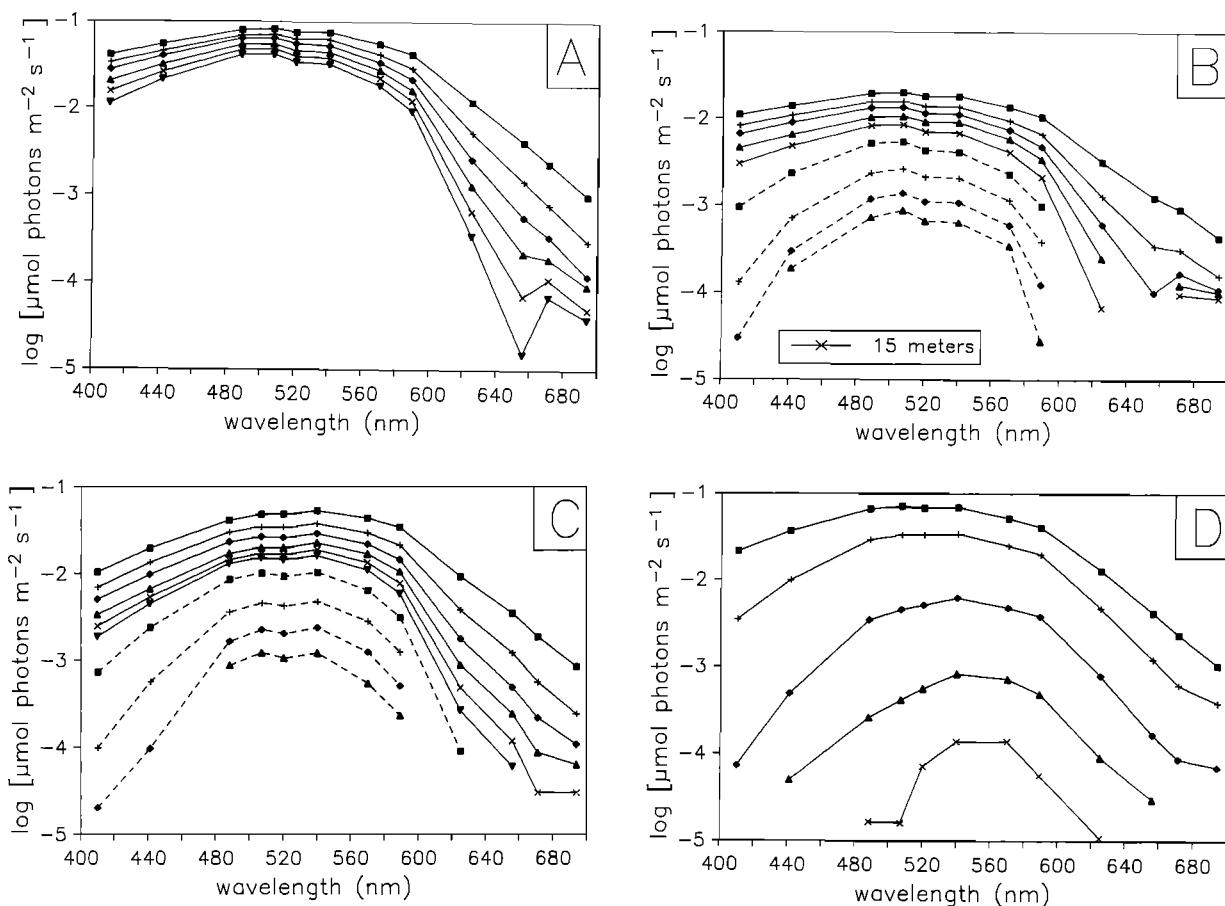


Fig. 4. Spectral downwelling irradiance at selected depths: (a) Lake Bonney on November 24, 1990; (b) Lake Bonney on December 10, 1990; (c) Lake Bonney on January 7, 1991; and (d) Lake Fryxell on December 7, 1990. Solid lines are measurements starting at 6 m and increasing depths at 2-m intervals (except as noted for Figure 4b). Dashed lines are measurements from 20 m to 35 m at 5-m intervals.

Lake Fryxell had the highest K_d values at all wave bands, with maximum attenuation of blue light. Materials other than water (pigments, particles, or dissolved molecules) apparently dominate light attenuation at wavelengths less than 650 nm in Lake Fryxell.

Diel and seasonal changes in incident irradiance, ice conditions, and water column characteristics may also influence the spectral quality of light in these lakes. During a single day the irradiance spectrum on the surface of Lake Bonney changed significantly between near noon and near midnight (Figure 7, for January 7) under similar atmospheric conditions: overcast with light clouds. The evening Sun passed behind mountains, producing a shadow on the lake surface and shifting the dominant wavelengths of surface irradiance from red to blue. A corresponding shift was also observed in the water column (Figure

7). Irradiance was measured during daylight (i.e., before the Sun passed behind the mountains) during November and December, and similar irradiance spectra were observed at the surface despite very different atmospheric conditions: clear skies and sunny in November and cloudy and overcast in December. Seasonally, surface irradiance spectra measured during the "day" were consistent, but the water column spectra indicated significant changes in January relative to consistent conditions in November and December (Figures 4, 5, and 7). The water column in January showed a greater attenuation of blue light (<500 nm) and a shift in maximal transmission from 507 nm to 540 nm. The January light profile followed several weeks of glacial streamflow that raised the height of the water column by at least 1 m and introduced allochthonous particulate material, primarily rock flour. The fresh stream water formed a

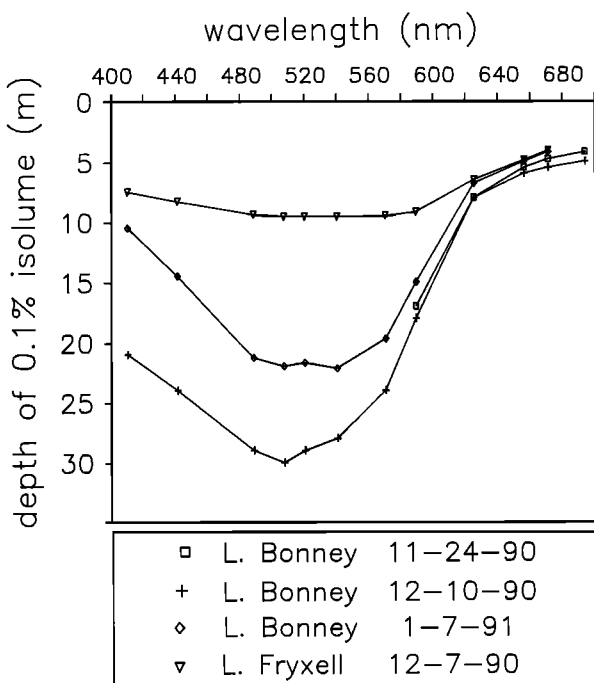


Fig. 5. Spectral distributions for the 0.1% isolume depth. Irradiance was measured only to 17 m for Lake Bonney on November 24, 1990.

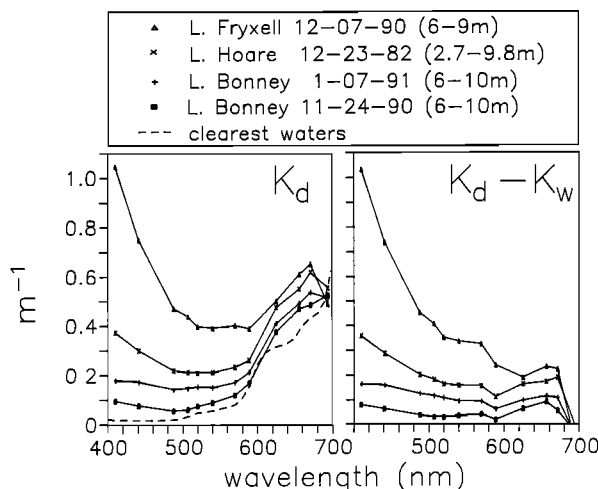


Fig. 6. Spectral distribution of bulk attenuation coefficients (K_d) and the difference between K_d and the attenuation due to water alone (K_w). The spectral attenuation coefficients for the clearest waters are from Smith and Baker [1981, Table 1]. Attenuation coefficients for Lake Hoare are derived from data presented by Palmisano and Simmons [1987]. Spectra for Lake Bonney on December 10, 1990, were intermediate between the spectrum shown for November and that shown for January. Note that K_d was determined from light extinction between different depths in the upper water column of each lake.

buoyant lens immediately beneath the ice, from which particulates were settling out. Interestingly, this increase in inorganic particulates coincided with increased chlorophyll concentrations in the water column (Figure 1).

One unique aspect of spectral irradiance measurements in the dry valley lakes is a measurable production of downwelling red light in the water column. At depths greater than 8 m, irradiance at the highest wavelengths (671 and 694 nm) increased relative to the next lowest wavelengths, and attenuation coefficients (Figure 6) were lower than the minimum values reported for pure water [Smith and Baker, 1981]. The most likely source of this anomaly is sunlight-induced fluorescence of phytoplankton chlorophyll *a*, which has an emission maximum at 683 nm. The extremely thick ice cover greatly reduces the flux of downwelling red light relative to open waters, and natural fluorescence of chlorophyll *a* becomes significant when the flux rates approach $10^{-4} \mu\text{mol photons m}^{-2} \text{s}^{-1} \text{nm}^{-1}$ in the far-red range. This is the approximate range of upwelling light at 683 nm measured with a Biospherical Instruments model PNF-300 [Lizotte and

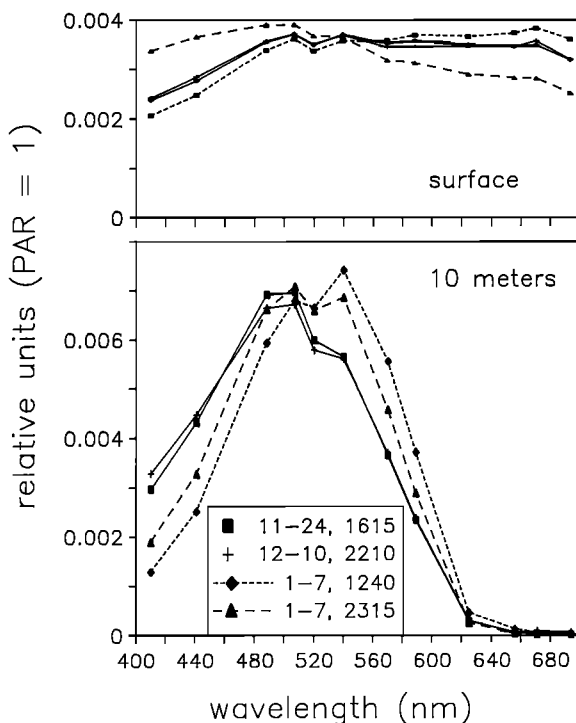


Fig. 7. Spectral downwelling irradiance normalized to total downwelling irradiance (PAR) at the surface and at 10 m in Lake Bonney over the field season (1990-1991) and near local noon and midnight of the same day.

Priscu, 1991; M. P. Lizotte, unpublished data, 1992]. Significant production of downwelling red light in the water column may be measurable in many polar lakes and seas with extremely thick ice covers. Because rates of chlorophyll fluorescence may be high relative to the flux of red light in these lakes, it would be difficult to apply optical models for the prediction of chlorophyll which utilize irradiance ratios or attenuation coefficients based on red light [e.g., Legendre and Gosselin, 1991].

Factors Contributing to Light Attenuation

Overall, the trend in light attenuation in the dry valley lakes (Lake Fryxell >> Lake Hoare > Lake Bonney) was similar to the trend in chlorophyll concentration; the same relationship was observed as chlorophyll concentration increased over the growth season in Lake Bonney. This trend implies that phytoplankton are responsible, directly or indirectly, for variations in light attenuation within these lakes. Difference spectra based on $K_d(\lambda)$ and $K_w(\lambda)$ all have blue and red peaks indicative of some combination of phytoplankton pigments and either particulate detritus or dissolved organic materials that may be derived from phytoplankton (Figure 6).

Further evidence for the relatively large contribution of phytoplankton toward optical properties of the water column can be obtained from shifts in spectral distribution of irradiance. Peak wavelength for downwelling irradiance increased from 507 to 540 nm with increasing chlorophyll in the water column. This spectral shift was observed with increasing depth, with time over the phytoplankton growth season, and in lakes containing higher phytoplankton concentrations. Similar spectral shifts and changes in the shape of irradiance spectra have been attributed primarily to changes in chlorophyll concentration [Morel and Smith, 1974; Tsuda and Nakanishi, 1990]. The dry valley lakes would be classified as case 1 waters [Morel and Prieur, 1977], that is, water columns in which phytoplankton and covarying detrital particulates dominate optical properties.

The attenuation of light by phytoplankton-derived particulate material is based primarily on the material's absorption spectrum (Figure 8), which is greatest at lower wavelengths. Particulate absorption is dominated by either algal pigments, with the major peak around 430 nm due to chlorophyll *a*, or detritus, with absorption increasing inversely relative to wavelength. The total particulate spectrum from Lake Fryxell is typical for phytoplankton cells and contained relatively little detrital absorption. Detrital absorption was greatest in Lake Bonney samples from January, primarily because of the introduction of

particulates (predominantly rock flour) from glacier-fed streams.

The range of K for PAR in the dry valley lakes (Table 2) was similar to ranges reported from coastal seas and estuaries or large lakes such as Lake Ontario and Lake Tanganyika (see Kirk [1983, Table 6.1] for a review). The lowest values were close to those reported for pelagic oceans [Kirk, 1983] such as the Sargasso Sea [Smith et al., 1989]. Absorption was typically dominated by water (38–75%), with phytoplankton usually secondary (11–47%) (Tables 2 and 3). In terms of the relative importance of light-absorbing components, the dry valley lakes appear to be more similar to an oligotrophic ocean [Smith et al., 1989] than to any of the coastal, estuarine, or inland waters described by Kirk [1983, Table 3.3]. Absorption by components other than water ($a - a_w$) was typically dominated by a_{ph} (25–83%) and under some circumstances by a_p (zero to 66%); a_{de} was always a minor component (5–31%). Lake Bonney, which has a gradient in dissolved organic carbon (DOC) that increases from 0.9 to 15.0 g m⁻³ between 10 and 20 m (J. C. Priscu and G. R. Aiken, unpublished data, December 8, 1990), consistently showed significant absorption due to gilvin at 17 m (DOC = 6.8 g m⁻³).

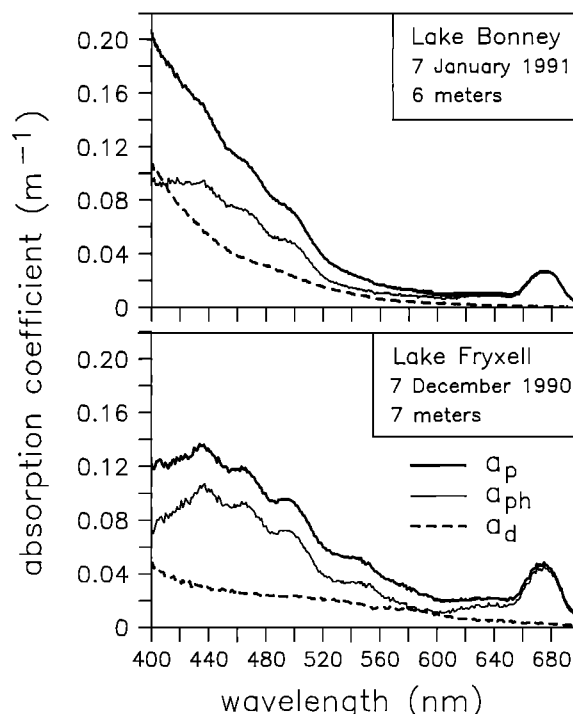


Fig. 8. Extreme examples of particulate absorbance spectra for the upper water column of dry valley lakes.

TABLE 2. Chlorophyll Concentrations and Coefficients for Attenuation (K), Scatter (b), Total Absorption (a), and Absorption Due to Water (a_w), Phytoplankton Pigments (a_{ph}), Detritus (a_{de}), and Gilvin (a_g) in Dry Valley Lakes

Lake	Depth, m	Date	Chl, mg m ⁻³	Coefficients, m ⁻¹						
				K	b	a	a_w	a_{ph}	a_{de}	a_g
Bonney	6	Nov. 24, 1990	1.17	0.143	0.365	0.096	0.062	0.021	0.011	0.003
	6	Dec. 10, 1990	0.93	0.138	0.316	0.098	0.062	0.018	0.009	0.009
	6	Jan. 7, 1991	1.45	0.246	0.402	0.205	0.077	0.023	0.020	0.085
	10	Nov. 24, 1990	0.53	0.094	0.227	0.065	0.049	0.011	0.001	0.004
	10	Dec. 10, 1990	0.93	0.107	0.320	0.066	0.049	0.019	0.004	-0.006
	10	Jan. 7, 1991	2.40	0.195	0.554	0.124	0.064	0.040	0.019	0.001
	17	Nov. 24, 1990	0.78	0.118	0.288	0.081	0.044	0.018	0.002	0.017
	17	Dec. 10, 1990	0.52	0.109	0.224	0.080	0.045	0.009	0.003	0.023
	17	Jan. 7, 1991	0.92	0.125	0.308	0.086	0.055	0.015	0.002	0.014
	Fryxell	7	Dec. 7, 1990	5.80	0.275	0.971	0.151	0.065	0.045	0.019
		8.5	Dec. 7, 1990	9.80	0.352	1.313	0.184	0.075	0.091	0.027
										-0.009

DOC concentrations of the same magnitude have been reported for Lake Fryxell [McKnight *et al.*, 1991], but high phytoplankton densities produce large values for a_{ph} and a_{de} relative to a_g . The relatively high a_g estimated for Lake Bonney at 6 m in January (41% of a) was coincident with the introduction of inorganic particulates by glacial streams. The stream water forms a layer immediately beneath the ice [Spigel *et al.*, 1991] from which particulates slowly settle out (higher a_d was measured at 6 and 10 m in January). These nonbiogenic particles will not have the same scattering properties as phytoplankton, and our estimate for b is probably low. Thus our estimates for a and a_g may be too high. It is also possible that a_g is inflated for the 6-m sample because of small rock flour particles that would not sink rapidly and may

have been too fine to be retained by the filters used to determine a_{ph} and a_{de} .

Linear regression of attenuation coefficients as a function of chlorophyll concentrations yields a slope and intercept that approximate the average pigment-specific attenuation coefficient (K_c) and a residual attenuation coefficient ($K_w + K_x$), respectively. Tyler [1975] suggested that linear regression through the points with the lowest K at a given pigment concentration can approximate conditions where the effects of constituents other than water and phytoplankton (e.g., gilvin and detritus) are minimized. All our data for both lobes of Lake Bonney, Lake Hoare, and Lake Fryxell were plotted to show the results of both types of regression analysis (Figure 9 and Table 4). The average K_c for all data and for the lowest points were

TABLE 3. Contribution of Partitioned Absorption Coefficients Due to Water (a_w), Phytoplankton Pigments (a_{ph}), Detritus (a_{de}), and Gilvin (a_g) to Total Absorption (a) in Dry Valley Lakes

Lake	Depth, m	Date	Contribution to a , %				Contribution to $(a - a_w)$, %			Type*	
			a_w	a_{ph}	a_{de}	a_g	a_{ph}	a_{de}	a_g		
Bonney	6	Nov. 24, 1990	64	22	11	3	61	31	8	W	
	6	Dec. 10, 1990	63	19	9	9	50	25	25	W	
	6	Jan. 7, 1991	38	11	10	41	18	16	66	GW	
	10	Nov. 24, 1990	75	17	2	6	69	6	25	W	
	10	Dec. 10, 1990	68	26	6	0†	83	17	0†	W	
	10	Jan. 7, 1991	52	32	15	1	67	31	2	W	
	17	Nov. 24, 1990	54	22	3	21	49	5	46	W	
	17	Dec. 10, 1990	56	11	4	29	25	9	66	W	
	17	Jan. 7, 1991	64	18	2	16	50	6	44	W	
	Fryxell	7	Dec. 7, 1990	43	30	13	14	52	22	26	WA
		8.5	Dec. 7, 1990	39	47	14	0†	77	23	0†	AW

*Dominant or codominant fractions sensu Kirk [1983]: water (W), algae (A), or gilvin (G).

†Negative a_g ; other contributions are based on sum of remaining partial coefficients.

similar, 0.029 and $0.027 \text{ m}^2 (\text{mg Chl} + \text{Phaeo})^{-1}$, respectively. The intercept for the line through the lowest points was approximately equal to the K_w estimated for similar depths in a hypothetically pure water column beneath the ice cap (Table 4). The difference between the intercept and the estimated K_w for all depths produced an estimate of 0.042 m^{-1} for K_x . However, it is important to consider that we made a conservative estimate of K_w by assuming a pure water column; this term would generally be larger if weighted to the in situ irradiance spectra influenced by the presence of phytoplankton, detritus, and gilvin (as for a_w in Table 2). Thus K_x is likely to be a high estimate. When the water column is divided into sections, K decreases and the intercept increases with depth (Table 4). The decrease in K_c with depth is consistent with observations and models for waters in which phytoplankton are important to light attenuation [e.g., *Atlas and Bannister*, 1980; *Dubinsky et al.*, 1984]. The increase in the intercept with depth is contrary to the trend for K_w , suggesting the increase is due to K_x ; the higher a estimated for deep samples (Table 2) implies that higher K_x may be associated with higher concentrations of gilvin.

Some of our values for K_c are high compared with other waters; *Kirk* [1983, Table 9.1] lists a range from 0.007 to $0.027 \text{ m}^2 (\text{mg Chl})^{-1}$ in his review. Our results corroborate the earlier observation of *Seaburg et al.* [1983] for Lake Bonney, Lake Fryxell, and Lake Hoare, where they estimated a K_c of $0.033 \text{ m}^2 (\text{mg Chl})^{-1}$ using the method of *Tyler* [1975] for the lowest points. High K_c results primarily from the spectrum of light transmitted through a thick ice cover, which is more amenable to phytoplankton absorption than the light typical of near-surface waters. Pigment packaging effects owing to high intracellular pigment concentration, which might be expected in phytoplankton populations under these low-light conditions, would have the opposite effect of lowering K_c [e.g., *Mitchell and Kiefer*, 1988].

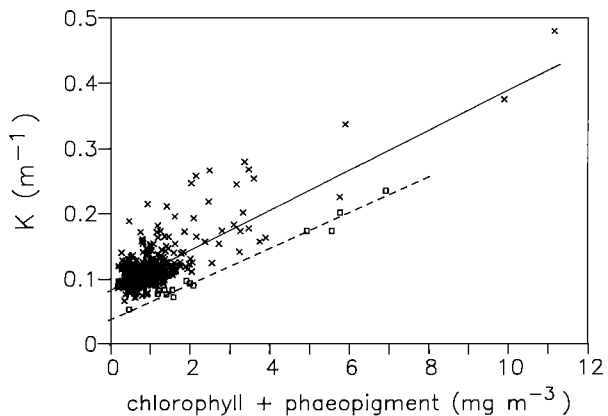


Fig. 9. Attenuation coefficients (K) plotted as a function of concentrations of chlorophyll plus phaeopigment in the dry valley lakes. The solid line is the regression line through all the data points, and the dashed line is the regression line through the points (squares) showing the lowest K values at a given pigment concentration. Regression coefficients for each line are given in Table 4.

The positive correlation between attenuation coefficients for downwelling irradiance and pigment concentrations suggests that phytoplankton biomass could be monitored from moored sensing of water column irradiance in these lakes. Phytoplankton pigments and covarying detritus were the major contributors to variation in attenuation coefficients. Gilvin may be a predictable component if DOC profiles are relatively stable over time. Exceptional conditions could follow the introduction of particulate material from glacial meltwater, but these streams flow only for a short period in summer and are subject to very large interannual variation. Because phytoplankton, gilvin, and glacial rock flour have

TABLE 4. Linear Regressions of Attenuation Coefficients on the Concentration of Chlorophyll Plus Phaeopigments (See Figure 9) for Dry Valley Lakes

	Depth, m	n	r^2	$\text{m}^2 (\text{mg Chl} + \text{Phaeo})^{-1}$	K_c^*	$K_w + K_x^{\dagger}$	$K_w^{\ddagger} \text{ m}^{-1}$	$K_x \text{ m}^{-1}$
All Data	6–20	289	0.621	0.029	0.088	0.046	0.042	
	6–10	98	0.710	0.033	0.088	0.054	0.034	
	11–15	83	0.514	0.024	0.090	0.040	0.050	
	16–20	108	0.201	0.014	0.097	0.035	0.062	
"Low" points	8–13	14	0.982	0.027	0.041	0.045	−0.004	

*Slope of regression.

†Intercept of regression.

‡Modeled on the basis of the spectrum of *Smith and Baker* [1981].

different optical properties, it may be possible to differentiate between periods in which light attenuation is affected by autochthonous materials (phytoplankton) and periods in which light attenuation is affected by allochthonous materials by monitoring irradiance at several wavelengths [e.g., *Smith et al.*, 1991; *Legendre and Gosselin*, 1991]. *Smith et al.* [1991] compared several optical models for predicting chlorophyll concentration from spectroradiometric data. They reported the best fit between the ratio of downwelling irradiance at 441 and 520 nm (E_{441}/E_{520}) and chlorophyll concentration based on a power function. This relationship is based on empirically derived constants which will vary with depth or any factor that affects spectral irradiance. Future studies of dry valley lakes should assess this approach as a rapid and potentially tractable remote method for estimating long-term changes in phytoplankton productivity, particularly when logistics preclude human presence.

CONCLUSIONS

The spectral distribution of downwelling irradiance differed significantly between Antarctic lakes, the difference being related primarily to differences in phytoplankton biomass. The spectrum of light transmitted by the ice caps was similar for both Lake Fryxell and Lake Bonney and was comparable to the spectra previously measured in Lake Hoare [*Palmisano and Simmons*, 1987]. The ice caps were most effective at attenuating red light, as does pure water, resulting in the predominance of blue and green wavelengths (440–580 nm) in the water column. Shorter wavelengths (<500 nm) were attenuated more strongly with increasing depth in these lakes. Several water column components preferentially attenuate blue light, including phytoplankton chlorophyll, detritus, and gilvin [Kirk, 1983]. An analysis of absorption due to water, phytoplankton, detritus, and, by difference, gilvin showed that water alone was the dominant component under most conditions in Lake Bonney and at shallow depths in Lake Fryxell. Exceptions were the dominance of phytoplankton absorption at the chlorophyll maxima of Lake Fryxell and the importance of gilvin absorption following the introduction of glacial stream water. Excepting the occasional periods following streamflow, the dry valley lakes have optical qualities similar to those shown for oligotrophic oceans and can be defined as case 1 waters.

The influence of spectral light quality on photosynthesis by phytoplankton is likely to be secondary to the effects of low total irradiance. For most of the phytoplankton populations in the dry valley lakes, the spectral distribution of light is predominantly

blue-green and can be efficiently absorbed by algal photosynthetic pigments. However, 3–4 m of ice with an attenuation coefficient of 1 m^{-1} reduces transmission of incident irradiance to 2–5%, with underice flux rates rarely exceeding $50\text{ }\mu\text{mol photons m}^{-2}\text{ s}^{-1}$. Results from photosynthesis-irradiance experiments suggest that phytoplankton populations in Lake Bonney, Lake Hoare, and Lake Fryxell are virtually always light-limited and are among the most shade-adapted phytoplankton reported [*Priscu et al.*, 1987; *Lizotte and Priscu*, 1991, 1992]. *Seaburg et al.* [1983] concluded that these phytoplankton either may have a high quantum efficiency for photosynthesis or are highly efficient at harvesting light. We have previously reported results suggesting that quantum efficiencies are not particularly high [*Lizotte and Priscu*, 1991, 1992], but our estimates of K_c corroborate the high values reported by *Seaburg et al.* [1983], suggesting that light-harvesting efficiency is high. The relatively high K_c in dry valley lakes appears to be a function of the blue-green dominated, water column irradiance spectra, which are conducive to absorption by photosynthetic pigments, as opposed to any adaptation or acclimation by the phytoplankton.

For remote sites such as Antarctic lakes, where logistical problems limit our ability to manually sample the environment over time, the application of moored sensors has enormous potential to expand our information base. Optical instrumentation has been successfully deployed in oceanographic time series studies, and various models have been proposed for estimating phytoplankton biomass from different types of optical data [e.g., *Smith et al.*, 1991; *Legendre and Gosselin*, 1991]. Photodiode-based optical sensors have the following advantages for future long-term deployment at remote sites: (1) no moving parts; (2) electronic data storage or transmission; (3) low cost, relative to manned field stations; and (4) appropriate instruments that are available commercially. Preliminary tests of one such optical method, based on the natural fluorescence of chlorophyll *a* measured as the upwelling irradiance at 683 nm, showed a strong relationship between predicted and measured chlorophyll concentration [*Lizotte and Priscu*, 1991]. Herein we have shown the potential for models that predict chlorophyll concentration on the basis of light attenuation. Because phytoplankton of the dry valley lakes appear to be under little grazing pressure, rates of growth and primary production can be estimated from seasonal increases in chlorophyll concentrations during the spring-summer growth season [*Sharp and Priscu*, 1991]. Hence estimates of chlorophyll alone can be used to model accurately phytoplankton production in these lakes. We suggest that future studies of long-

term changes in phytoplankton production in Antarctic lakes deploy a string of sensors to make continuous measurements of PAR, irradiance at several wavelengths (e.g., 410, 441, 507, 520, and 540 nm), and natural fluorescence to determine the most accurate model for predicting chlorophyll concentration. Such data could also be used to corroborate models developed for the open ocean.

Acknowledgments. We thank T. R. Sharp, P. J. Neale, R. H. Spigel, I. Forne, I. Sheppard, B. Hatcher, R. Nugent, B. Kelly, J. Rudek, E. Norton, and C. Taylor for their assistance in the field. Antarctic Support Associates and the U.S. Navy furnished logistical support. We also thank Anna Palmisano for providing original spectroradiometer data from her published studies of Lake Hoare. This work was supported by the National Science Foundation's Division of Polar Programs under grant DPP-882-0591 to J. C. P.

REFERENCES

- Angino, E. E., K. B. Armitage, and J. C. Tash, Physicochemical limnology of Lake Bonney, Antarctica, *Limnol. Oceanogr.*, 9, 207–217, 1964.
- Atlas, D., and T. T. Bannister, Dependence of mean spectral extinction coefficient of phytoplankton on depth, water color, and species, *Limnol. Oceanogr.*, 25, 157–159, 1980.
- Baker, K. S., and R. Frouin, Relation between photosynthetically available radiation and total insolation at the ocean surface under clear skies, *Limnol. Oceanogr.*, 32, 1370–1377, 1987.
- Bolsenga, S. J., Radiation transmittance through lake ice in the 400–700 nm range, *J. Glaciol.*, 27, 57–66, 1981.
- Bricaud, A., and D. Stramski, Spectral absorption coefficients of living phytoplankton and nonalgal biogenous matter: A comparison between the Peru upwelling area and the Sargasso Sea, *Limnol. Oceanogr.*, 35, 562–682, 1990.
- Dubinsky, Z., T. Berman, and F. Schanz, Field experiments for in situ measurement of photosynthetic efficiency and quantum yield, *J. Plankton Res.*, 6, 339–349, 1984.
- Gordon, H. R., Can the Lambert-Beer law be applied to the diffuse attenuation coefficient of ocean water?, *Limnol. Oceanogr.*, 34, 1389–1409, 1989.
- Holm-Hansen, O., C. J. Lorenzen, R. W. Holmes, and J. D. H. Strickland, Fluorometric determination of chlorophyll, *Cons. Int. Explor. Mer.*, 30, 3–15, 1965.
- Kirk, J. T. O., Monte Carlo study of the nature of the underwater light field in, and the relationship between optical properties of, turbid yellow waters, *Aust. J. Mar. Freshwater Res.*, 32, 517–532, 1981.
- Kirk, J. T. O., *Light and Photosynthesis in Aquatic Ecosystems*, 401 pp., Cambridge University Press, New York, 1983.
- Kishino, M., M. Takahashi, N. Okami, and S. Ichimura, Estimation of the spectral absorption coefficients of phytoplankton in the sea, *Bull. Mar. Sci.*, 37, 634–642, 1985.
- Koob, D. D., and G. L. Leister, Primary productivity and associated physical, chemical, and biological characteristics of Lake Bonney: A perennially ice-covered lake in Antarctica, in *Antarctic Terrestrial Biology*, *Antarct. Res. Ser.*, vol. 20, edited by G. A. Llano, pp. 51–68, AGU, Washington, D. C., 1972.
- Legendre, L., and M. Gosselin, In situ spectroradiometric estimation of microalgal biomass in first-year sea ice, *Polar Biol.*, 11, 113–115, 1991.
- Lizotte, M. P., and J. C. Priscu, Natural fluorescence and photosynthetic quantum yields in vertically stable phytoplankton from perennially ice-covered lakes (dry valleys), *Antarct. J. U.S.*, 26, 226–228, 1991.
- Lizotte, M. P., and J. C. Priscu, Photosynthesis-irradiance relationships in phytoplankton from the physically stable water column of a perennially ice-covered lake (Lake Bonney, Antarctica), *J. Phycol.*, 28, 179–185, 1992.
- McKnight, D. M., G. R. Aiken, and R. L. Smith, Aquatic fulvic acids in microbially based ecosystems: Results from two desert lakes in Antarctica, *Limnol. Oceanogr.*, 36, 998–1006, 1991.
- Mitchell, B. G., and D. A. Kiefer, Chlorophyll *a* specific absorption and fluorescence excitation spectra for light-limited phytoplankton, *Deep Sea Res.*, 35, 639–663, 1988.
- Morel, A., Optical modeling of the upper ocean in relation to its biogenous matter content (case I waters), *J. Geophys. Res.*, 93, 10,749–10,768, 1988.
- Morel, A., and L. Prieur, Analysis of variations in ocean color, *Limnol. Oceanogr.*, 22, 709–722, 1977.
- Morel, A., and R. C. Smith, Relation between total quanta and total energy for aquatic photosynthesis, *Limnol. Oceanogr.*, 19, 591–600, 1974.
- Palmisano, A. C., and G. M. Simmons, Jr., Spectral downwelling irradiance in an Antarctic lake, *Polar Biol.*, 7, 145–151, 1987.
- Parker, B. C., G. M. Simmons, Jr., K. G. Seaburg, D. D. Cathay, and F. C. T. Allnut, Comparative ecology of plankton communities in seven Antarctic oasis lakes, *J. Plankton Res.*, 4, 271–286, 1982.
- Phillips, D. M., and J. T. O. Kirk, Study of the spectral variation of absorption and scattering in some Australian coastal waters, *Aust. J. Mar. Freshwater Res.*, 35, 635–644, 1984.
- Priscu, J. C., Variation in light attenuation by the permanent ice cap of Lake Bonney during spring and summer, *Antarct. J. U.S.*, 26, 223–224, 1991.
- Priscu, J. C., L. R. Priscu, W. F. Vincent, and C. Howard-Williams, Photosynthate distribution by microplankton in permanently ice-covered Antarctic desert lakes, *Limnol. Oceanogr.*, 32, 260–269, 1987.
- Priscu, J. C., W. F. Vincent, and C. Howard-Williams, Inorganic nitrogen uptake and regeneration in perennially ice-covered lakes Fryxell and Vanda, Antarctica, *J. Plankton Res.*, 11, 335–351, 1989.
- Priscu, J. C., T. R. Sharp, M. P. Lizotte, and P. J. Neale, Photoadaptation by phytoplankton in permanently ice-covered Antarctic lakes: Response to a nonturbulent environment, *Antarct. J. U.S.*, 25, 221–222, 1990.

- Seaburg, K. G., M. Kaspar, and B. C. Parker, Photosynthetic quantum efficiencies of phytoplankton from perennially ice covered Antarctic lakes, *J. Phycol.*, **19**, 446–452, 1983.
- Sharp, T. R., and J. C. Priscu, Ambient nutrient levels and the effects of nutrient enrichment on primary productivity in Lake Bonney, *Antarct. J. U.S.*, **25**, 226–227, 1990.
- Sharp, T. R., and J. C. Priscu, Rates of primary production and growth for phytoplankton in Lake Bonney, *Antarct. J. U.S.*, **26**, 225, 1991.
- Smith, R. C., and K. S. Baker, Optical properties of the clearest natural waters, *Appl. Opt.*, **20**, 177–184, 1981.
- Smith, R. C., J. Marra, M. J. Perry, K. S. Baker, E. Swift, E. Buskey, and D. A. Kiefer, Estimation of a photon budget for the upper ocean in the Sargasso Sea, *Limnol. Oceanogr.*, **34**, 1673–1693, 1989.
- Smith, R. C., K. J. Waters, and K. S. Baker, Optical variability and pigment biomass in the Sargasso Sea as determined using deep-sea optical mooring data, *J. Geophys. Res.*, **96**, 8665–8686, 1991.
- Spigel, R. H., I. Forme, I. Sheppard, and J. C. Priscu, Differences in temperature and conductivity between the east and west lobes of Lake Bonney: Evidence for circulation within and between lobes, *Antarct. J. U.S.*, **26**, 221–222, 1991.
- Stewart, K. M., and B. E. Brockett, Transmission of light through ice and snow of Adirondack lakes, New York, *Verh. Int. Ver. Theor. Angew. Limnol.*, **22**, 72–76, 1984.
- Tsuda, R., and M. Nakanishi, Spectral distribution characteristics in downwelling irradiance and optical properties within the euphotic layer in the north basin of Lake Biwa, *Arch. Hydrobiol.*, **119**, 279–292, 1990.
- Tyler, J. E., The in situ quantum efficiency of natural phytoplankton populations, *Limnol. Oceanogr.*, **20**, 976–980, 1975.
- Vincent, W. F., Production strategies in Antarctic inland waters: Phytoplankton eco-physiology in a permanently ice-covered lake, *Ecology*, **62**, 1215–1224, 1981.

(Received September 20, 1991;
accepted April 30, 1992.)

OXYGEN ISOTOPE STUDY OF THE ICE FIELDS SURROUNDING THE RECKLING MORAINE ON THE EAST ANTARCTIC ICE SHEET

GUNTER FAURE

Byrd Polar Research Center, Ohio State University, Columbus, Ohio 43210

PIETER GROOTES

Quaternary Isotope Laboratory, University of Washington, Seattle, Washington 98195

DAVID BUCHANAN AND ERIK H. HAGEN

Byrd Polar Research Center, Ohio State University, Columbus, Ohio 43210

The model that has been proposed for the accumulation of meteorite specimens on ice fields of the East Antarctic ice sheet suggests that partial stratigraphic sections of the ice sheet are exposed at such locations. In order to verify this hypothesis, isotope compositions of oxygen were determined in ice samples collected along three survey lines across the Reckling Moraine ($76^{\circ}15'S$, $158^{\circ}40'E$). The $\delta^{18}\text{O}$ values of the ice vary from -37.9 to -51.2‰ relative to standard mean ocean water. The strongly ^{18}O -depleted ice is identified as basal ice that formed during the glacial stages of the Pleistocene epoch. However, the large number of apparent transitions from glacial to interglacial ice revealed by the data suggests that the stratigraphy of the ice, and hence the climatic record it contains, may have been disturbed locally by the structural deformation of the ice sheet. Large exposures of ice that appear to lack the variations in $\delta^{18}\text{O}$ that characterize most of the ice in this area were discovered within and adjacent to the Reckling Moraine, but the cause for this phenomenon remains to be determined.

INTRODUCTION

The Reckling Moraine (informal name) is located at $76^{\circ}15'S$, $158^{\circ}40'E$ at an elevation of about 2000 m on the East Antarctic ice sheet south of the ice flow basin of the David Glacier. The moraine lies about 18 km west of Reckling Peak ($76^{\circ}16'S$, $159^{\circ}15'E$) but is otherwise not related to it. The Reckling Moraine occurs within a broad band of exposed ice which extends west from the vicinity of Reckling Peak for about 75 km (Figure 1). The ice fields in this area have yielded more than 3300 meteorite specimens, of which 89 were collected near the Reckling Moraine (W. A. Cassidy, personal communication, 1991).

The Reckling Moraine is located in a basin that is bordered by an ice ramp along its eastern and southern sides but opens toward the northwest. The difference

in elevation between the ice plateau and the bottom of the ice basin increases from about 75 m to more than 110 m in a depression in the northeastern part of the basin. Systematic measurements of ice thickness by means of a monopulse radar device have indicated that the ice basin is underlain by a subglacial bedrock basin and that the ice forming the ramp is less than 100 m thick in some places [Faure et al., 1987; Faure, 1990a, b, c, d].

The ice underlying the Reckling Moraine contains layers of sediment-rich ice, including faceted and striated clasts of sandstone and dolerite, thus providing compelling evidence that basal ice is exposed here. Similar evidence exists in the neighboring Elephant Moraine (informal name, $76^{\circ}17'S$, $157^{\circ}20'E$) and in the area adjacent to Allan Hills ($76^{\circ}45'S$, $159^{\circ}40'E$). The basal ice crops out in these areas because the flow

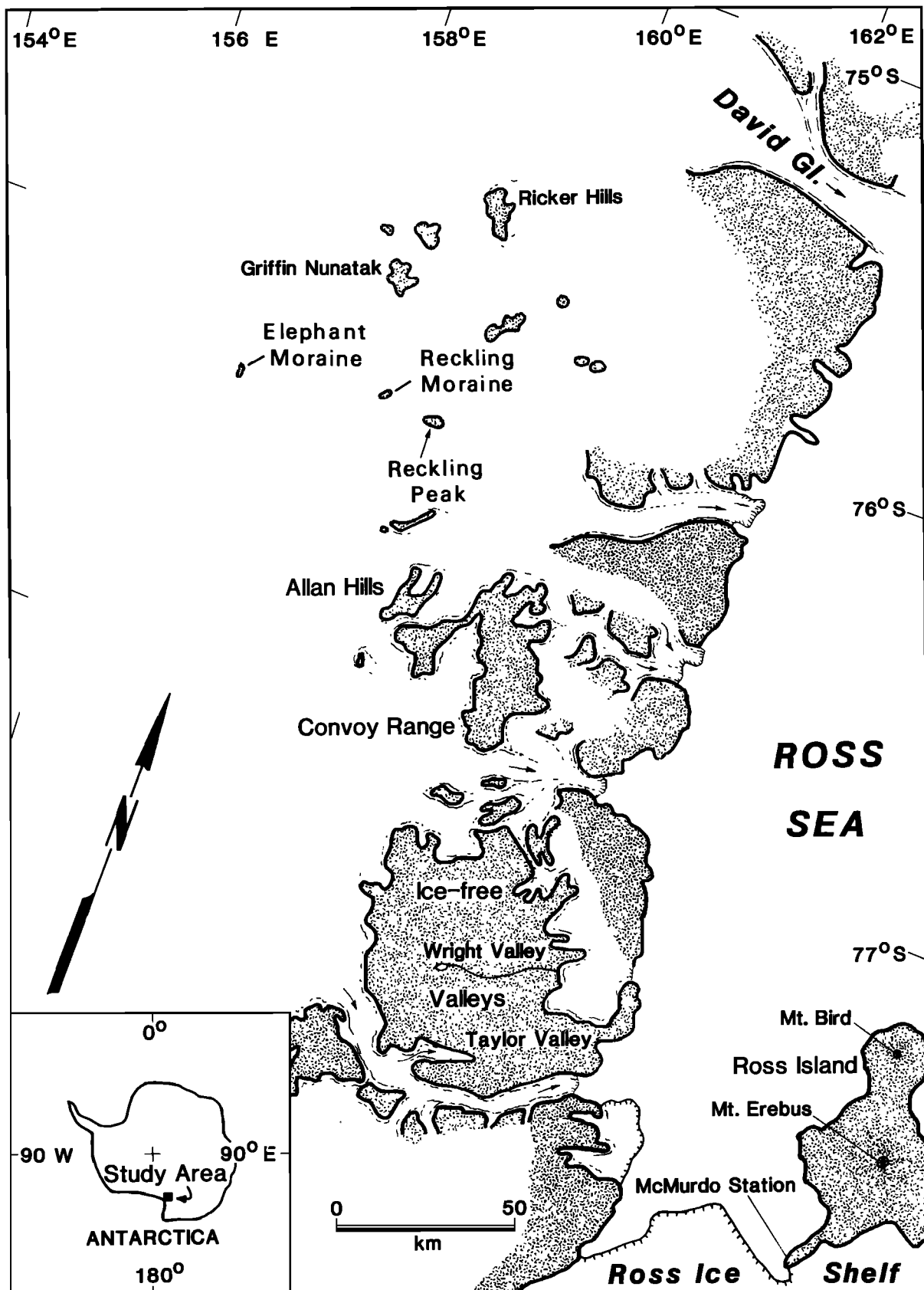


Fig. 1. Map of the eastern margin of the East Antarctic ice sheet adjacent to the Transantarctic Mountains of southern Victoria Land. The ice at the Reckling and Elephant moraines is located south of the ice drainage basin of the David Glacier.

of the East Antarctic ice sheet is locally obstructed by the mountainous subglacial bedrock topography of the western flanks of the Transantarctic Mountains [Whillans and Cassidy, 1983; Faure, 1990a; Delisle and Sievers, 1991; Faure and Buchanan, 1991]. Consequently, the ice fields adjacent to the Reckling Moraine and elsewhere may expose stratigraphic cross sections of ice ranging in age from Holocene to older than 100,000 years for basal ice.

In central East Antarctica the transition from glacial to interglacial conditions is recorded by about a 5‰ increase of the abundance of ^{18}O in the ice over a relatively short depth interval [Grootes and Stuiver, 1987; Lorius et al., 1985; Jouzel et al., 1987]. Therefore a sharp increase in $\delta^{18}\text{O}$ of about 5‰ in deep ice now exposed on the ice fields indicates a glacial to interglacial transition. For this reason the objective of this study was to use the isotope composition of oxygen of systematically collected ice samples to confirm the presence of old Pleistocene age ice in the vicinity of the Reckling Moraine by this characteristic glacial-interglacial transition in $\delta^{18}\text{O}$.

SAMPLE COLLECTION AND ANALYSIS

Samples were collected during the 1986–1987 and 1988–1989 field seasons along crosslines at 1000 E, zero, and 1000 W (Figure 2). The sampling interval in most cases was 100 m, and the ice was taken from the bottoms of shallow pits, 5–10 cm deep, in order to avoid contamination with modern snow and meltwater ice. During the 1988–1989 field season, certain segments of the survey lines were resampled at 10-m intervals in order to obtain additional information in places where major changes had been detected in the isotope composition of oxygen in the ice.

In addition, eight 1-m ice cores were taken along the zero crossline at sites marked in Figure 2. Two cores were taken at 600 S about 1 m apart in order to assess the spatial variability of the isotope composition of the ice over short distances. The ice cores were stored in plastic liners inside core tubes and shipped frozen to the Quaternary Isotope Laboratory of the University of Washington, Seattle. The cores were split in half and analyzed in 1-cm increments. Samples were cut and melted in a closed container and analyzed immediately.

The samples of near-surface ice were melted at about 24°C in sealed polyethylene bags, and the meltwater was stored in 125-mL screw-cap polyethylene bottles filled to overflowing. The bottles of meltwater were shipped unfrozen to Ohio State University.

The isotope composition of oxygen of the near-surface samples from the zero crossline (2400 N to

1800 S) and of the ice cores was determined by standard methods at the Quaternary Isotope Laboratory of the University of Washington [Grootes and Stuiver, 1986]. All other samples were analyzed by Krueger Enterprises, Cambridge, Massachusetts. The reproducibility of the $\delta^{18}\text{O}$ measurements is $\pm 0.1\text{‰}$ or better. The results are listed in the appendix.

The $\delta^{18}\text{O}$ parameter is defined as the per mil difference between the atomic $^{18}\text{O}/^{16}\text{O}$ ratio of oxygen in the sample and that of standard mean ocean water:

$$\delta^{18}\text{O} = \left[\frac{(^{18}\text{O}/^{16}\text{O})_{\text{spl}} - (^{18}\text{O}/^{16}\text{O})_{\text{std}}}{(^{18}\text{O}/^{16}\text{O})_{\text{std}}} \right] \times 10^3 \text{ ‰} \quad (1)$$

Meteoric water in Antarctica is strongly depleted in ^{18}O relative to seawater as a result of isotope fractionation in the hydrologic cycle and therefore has negative $\delta^{18}\text{O}$ values [Faure, 1986]. However, within a given set of Antarctic water samples some may be enriched in ^{18}O relative to others in that set, and their $\delta^{18}\text{O}$ values are less negative.

RESULTS AND DISCUSSION

Ice Cores

The $\delta^{18}\text{O}$ depth profiles of the cores (Figure 3) show the small-scale spatial variability in $\delta^{18}\text{O}$ in the ice as well as surface contamination. Surface contamination is expected to lead to less negative $\delta^{18}\text{O}$ values at and near the top of the cores. If the ice was formed at higher elevation in the East Antarctic interior, its ^{18}O values will be more negative than those of local snowfall. On December 19, 1986, for instance, snowfall on the Reckling Moraine had a $\delta^{18}\text{O}$ of -32.1‰ , whereas the $\delta^{18}\text{O}$ values of the neighboring ice fields range from -37.9‰ to -51.2‰ (appendix Table A1). Modern snow and/or meltwater derived from it that freezes onto the ice surface or gets incorporated in surface cracks will cause less negative $\delta^{18}\text{O}$ values at and near the surface. Enrichment of ^{18}O during ablation/sublimation may likewise produce less negative surface $\delta^{18}\text{O}$ values. Most ice cores (Figure 3) have higher $\delta^{18}\text{O}$ values at the top. In cores taken at 200 S, 601 S, and 1000 S, the contamination is limited to the top 1 cm. For 600 S and 1400 S, $\delta^{18}\text{O}$ values are higher at the surface, but the values continue to decrease with increasing depth down to about 10 cm. Although this decrease probably is a real change in the isotope composition of the ice (especially in core 1400S), it could also indicate surface contamination reaching down to about 10 cm in cracks. Contamination down to 10 cm is clearly indicated in the 000 and

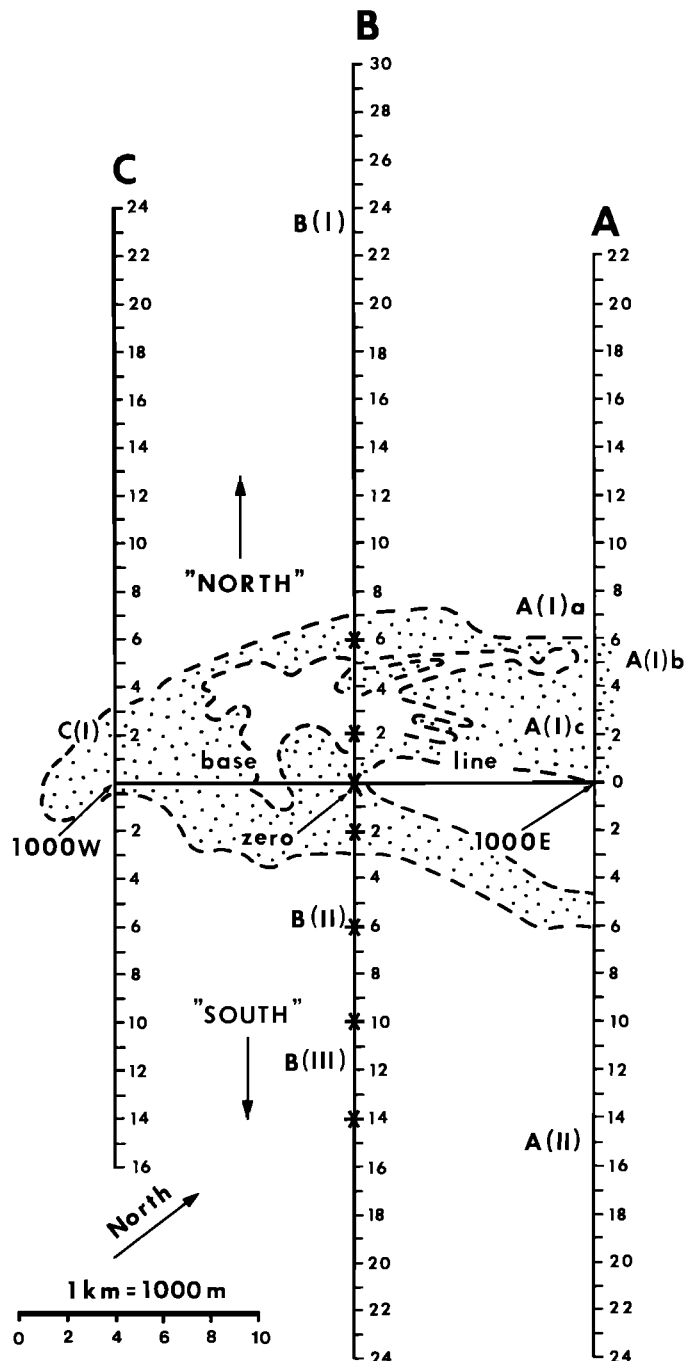


Fig. 2. Survey grid on the Reckling Moraine ($76^{\circ}15'S$, $158^{\circ}40'E$) and surrounding ice fields. The cross lines at 1000 E, zero, and 1000 W are labeled A, B, and C, respectively. Ice samples were collected at 100-m intervals, except along line segments A(I)a, A(I)b, A(I)c, A(II), B(I), B(II), B(III), B(IV), and C(I), which were sampled at 10-m intervals. The asterisks identify sites where 1-m ice cores were taken.

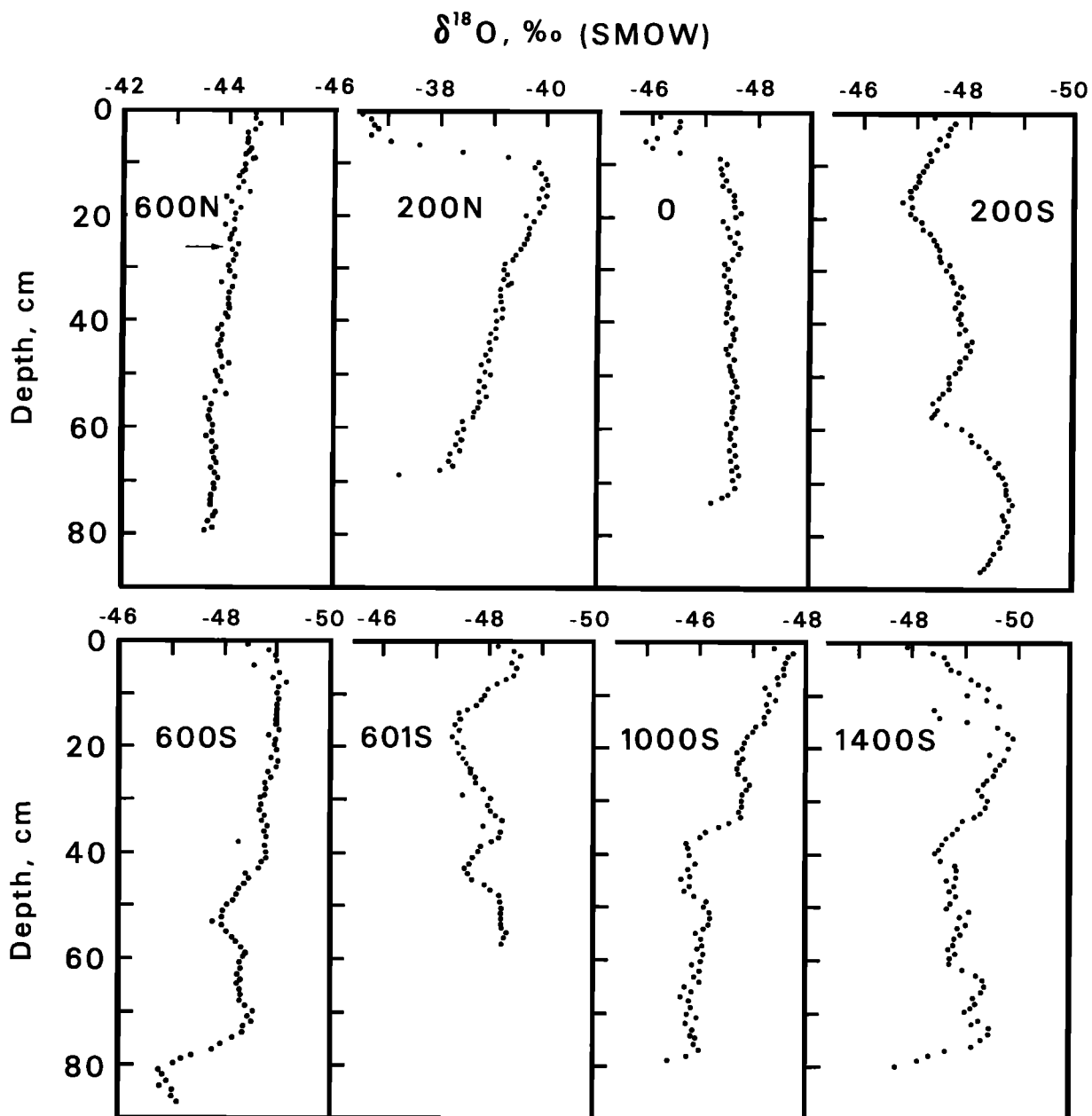


Fig. 3. The $\delta^{18}\text{O}$ profiles of 1-m ice cores taken along survey line "zero" at locations marked by asterisks in Figure 2. The oxygen in the ice cores taken at 600 N, 200 N, and zero lacks the fine structure in the isotope composition of oxygen displayed by the other cores. A discontinuity (arrow) in the $\delta^{18}\text{O}$ values at a depth of 26 cm in core 600 N was caused in our opinion by the accidental misplacement of a core segment from the bottom of the core to the top, and has been corrected in this diagram.

200 N cores. However, in core 600 N no surface contamination is evident. Therefore it appears that for surface samples, collected 5–10 cm below the surface, the probability of contamination is generally low. The most critical area is under the moraine, where water has been observed on the ice on sunny days in the summer.

Small-scale spatial variability in $\delta^{18}\text{O}$ is evident in five of eight profiles (200 S to 1400 S) in Figure 3. In these cores, $\delta^{18}\text{O}$ variations of 1–2‰ occur over distances of 20–40 cm. When we try to interpret isotope changes along the three long transects, this small-scale variability of 1–2‰ must be considered. In the remaining three cores (000, 200 N, 600 N) the $\delta^{18}\text{O}$ values are constant (000) or vary monotonically with depth (200 N, 600 N). Although the isotopic fine structure has apparently been smoothed out, the change of 1–2‰ of the $\delta^{18}\text{O}$ values in the core 200 N indicates the magnitude of the uncertainty in the interpretation of the isotope transects along the surveyed lines in Figure 2.

The reliability of the $\delta^{18}\text{O}$ values of surface samples taken from shallow pits can be checked by comparing them with the average $\delta^{18}\text{O}$ value of adjacent cores in Table 1. The difference (average $\delta^{18}\text{O}$ of core minus $\delta^{18}\text{O}$ of adjacent surface sample) ranges from -1.23 to $+2.23\text{‰}$ and has an average value of $-0.27 \pm 0.42\text{‰}$ with a single-sample scatter of 1.19‰ . The 1.2‰ scatter corresponds to that expected from the 1–2‰ small-scale variability in $\delta^{18}\text{O}$ observed in the cores. The average difference is not significantly different from zero. The difference between the average $\delta^{18}\text{O}$ values of cores 600 S and 601 S, taken 1 m apart, is $0.46\text{‰} \pm 0.08\text{‰}$, based on the uncertainty in the average $\delta^{18}\text{O}$ values of the two cores. Therefore, in this case, ice sampled 1 m

apart is isotopically different, even when averaged over a 50- to 60-cm depth interval.

Additional information about the variability of the isotope composition of oxygen is provided by analyses of 20 replicate ice samples collected during 1988–1989 at the same survey coordinates as the 1986–1987 samples (appendix Table A1). However, the second set of ice samples was not collected from the same pits because ablation of exposed ice near the Reckling Moraine (4.7 ± 0.2 cm/yr [Faure and Buchanan, 1991]) had removed nearly 10 cm of ice between 1986–1987 and 1988–1989. The average difference of $\delta^{18}\text{O}$ values of replicate samples, calculated as $\delta^{18}\text{O}_{(86/87)} - \delta^{18}\text{O}_{(88/89)}$, is $-0.3 \pm 0.3\text{‰}$, where the error is one standard deviation of the mean for 20 data sets. This result indicates that $\delta^{18}\text{O}$ values of replicate samples do not differ from each other on the average and confirms the result of the comparison of the core and surface samples.

In conclusion, the surface samples taken from a depth of more than 5 cm below the ice surface are generally unaffected by contamination and are representative of local ice with an uncertainty of about 1‰ caused by the small-scale spatial variability in the isotope composition of oxygen in the ice. This variability is the major uncertainty in interpreting the $\delta^{18}\text{O}$ profiles of the long transects.

The smoothed appearance of the $\delta^{18}\text{O}$ profiles in cores 600 N, 200 N, and 000 suggests that this ice comes from the basal parts of the ice sheet, where a long residence time, strong layer thinning, and temperature close to melting contribute to the attenuation of variability of $\delta^{18}\text{O}$ initially present in the ice. The location of these cores in the area of the moraine supports the conclusion that these cores contain basal ice.

Structure of the Ice Sheet at the Reckling Moraine

The apparent bilateral symmetry of the Reckling Moraine suggested by its shape in Figure 2 is confirmed by the layers of sediment-rich ice that crop out within it. These layers were mapped by tracing them between the surveyed lines in the moraine. The resulting map in Figure 4 reveals that the southeastern limb of the moraine contains eight layers of sediment-rich ice. At least two of these were traced in the field for more than 800 m along strike of the moraine. The southern end of the Reckling Moraine contains a well-developed layer of black ice whose outcrop pattern forms a complex "V" that opens to the north. Therefore the southern end of the Reckling Moraine appears to be the apex of a large fold in the ice sheet. The northwestern limb of the moraine also contains outcrops of black-ice layers; however, they

TABLE 1. Average $\delta^{18}\text{O}$ Values of Ice Cores From the Reckling Moraine Analyzed in 1-cm Slices

Location of Core in Survey Coordinates	Average $\delta^{18}\text{O}$, ‰	1 σ Error	Number of Analyses Included*
600 N	-43.9	±0.3	80
200 N	-39.1	±0.5	59
000	-47.5	±0.09	65
200 S	-47.8	±0.6	86
600 S	-48.4	±0.6	83
601 S	-47.9	±0.3	53
1000 S	-46.4	±0.6	76
1400 S	-49.0	±0.3	55

The locations are identified in Figure 2.

* $\delta^{18}\text{O}$ -enriched ice at the ends of the cores was excluded.

are fewer in number and less continuous than those of the southeastern limb.

The northwestern limb of the Reckling Moraine contains a large irregularly shaped area on which no sediment has accumulated. Although most of this area is covered by firn, close examination in the field indicated that the ice underlying this area does not contain sediment. Therefore this ice probably represents an interior rather than a basal section of the ice sheet and may have been associated with the basal ice underlying the moraine as a result of deformation of the ice sheet. The other large sediment-free area between the two limbs of the moraine is also underlain by clean ice.

Systematic measurements of surface elevations and ice thicknesses by Faure [1990c] indicate that the Reckling Moraine is located in the lee of a subglacial bedrock ridge which defines a large topographic basin in the subglacial bedrock and that this basin also opens toward the northwest. Therefore the horseshoe-shaped outcrop pattern of basal ice from which the Reckling Moraine has formed is apparently controlled by the local bedrock topography.

Isotope Profiles of Oxygen in the Ice

The $\delta^{18}\text{O}$ values of ice samples collected along crosslines A, B, and C (appendix Table A1) are presented graphically in Figure 5. The oxygen-isotope profiles indicate variations of the $\delta^{18}\text{O}$ parameter between -41.2‰ (line A, 800 N) and -51.2‰ (line B, 2370 N), or a range of 10.0‰ . Three sites having $\delta^{18}\text{O}$ values between -37 and -39‰ (line A, 2400 S; line B, 200 N and 2400 S) were omitted from consideration because their ^{18}O enrichment may have been caused by contamination with recent snow. The location of 200 N on line A is in the moraine where water has been observed, whereas the ice at 2400 S on lines A and B is crevassed and covered with firn. However, even in this trimmed data set the range of $\delta^{18}\text{O}$ values exceeds the analytical error as well as the small-scale heterogeneity of the oxygen isotope composition of the ice. Therefore the variation of the $\delta^{18}\text{O}$ values conveys information about major changes in paleoclimatic conditions in the source areas of the ice. In addition, the $\delta^{18}\text{O}$ profiles may reflect the structure of the ice fields adjacent to the Reckling Moraine (see Figure 5).

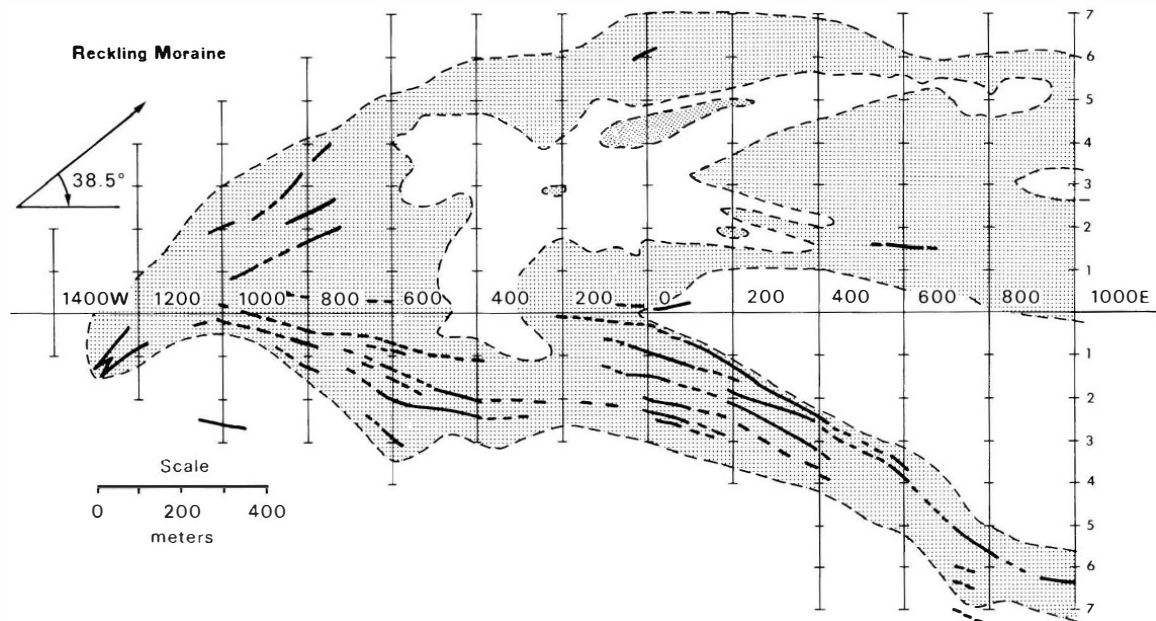


Fig. 4. Map of the outcrop pattern of layers of black, sediment-rich ice underlying the Reckling Moraine. The map suggests that the southern end of the moraine is the apex of a large fold in the ice sheet and that the shape of the moraine reflects the structure of the ice sheet at this location.

In the low-accumulation areas of the East Antarctic plateau the main features in $\delta^{18}\text{O}$, preserved in the ice, are the glacial/interglacial difference of about 5‰ and differences related to the elevation of the ice sheet. Ice flow lines in the area of the Reckling Moraine originate on the central East Antarctic ice divide near Dome Charlie (Dome C) [Drewry and Robin, 1983]. Mean surface $\delta^{18}\text{O}$ values range from -50.3‰ at Dome Charlie (elevation 3240 m) to -45‰ at about 2000 m near the Transantarctic Mountains [Loriis, 1983]. Therefore the 10‰ range in $\delta^{18}\text{O}$ values along the transects at the Reckling Moraine indicates major differences in the origin of the sampled ice. Because the observed range of $\delta^{18}\text{O}$ values is significantly greater than the 5–6‰ expected for glacial-interglacial transitions, differences in elevation of the source are also called for. The most negative $\delta^{18}\text{O}$ values observed (<-50‰) correspond with current mean surface snow values at Dome Charlie. The observed $\delta^{18}\text{O}$ range from -41.2‰ to -51.2‰ thus supports the model of Whillans and Cassidy [1983], which identifies the interior of East Antarctica as the source of the ice in the ice fields located adjacent to the Transantarctic Mountains.

Because of the long residence time of ice formed near the East Antarctic ice divide and the strong compression of the time scale near the bottom of the ice sheet, the deep sections of the ice sheet exposed in the blue-ice areas near the Reckling Moraine may encompass several hundred thousand years and several glacial/interglacial cycles.

The $\delta^{18}\text{O}$ profiles in Figure 5 also suggest the occurrence of ice that lacks the variations in the isotopic composition of oxygen that characterize the ice fields adjacent to the Reckling Moraine. Whereas some of the ice cores demonstrate the absence of isotopic variability on a scale of 1 m, the $\delta^{18}\text{O}$ profiles based on surface ice reveal areas up to 400 m in diameter in which the isotope composition of oxygen varies only within a narrow range of values when sampled in 100-m intervals. The best example of this phenomenon occurs along line C (Figure 5) from 600 S to 1000 S, where $\delta^{18}\text{O}$ changes from -45.1‰ (600 S) to -45.9‰ (1000 S), or only 0.2‰ per 100 m of linear distance. Additional exposures of ice with nearly constant $\delta^{18}\text{O}$ values can be readily identified along lines A and B. The origin of this kind of ice is not known at this time, but large-scale isotopic

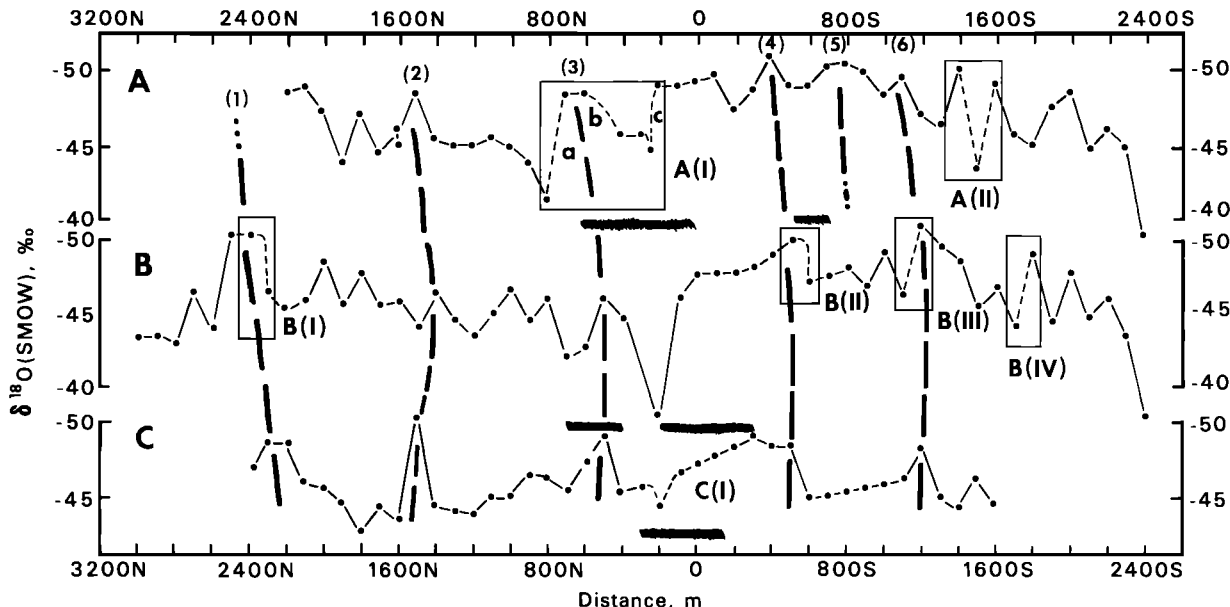


Fig. 5. Profiles of $\delta^{18}\text{O}$ values of ice sampled at 100-m intervals along survey lines A, B, and C identified in Figure 2. Correlations of layers of ^{18}O -depleted ice between the lines are suggested, and the layers are numbered from 1 to 6 for reference. Line segments IAa, IAb, etc., were sampled at 10-m intervals, and the resulting $\delta^{18}\text{O}$ profiles are assembled in Figure 6. The lateral continuity of the ice suggested here is supported by the sediment bands on the ice and the layers of sediment-rich (black) ice under the moraine shown in Figure 4. The shaded areas represent the sediment of the moraine.

homogenization of ice at the bottom of the East Antarctic ice sheet is a possible explanation.

The 10-m $\delta^{18}\text{O}$ Profiles

If the $\delta^{18}\text{O}$ profiles in Figure 5 represent continuous or fragmented stratigraphic cross sections of the East Antarctic ice sheet, the question arises whether the 100-m sampling interval is adequate to detect all of the major features of such profiles. For this reason, samples were collected at 10-m intervals along each of the three survey lines in places where significant changes in the $\delta^{18}\text{O}$ parameter had been recorded. These more closely sampled profiles are identified in Figure 5 and have been assembled in Figure 6. Not surprisingly, in some cases the closer spacing reveals additional detail in the $\delta^{18}\text{O}$ profiles, whereas in other cases the pattern of variation suggested by the 100-m samples is confirmed by the additional samples. In the latter category are profiles A(I)a, A(II), and B(IV). However, the remaining profiles contain new information and therefore require closer examination.

The detailed pattern at A(I)b indicates five significant decreases of $\delta^{18}\text{O}$ over a horizontal distance of 200 m. The amplitude of these excursions

ranges from about 3.5 to 5.0‰ and significantly exceeds the small-scale heterogeneity of $\delta^{18}\text{O}$ in the ice. In principle, this $\delta^{18}\text{O}$ profile may record multiple climatic transitions from glacial to interglacial conditions. If that is so, then the ice in section A(I)b may have formed over a long period of time in the course of the Pleistocene epoch, which lasted about 2×10^6 years. The terrestrial ages of meteorites recovered from the surface of the East Antarctic ice sheet vary widely from 2×10^3 to 1×10^6 years [Nishiizumi et al., 1989] and therefore support the conclusion that old ice is exposed in some of the ice fields on which meteorites have accumulated.

However, when every fluctuation of $\delta^{18}\text{O}$ is interpreted as a climate event, the number becomes excessive. The presence of the Reckling Moraine is evidence that the ice flow in the area is obstructed and that basal ice is forced to the surface. Under these conditions, one may expect low-angle thrust faulting, which could intercalate ice with different $\delta^{18}\text{O}$ values from different parts of the ice sheet. Support for this suggestion is provided by the occurrence of sediment in the Reckling Moraine in the form of parallel stripes, one of which is shown in Figure 7. Typically, these stripes have a sharply defined boundary on one side

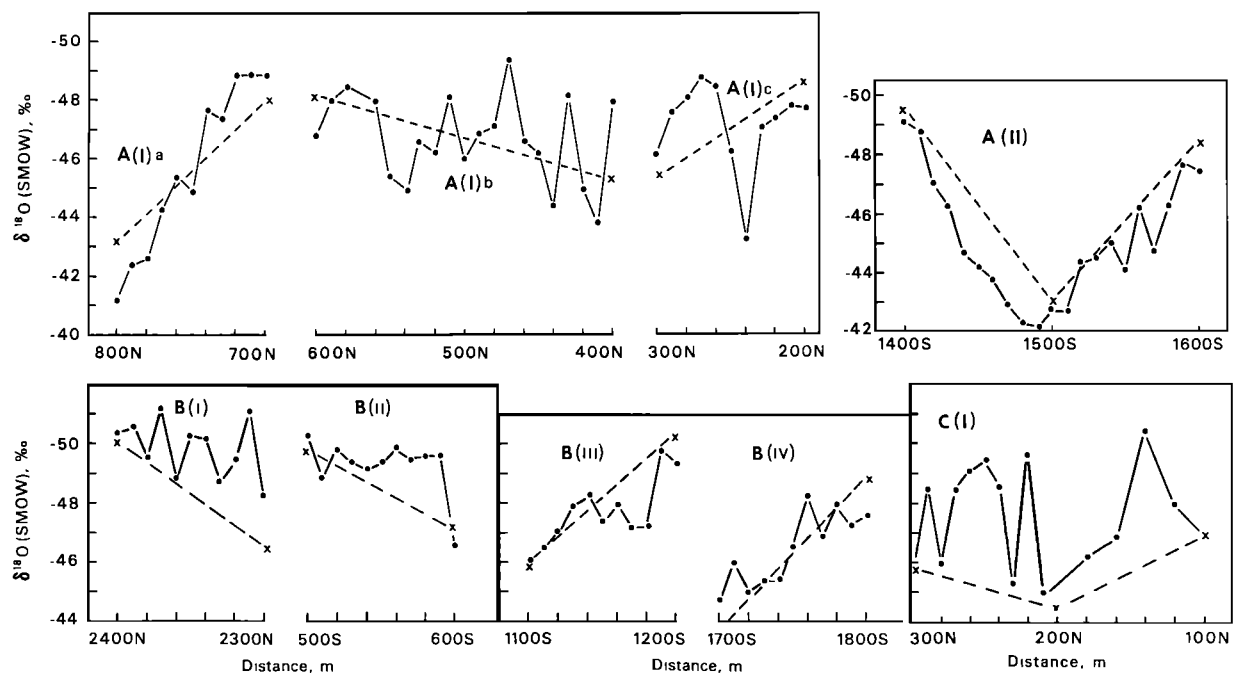


Fig. 6. Profiles of $\delta^{18}\text{O}$ values of ice sampled at 10-m intervals along segments of the survey lines identified in Figure 5. The dashed lines are linear interpolations of $\delta^{18}\text{O}$ values of ice samples collected at 100-m intervals.

and a more gradual boundary on the other. According to the interpretation suggested above, each sediment stripe may consist of a faulted section of basal ice grading up-section into ice that contains scattered rock clasts transported englacially.

Therefore at least some of the multiple transitions of $\delta^{18}\text{O}$ in segment A(I)b and others in Figures 5 and 6 may be caused by intercalation of $\delta^{18}\text{O}$ -depleted ("cold") ice with less ^{18}O -depleted ("warm") ice from another part of the section.

SUMMARY

The blue-ice area of the Reckling Moraine thus exposes ice from past glacial period(s) whose age may exceed 10^5 years. However, it is not easy to interpret a horizontal "core" along the surface because faulting may repeat time intervals and alter the sequence of climatic events recorded by the ice.

The parallel sediment stripes and layers of black ice observed in the Reckling Moraine suggest that layers



Fig. 7. Sediment stripe on the Reckling Moraine. The stripes may represent fault slices of basal ice from which sediment is liberated by sublimation of the enclosing ice. Part of the ice ramp associated with the Reckling Moraine is visible in the background.

of basal ice are exposed at the surface and are being sampled along each of the three transects. Therefore the three $\delta^{18}\text{O}$ profiles of Figure 5 should be correlated, and some tentative correlations are indicated by the dashed lines (1) to (6).

The results of the sampling at 10-m intervals indicate that even more detailed sampling will be required to reveal the true pattern of $\delta^{18}\text{O}$ fluctuations exposed at the surface. In addition, the correlations between the different profiles must be confirmed before a climate and flow history of the ice sheet can be constructed from ice exposed at the surface.

TABLE A1. $\delta^{18}\text{O}$ Values of Ice From the Reckling Moraine and the Surrounding Ice Fields

Location	$\delta^{18}\text{O}$, ‰	Location	$\delta^{18}\text{O}$, ‰
<i>A, Crossline 1000 E (see Figure 2), 1986–1987</i>			
0	-48.9		
100 N	-48.7	100 S	-49.3
200 N	-48.7, -47.7	200 S	-47.1
300 N	-45.4, -46.2	300 S	-48.3
400 N	-45.3, -48.0	400 S	-50.7
500 N	-46.0	500 S	-48.5
600 N	-48.2, -46.8	600 S	-48.4
700 N	-48.1, -48.9	700 S	-49.9
800 N	-43.2, -41.2	800 S	-50.0
900 N	-43.7	900 S	-49.4
1000 N	-44.7	1000 S	-47.8
1100 N	-45.3	1100 S	-49.0
1200 N	-44.8	1200 S	-46.4
1300 N	-44.8	1300 S	-45.6
1400 N	-45.1	1400 S	-49.6, -49.1
1500 N	-48.3	1500 S	-43.1, -42.7
1600 N	-45.9, -45.0	1600 S	-48.5, -47.5
1700 N	-44.3	1700 S	-45.0
1800 N	-47.0	1800 S	-44.5
1900 N	-43.7	1900 S	-46.9
2000 N	-47.3	2000 S	-47.8, -44.7
2100 N	-48.8	2100 S	-44.1
2200 N	-48.5	2200 S	-45.3
		2300 S	-44.2
		2400 S	-38.3
<i>A(I)a, Crossline 1000 E, 1988–1989</i>			
		760 N	-45.4
710 N	-48.9,	770 N	-44.3
720 N	-48.9	780 N	-42.6
730 N	-47.4	790 N	-42.4
740 N	-47.7		
750 N	-44.9		
<i>A(I)b, Crossline 1000 E, 1988–1989</i>			
410 N	-43.8	510 N	-48.1
420 N	-45.0	520 N	-46.2
430 N	-48.2	530 N	-46.6
440 N	-44.4	540 N	-44.9
450 N	-46.2	550 N	-47.4
460 N	-46.6	560 N	-48.0
470 N	-49.4	570 N	

TABLE A1. (continued)

Location	$\delta^{18}\text{O}$, ‰	Location	$\delta^{18}\text{O}$, ‰
480 N	-47.1	580 N	-48.5
490 N	-46.9	590 N	-48.0
<i>A(I)c, Crossline 1000 E, 1988–1989</i>			
210 N	-47.8	260 N	-48.5
220 N	-47.4	270 N	-48.8
230 N	-47.1	280 N	-48.1
240 N	-43.3	290 N	-47.6
250 N	-46.3		
<i>A(II) Crossline 1000 E, 1988–1989</i>			
1410 S	-48.8	1510 S	-42.7
1420 S	-47.0	1520 S	-44.3
1430 S	-46.3	1530 S	-44.5
1440 S	-44.6	1540 S	-45.0
1450 S	-44.2	1550 S	-44.1
1460 S	-43.8	1560 S	-46.2
1470 S	-42.9	1570 S	-44.7
1480 S	-42.3	1580 S	-46.3
1490 S	-42.2	1590 S	-47.7
<i>B, Crossline Zero (see Figure 2), 1986–1987</i>			
0	-48.2		
100 N	-46.7	100 S	-47.4
200 N	-37.9, -38.1	200 S	-47.6
300 N		300 S	-47.9
400 N	-45.3	400 S	-48.9
500 N	-45.7	500 S	-49.9, -50.3
600 N	-42.8	600 S	-47.2, -46.6
700 N	-41.8	700 S	-47.1
800 N	-45.6	800 S	-47.7
900 N	-44.2	900 S	-46.6
1000 N	-47.0	1000 S	-48.7
1100 N	-44.6	1100 N	-46.1, -46.1
1200 N	-44.0	1200 S	-50.4, -49.4
1300 N	-44.4	1300 S	-49.2
1400 N	-47.0	1400 S	-48.2
1500 N	-44.2	1500 S	-45.2
1600 N	-45.5	1600 S	-46.6
1700 N	-46.1	1700 S	-43.8, -44.7
1800 N	-47.5	1800 S	-49.0, -47.6
1900 N	-45.2	1900 S	-43.9
2000 N	-49.2	2000 S	-46.8
2100 N	-45.2	2100 S	-44.6
2200 N	-45.9	2200 S	-45.8
2300 N	-46.7, -48.3	2300 S	-43.3
2400 N	-49.8, -50.4	2400 S	-37.8
2500 N	-50.2	Snow	-32.1
		Dec. 19, 1986	
2600 N	-43.8	Firm	-36.1
2700 N	-46.4		
2800 N	-43.0		
2900 N	-43.6		
3000 N	-43.5		
<i>B(I), Crossline Zero, 1988–1989</i>			
2310 N	-51.1	2360 N	-48.8
2320 N	-49.4	2370 N	-51.2
2330 N	-48.7	2380 N	-49.5
2340 N	-50.2	2390 N	-50.5
2350 N	-50.3		

TABLE A1. (continued)

Location	$\delta^{18}\text{O}$, ‰	Location	$\delta^{18}\text{O}$, ‰
510 S	-48.8	560 S	-49.8
520 S	-49.8	570 S	-49.5
530 S	-49.4	580 S	-49.6
540 S	-49.2	590 S	-49.6
550 S	-49.4		
<i>B(II), Crossline Zero, 1988–1989</i>			
1110 S	-46.5	1160 S	-47.9
1120 S	-47.0	1170 S	-47.2
1130 S	-47.9	1180 S	-47.2
1140 S	-48.2	1190 S	-49.8
1150 S	-47.4		
<i>B(III), Crossline Zero, 1988–1989</i>			
1710 S	-46.0	1760 S	-48.3
1720 S	-45.0	1770 S	-46.9
1730 S	-45.4	1780 S	-47.9
1740 S	-45.4	1790 S	-47.3
1750 S	-46.5		
<i>C, Crossline 1000 W (see Figure 2), 1988–1989</i>			
0	-47.3		
100 N	-46.9	100 S	-48.1
200 N	-44.4	200 S	-48.5
300 N	-45.8	300 S	-49.2
400 N	-45.6	400 S	-48.7
500 N	-49.6	500 S	-48.6
600 N	-47.3	600 S	-45.1
700 N	-45.6	700 S	-45.3
800 N	-46.7	800 S	-45.5
900 N	-47.0	900 S	-45.8
1000 N	-45.1	1000 S	-45.9
1100 N	-45.0	1100 S	-46.4
1200 N	-44.8	1200 S	-48.5
1300 N	-44.3	1300 S	-45.2
1400 N	-44.5	1400 S	-44.3
1500 N	-50.4	1500 N	-46.5
1600 N	-43.6	1600 N	-44.7
1700 N	-44.6	1700 N	-44.6
1800 N	-42.8	1800 N	-42.8
1900 N	-44.8	1900 N	-44.8
2000 N	-45.8	2000 N	-45.8
2100 N	-46.1	2100 N	-48.7
2200 N	-48.7	2200 N	-48.7
2300 N	-48.8	2300 N	-48.8
2400 N	-46.9	2400 N	-46.9
<i>C(I), Crossline 1000 W, 1988–1989</i>			
120 N	-47.9	230 N	-45.2
140 N	-50.4	240 N	-48.6
160 N	-46.8	250 N	-49.4
180 N	-46.2	260 N	-49.1
200 N	-44.4	270 N	-48.5
210 N	-44.9	280 N	-45.9
220 N	-49.7	290 N	-48.5

The survey coordinates of each site refer to Figure 2. All distances are in meters, and the $\delta^{18}\text{O}$ values are expressed relative to standard mean ocean water.

Acknowledgments. We thank Michael L. Strobel, R. J. Elliot, and T. A. Aebie for assistance in the field and Kathleen L. Doddroe for typing this manuscript. We thank two anonymous reviewers for their comments that helped us to improve this paper. This paper is contribution 81 of the Laboratory for Isotope Geology and Geochemistry of the Department of Geological Sciences, The Ohio State University. The research on which this paper is based was supported by the National Science Foundation through grants DPP-8314136 and DPP-8716088.

REFERENCES

- Delisle, G., and J. Sievers, Sub-ice topography and meteorite finds near the Allan Hills and the Near Western ice field, Victoria Land, Antarctica, *J. Geophys. Res.*, 96(E1), 15,577–15,587, 1991.
- Drewry, D. J., and G. de Q. Robin, Form and flow of the Antarctic ice sheet during the last million years, in *The Climatic Record in Polar Ice Sheets*, edited by G. de Q. Robin, pp. 28–36, Cambridge University Press, New York, 1983.
- Faure, G., *Principles of Isotope Geology*, 2nd ed., 589 pp., John Wiley, New York, 1986.
- Faure, G., Origin of stranding surfaces, *LPI Tech. Rep.* 90-03, 11–15, 1990a.
- Faure, G. Physical description of the Elephant and Reckling moraines, *LPI Tech. Rep.* 90-03, 24–25, 1990b.
- Faure, G., Subice topography and the formation of supraglacial moraines, *LPI Tech. Rep.* 90-03, 32–33, 1990c.
- Faure, G. Supraglacial moraines, associated meteorites and climate change, *LPI Tech. Rep.* 90-03, 33–35, 1990d.
- Faure, G., and D. Buchanan, Ablation rates of the ice fields in the vicinity of the Allan Hills, Victoria Land, Antarctica, in *Contributions to Antarctic Research II*, edited by D. E. Elliot, *Antarct. Res. Ser.*, vol. 53, pp. 19–31, AGU, Washington, D. C., 1991.
- Faure, G., M. L. Strobel, E. H. Hagan, and D. Buchanan, Glacial geology of the Reckling Moraine on the East Antarctic ice sheet, *Antarct. J. U.S.*, 22(5), 61–63, 1987.
- Grootes, P. M., and M. Stuiver, Ross Ice Shelf oxygen isotopes and West Antarctic climate history, *Quat. Res.*, 26, 49–67, 1986.
- Grootes, P. M. and M. Stuiver, Ice sheet elevation changes from isotope profiles, in *The Physical Basis of Ice Sheet Modelling*, IAHS Publ. 170, pp. 269–281, International Association of Hydrological Sciences, Washington, D. C., 1987.
- Jouzel, J., C. Lorius, J. R. Petit, C. Genthon, N. I. Barkov, V. M. Kotlyakov, and V. M. Petrov, Vostok ice core: A continuous isotope temperature record over the last climatic cycles (160,000 years), *Nature*, 239, 403–407, 1987.
- Lorius, C., Antarctica: Survey of near-surface mean isotopic values, in *The Climatic Record of Polar Ice Sheets*, edited by G. de Q. Robin, pp. 52–56, Cambridge University Press, New York, 1983.
- Lorius, C., J. Jouzel, C. Ritz, L. Merlivat, N. I. Barkov, Y. S. Korotkevich, and V. M. Kotlyakov, A 150,000-year climatic record from Antarctic ice, *Nature*, 316, 519–596, 1985.
- Nishizumi, K., D. Elmore, and P. W. Kubik, Update on terrestrial ages of Antarctic meteorites, *Earth Planet Sci. Lett.*, 93, 299–313, 1989.
- Whillans, I. M., and W. A. Cassidy, Catch a falling star: Meteorites and old ice, *Science*, 222, 55–57, 1983.

(Received December 15, 1991;
accepted March 20, 1992.)

**SCALLOP SHELL MINERALOGY AND CRYSTALLINE CHARACTERISTICS:
PROXY RECORDS FOR INTERPRETING ANTARCTIC NEARSHORE
MARINE HYDROCHEMICAL VARIABILITY**

PAUL ARTHUR BERKMAN

Byrd Polar Research Center, Ohio State University, Columbus, Ohio 43210

DENNIS W. FOREMAN AND JOHN C. MITCHELL

Department of Geological Sciences, Ohio State University, Columbus, Ohio 43210

ROBERT J. LIPTAK

Springfield Environmental, Incorporated, Springfield, Ohio 45501

The mineralogy of nearshore Antarctic scallop shells may reveal hydrochemical variations associated with ice sheet marginal changes around the continent during the last 10,000 years. However, as a first step, it is necessary to understand how shell composition and shell formation vary with environmental conditions today. X ray diffraction analysis is a technique that can be used to interpret the mineralogy of a shell in relation to its crystalline characteristics, from the unit cells (angstrom scale) that contain the basic symmetry of the crystals to the proportions of aragonite and calcite in the microstructures that can be visualized with scanning electron microscopes. Trace element concentrations in modern Antarctic scallop shells, collected across a nearshore depth gradient adjacent to a summer glacial meltwater stream in west McMurdo Sound, significantly decreased with depth. These Antarctic scallop shells, as with bay scallop and sea scallop shells, reveal that isomorphous substituents with atomic radii larger than that of calcium are substituted into the intracrystalline lattice sites of the unit cells. Divalent cations with smaller atomic radii, even if they reflect nearshore environmental variation today, may occur outside of the unit cells in intercrystalline spaces that would be susceptible to diagenesis over time. Significant differences between the crystalline characteristics and the mineralogy of the upper and lower scallop valves also indicate that the shell valves cannot be indiscriminately used to assess environmental variation. Future mineralogical analyses of Antarctic scallop shells, and other coastal marine species that have fossils around the continent, should focus on the relatively stable compositional characteristics of the unit cells to interpret Holocene environmental variability associated with the ice sheet margins.

INTRODUCTION

The Antarctic scallop *Adamussium colbecki* is widely distributed in nearshore marine environments around the continent today [Berkman, 1988a] and in adjacent beaches over the last 10,000 years [Berkman, 1992]. These extant and fossil pectinid bivalve mollusc assemblages are proximal to the margins of the Antarctic ice sheets and, along with other coastal

marine species, they may be impacted by variations in meltwater production (Figure 1). Preliminary isotopic and trace element analyses of modern *A. colbecki* shells, collected in the vicinity of a glacial meltwater stream in west McMurdo Sound, suggest that they may contain meltwater signatures [Berkman, 1991]. These data indicate that the composition of nearshore shells of *A. colbecki* may provide a framework for interpreting how the Antarctic ice sheet margins have

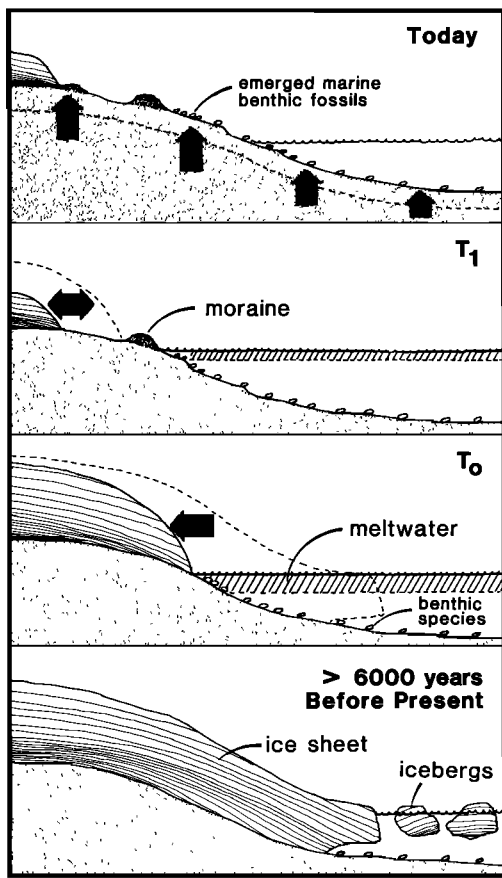


Fig. 1. Illustration of marine benthic species responses to ice sheet changes around Antarctica during the Holocene (last 10,000 years) based on interpretations from Wilson [1978], Denton et al. [1989], and Berkman [1992]. After the ice sheet margins retreated (>6000 years B.P.), benthic species migrated into shallow water (T_0). These nearshore marine benthic species would have been impacted by meltwater pulses associated with ice sheet marginal fluctuations that also may have impacted eustatic sea level (T_1). Ultimately, these nearshore marine benthic species became incorporated into beaches which emerged above sea level (today). It is hypothesized that emerged marine benthic fossils around the continent may retain records of meltwater input that can be used for interpreting how the margins of the Antarctic ice sheets responded to different climatic conditions during the Holocene and how they influenced eustatic sea level changes during this period.

responded to different climatic conditions during the Holocene.

Molluscan shell composition has been studied extensively in relation to environmental variability [Rhoads and Lutz, 1980]. Among modern molluscan assemblages, variations in shell trace element concentrations have been attributed to temperature

[Dodd, 1965], salinity [Rucker and Valentine, 1961; Eisma et al., 1976], productivity [Mullin and Riley, 1956], depositional regime [Brooks and Rumsby, 1965; Windom and Smith, 1972], and pollution [Eisler, 1981]. These environmental signatures would be superimposed on trace element variations associated with ontogenetic [Rosenberg, 1980; Carricker et al., 1982] and generic calcite:aragonite characteristics [Turekian and Armstrong, 1960; Carter, 1980] of the shells. Problems arise when these modern environmental analogs are extrapolated to fossil assemblages because shell mineralogy can be diagenetically altered over time [Curtis and Krinsley, 1965; Nelson, 1967; Rosenberg, 1980]. Constraining the diagenetic susceptibility of the elements in a shell matrix would enhance their utility as proxies for evaluating environmental variation, especially among extant species that have fossil chronologies for interpreting environmental conditions into the geologic past.

Mollusc shells are predominantly composed of calcium carbonate which is precipitated as aragonite and calcite, and less commonly as vaterite. Crystals associated with these phases have characteristic symmetry and chemical compositions, and in molluscan shells they form distinct microstructures [Wilbur, 1972; Carter and Clark, 1985] that vary among molluscan taxa [Boggs, 1930; Carter, 1980, 1990a, b]. These microstructures, which generally are composed of aragonite or calcite, can be visualized with scanning electron microscopes [Taylor et al., 1969; Gregoire, 1972; Barrera et al., 1990]. The average proportions of aragonite and calcite in whole shells, another molluscan generic characteristic, can be determined by X ray diffraction analysis [Turekian and Armstrong, 1960].

More importantly, X ray diffraction analysis can be used to resolve the physical-chemical properties of the crystals [Hurlbut, 1959] in molluscan shells [Lorens and Bender, 1977; Runnegar, 1983]. These crystalline characteristics extend from the calcite and aragonite proportions in the microstructures (micron scale) to the unit cells (angstrom scale) which are the basic components of the crystalline lattice.

Isomorphous substitutions for calcium in the unit cells, by cations with smaller or larger atomic radii, can be determined by comparison with pure calcite or aragonite standards. Elements substituting within the intracrystalline lattice sites of the unit cells would be thermodynamically stable [Swalin, 1962] relative to those in the intercrystalline spaces outside and therefore less susceptible to diagenesis. Understanding the mineralogical characteristics of modern *Adamussium colbecki* shells in relation to nearshore environmental variation today will provide constraints for interpreting the hydrochemical conditions that

impacted fossil scallop shells adjacent to the Antarctic ice sheet margins earlier in the Holocene.

This paper examines the geochemistry of modern scallop shells that lived adjacent to meltwater streams in west McMurdo Sound, Antarctica. Results of atomic absorption analyses will be used to document the trace element concentrations in shells collected across a nearshore depth gradient. Results of X ray diffraction analyses will be used to identify their calcite:aragonite ratios and calcite unit cell characteristics. Together, these data will provide a framework for interpreting hydrochemical signatures in Antarctic scallop shells exposed to meltwater in nearshore marine environments.

MATERIALS AND METHODS

Samples

Live Antarctic scallops (*Adamussium colbecki*) were collected in January 1987 with scuba across a depth gradient adjacent to the Wales Glacier meltwater stream at Explorers Cove ($77^{\circ}35'S$, $163^{\circ}40'E$), Antarctica, which is on the western side of McMurdo Sound in the southern Ross Sea [Berkman, 1990]. Four *A. colbecki* shells from 6, 10, and 21 m depth were analyzed by atomic absorption to determine their trace element concentrations. Three additional *A. colbecki* shells from 15 m depth were analyzed by X ray diffraction along with three shells each from two temperate scallop species; these provided a control for interpreting the relation between shell mineralogy and crystalline characteristics. The bay scallop (*Argopecten irradians*) was collected in July 1986 from 2 m depth in Charlestown Pond ($41^{\circ}21'N$, $71^{\circ}30'E$), which is a coastal lagoon in Rhode Island [Berkman, 1986]. The sea scallop (*Placopecten magellanicus*) was collected in July 1987 with the submersible *Delta* at 200 m depth on Fippennies Ledge ($42^{\circ}47'N$, $69^{\circ}17'E$) in the Gulf of Maine [Berkman, 1988b]. Each shell in the above analyses included both the upper and the lower valves.

Sample Preparation

Each shell valve was scrubbed with a brush, and all remaining epizoic species (such as foraminifera, bryozoans, and barnacles) were scraped from the shell surface with a clean scalpel blade. The shells then were ultrasonicated in double-distilled demineralized water. When completely dry, each valve was weighed and measured. The heights, weights, and weight:area ratios of the three shells from each scallop species, separated into upper and lower valves, are shown in Table 1 for the X ray diffraction analyses.

Each whole valve then was cut with a diamond surface low-speed rotary saw into 1-cm² fragments that were ground into a fine-grained homogenized powder by an eccentric sliding disc mill for 1 to 2 hours. This procedure disrupted the microstructures but was not sufficient to cause a phase transformation of calcite into aragonite, which is known to occur after prolonged mechanical grinding greater than 12 hours [Burns and Bredig, 1956; Jamieson and Goldsmith, 1960; Lippman, 1973]. The bulk powder samples of each shell valve provided approximately 4 cm³ for the atomic absorption and X ray diffraction analyses.

Atomic Absorption Analysis

The homogenized powders of the whole shell valves were dissolved in HNO₃ using a modified version of the U.S. Environmental Protection Agency SW846, method 3050 for flame atomic absorption

TABLE 1. Shell Height and Weight Relationships of the Antarctic, Bay, and Sea Scallop Species

Specimens	Height, cm	Weight, g	Shell Weight:Area,* g/cm ²
<i>Antarctic Scallop</i>			
1	9.07	4.82	0.08
2		5.64	0.09
3	7.94	2.96	0.06
4		3.51	0.07
5	8.90	3.96	0.06
6		4.39	0.07
Mean			0.07 ± 0.01
<i>Bay Scallop</i>			
7	4.43	2.79	0.18
8		3.24	0.21
9	4.30	2.09	0.14
10		2.67	0.18
11	4.75	3.17	0.18
12		4.11	0.23
Mean			0.19 ± 0.03
<i>Sea Scallop</i>			
13	11.67	36.76	0.34
14		36.62	0.34
15	12.13	57.97	0.50
16		56.92	0.49
17	13.40	42.56	0.30
18		44.51	0.32
Mean			0.38 ± 0.08

Standard deviation (plus or minus) is given for the means. Odd-numbered specimens are upper valves, and even-numbered specimens are lower valves.

*Area estimated by treating scallop shell as a circle with radius equal to half of the shell height.

analyses. After weighing the shell samples, they were placed in 10 mL of 1:1 HNO₃, which was refluxed for 10–15 min at 95°C without boiling. The samples then were cooled, 5 mL of concentrated HNO₃ was added, and they were refluxed for another 30 min. This last step was repeated to ensure complete oxidation. The samples were cooled again, and 2 mL of deionized water together with 3 mL of 30% H₂O₂ was added to start the peroxide reaction. One-millimeter aliquots of H₂O₂ (not more than 10 mL altogether) then were added until the effervescence was minimal. Afterward, 5 mL of concentrated HCl and 10 mL of deionized water were added to the samples, which were refluxed for another 15 min. The samples then were diluted and deionized water to a volume of 100 mL.

Concentrations of iron, manganese, copper, chromium, zinc, lead, nickel, and cadmium were analyzed with the Perkin-Elmer 1100B atomic absorption spectrophotometer. Three standards were made for each of the metal analyses and were used to determine that the spectrophotometer was operating within instrumental specifications. Three replicates of the dissolved shell samples, along with standards for each metal and blanks, were aspirated into the flame, and the mean values were recorded. On the basis of a sample volume of 100 mL and a sample weight of 1 g, the adjusted minimum detection limits for each element were as follows: iron, 3 µg g⁻¹, or 3 ppm; manganese, 1 ppm; copper, 2 ppm; chromium, 5 ppm; zinc, 1 ppm; lead, 10 ppm; nickel, 4 ppm; and cadmium, 1 ppm. Shell trace element concentrations were reported on a weight-specific basis in parts per million.

X Ray Diffraction Analysis

X ray diffraction analysis of homogenized powders from whole shell valves was conducted to determine their average crystalline characteristics. After determining the average calcite:aragonite proportions in the shells, the Miller (*hkl*) indices were used for representing the spectral directions in which the X ray beams were diffracted by the calcite crystalline phase. The aragonite crystalline phase was not interpreted because of the possibility that it may have been contaminated by the addition of some small amount of transformed aragonite during shell preparation (discussed above).

Structure amplitude (*F*), which is a function of the Miller indices (see (1), below), was the primary physical factor controlling the intensity of the diffracted beams. Although calcite is a member of the rhombohedral division of crystals, it is possible to express the crystallographic characteristics of calcite in the "hexagonal system" [Reeder, 1983], as in this paper.

X ray diffraction records were produced using a Philips 1316/90 goniometer with an XRG 3100 generator operating at 35 kV and 15 mA with a Ni-filtered copper target. Detector signals were sampled at 0.05° increments from 15° to 55° in 2θ. The precise diffraction angle, 2θ₀, for each reflection maximum was determined by means of least squares fit to a second-order polynomial expression relating spectral intensity with diffraction angle. Unit cell parameters and their standard errors were determined by an iterative least squares refinement of observed 2θ values against those calculated for the crystal system using an IBM 3081-D mainframe computer.

The method used to establish the mass distribution between the calcite and the aragonite phases was based on the ratios of the relative intensities from the calcite (104) and aragonite (111) spectra. The *hkl* values (104) and (111) represent the most reliable Miller indices for characterizing these two phases, respectively. An absolute value for the structure amplitude *F*₁₁₁ was obtained from an earlier work [Dickens and Bowen, 1971], while the corresponding structure amplitude *F*₁₀₄ was taken from a thermal motion investigation for calcite [Felty, 1964] and placed on an absolute basis using the results of a study of oxygen planes [Chessin et al., 1965].

Experimental unit cell volumes were calculated from measurements of axial dimensions and compared to standard unit cell volumes which were determined in a previous study [Swanson and Fuyat, 1953]. Linear absorption coefficients (factors attenuating the intensity of the diffracted beams) were calculated for the calcite and aragonite phases, and Lorentz polarization factors were obtained from Lonsdale [1967a, b]. Finally, the determination of intensity (*I*) for each of the paramount reflections between the calcite and the aragonite phases was accomplished using the expression

$$I_{hkl} = F_{hkl}^2 p B_t (1 + \cos^2 \theta) \csc^2 \theta \sec \theta / 2\mu v^2 \quad (1)$$

where *p* is the multiplicity factor; μ is the linear absorption coefficient of the sample; *v* is the volume of the unit cell; the compound trigonometric factor is the Lorentz polarization factor; and *B_t* is the Debye general temperature factor. The structure amplitude *F* is a function of the total unit cell content, specifically identified by atom location in three dimensions.

The Debye temperature factor (*B_t*) can be simplified because it is a function of $\sin \theta / \lambda$, which is 0.16 for the calcite (104) and 0.14 for the aragonite (111) diffraction spectra. Within these two limits, *B_t* varies insignificantly and is nearly unity. Having determined *I*₁₁₁ and *I*₁₀₄, the weight percentage of aragonite (*w*) in binary mixtures with calcite can be calculated:

TABLE 2. Atomic Absorption Analyses of *Adamussium colbecki* Shells From Explorers Cove, Antarctica

Element	Depth			Regression with Depth (10 degrees of freedom)
	6 m	10 m	21 m	
<i>Upper Valves</i>				
Iron	273.43 ± 33.84	84.52 ± 13.96	41.89 ± 6.07	y = -12.97x + 293.33, r = 0.80*
Manganese	20.80 ± 0.70	14.52 ± 0.54	10.90 ± 1.31	y = -0.59x + 22.77, r = 0.89*
Copper	16.02 ± 5.38	10.44 ± 0.39	8.99 ± 0.71	y = -0.40x + 16.71, r = 0.58†
Zinc	13.01 ± 1.80	4.82 ± 0.84	3.14 ± 0.55	y = -0.55x + 13.83, r = 0.79*
Chromium	10.22 ± 0.85	8.02 ± 0.86	6.19 ± 0.42	y = -0.25x + 11.19, r = 0.71*
Lead‡				
Nickel‡				
Cadmium‡				
<i>Lower Valves</i>				
Iron	109.21 ± 16.40	56.78 ± 3.67	37.01 ± 4.49	y = -4.17x + 119.12, r = 0.82*
Manganese	49.05 ± 3.05	21.85 ± 8.11	14.02 ± 0.58	y = -1.99x + 52.84, r = 0.80*
Copper	9.65 ± 0.82	9.18 ± 0.50	8.34 ± 0.83	y = -0.08x + 10.11, r = 0.59†
Zinc	5.19 ± 0.24	4.22 ± 0.62	2.96 ± 0.47	y = -0.14x + 5.87, r = 0.87*
Chromium	10.69 ± 1.39	6.67 ± 0.29	7.01 ± 0.16	y = -0.18x + 10.42, r = 0.48

Element concentrations are in parts per million. Standard deviation (plus or minus) is given.

*Significant at 0.01 level.

†Significant at 0.05 level.

‡Concentrations below minimum detection limit.

$$\omega = \omega_{111} I_{111} / [\omega_{111} I_{111} + \omega_{104} I_{104}] \quad (2)$$

where ω_{111} and ω_{104} are the weight fractions of aragonite and calcite, respectively. Values calculated for the working curve of ω in (2) were fit to a fourth-order polynomial expression to facilitate the determination of ω' in our samples, with the following result:

$$\omega' = 2.83q - 4.00q^2 + 3.22q^3 - 1.05q^4 \quad (3)$$

where $q = I_{111} / (I_{111} + I_{104})$ and ω' is significantly correlated with the working curve ω ($r = 0.995$, d.f. = 11, $p < 0.001$).

RESULTS

Atomic absorption analyses of modern *Adamussium colbecki* shells, collected across a nearshore depth gradient adjacent to a meltwater stream in west McMurdo Sound, Antarctica, indicate that the concentrations of iron, manganese, copper, and zinc significantly decreased with depth in both the upper and the lower valves (Table 2). These depth-dependent changes in the elemental concentrations also were significantly different between the valves (Table 3).

X ray diffraction spectra for all scallop shell specimens indicated that the predominant phase was

calcite, with a secondary aragonite phase ranging from an average of $1.2 \pm 0.4\%$ for the bay scallop to $4.2 \pm 2.5\%$ for the Antarctic scallop (Table 4). The calcite was highly crystalline with the principal spectral maximum having a peak-to-background ratio of 100:1.

The calcite unit cell dimensions are shown in Table 4 where the designation of the principal phase as calcite is supported by comparison with a standard synthetic calcite specimen [Swanson and Fuyat, 1953] which has unit cell dimensions of 4.9898 \AA and 17.062 \AA . Among the three scallop species, the unit

TABLE 3. Trace Element Comparisons Between Upper and Lower Antarctic Scallop Shell Valves

Analysis of Covariance	Iron	Manganese	Copper	Zinc	Covariate	
					Depth	F
					p(1, 21 d.f.)	<0.001
						<0.001
Valve	F	8.02	12.98	7.65	<0.032	<0.012

F is the F ratio; p, probability; and d.f., degrees of freedom.

cell dimensions of the calcite phase are consistent, as indicated by their small standard errors, $\pm 0.007 \text{ \AA}$ and $\pm 0.04 \text{ \AA}$ for the a axial and c axial dimensions, respectively.

Factorial analyses were used for comparing shell crystalline characteristics between scallop shells and shell valves. The interactions between scallop species and valves were not significant, which provided a basis for interpreting the main effects (Table 5). Between species, there were significant differences in shell weight:area and weight percentage of aragonite. Among valves, there also were significant differences in the weight percentage of aragonite. Despite the above differences between scallop species and valves, there were no significant differences between their unit cell dimensions. Moreover, the unit cell dimen-

TABLE 4. Shell Crystalline Characteristics of the Antarctic, Bay, and Sea Scallop Species

Specimens	Unit Cell Dimensions*		Aragonite, [†] wt %
	a , \AA	c , \AA	
<i>Antarctic Scallop</i>			
1	5.011 (4)	17.16 (2)	2.7
2	5.016 (4)	17.17 (2)	7.4
3	5.003 (1)	17.12 (0)	1.9
4	5.003 (2)	17.12 (1)	3.1
5	5.017 (4)	17.16 (1)	2.7
6	4.999 (1)	17.12 (1)	7.4
Mean	5.008 ± 0.008	17.14 ± 0.02	4.2 ± 2.5
<i>Bay Scallop</i>			
7	5.001 (1)	17.10 (0)	1.4
8	5.000 (1)	17.11 (1)	1.5
9	5.001 (2)	17.11 (1)	0.6
10	5.009 (3)	17.12 (1)	1.1
11	5.006 (3)	17.11 (1)	1.2
12	5.009 (3)	17.11 (1)	1.6
Mean	5.004 ± 0.004	17.11 ± 0.01	1.2 ± 0.4
<i>Sea Scallop</i>			
13	5.006 (2)	17.12 (1)	2.8
14	5.003 (2)	17.13 (1)	1.9
15	5.027 (5)	17.26 (3)	4.2
16	5.008 (3)	17.14 (1)	3.3
17	5.004 (2)	17.13 (1)	1.8
18	5.004 (2)	17.12 (1)	3.9
Mean	5.009 ± 0.009	17.15 ± 0.05	3.0 ± 1.0

*For the unit cell dimensions, the standard deviation of the least significant digit is given in parentheses, and the standard error is expressed as plus or minus.

[†]The standard deviation for aragonite is expressed as plus or minus.

TABLE 5. Comparisons of Shell Crystalline Characteristics Among the Antarctic, Bay, and Sea Scallop Species

Analysis of Variance	Shell Weight Area	Aragonite, wt %	Axial Dimensions	
			a	c
<i>Main Effects</i>				
Species				
F	41.57	8.77	0.65	2.10
p (2, 12 d.f.)	<0.001	<0.005	NS	NS
Valves				
F	0.40	5.17	0.57	0.74
p (2, 12 d.f.)	NS	<0.04	NS	NS
<i>Interactions</i>				
Species-Valves				
F	0.16	3.63	0.87	0.66
p (2, 12 d.f.)	NS	NS	NS	NS

F is the F ratio; p , probability; d.f., degrees of freedom; and NS, not significant.

sions in all three scallop species were larger than those of the synthetic calcite standard of Swanson and Fuyat [1953].

The integrated intensities and interplanar spacings (Table 6) corresponded closely with those of synthetic calcite [Swanson and Fuyat, 1953], except for the diffraction intensities in the (108) and (116) crystal planes, which were much larger in our samples. Greatly enlarged (108) peaks also have been noted in the scallops *Pecten albicans* and *Amusium japonicum balloti* [Runnegar, 1983].

To determine the reliability of the diffractometric raw data for calcite, precision indices were evaluated from the fit of the integration of the calcite (104) spectral profile to a Gaussian distribution and were determined to be highly correlated (Table 7). The precision of these analyses results, in part, from the direct analysis of digital output, rather than from interpolating strip chart records or from single ratemeter values. For example, our determination of $3.0 \pm 0.9\%$ aragonite for the sea scallop differs from that of Turekian and Armstrong [1960], who suggested, on the basis of museum samples of undefined age, that there was 0% aragonite. However, some aragonite would be expected because it occurs in scallop shell microstructures [Carter, 1980], and its lack of detection would seem to reflect the lower accuracy associated with analyzing strip chart records. It is also possible that the earlier results may reflect the conversion of the metastable aragonite phase into the stable calcite phase [Lippman, 1973] which occurs over time [Lowenstam, 1954].

DISCUSSION

Trace Element Concentrations in Nearshore Antarctic Scallop Shells

Numerous studies on the trace element concentrations in the soft tissues of marine species from around Antarctica have been published [Honda *et al.*, 1987; Yamamoto *et al.*, 1987; Mauri *et al.*, 1990; Lenihan *et al.*, 1990; Berkman and Nigro, 1992]. However, soft tissues rapidly decompose and are rarely preserved after the animal dies. In contrast, shells or other hard parts of marine species are commonly preserved over geological time scales. This paper presents the first mineralogical analyses of shells from a modern Antarctic marine species that has a broad fossil distribution in Holocene beaches around the continent [Berkman, 1992].

If Antarctic scallops, or other nearshore marine species which produce calcium carbonate shells, are influenced by hydrochemical variations, then these variations should be reflected in modern assemblages across known environmental gradients. In the McMurdo Dry Valleys, Antarctica, glacial meltwater streams contain trace element concentrations that are orders of magnitude higher than in seawater [Boswell *et al.*, 1967]. At Explorers Cove, at the base of the McMurdo Dry Valleys in west McMurdo Sound, glacial meltwater has been introduced into the marine environment through the Holocene [Porter and Beget, 1981] and is known to stratify in nearshore areas today [Berkman, 1991] (Figure 2).

The overall ranking of the trace element concentrations in nearshore *Adamussium colbecki* shells (Fe > Mn > Cu > Zn > Cr > Pb, Ni, Cd) was similar, with the major exception of zinc, to the mean concentrations described by Honda *et al.* [1987] for seawater

TABLE 7. Analysis of Experimental Precision

Scallop Species	θ_{104} , deg	S_θ , deg	r	p
Antarctic	14.64	0.029	0.949	<0.005
Bay	14.65	0.016	0.943	<0.004
Sea	14.62	0.038	0.871	<0.05

Variables are defined as follows: Bragg angle, θ_{104} ; standard deviation, S_θ ; correlation coefficient for Gaussian fit with $n = 6$, r; probability, p.

around Antarctica (Zn, Fe > Mn > Cu > Pb, Ni > Cd). Differences between the ranking of the trace element concentrations in the Antarctic scallop shells and seawater could be due to selective biological uptake or to local environmental processes.

Trace element concentrations were higher in Antarctic scallop shells collected in shallow water adjacent to the glacial runoff. The significant decreases in the concentrations of iron, manganese, copper, and zinc with depth (Table 2) would suggest that the composition of these scallop shells was influenced by local environmental processes.

However, trace element concentrations also varied consistently between the upper and the lower shell valves across this nearshore depth gradient. The concentrations of iron, copper, and zinc were significantly higher in the upper valve, whereas manganese was significantly greater in the lower valve (Table 3). Similar mineralogical differences between the upper and the lower valves of scallops have been observed previously [Segar *et al.*, 1971]. These results indicate that biological processes also were influencing the concentrations of trace metals in the scallop shells. In general, these data suggest that indis-

TABLE 6. Calcite Diffraction Intensities and Interplanar Spacings of the Antarctic, Bay, and Sea Scallop Species

<i>hkl</i>	Intensities				Interplanar Spacings			
	A	B	S	S&F	A	B	S	S&F
102	5	5	11	12	3.868	3.866	3.871	3.860
104	100	100	100	100	3.047	3.044	3.049	3.035
006	3	5	9	3	2.854	2.852	2.858	2.845
110	13	16	18	14	2.502	2.502	2.505	2.495
113	17	30	20	18	2.292	2.291	2.294	2.285
022	15	28	16	18	2.101	2.100	2.103	2.095
204	6	7	7	5	1.938	1.933	1.935	1.927
108	58	54	71	17	1.921	1.918	1.922	1.913
116	29	74	42	17	1.882	1.882	1.884	1.875

Miller indices (hexagonal setting) are expressed as *hkl*. Other variables are defined as follows: A, Antarctic scallop; B, bay scallop; S, sea scallop; and S&F, the standard from Swanson and Fuyat [1953].

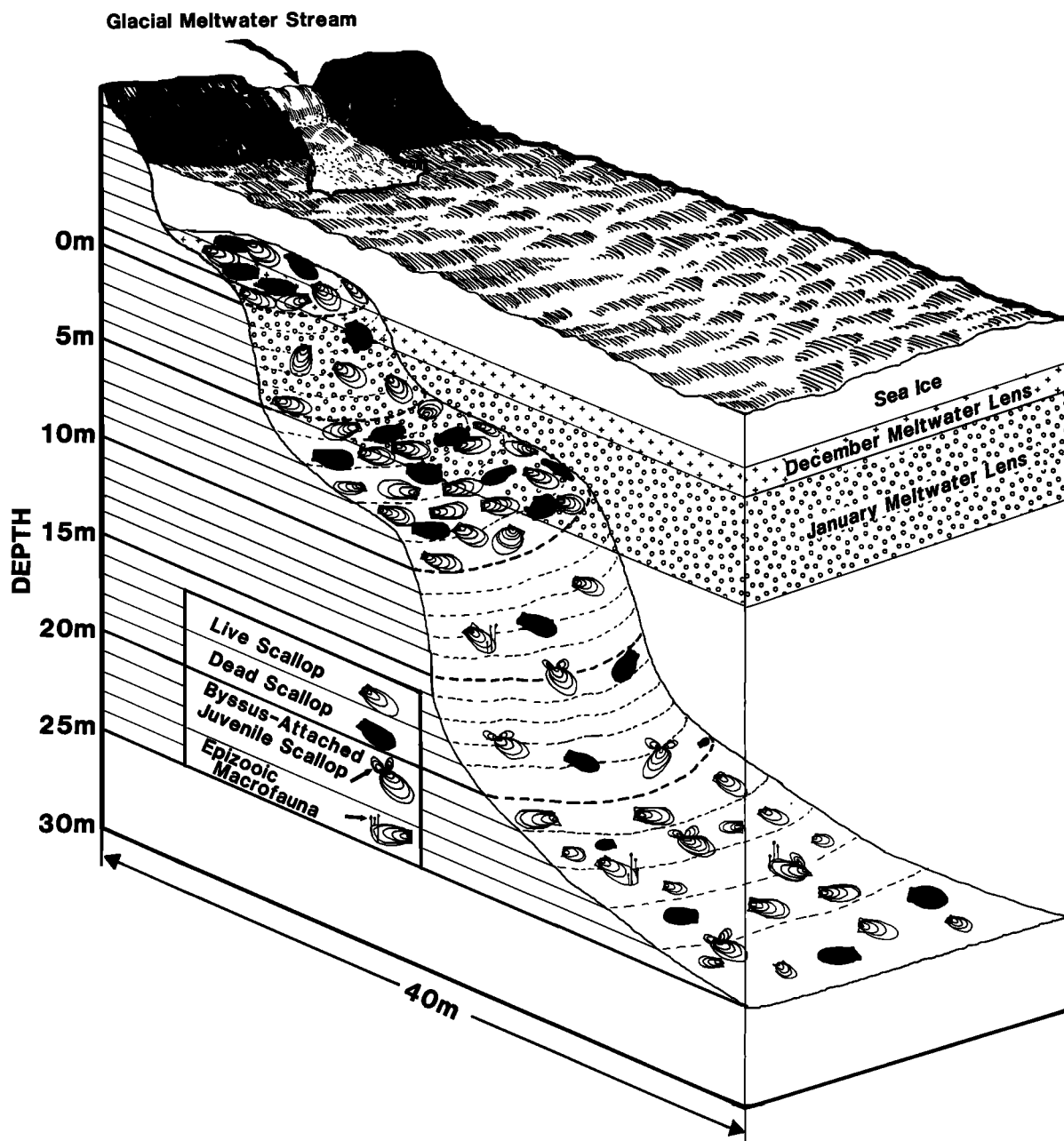


Fig. 2. Illustration of the modern scallop population at Explorers Cove, Antarctica, across a nearshore depth gradient that was impacted by glacial stream runoff, sea ice melting, and the summer stratification of meltwater (modified from Berkman [1991]). The mineralogy and crystalline characteristics of scallop shells collected across nearshore meltwater gradients today may provide analogs for interpreting adjacent fossil scallop shells in relation to meltwater variability associated with ice sheet fluctuations earlier in the Holocene.

criminate mineralogical comparisons between the upper and the lower valves of bivalve mollusc species should be viewed with skepticism.

Scallop Shell Crystalline Characteristics

X ray diffraction analysis provides a basis for interpreting the mineralogical variations in *Adamussium colbecki* shells (Tables 2 and 3) in relation to the crystalline characteristics of shell formation. X ray diffraction records indicated that shells of the Antarctic, bay, and sea scallop were composed of a highly crystalline calcite phase without indications of amorphous scattering. There also was no evidence in the X ray diffraction records of polysaccharide or protein components among the analyzed 2θ values. These conclusions are supported by the determination that Antarctic scallop shells are composed of less than 0.3% organic carbon [Berkman, 1991] and that, in general, the abundance of organic components in mollusc shells ranges from 0.01% to 5% of the sample mass [Weiner and Traub, 1984].

The proportions of aragonite in the shells of the three scallop species varied significantly, as would be expected since they were being influenced by the markedly different environmental conditions in which they were grown [Dodd, 1964]. However, as with the mineralogy of Antarctic scallop shells, the proportion of aragonite in the shells of the three scallop species varied significantly between their upper and their lower valves (Tables 4 and 5). These results suggest that the mineralogical variations between Antarctic scallop shell valves (Tables 2 and 3) are influenced by endogenous processes that are independent of environmental variation.

Decreasing seawater temperatures would increase the solubility of calcium carbonate [Broecker and Peng, 1982] and make it more difficult for the scallops to precipitate their shells. This suggestion is supported by the extremely low shell weight-area ratio for the Antarctic scallop relative to the temperate scallop species (Tables 1 and 5). The evolutionary implications of increasing calcium carbonate solubility are further reflected by the replacement of thick-shelled *Chlamys* species with wafer-thin-shelled *Adamussium* species in coastal environments around Antarctica as it cooled during the Cenozoic [Berkman et al., 1991].

Although there were differences in their gross shell characteristics, the unit cell dimensions among the shells of the three scallop species were not significantly different (Tables 4 and 5). Mean unit cell volumes of the Antarctic, bay, and sea scallops were 372.3 \AA^3 , 371.0 \AA^3 , and 372.0 \AA^3 , respectively. These mean unit cell volumes were 3 to 4 \AA^3 larger than in

pure calcite, which has a unit cell volume of 367.9 \AA^3 [Swanson and Fuyat, 1953]. This discrepancy suggests that there were isomorphous substitutions in the unit cells of the calcite by cations with larger ionic radii than calcium. The relatively high concentrations of strontium relative to magnesium in sea scallop shells [Turekian and Armstrong, 1960] would support this conclusion.

Magnesium (0.65 \AA), manganese (0.80 \AA), and iron (0.80 \AA) are known to be isomorphous substituents in calcite [Wilbur, 1972; Dodd, 1967; Berry et al., 1983]. However, these divalent cations would decrease the volume of the unit cells in the calcite lattice because of their smaller ionic radii compared to that of calcium, which is 0.99 \AA [Evans, 1964]. This decreased unit cell volume result has been experimentally demonstrated for mytilid bivalve shells cultured under elevated magnesium concentrations [Lorens and Bender, 1977].

In contrast, strontium (1.13 \AA) and barium (1.35 \AA) are larger divalent cations that are known to be isomorphous substituents in calcite and which increase the unit cell volume without space group disruption [Dana, 1932; Dodd, 1967; Vorob'ev and Afronin, 1973]. Radium (1.43 \AA), which is another large divalent cation that occurs in marine shells [Blanchard and Oakes, 1965], also is a possible isomorphous substituent of Ca^{2+} in scallop shells. Sr^{2+} , Ba^{2+} , and Ra^{2+} all have greater atomic scattering factors than Ca^{2+} [Lonsdale, 1967a, b] that would account for the increased diffraction intensities noted in Table 6.

Calcite exhibits its maximum diffraction intensity in the (104) reflection because this crystal plane contains the densest concentration of calcium ions. However, calcium also contributes to diffraction from the (108) and (116) crystal planes of the unit cell, and in this study all of the scallop species had intensities in these two crystal planes that were much greater than those in the calcite standard (Table 6). These results further support the conclusion that there were isomorphous substitutions in the calcite lattice of scallop shells by cations with greater atomic scattering factors than calcium.

Future Research

Because of diagenetic alterations in shell chemistry [Lowenstam, 1954; Pilkey and Goodell, 1964; Walls et al., 1977], only the most stable components of fossil shells should be investigated to interpret past environmental conditions. X ray diffraction intensities, which are the result of interference phenomena, are directly controlled by the elements occupying specific unit cell sites. Isomorphous substituents in the

unit cells contribute to the lattice energy [Lippman, 1973] of the shell matrix and are thermodynamically stable [Swalin, 1962] compared to those elements which appear in the intercrystalline spaces. These unit cell constituents cannot be inferred by microprobe, energy dispersive, spectrographic, or gravimetric analyses which indiscriminately sample intracrystalline and intercrystalline locations. Analyzing the unit cell characteristics (dimensions and diffraction intensities) would reflect the integrated concentration of the stable elements in the shell.

In addition, if ^{226}Ra substitutes isomorphously into the unit cells of the calcite lattice in scallop shells, then these shells could be treated as closed systems for this isotope. Because ^{226}Ra has a half-life of 1622 years and relatively high concentrations in surface waters around Antarctica [Broeker and Peng, 1982], age estimates derived from ^{226}Ra [e.g., Blanchard and Oakes, 1965] would complement and be independent of those determined from ^{14}C . In the southern oceans where there is no accepted correction for the age of the radiocarbon reservoir [Stuiver et al., 1981; Omoto, 1983; Berkman, 1992], developing an alternative to the ^{14}C dating methodology would be extremely useful.

CONCLUSIONS

Average dimensions of the unit cells in shells of the Antarctic, bay, and sea scallops were larger than in pure synthetic calcite (Table 5). Together with the increased diffraction intensities (Table 6), these data demonstrate that cations with relatively large ionic radii isomorphically substitute for the calcium in the calcite of scallop shells. Despite scallop shell concentrations that change significantly across an environmental gradient (Tables 2 and 3), trace elements with smaller atomic radii than Ca^{2+} may occur outside of the unit cells in intercrystalline spaces that would be susceptible to diagenesis over time. Unit cell dimensions and diffraction intensities, because they reflect only the composition of the relatively stable intracrystalline lattice sites, may be more reliable proxies of hydrochemical variability in the nearshore marine environment.

Significant differences between the mineralogy and the crystalline characteristics of upper and lower scallop valves were observed (Tables 1–5). These data indicate that indiscriminate mineralogical comparisons between the shell valves of scallops, and probably other bivalve molluscs, should be viewed with skepticism in relation to interpreting environmental conditions.

Acknowledgments. We thank J. M. Bigham and S. Jones from the Department of Agronomy at The Ohio State

University for their assistance with the X ray diffractometry. We also thank G. Faure, T. R. Waller, and K. M. Towe for their helpful comments and J. C. Nagy for his assistance with the illustrations. This research was generously supported by the Byrd Fellowship (to P.A.B.) from the Byrd Polar Research Center at The Ohio State University (contribution 738).

REFERENCES

- Barrera, E., J. S. Tevesz, and J. G. Carter, Variations in oxygen and carbon isotopic compositions and microstructure of the shell of *Adamussium colbecki* (Bivalvia), *Palaios*, 5, 149–159, 1990.
- Berkman, P. A., Ecological relationships between the bay scallop, *Argopecten irradians*, and its epizoic assemblages in Charleston Pond, Rhode Island, Masters thesis, Univ. of R.I., Narragansett, 1986.
- Berkman, P. A., Ecology of the circumpolar Antarctic scallop, *Adamussium colbecki* (Smith, 1902), doctoral dissertation, Univ. of R.I., Narragansett, 1988a.
- Berkman, P. A., Sea scallop tagging experiments using manned-submersibles, in National Underseas Research Program Research Report, edited by I. Babb and M. DeLuca, Rep. 88-3, pp. 231–243, U.S. Dep. of Commer., Natl. Oceanic and Atmos. Admin., Rockville, Md., 1988b.
- Berkman, P. A., The population biology of the Antarctic scallop, *Adamussium colbecki* (Smith 1902) at New Harbor, Ross Sea, in *Antarctic Ecosystems: Ecological Change and Conservation*, edited by K. Kerry and G. Hempel, pp. 281–288, Springer-Verlag, New York, 1990.
- Berkman, P. A., Holocene meltwater variations recorded in Antarctic coastal marine benthic assemblages, in *Proceedings of the International Conference on the Role of the Polar Regions in Global Change*, edited by G. Weller, C. L. Wilson, and B. A. B. Severin, pp. 440–449, University of Alaska, Fairbanks, 1991.
- Berkman, P. A., Circumpolar distribution of Holocene marine fossils in Antarctic beaches, *Quat. Res.*, 37, 256–260, 1992.
- Berkman, P. A., and M. Nigro, Trace metal concentrations in scallops around Antarctica: Extending the Mussel Watch Programme to the Southern Ocean, *Mar. Pollut. Bull.*, 24, 322–323, 1992.
- Berkman, P. A., T. R. Waller, and S. P. Alexander, Unprotected larval development in the Antarctic scallop, *Adamussium colbecki*, (Mollusca: Bivalvia: Pectinidae), *Antarct. Sci.*, 3, 151–157, 1991.
- Berry, L. G., B. Mason, and R. V. Dietrich, *Mineralogy Concepts, Descriptions and Determinations*, 2nd ed., pp. 127–130, 550–551, W. H. Freeman, New York, 1983.
- Blanchard, R. L., and D. Oakes, Relationship between uranium and radium in coastal marine shells and their environment, *J. Geophys. Res.*, 70, 2911–2921, 1965.
- Bøggild, O. B., The shell structure of the mollusks, *K. Dan. Vidensk. Selsk. Skr. Naturvidensk. Mat. Afd.*, 9(2), 231–326, 1930.
- Boswell, C. R., R. R. Brooks, and A. T. Wilson, Some trace elements in lakes of McMurdo oasis, Antarctica, *Geochim. Cosmochim. Acta*, 31, 731–736, 1967.

- Broecker, W. S., and T.-H. Peng, *Tracers in the Sea*, pp. 61–68, 200–203, 243–245, Eldigio Press, New York, 1982.
- Brooks, R. R., and M. G. Rumsby, The biogeochemistry of trace element uptake by some New Zealand bivalves, *Limnol. Oceanogr.*, 10, 521–527, 1965.
- Burns, J. F., and M. A. Bredig, Transformation of calcite to aragonite by grinding, *J. Chem. Phys.*, 25, 1281, 1956.
- Carriker, M. R., C. P. Swann, and J. W. Ewart, An exploratory study with the proton microprobe of the ontogenetic distribution of 16 elements in the shell of living oysters (*Crassostrea virginica*), *Mar. Biol.*, 69, 235–246, 1982.
- Carter, J. G., Environmental and biological controls of bivalve shell mineralogy and microstructures, in *Skeletal Growth of Aquatic Organisms*, edited by D. C. Rhoads and R. A. Lutz, pp. 69–113, Plenum, New York, 1980.
- Carter, J. G., (Ed.), *Skeletal Biomimetication: Patterns, Processes and Evolutionary Trends*, vol. 1, Van Nostrand Reinhold, New York, 1990a.
- Carter, J. G. (Ed.), *Skeletal Biomimetication: Patterns, Processes and Evolutionary Trends*, vol. 2, Van Nostrand Reinhold, New York, 1990b.
- Carter, J. G., and G. R. Clark, Classification and phylogenetic significance of molluscan shell microstructure, in *Mollusks: Notes for a Short Course*, edited by T. W. Broadhead, pp. 50–71, Paleontological Society, Knoxville, Tenn., 1985.
- Chessin, H., W. C. Hamilton, and B. Post, Position and thermal parameters of oxygen atoms in calcite, *Acta Crystallogr.*, 18, 689–693, 1965.
- Curtis, C. D., and D. Krinsley, The detection of minor diagenetic alteration in shell material, *Geochim. Cosmochim. Acta*, 29, 71–84, 1965.
- Dana, E. S., *A Textbook of Mineralogy With an Extended Treatise on Crystallography and Physical Mineralogy*, 4th ed., John Wiley, New York, 1932.
- Denton, G. H., J. G. Bockheim, S. C. Wilson, and M. Stuiver, Late Wisconsin and early Holocene glacial history, Inner Ross Embayment, Antarctica, *Quat. Res.*, 31, 151–182, 1989.
- Dickens, B., and J. S. Bowen, Refinement of the crystal structure of the aragonite phase of CaCO_3 , *J. Res. Natl. Bur. Stand., Sect. A*, 7(1), 27–31, 1971.
- Dodd, J. R., Environmentally controlled variation in the shell structure of a pelecypod species, *J. Paleontol.*, 38, 1065–1071, 1964.
- Dodd, J. R., Environmental control of strontium and magnesium in *Mytilus*, *Geochim. Cosmochim. Acta*, 29, 385–398, 1965.
- Dodd, J. R., Magnesium and strontium in calcereous skeletons: A review, *J. Paleontol.*, 41, 1313–1329, 1967.
- Eisler, R., *Trace Metal Concentrations in Marine Organisms*, Pergamon, New York, 1981.
- Eisma, D., W. G. Mook, and H. A. Das, Shell characteristics, isotope composition and trace-element contents of some euryhaline molluscs as indicators of salinity, *Palaeogeogr. Palaeoclimatol. Palaeoecol.*, 19, 39–62, 1976.
- Evans, R. C., *An Introduction to Crystal Chemistry*, p. 38, Cambridge University Press, New York, 1964.
- Felty, E. J., Interatomic distances and amplitudes of vibration in calcite type crystals, *Dissertation Abstracts*, vol. 24(11), p. 4423, University Microfilms, Ann Arbor, Mich., 1964.
- Gregoire, G., Structure of the molluscan shell, in *Chemical Zoology*, vol. VII, *Mollusca*, edited by M. Florkin and B. T. Scheer, pp. 45–102, Academic, San Diego, Calif., 1972.
- Honda, K., Y. Yamamoto, and R. Tatsukawa, Distribution of heavy metals in Antarctic marine ecosystem, *Proc. Natl. Inst. Polar Res. Symp. Polar Biol.*, 1, 184–197, 1987.
- Hurlbut, C. S. (Ed.), *Dana's Manual of Mineralogy*, pp. 13–91, John Wiley, New York, 1959.
- Jamieson, J. C., and J. R. Goldsmith, Some reactions produced in carbonates by grinding, *Am. Mineral.*, 45, 818–827, 1960.
- Lenihan, H. S., J. S. Oliver, J. M. Oakden, and M. D. Stephenson, Intense and localized benthic marine pollution around McMurdo Station, Antarctica, *Mar. Pollut. Bull.*, 9, 422–430, 1990.
- Lippman, F., *Sedimentary Carbonate Minerals*, Springer-Verlag, New York, 1973.
- Lonsdale, K. (Ed.), *International Tables for X-ray Crystallography*, vol. II, pp. 266–290, Kynoch Press, Birmingham, Ala., 1967a.
- Lonsdale, K. (Ed.), *International Tables for X-ray crystallography*, vol. III, pp. 68, 136–140, 201–207, Kynoch Press, Birmingham, Ala., 1967b.
- Lorens, R. B., and M. L. Bender, Physiological exclusion of magnesium from *Mytilus edulis* calcite, *Nature*, 269, 793–794, 1977.
- Lowenstam, H. Factors affecting the aragonite/calcite ratios in carbonate-secreting marine organisms, *J. Geol.*, 62, 284–322, 1954.
- Mauri, M., E. Orlando, M. Nigro, and F. Regoli, Heavy metals in the Antarctic scallop, *Adamussium colbecki*, *Mar. Ecol. Prog. Ser.*, 67, 27–33, 1990.
- Mullin, J. B., and J. P. Riley, The occurrence of cadmium in seawater and in marine organisms and sediment, *J. Mar. Res.*, 15, 103–122, 1956.
- Nelson, D. J., Microchemical constituents in contemporary and pre-Columbian clamshell, in *Quaternary Paleoecology, Proceedings of the VIIth Congress of the International Association for Quaternary Research*, edited by E. J. Cushing and H. E. Wright, pp. 185–204, Yale University Press, New Haven, Conn., 1967.
- Omoto, K., The problem and significance of radiocarbon geochronology in Antarctica, in *Antarctic Earth Science*, pp. 450–452, edited by R. L. Oliver, P. R. James, and J. B. Jago, Cambridge University Press, New York, 1983.
- Pilkey, O. H., and H. G. Goodell, Comparison of the composition of fossil and recent mollusk shells, *Geol. Soc. Am. Bull.*, 75, 217–228, 1964.
- Porter, S. C., and J. E. Beget, Provenance and depositional environments of Late Cenozoic sediments in permafrost cores from lower Taylor Valley, Antarctica, in *Dry Valley Drilling Project, Antarctic Res. Ser.*, vol. 33, edited by L. D. McGinnis, pp. 351–363, AGU, Washington, D. C., 1981.
- Reeder, R. J., (Ed.), *Carbonates: Mineralogy and Chemistry*, vol. 11, *Reviews in Mineralogy*, pp. 191–225, Mineralogical Society of America, Washington, D. C., 1983.

- Rhoads, D. C., and R. A. Lutz (Eds.), *Skeletal Growth of Aquatic Organisms*, Plenum, New York, 1980.
- Rucker, J. B., and J. W. Valentine, Salinity response of trace element concentrations in *Crassostrea virginica*, *Nature*, 190, 1099–1100, 1961.
- Runnegar, B., Crystallography of the foliated calcite shell layers of bivalve molluscs, *Alcheringa*, 8, 273–290, 1983.
- Segar, D. A., J. D. Collins, and J. P. Riley, The distribution of the major and some minor elements in marine animals, II, Molluscs, *J. Mar. Biol. Assoc. U.K.*, 51, 131–136, 1971.
- Stuiver, M. L., G. H. Denton, T. J. Hughes, and J. L. Fastook, History of the marine ice sheet in west Antarctica during the last glaciation: A working hypothesis, in *The Last Great Ice Sheets*, edited by G. H. Denton and T. J. Hughes, pp. 319–436, John Wiley, New York, 1981.
- Swalin, R. A., *Thermodynamics of Solids*, pp. 59–71, 272–321, John Wiley, New York, 1962.
- Swanson, H. E., and R. K. Fuyat, Standard X-ray diffraction powder patterns: Carbonates, *Circ.* 539(II), pp. 51–54, Natl. Bur. Stand., Gaithersburg, Md., 1953.
- Taylor, J. D., N. J. Kennedy, and A. Hall, The shell structure and mineralogy of the Bivalvia: Introduction: Nuculacea-Trigonacea, *Bull. Br. Mus. Nat. Hist. Zool.*, 3, suppl., 1–125, 1969.
- Turekian, K. K., and R. L. Armstrong, Magnesium, strontium, and barium concentrations and calcite-aragonite ratios of some recent molluscan shells, *J. Mar. Res.*, 18, 133–151, 1960.
- Vorob'ev, E. I., and V. P. Afronin, Form of strontium and barium in calcite, (in Russian), *Zap. Vses. Mineral. Obshchest.*, 102, 121–123, 1973.
- Walls, R. A., P. C. Ragland, and E. L. Crisp, Experimental and natural early diagenetic mobility of Sr and Mg in biogenic carbonates, *Geochim. Cosmochim. Acta*, 41, 1731–1737, 1977.
- Weiner, S., and W. Traub, Macromolecules in mollusc shells and their functions in biomimicry, *Philos. Trans. R. Soc. London, Ser. B*, 304, 425–434, 1984.
- Wilbur, K. M., Shell formation in mollusks, in *Chemical Zoology*, vol. VII, *Mollusca*, edited by M. Florkin and B. T. Scheer, pp. 103–145, Academic, San Diego, Calif., 1972.
- Wilson, A. T., Past surges in the west Antarctic ice sheet, *Antarctic Glacial History and World Paleoenvironments*, edited by E. M. van Zinderen Bakker, pp. 33–39, A. A. Balkema, Rotterdam, Netherlands, 1978.
- Windom, H. L., and R. G. Smith, Distribution of iron, magnesium, copper, zinc, and silver in oysters along the Georgia coast, *J. Fish. Res. Board Can.*, 29, 450–452, 1972.
- Yamamoto, Y., K. Honda, and R. Tatsukawa, Heavy metal accumulation in Antarctic krill, *Euphausia superba*, *Proc. Natl. Inst. Polar Res. Symp. Polar Biol.*, 1, 198–204, 1987.

(Received July 5, 1991;
accepted October 29, 1991.)

EVIDENCE FOR A GROUNDED ICE SHEET ON THE ROSS SEA
CONTINENTAL SHELF DURING THE LATE PLEISTOCENE
AND PRELIMINARY PALEODRAINAGE RECONSTRUCTION

JOHN B. ANDERSON AND STEPHANIE S. SHIPP

Department of Geology and Geophysics, Rice University, Houston, Texas 77251

LOUIS R. BARTEK

Department of Geology, University of Alabama, Tuscaloosa, Alabama 35487

DAVID E. REID

Amoco Production Company, Houston, Texas 77253

The Ross Sea exhibits north-south oriented troughs associated with modern ice streams and outlet glaciers. Seismic reflection profiles across the troughs show evidence that they were glacially eroded. Seismic records show morphologic features interpreted as till tongues, morainal banks and possibly glacial deltas formed near the grounding line of the former marine ice sheet. Piston cores from the continental shelf penetrated diamictites whose origin and age are problematic. Detailed petrographic analyses of the minerals and rocks comprising these diamictites were conducted to determine subglacial versus glacial marine origin and to reconstruct the glacial setting of the Ross Sea during the most recent glacial maximum. The most detailed work was conducted in the western Ross Sea. The results show that diamictites do occur in distinct petrologic provinces. This is consistent with deposition from the basal debris zone of either an ice sheet or an ice shelf. Overcompaction, in conjunction with the widespread nature of these deposits, favors deposition from marine ice sheets; ice shelves are believed to deposit their basal debris close to their grounding line. The data demonstrate that the East Antarctic Ice Sheet and West Antarctic Ice Sheet grounded on the continental shelf during the last glacial maximum. In the western Ross Sea the grounding line existed near the shelf break. Diamictites from the central and eastern portion of the continental shelf contain stable mineral and rock fragments, indicating considerable recycling of these particles. Because of this, the grounding line positions and paleodrainage divides within the eastern Ross Sea cannot be constrained as confidently as those in the western Ross Sea. In the western Ross Sea, glacial marine sediments of the outer shelf are correlated with subglacial tills on the inner shelf. The glacial marine sediments yield radiocarbon ages of >35,510 years B.P. to 17,390 years B.P. The majority of piston cores from the continental shelf penetrated diatomaceous muds resting in sharp contact on glacial marine sediments and subglacial tills. This implies rapid retreat of the ice sheet from the shelf. Future work will concentrate on obtaining a better paleodrainage map, using geochemical methods, and on obtaining better radiometric age control of the retreat history of the ice sheets.

INTRODUCTION

One of the key problems in glacial geology concerns the expansion of marine ice sheets onto continental shelves during glacial maxima. It is an

important problem because the continental shelves represent a significant area over which ice sheets could be grounded during glacial maxima. A proper estimate of ice volume changes during glacial and interglacial periods hinges on whether such ice sheets

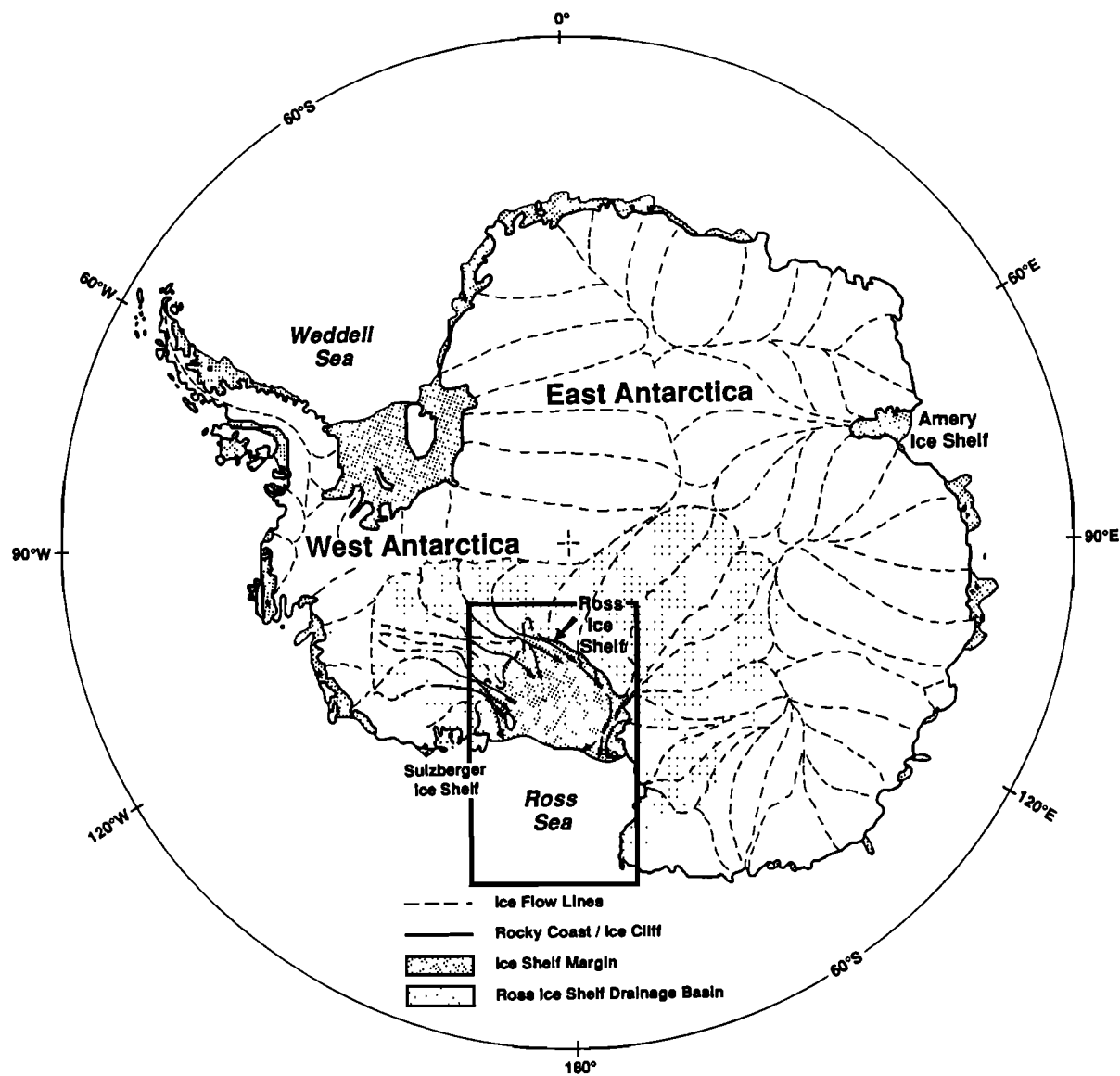


Fig. 1. Glacial drainage map of Antarctica. The boxed region marks the Ross Sea study area. Note that drainage into the Ross Sea is from both East and West Antarctica. The area of the Ross Sea drainage basin is highlighted.

existed and, if so, the extent of the ice sheets. Furthermore, marine ice sheets are inherently unstable and may be subject to rapid disintegration [Hughes, 1977, 1973] that could trigger rapid sea level rises [Hollin, 1962; Lingle and Clark, 1979; Thomas and Bentley, 1978; Hughes, 1987]. Some postulate that the West Antarctic Ice Sheet (WAIS) is still unstable and thus may experience another episode of mass wasting [Hughes, 1973, 1987; Alley, 1990], while others [i.e., Whillans, 1976] argue for a more stable ice sheet.

The Ross Sea has long been recognized as a crucial area for testing glaciological models of marine ice sheet dynamics and stability; a significant component of the West Antarctic and East Antarctic ice sheets drain into the Ross Sea (Figure 1). In addition, the WAIS is the world's only extant marine ice sheet. Glaciological geologists and glaciologists [Drewry, 1979; Stuiver *et al.*, 1981; Denton *et al.*, 1989] have developed extreme glacial maximum ice sheet reconstructions for the Ross Sea region (Figure 2).

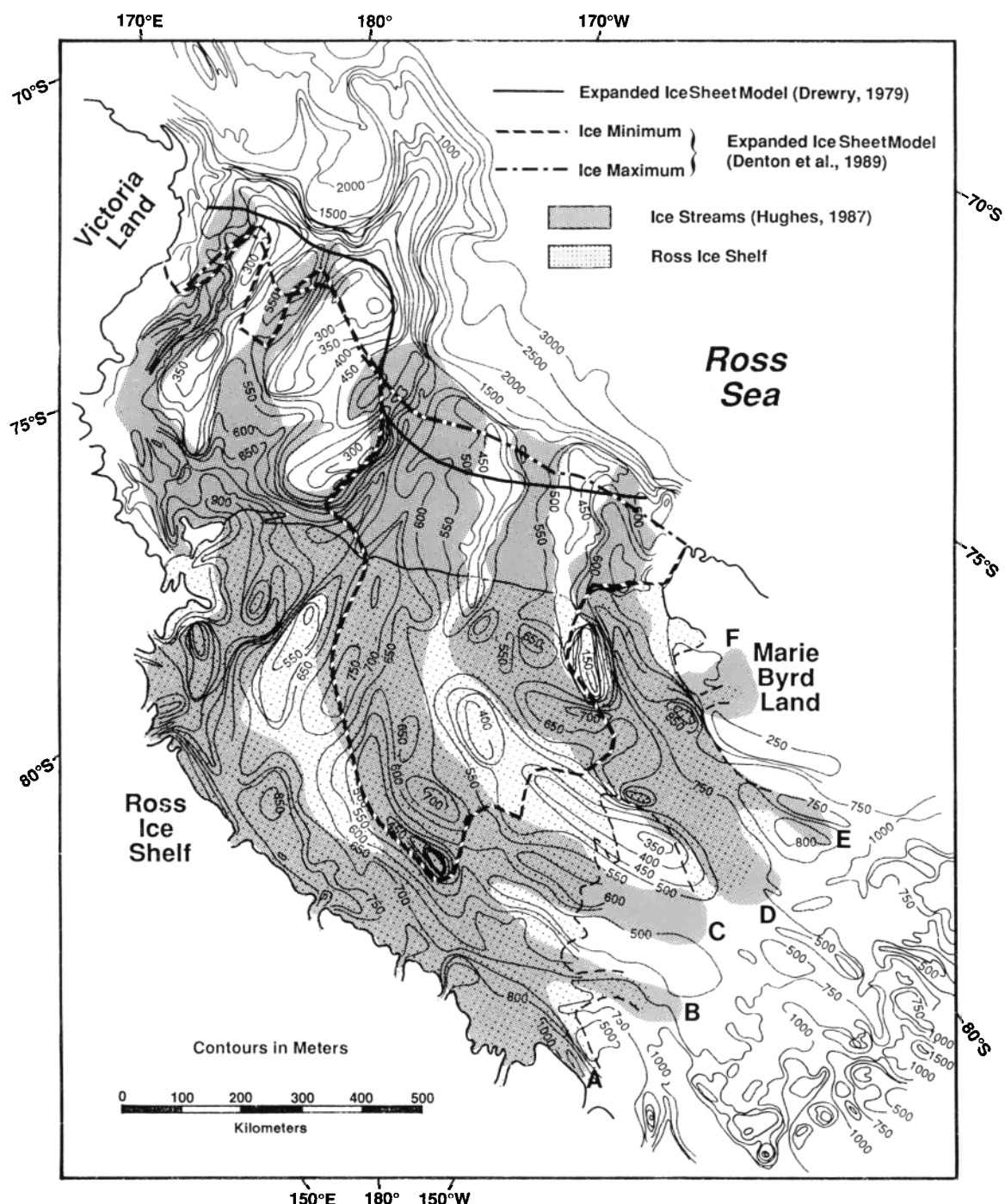


Fig. 2. Glacial maximum reconstructions for Ross Sea. Drewry's [1979] model calls for an extensive ice shelf covering most of the continental shelf. Denton *et al.* [1989] propose two scenarios, one in which the expanded ice sheet covers the entire shelf and the other calling for an ice sheet that extends to the shelf edge only in the western Ross Sea. Bathymetric and topographic contours are in meters [from Bentley and Jezek, 1981]. The stippled area indicates the extent of the present ice shelf.

These models differ in the extent and thickness of the marine ice sheet and ice shelf. *Drewry's* [1979] model calls for an extensive ice shelf over most of the continental shelf (Figure 2). *Denton et al.* [1989] proposed two models, a maximum model with a marine ice sheet covering most of the continental shelf (Figure 2) and a minimum model in which the ice sheet is grounded on the outer shelf in the western Ross Sea but restricted to the middle and inner shelf in the eastern Ross Sea (Figure 2).

The aim of this investigation was to test these different models. A detailed analysis of high-resolution seismic profiles and piston cores from the Ross Sea continental shelf was conducted. Seismic records were examined for evidence of glacial erosion and subglacial deposition. The majority of the piston cores included in this study penetrated the last glacial/interglacial boundary. The diamictites obtained by these cores were subjected to petrographic analysis to assist in reconstruction of the paleodrainage of former ice sheets. Finally, the sediments overlying subglacial and sub-ice shelf deposits were examined to understand the rate of retreat of these ice masses from the shelf.

PREVIOUS WORK

Scott [1905a, b] was the first to speculate that the Ross Sea once was covered by an extensive ice sheet, the "Great Ice Sheet." He believed this expanded ice sheet grounded on the continental shelf as far north as Cape Adare (Figure 3). *David and Priestley* [1914] corroborated Scott's ideas. They discovered erratics and moraines perched well above present sea level (up to +305 m) at Cape Royds and Ross Island (Figure 3). From this they concluded that the Great Ice Sheet once extended approximately 320 km north of its present position. Later, *Priestley* [1923] discovered metamorphic and dioritic erratics resting on the basaltic rocks of Cape Adare. He inferred that the East Antarctic Ice Sheet (EAIS) once had flowed over and through the mountains of northern Victoria Land and onto the adjacent continental shelf, filling Robertson Bay (Figure 3) with at least 300 m of ice. *Debenham* [1921] made similar observations in the McMurdo Dry Valleys region (Figure 3), but he felt that raised moraines and erratics in this area resulted from more localized glacial expansion. *Stuiver et al.* [1981] cite widespread occurrences of striated surfaces, erratics, and moraines, located well above the present ice surface, as evidence for former expansion of the ice sheet in the Ross Sea region. The most widespread deposit, the "Ross Sea Drift," is perched 240 m to 610 m above present sea level [*Stuiver et al.*, 1981].

Numerous radiocarbon dates have been obtained in the Ross Sea region. These indicate that the late

Wisconsin glacial maximum occurred between 21,200 and 17,000 years B.P. [*Stuiver et al.*, 1981]. During the maximum an estimated 1325-m-thick ice sheet is believed to have been grounded in McMurdo Sound [*Stuiver et al.*, 1981]. This ice sheet pushed westward into the McMurdo Dry Valleys and grounded in the Ross Sea to the edge of the continental shelf [*Stuiver et al.*, 1981]. Perched erratics on Beaufort and Franklin islands, some resting at elevations of 320 m above present sea level (Figure 3), provide evidence that an ice sheet once extended onto the continental shelf. Alternatively, these erratics could have been deposited from icebergs prior to the uplift of the islands, which occurred since the initiation of ice rafting in the Ross Sea [*Stuiver et al.*, 1981].

On the basis of the continental record the ice front began its retreat approximately 17,000 years ago and reached its present position by 6190 years B.P. [*Stuiver et al.*, 1981]. This retreat is believed to have been triggered by a sea level rise in response to deteriorating ice sheets in the northern hemisphere [*Thomas and Bentley*, 1978].

Stuiver et al. [1981] suggested that during the last glacial maximum, the expansion of the WAIS was not coupled with an advance of the EAIS, at least not in southern Victoria Land. However, evidence for thickening and expansion of the EAIS in northern Victoria Land occurs in the form of perched erratics, moraines, and striations along the coast between Cape Adare and Rennick Glacier (Figure 3) [*Harrington et al.*, 1967; *Hamilton*, 1972; *Mayewski*, 1975, 1982; *Duphorn*, 1981; *Stuiver et al.*, 1981; *Denton and Wilson*, 1982]. *Duphorn* [1981] suggests that two episodes of glacial expansion occurred, the first in the late Miocene-Pliocene. A second event is believed by *Denton and Wilson* [1982] to have occurred during late Wisconsin time. *Mayewski* [1982] suggests that during the older "Evans" glaciation, the ice sheet was grounded 43 km farther north than it is at present. This places the ice well out onto the continental shelf and about 18 km north of the present grounding line during the more recent glacial expansion.

The arguments for a more extensive ice sheet in the Ross Sea during the last glacial maximum have not gone uncontested. As early as 1921, *Debenham* [1921] argued that raised moraines and erratics of the southern Victoria Land region could be explained by localized glacial expansions. *Mayewski* [1975] mapped ancient moraines associated with the Scott, Amundsen, Shackleton, and Beardmore glaciers and concluded that they were deposited by a much thickened EAIS and that the grounding line of the Ross Ice Shelf could have been very near its present position during these events. On the basis of glaciological arguments, *Whillans* [1976] argued that

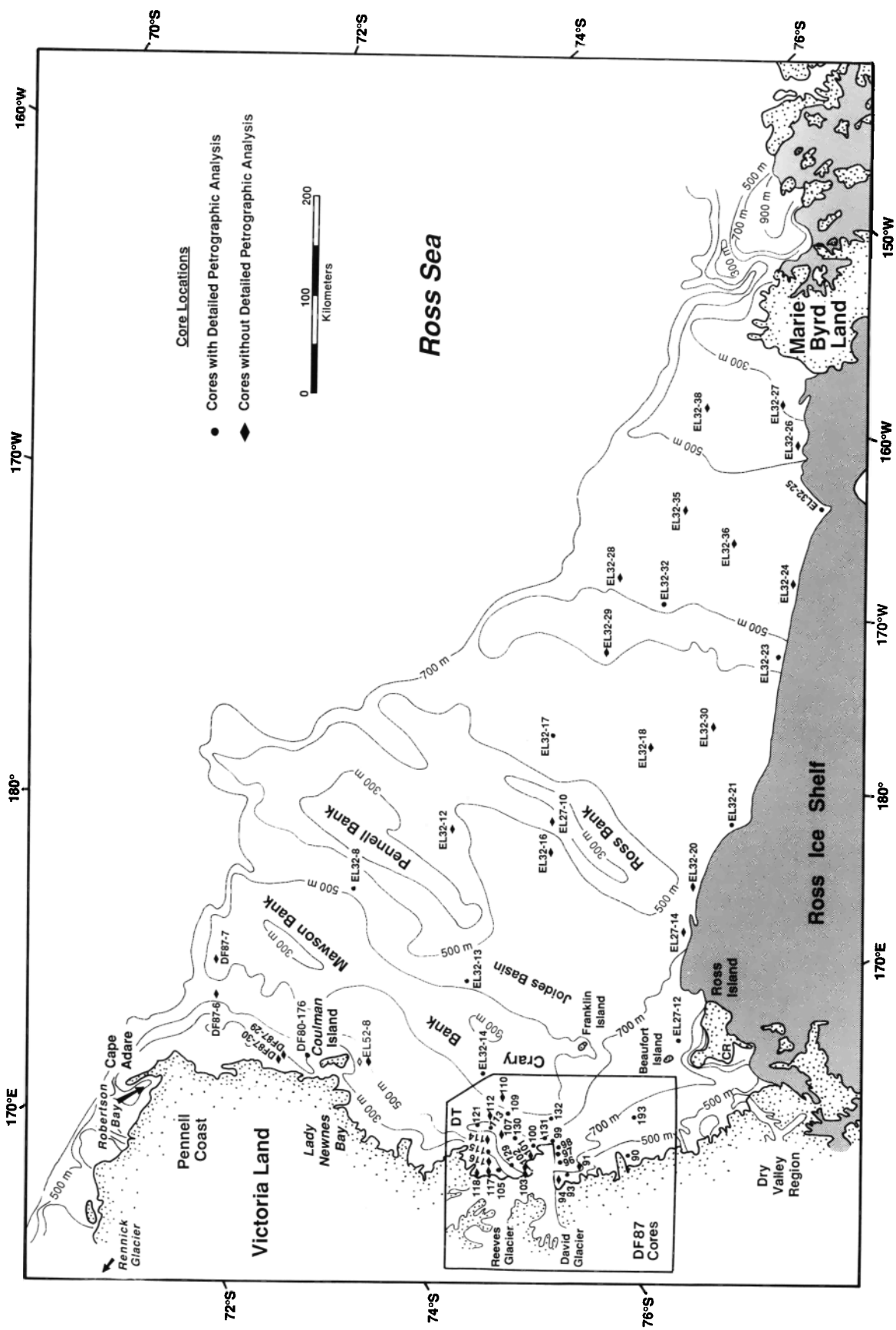


Fig. 3. Geography and bathymetry of Ross Sea. Also shown are locations of piston cores used in this study. DT is the Drygalski Trough, and CR is Cape Royds.

the WAIS probably has varied little in extent and thickness during the last 30,000 years.

Drewry [1979] reviewed the evidence for ice sheet expansion onto the Ross Sea continental shelf during the last glacial maximum. He concluded that the grounding line of the ice sheet was slightly seaward of its present position 18,000 years ago, but that the ice shelf might have extended over much of the continental shelf (Figure 2). His argument is based on the concept that a eustatic sea level fall of greater than 120 to 130 m, sustained over a period of 5000 to 10,000 years, would be required to fully ground the ice sheet [Thomas and Bentley, 1978; Drewry, 1979]. It is estimated that the maximum sea level fall around Antarctica, in response to the late Wisconsin northern hemisphere ice buildup, was only approximately 75 to 100 m [Clark *et al.*, 1978; Lingle and Clark, 1979].

Piston cores from the Ross Sea shelf have been examined by several investigators to establish subglacial versus glacial marine origin of diamictons [Fillon, 1975; Kellogg and Truesdale, 1979; Anderson *et al.*, 1980, 1984; Domack *et al.*, 1980; Edwards *et al.*, 1987]. The results of these studies are contradictory. Fillon [1975] favored a glacial marine origin; Kellogg *et al.* [1979], Anderson *et al.* [1980, 1984], and Domack *et al.* [1980] argued in favor of a subglacial origin.

The evidence provided by Kellogg *et al.* [1979] for a subglacial origin of diamictons (their unit B) includes (1) the widespread occurrence of this unit, (2) its compact nature and lack of sorting, and (3) the presence of reworked microfossils. Anderson *et al.* [1980, 1984] and Domack *et al.* [1980] reexamined these diamictons and added textural and mineralogic homogeneity of individual units, pebble fabric (relative to the vertical plane), and pebble shape to the list of glacial criteria. These combined criteria imply rapid deposition from basal debris zones but do not allow conclusions concerning the subglacial (subglacial till) versus expanded ice shelf depositional nature of the diamictons.

Diamictons from the Ross Sea continental shelf typically exhibit shear strength values that exceed 2.5 kg/cm² [Anderson *et al.*, 1980]. Overcompaction implies subglacial deposition but also can result from sediment overburden. Edwards *et al.* [1987] performed geotechnical tests on these diamictons and concluded that they are overcompacted, but the degree of overcompaction is minor and implies grounded ice with thicknesses only tens of meters greater than the water depth of the shelf. However, the piston cores that Edwards and his colleagues examined penetrated only a short distance into the diamicton. Hence they measured the physical properties of sediments that may have been deposited just prior to ice sheet decoupling from the seafloor.

METHODS

Seismic profiles used in this study were acquired during two separate cruises, the Deep Freeze 87 cruise and the U.S. Antarctic Program 1990 (USAP 90) cruise (Figure 4). Deep Freeze 87 data were acquired with an EG&G sparker system using 1 and 4.6 kJ of power, and USAP 90 data were acquired with a bubble-free air gun (SSI Generator-Injector Gun). Sparker data were obtained with a 20-element, single-channel benthos steamer, and data were recorded by analogue recorder. Air gun data were acquired digitally using a 50-m single-channel streamer. Global positioning system (GPS) and satellite navigation were used to record shot point locations.

During *Eltanin* cruises 27, 32, and 52, and Deep Freeze cruises 76 and 78, piston cores were collected from the Ross Sea continental shelf (Figure 3). Most of these cores were acquired from the central and eastern portion of the shelf (Figure 3). Later, during Deep freeze cruises in 1980 and 1987, additional piston cores were collected from the continental shelf of the western Ross Sea (Figure 3). The length of piston cores ranges from a few centimeters to just over 5 m.

Prior to, or soon after, cutting the cores, sediment physical properties (shear strength and cohesiveness) were determined using a torvane and penetrometer. These combined measurements provide an estimate of sediment overcompaction. These measurements were not made on the older *Eltanin* cores.

X radiographs of cores allowed estimation of pebble content and identification of sedimentary structures. Lithological descriptions were made using the cut core, the X radiograph, and smear slides. The concentration of different microfossil groups (planktic and benthic foraminifera, diatoms, and sponge spicules) was determined microscopically; only the benthonic foraminiferal fraction was examined for species content. Sediment texture was determined using an automated settling tube (for particles larger than 32 µm) and hydrophotometer (for particles smaller than 32 µm).

Pebbles greater than 1 cm in diameter were located in each core through surface expression, X radiography, and probing. Once removed from the core, estimates of sphericity and roundness of each pebble were made using the method of Krumbein [1941]. These values were plotted against each other to determine the glacial transport mode, on the basis of the method described by Boulton [1978].

Petrographic analyses were conducted on the coarse sand and pebble fractions of samples from diamictons and on the glacial marine sediments which overlie

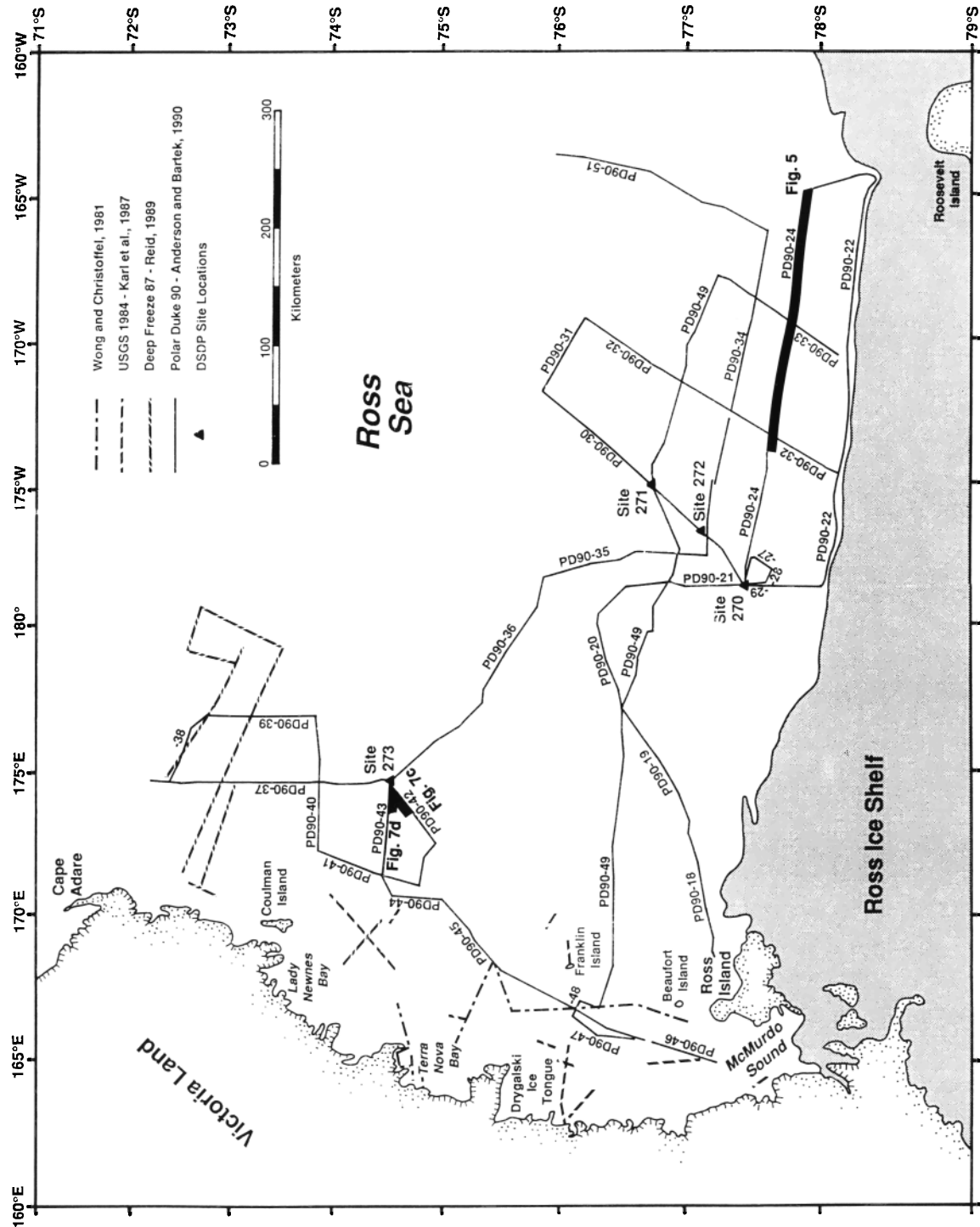
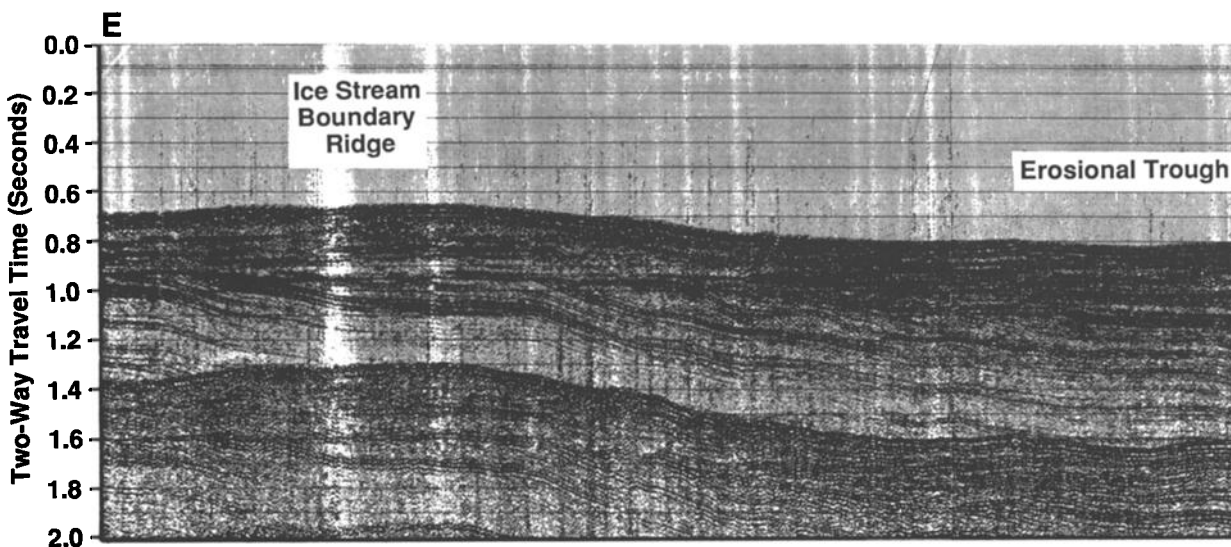


Fig. 4. High-resolution seismic reflection profiles used in this study. Figure numbers adjacent to highlighted lines indicate portions of seismic lines shown in this text.



PD90-24

Fig. 5. Portion of high-resolution seismic reflection profile USAP 90-24 from the Ross Sea continental shelf showing broad (tens of kilometers) erosional surfaces that are interpreted as glacial troughs cut by ice streams. Note that the dimensions are similar to those of modern ice streams. See Figure 4 for profile location.

them. A minimum of 100 pebbles per core was counted where possible. Thin sections were made of selected pebbles to confirm lithologies.

Matrix samples, collected at approximately 50-cm intervals, were wet-sieved to remove fine-grained material and then dry-sieved to separate the coarse sands (0.5 mm to 2.0 mm). Coarse sands were counted using the area method [Galehouse, 1971]. At least 300 grains were counted and examined using a petrographic microscope with both transmitted and reflected light and an automated point-counting stage. Results were recorded as number percents.

Factor analysis permitted definition of the major petrologic provinces of sands, heavy minerals, and pebbles gathered from diamictites and diatomaceous muds. *Q* mode factor analysis distinguished the relationship among the variables of this relatively large number of samples in terms of a smaller number of compositionally extreme theoretical end-members or factors [Chriss and Frakes, 1972]. The factor analysis was performed using BrainPower's STATVIEW 512+ software on an Apple Macintosh microcomputer. The factor extraction used in this study was principal components analysis, a well-established factor method that performs an eigenvalue-eigenvector analysis of the correlation matrix in its original form.

The Orthotran/Varimax Oblique Solution transformation method used on the initial factor solution

rotated the factors to positions in which the variance of the loadings of samples on the axes was maximized [Davis, 1973]. The factors were rotated to positions where each factor coincided with one of the original samples, which then became the end-members [Davis, 1973]. The "end-members" were used in conjunction with geographical constraints to define the petrologic provinces.

The relationship between the factors and the compositional variation of the samples was determined by simple linear regression of factor loading (dependent variable) on the compositional data (independent variables) [Chriss and Frakes, 1972]. Lithologies or mineralogies displaying a high positive correlation with a factor loading are regarded as the distinguishing features that characterize that factor (end-member).

RESULTS

Seismic Reflection Investigations

The following section describes features believed to be deposited in proximity to the ice sheet grounding line. The terminology used (till tongues, subglacial deltas, morainal banks) makes certain assumptions about the origin of these features, namely, that they are subglacial in origin, which still requires testing. However, these terms are employed because they

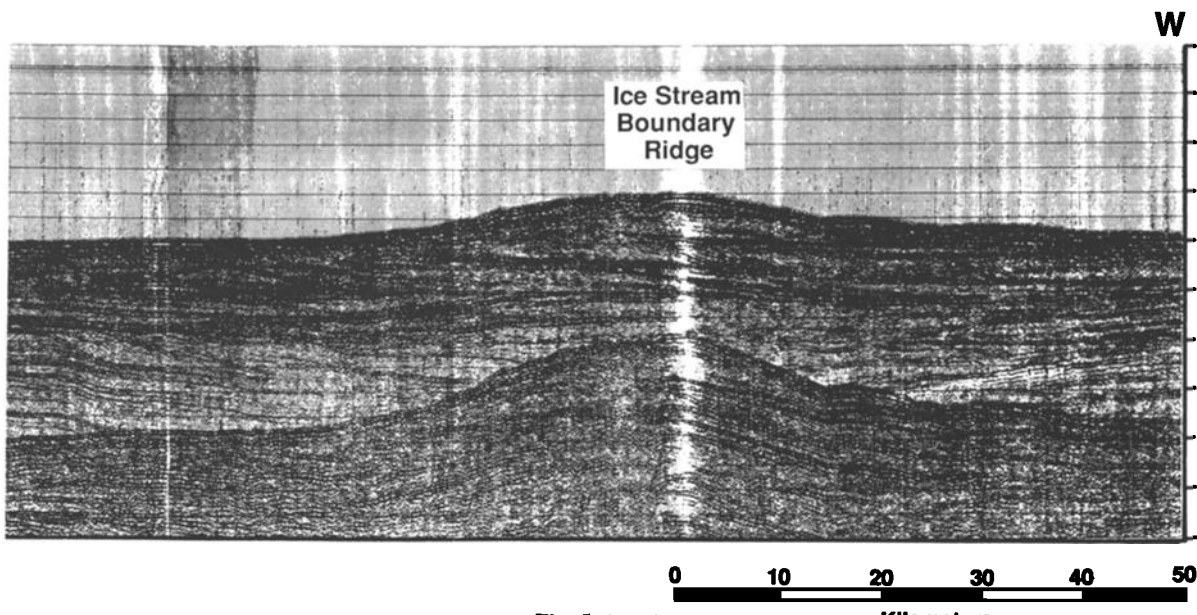


Fig. 5. (continued)

occur in the literature; use of new terms might introduce confusion until a better understanding of the origin of these features is obtained.

A series of north-northeast to south-southeast oriented basins and ridges characterizes the bathymetry of the Ross Sea (Figures 2 and 3). These features extend beneath the Ross Ice Shelf where they have a more northwest to southeast orientation [Drewry, 1983]. *Hughes* [1977] observed that the linear basins of the inner shelf correspond to the locations of modern ice streams at the grounding line of the Ross Ice Shelf. From this he argued that the linear basins of the shelf were formed by accelerated glacial erosion beneath ice streams during a previous expansion of the West Antarctic Ice Sheet. The reconstructions shown in Figure 2 were partially constructed using these bathymetric features.

East-west oriented seismic profiles collected during USAP 90 aboard the R/V *Polar Duke* (PD90 profiles) in the eastern Ross Sea also display the ridge and trough topography (Figure 5). The troughs are products of glacial erosion and can be traced across several east-west profiles (Figure 6). The troughs are believed to be the erosional remnant of ice streams and agree relatively well with the positions of the ice streams presented by *Stuiver et al.* [1981] (Figure 6). Erosion probably occurred during several glacial advances [Bartek et al., 1991; Anderson and Bartek, 1992; Alonso et al., this volume], as evidenced by repeated troughlike features at deeper positions in the profiles (Figure 5). Trough widths average 125 km; depths average 140 m, measured from the trough shoulders. The dimensions are used to infer that these

features were formed by ice streams of sizes similar to those of modern ice streams in the region.

The trough boundaries are marked by a series of 50-km-wide (average), 150-m-high, concave-down, depositional ridges with some internal stratification (Figure 5). Discrete stacked packages, laterally grading into the trough floor, comprise the ridges. They are continuous across the east-west seismic profiles and are interpreted to mark the positions of ice stream boundaries (Figure 6), as presented by *Stuiver et al.* [1981]. Similar features, though laterally offset from the surficial deposits, occur lower in the record (Figure 5).

The ridge and trough system in the western Ross Sea is not developed as extensively as that of the eastern Ross Sea. Positions of the ice streams may be more dependent on structural boundaries (i.e., the structural high separating the eastern and the western Ross Sea).

Positions of some of the troughs and ridges have varied through time (Figure 5), indicating the major ice stream boundaries also have shifted to some degree. Other troughs, associated with structural features, do not appear to have migrated with time and may have stabilized the entire system.

Within the western Ross Sea, conspicuous evidence of glacial erosion of the seafloor also exists as glacial troughs located offshore of the modern outlet glaciers of northern Victoria Land. The largest of these troughs, Drygalski Trough (Figure 3), lies offshore of David Glacier, one of the largest outlet glaciers in Northern Victoria Land. A morainal bank extends along the northern rim of Drygalski Trough (Figure 7a).

High-resolution seismic profiles from the western Ross Sea record a widespread erosional surface draped by a unit characterized seismically by discontinuous reflectors and hyperbola [Karl, 1989]. In places the upper unit contains sedimentary bodies interpreted as subglacial in origin. For example, U.S. Geological Survey (USGS) profile 413 from the western Ross Sea [Karl et al., 1987] shows a wedge-shaped body of deposits which thickens to the north and has seaward dipping clinoforms at its northern end. Internal reflectors are discontinuous, and hyperbolic reflectors characterize the upper surface (Figure 7b). Given this internal (clinoform) geometry, these bodies are interpreted as "subglacial deltas" and possibly were produced by processes similar to those acting near the

grounding line of ice stream B today [Alley et al., 1989]. Similar features were recognized in seismic records acquired during Deep freeze 87 and USAP 90 [Anderson and Bartek, 1992]. Other features are identical to till tongues (Figures 7c and 7d) shown in high-resolution seismic records from the southeastern Canadian shelf [King and Fader, 1986; King et al., 1991]. Both subglacial deltas and till tongues rest on regional erosional surfaces.

Work by Karl [1989] on high-resolution seismic records from the western Ross Sea shelf led to the conclusion that the ice sheet was grounded there during the last glacial maximum at least as far north as the approximate latitude of Coulman Island (Figure 4). Seismic records acquired during Deep Freeze 87

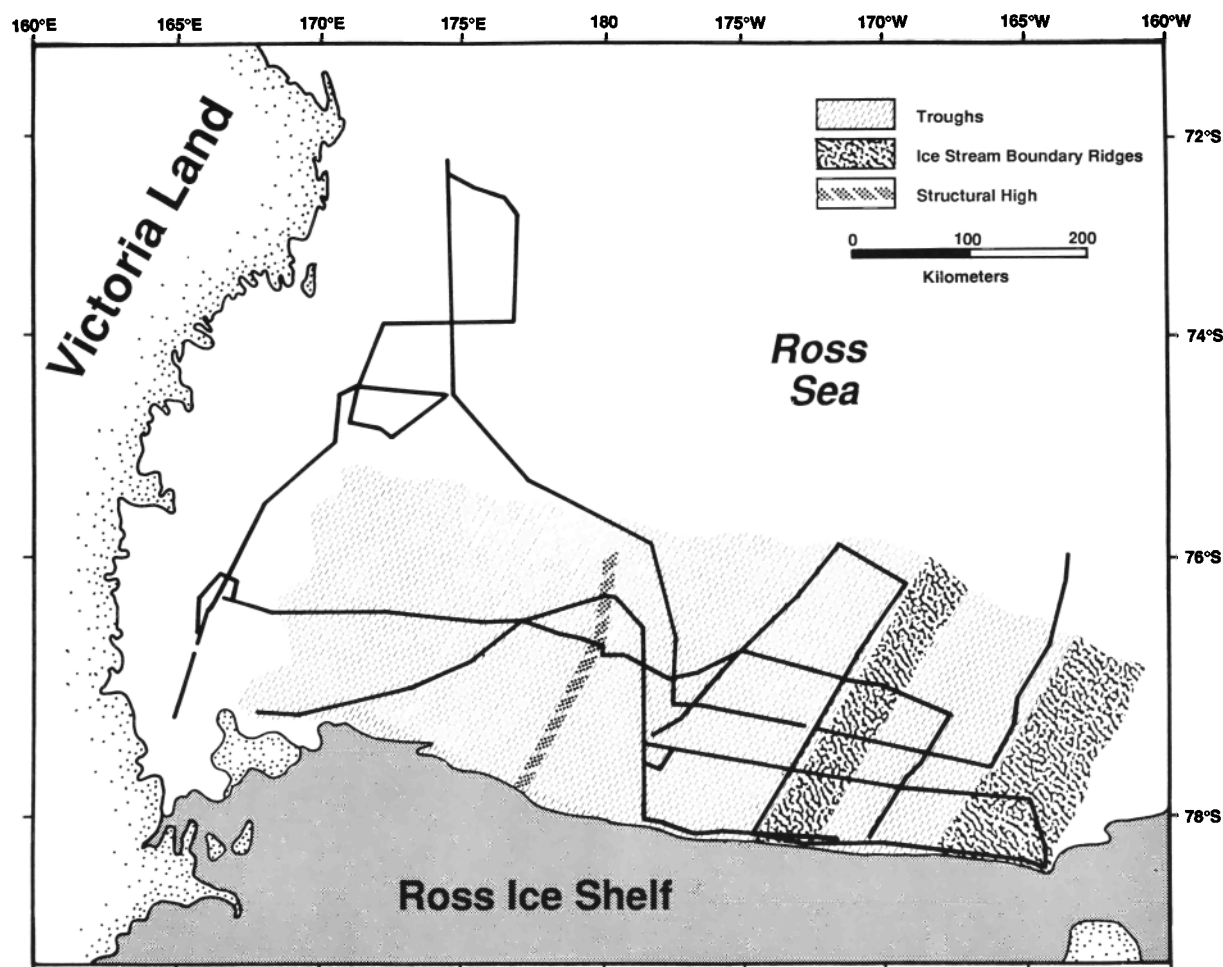


Fig. 6. Map illustrating areal extent of troughs associated with ice stream drainage, and ridges interpreted to be ice stream boundary indicators. The troughs and ridges are more easily identified in the eastern Ross Sea than in the western Ross Sea.

and USAP 90 extend the high-resolution seismic coverage north of Coulman Island to the continental slope. These data show a change in the character of near-surface deposits from north to south within the western Ross Sea. Intercutting erosional surfaces, some of which define troughs similar in scale to modern troughs of the inner shelf, display relatively high relief on individual reflectors, and till tongues characterize the southern part of the area. Much of the late Miocene and younger section has been eroded. The northern part of the survey area shows generally flat, coherent reflectors separated by acoustically transparent zones. *Reid* [1989] suggests that the boundary between these different seismic provinces marks the northern limit of the grounding line of an expanded ice sheet during the most recent glacial maximum.

In summary, high-resolution seismic reflection profiles from the Ross Sea provide abundant evidence that ice sheets grounded here on more than one occasion. The questions remain as to when ice sheets last grounded on the shelf and what was the geometry of the paleodrainage of the ice sheet during the last glacial maximum.

Petrographic Analyses of Diamictons

Piston cores from the Ross Sea continental shelf penetrated a variety of lithologies ranging from diamicton to diatomaceous ooze and carbonate (Figure 8). In general, the stratigraphy of piston cores from the Ross Sea can be described as one in which younger glacial marine sediments, reflecting a dominance of marine influence on sedimentation, rest on glacial and glacial marine deposits that indicate a predominance of glacial influence [Fillon, 1975; Kellogg et al., 1979; Anderson et al., 1980, 1984].

Massive diamictons are, by far, the most widespread subsurface deposits; they were penetrated in most piston cores from the shelf except those acquired in the western Ross Sea north of Coulman Island (Figure 8). Previously, detailed analyses of the diamictons yielded results which favor a subglacial origin [Kellogg et al., 1979; Anderson et al., 1980, 1984; Domack et al., 1980]. These criteria include (1) lack of sorting and stratification; (2) absence of fossils, other than reworked; (3) overcompaction; and (4) pebble shape. These combined criteria offer strong, but not conclusive, evidence of a subglacial origin, and they provide no information concerning paleodrainage from which to reconstruct former ice sheets. Also, these diamictons are virtually devoid of calcereous and carbonaceous material from which radiocarbon dates can be derived. Thus their age is uncertain.

One of the most crucial criteria for determining a subglacial origin of diamictons involves petrographic analysis. Since the turn of the century, glacial geologists have utilized petrographic data (mineral and clast content) to identify tills and to determine the source area of these deposits, thus providing a basis for construction of glacial paleodrainage maps. The concept of petrologic provinces necessitates that glacial sediments exhibit spatial as well as compositional affinities.

The underlying assumption in this study is that marine ice sheets transport and deposit sediment at their base in a fashion similar to that of terrestrial ice sheets. Subglacial tills should consist of fewer varieties of rocks and minerals than iceberg-raftered sediments, whose source area may be quite extensive, at least in the Ross Sea region. The provenance of basal tills can be established where the geology of the source area is known. *Domack* [1982] demonstrated that glacial sediments from the continental shelf of the George V Coast can be correlated positively with exposures of continental rocks. Similar results have been acquired from a study of diamictons on the Weddell Sea continental shelf [Anderson et al., 1991] and in Marguerite Bay [Kennedy and Anderson, 1989].

Petrographic analyses were conducted on three components of diamictons and the glacial marine sediments that overlie them; rock clasts, coarse sand, and heavy minerals. The results of these analyses were combined with the results from an earlier petrographic investigation of Ross Sea diamictons [Myers, 1982]. Clay mineralogical analyses of several of the cores were conducted previously by *Balshaw* [1981]. Tables 1 and 2 present the results of coarse sand and heavy mineral analyses, respectively. Too few pebbles were recovered to enable statistical analysis of these data. However, these data are reported because pebbles provide actual rock specimens with which to check petrographic results and provide additional insight into the geology of the source area.

Coarse sand data fit into four factors (Table 1). When plotted on a map, the factors fall into seven provinces whose boundaries follow the northeast-southwest bathymetric trend of the shelf (Figure 9). These provinces are believed to represent the former positions of the ice streams on the shelf.

Petrographic data for diamictons from the central and eastern Ross Sea continental shelf display only subtle petrographic differences (Tables 1 and 2), which distinguished provinces 4 through 7. These diamictons presently occur many hundreds of kilometers from the grounding line of the Ross Ice Shelf. Sedimentary basins with thick sedimentary sequences are believed to exist beneath Ross Ice Shelf [Davey, 1981; Truswell and Drewry, 1984]. Hence the

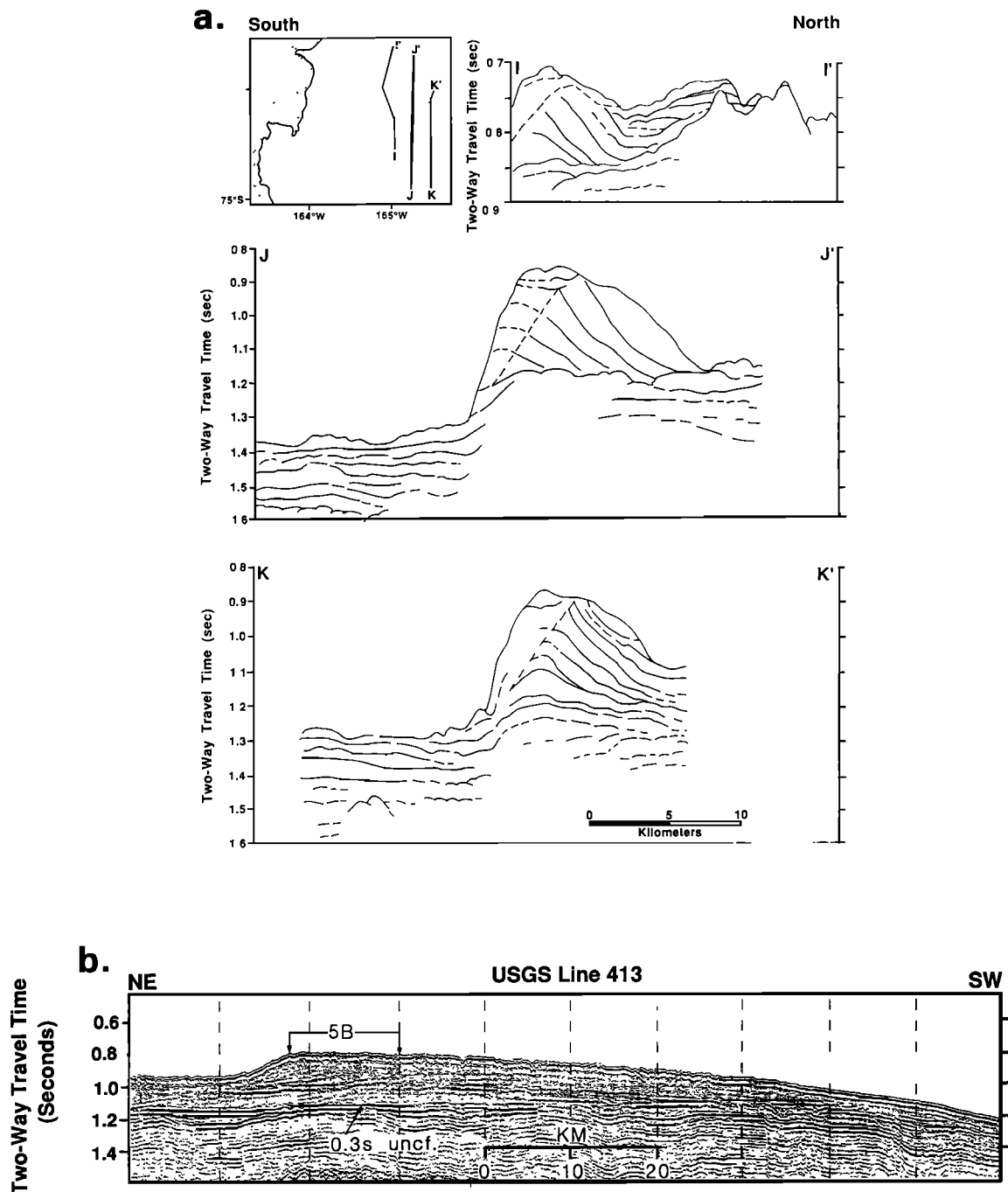


Fig. 7. Examples of subglacial features on the Ross Sea continental shelf: (a) a morainal bank [from Wong and Christoffel, 1981], (b) a subglacial delta [from Karl et al., 1987], (c) till tongue on a dip profile, and (d) till tongue on a strike profile. Locations of Figures 7c and 7d are shown in Figure 4.

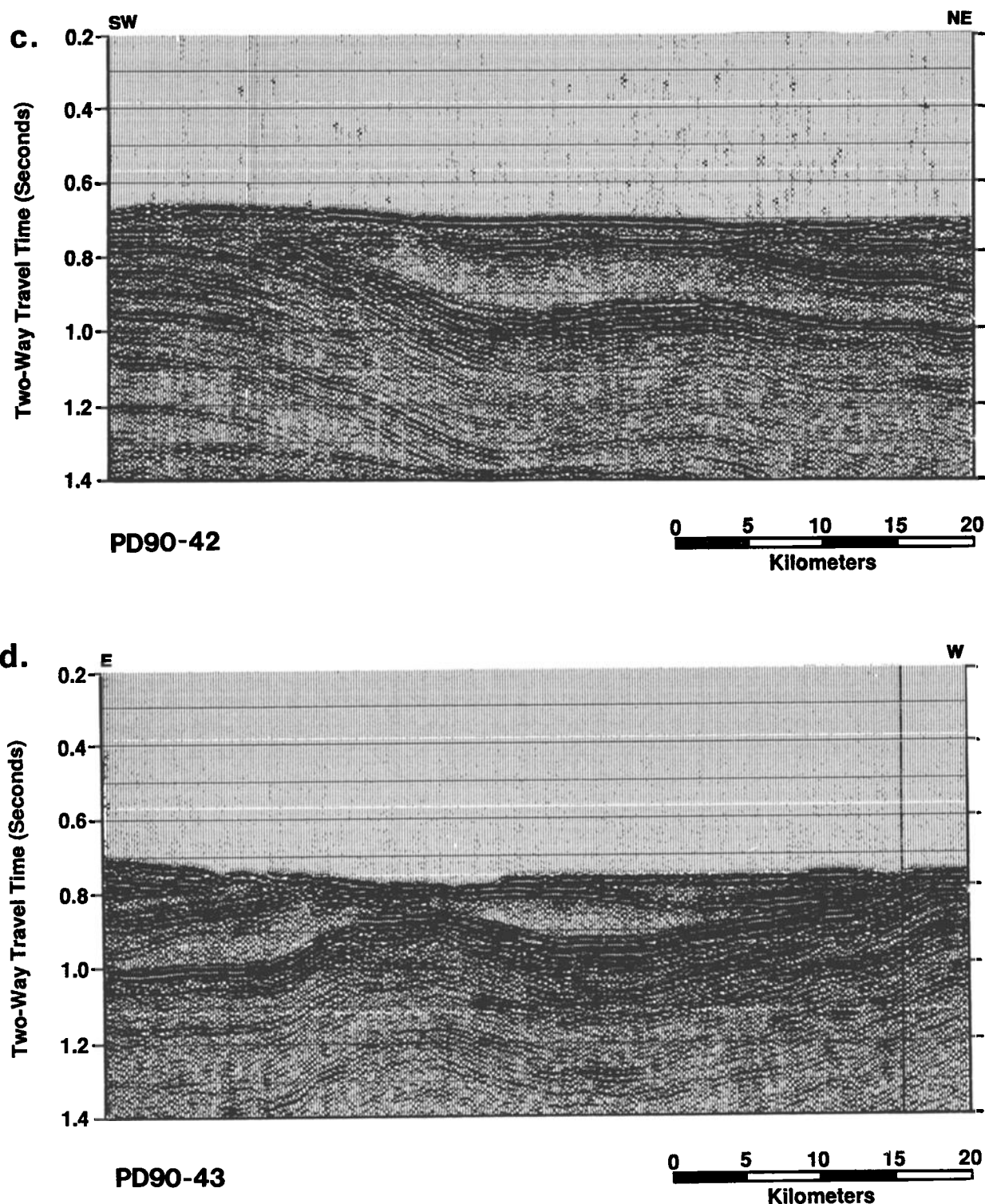


Fig. 7. (continued)

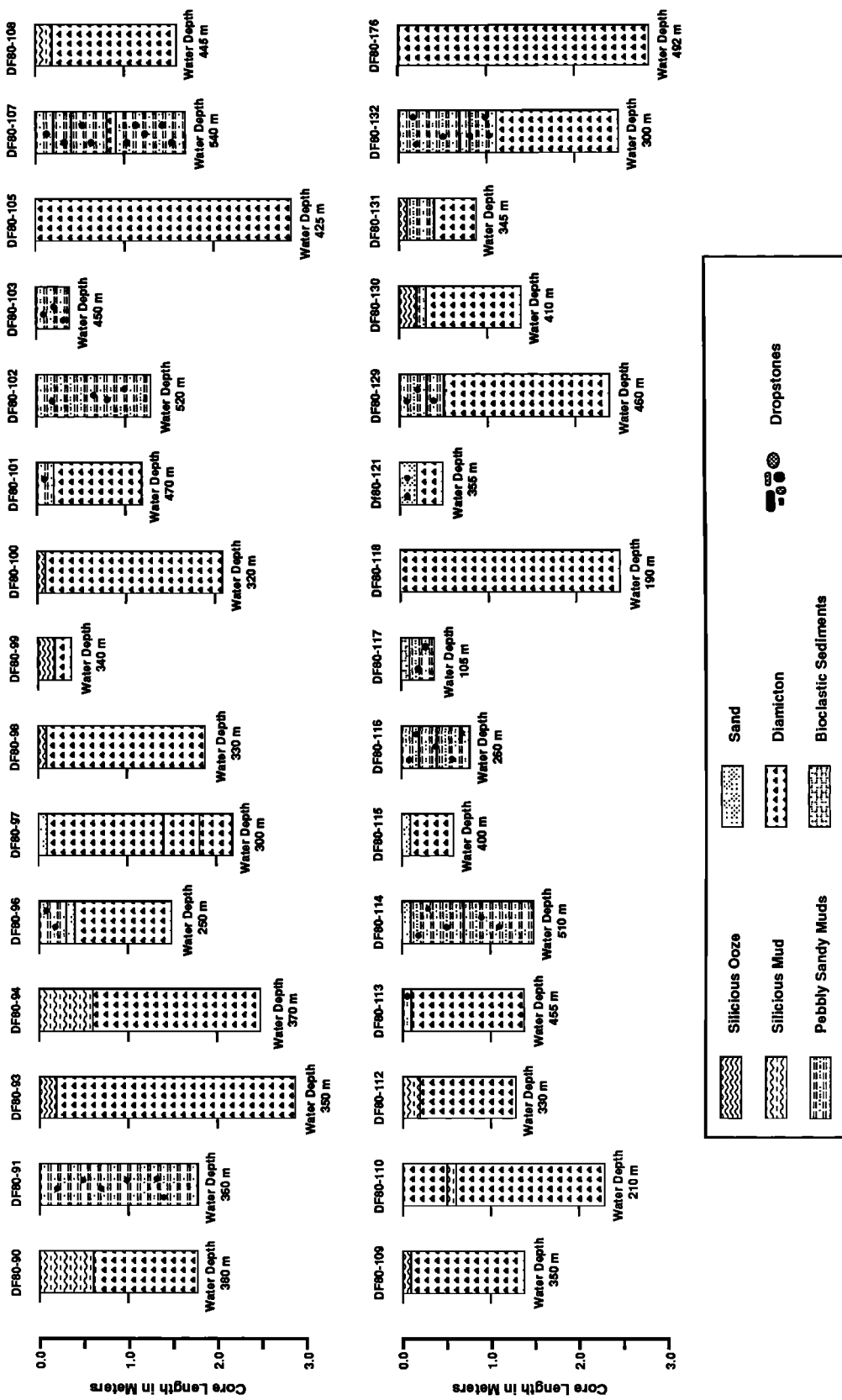


Fig. 8. Generalized lithologies of piston cores from the Ross Sea continental shelf. See Figure 3 for locations of cores.

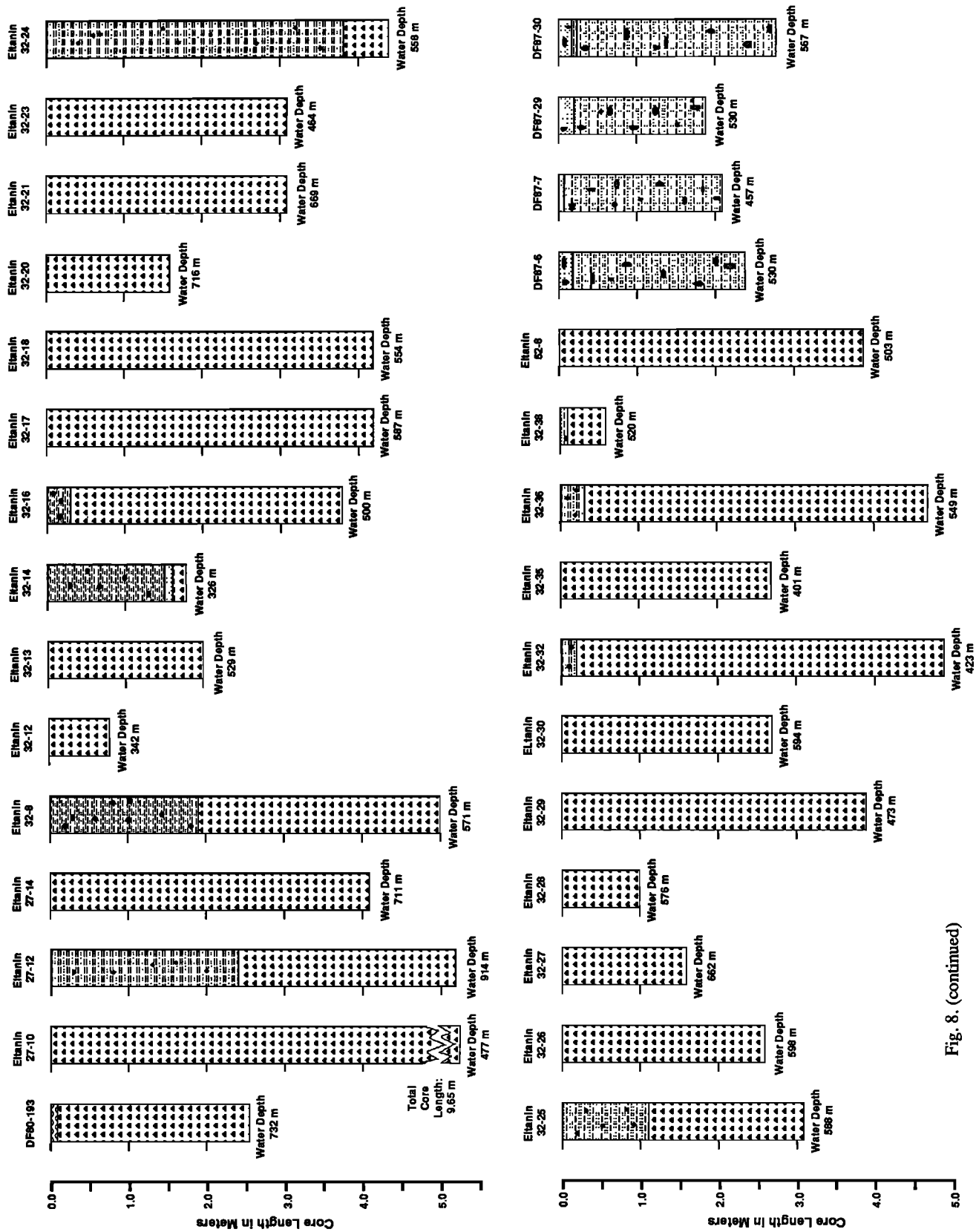


Fig. 8. (continued)

tills that occur on the outer shelf have been transported great distances and undoubtedly have been recycled numerous times. Combined comminution and mixing has led to less distinct compositional differences in these deposits than is observed in diamictons of the western shelf. For this reason the clay compositions [Balshaw, 1981] of these diamictons, and their coarse sand and pebble components, were used to define provinces.

Schist, gneiss, rounded quartz, granite, and diabase comprise the dominant coarse sand components of diamictons from the central and eastern shelf (Table 1). There is a slight difference in the heavy mineral compositions of diamictons collected east and west of approximately 180° (Table 2). Cores from west of this line exhibit heavy mineral compositions dominated by biotite and hornblende, with lesser amounts of pyroxene and garnet. Cores east of this line contain significantly less pyroxene and garnet. Clay mineral analyses also distinguish the boundary between these two petrographic provinces. Diamictons collected east of approximately 180° have a fine-grained matrix richer in smectite than that of cores collected farther to the west [Balshaw, 1981]. These petrographic boundaries coincide approximately with the glacial drainage divide between Hughes's [1977] ice streams A and B, which receive drainage from the Transantarctic Mountains, and ice streams C, D, E, and F, which drain the Marie Byrd Land area (Figure 2). Province 4 is comprised of sediments derived from ice streams A and B; province 5 from ice streams B and C; province 6 from ice streams B, C, D, and E; and province 7 from ice streams E and F (Figure 9).

Truswell and Drewry [1984] examined reworked palynomorphs in diamictons from the central and eastern Ross Sea shelf. They found distribution patterns broadly similar to the petrographic provinces presented here. Both distributions show assemblage boundaries that are subparallel to the bathymetric features of the shelf.

Half (20) of the cores collected from the western Ross Sea penetrated diamictons that bear all the characteristics of subglacial till. The other 20 cores penetrated either glacial marine sediments or sediment gravity flows, including debris flows and turbidites (Figures 8 and 9). The glacial marine sediments and sediment gravity flow deposits appear to thicken to the north and toward the coast and may overlie subglacial tills in these areas [Reid, 1989]. North of Coulman Island (Figure 3), piston cores penetrated a wide range of glacial marine sediments, including carbonates, but no overcompacted diamictons were recovered [Reid, 1989].

The diamictons from the southwestern Ross Sea are segregated into three petrographic provinces on the

basis of their coarse sand mineralogies (Figure 9). The boundaries between these provinces parallel northeast-southwest oriented bathymetric features, most notably Drygalski Basin.

Although pebble concentrations are too small to allow statistical analysis, they show similar trends to the coarse sand data. Geologic exposures along the Victoria Land coast are sufficiently widespread to allow a comparison between diamicton petrologic provinces and the rocks of the inferred source areas. This provides additional information with which to locate paleodrainage divides. For example, biotite and unweathered biotite schists are abundant constituents of province 1 diamictons (Tables 1 and 2). This province corresponds to coastal outcrops of biotite schists and gneisses exposed near Priestley Glacier [Gair, 1967]. Volcanic glass in these diamictons also is derived from coastal outcrops located north of David Glacier.

Well-rounded quartz grains are abundant in diamictons from province 2 (Tables 1 and 2) and are believed to be derived from Beacon Group sandstones, which are exposed predominantly south of David Glacier [Gair, 1967]. Dolerite, a relatively minor constituent of province 2 diamictons, is derived from the Ferrar Group, which is widely exposed near the coast south of David Glacier. Province 2 extends north to Coulman Island.

Province 3 diamictons are distinguished by their relatively high volcanic glass content (Tables 1 and 2). These volcanic sands probably are derived from volcanic islands, and possibly seamounts, of the McMurdo Volcanic Province, which is aligned with this petrographic province (Figure 9).

DISCUSSION

Core coverage in the eastern and central Ross Sea is too sparse to allow detailed reconstruction of grounding line positions and the glacial marine setting following ice sheet retreat from the continental shelf. During Deep Freeze 87, additional cores were acquired from the western Ross Sea to permit such reconstructions in this region. Analysis of these piston cores and seismic data provided evidence for a grounding line located just north of Coulman Island. Key cores in this reconstruction include DF 80-176, DF 87-6, DF 87-7, DF 87-29, DF 87-30, and EL 52-8 (Figure 10).

Piston Cores DF 80-176 and EL 52-8 penetrated subglacial till. Cores collected north of the DF 80-176 core site penetrated glacial marine deposits. Hence the maximum grounding line position is placed between these two cores.

The glacial marine deposits in cores DF 87-29 and DF 87-30 are overlain by silty, fossiliferous sands.

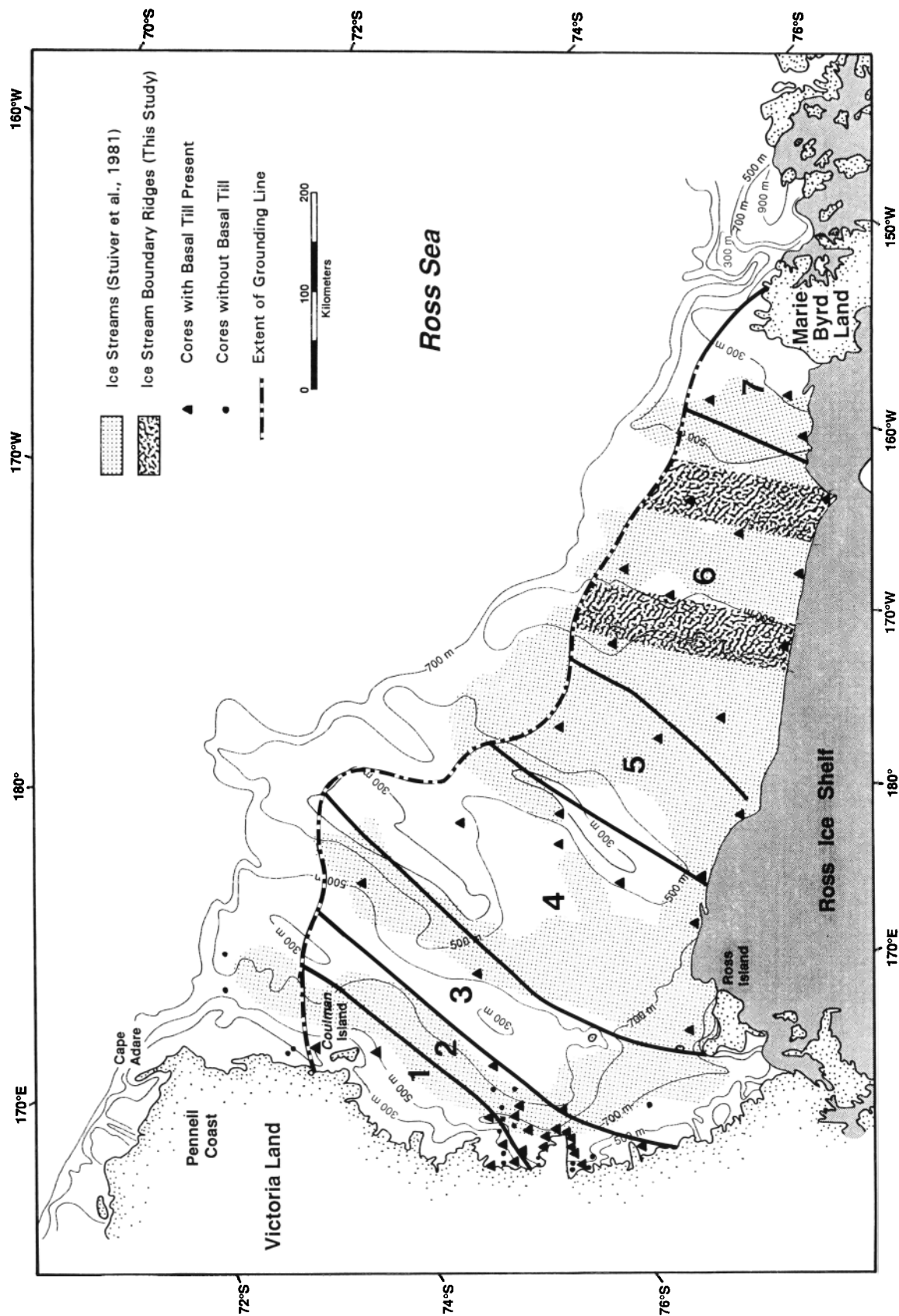


Fig. 9. Petrographic provinces of diamictites (subglacial tills) on the Ross Sea continental shelf. Also indicated is a reconstruction of the ice sheet based on the results from this investigation.

TABLE 1. Results of Coarse Sand Mineralogical Analysis

	Description	Piston core
Factor 1	Contains schist and small but significant quantity of gneiss.	DF 80-105 DF 80-115 DF 80-121 DF 80-176 EL 27-12 EL 32-17 EL 32-21 EL 32-23 EL 32-25 EL 32-27 EL 32-32
Factor 2	Contains rounded quartz, granite, and very small but significant quantities of diabase.	DF 80-96 DF 80-97 DF 80-98 DF 80-108 DF 80-129 DF 80-130 DF 80-193
Factor 3	Contains diamictite fragments and very small but significant quantities of litharenites.	DF 80-90 DF 80-93 DF 80-99 DF 80-109 EL 32-13
Factor 4	Contains volcanic glass.	DF 80-132 EL 32-14 EL 52-8
Mixtures	Factors 2 and 3* Factors 2* and 3 Factors 2 and 3 Factors 1, 2,* and 3 Factors 1 and 2* Factors 3 and 4* Factors 1* and 3 Factors 1 and 2* Factors 1* and 2 Factors 1, 3,* and 4 Factors 3* and 4 Factors 1* and 3 Factors 1* and 3 Factors 1* and 2 Factors 1 and 4*	DF 80-90 DF 80-97 DF 80-100 DF 80-108 DF 80-131 DF 80-132 DF 80-176 DF 80-193 EL 27-12 EL 32-8 EL 32-13 EL 32-17 EL 32-21 EL 32-27 EL 52-8
Sand - province 1 (heavy mineral provinces 1 and 4)	Drygalski Trough, predominantly contains factor 4 and a component of factor 1. EL 52-8	DF 80-105 DF 80-115 DF 80-121 DF 80-176
Sand - province 2 (heavy mineral)	Western Ross Sea; contains factors 2, 3, and 4.	DF 80-90 DF 80-93 DF 80-96 DF 80-97

TABLE 1. (continued)

	Description	Piston core
	provinces 2 and 3)	DF 80-98 DF 80-99 DF 80-100 DF 80-108 DF 80-109 DF 80-129 DF 80-130 DF 80-131
	Sand - province 3 (heavy mineral provinces 3 and 4)	Western central Ross Sea; contains factors 3 and 4. DF 80-132 EL 32-8 EL 32-13 EL 32-14
	Sand province 4 (heavy mineral provinces 1 and 2)	Southwestern Ross Sea; contains factors 1 and 2. DF 80-193 EL 27-12
	Sand province 5 (heavy mineral provinces 1 and 2)	Central Ross Sea; predominantly contains factor 1 and a component of factor 2. EL 32-17 EL 32-21
	Sand province 6 (heavy mineral province 1)	East central Ross Sea; contains factor 1 EL 32-23 EL 32-25 EL 32-32
	Sand province 7 (heavy mineral provinces 1 and 2)	Eastern Ross Sea; predominantly contains factor 1 and a component of factor 2. EL 32-27

* Dominant factor.

The contact between the glacial marine deposits and the overlying sand unit is gradational. The grain size and the concentration of volcanic material comprising these sand fractions increase upward in the core (Figure 10). The increase in volcanic material implies a greater contribution of debris from nearby Coulman Island and coastal volcanic deposits. Additionally, clasts within the upper unit are more angular than clasts in the underlying glacial marine sediment (Figure 11). This implies higher-level (englacial and supraglacial) transport for some of the pebbles in the

TABLE 2. Results of Heavy Mineral Analysis

	Description	Piston Core
Factor 1	Contains colorless and green pyroxene and very small but significant quantity of colorless garnet.	DF 80-98
		DF 80-99
		DF 80-100
		DF 80-108
		DF 80-109
		DF 80-129
		DF 80-130
		DF 80-131
		DF 80-132
		DF 80-193
		EL 27-12
		EL 32-8
Factor 2	Contains biotite and hornblende.	EL 32-13
		EL 32-14
		DF 80-105
		DF 80-115
		DF 80-121
		EL 32-17
		EL 32-21
		EL 32-23
		EL 32-25
		EL 32-32
Factor 3	Contains actinolite and small but significant quantities of red garnet and volcanic glass.	EL 52-8
		DF 80-93
		DF 80-96
		DF 80-97

TABLE 2. (continued)

	Description	Piston core
Mixtures	Factors 1 and 3	DF 80-90
	Factors 1 and 2	DF 80-176
	Factors 1 and 2	EL 52-8
Heavy mineral province 1	Drygalski Trough. Contains factor 2 and a very small but significant component of factor 1. Contains materials from sand provinces 2, 3, and 7.	DF 80-105
		DF 80-115
		DF 80-121
		DF 80-176
		EL 52-8
	Heavy mineral province 2	Western Ross Sea. Contains factors 1 and 3. Contains materials from sand province 1.
		DF 80-98
		DF 80-99
		DF 80-100
		DF 80-108
		DF 80-109
		DF 80-130
Heavy mineral province 3	Central and eastern Ross Sea. Contains factor 2. Contains materials from sand provinces 4, 5, and 6.	DF 80-131
		DF 80-132
		DF 80-193
		EL 27-12
		EL 32-8
		EL 32-13
		EL 32-14

upper unit and basal transport for the older unit. These combined data indicate that the upper units in cores DF 87-29 and DF 87-30 were deposited in a continental shelf setting located seaward of a permanent ice cover where icebergs delivered glacial debris to these sites. The lower glacial marine unit in these cores is interpreted to be a transitional glacial marine deposit, implying deposition near the grounding line [Anderson et al., 1991].

Several cores from shallow banks of the outer shelf terminated in carbonate gravels. Radiocarbon dates of these carbonate gravels yielded ages greater than 35,000 years. Cores DF 87-6 and DF 87-7, collected north of Coulman Island, penetrated a thin (<10 cm) sand unit resting on, and in sharp contact with, a carbonate-rich, gravelly sandy silt and silty sand (Figure 10). Abundant fossils and minor sorting within the matrix are the two main criteria used as evidence of a glacial marine origin for these deposits. Fossils include bryozoans, barnacles, bivalves,

echinoids, gastropods, ostracods, and foraminifera, including planktonic foraminifera. The pebbles and coarse sand fraction within these sediments consist predominantly of volcanic material, which probably was derived from nearby coastal outcrops. These sediments probably were deposited in a glacial marine setting with only seasonal sea ice cover, indicated by the presence of planktonic foraminifera, but a setting where ice rafting exceeded marine sedimentation. The source of ice-rafted debris included valley and outlet glaciers of the Transantarctic Mountains. The thin sand unit that rests on these glacial marine sediments marks a change to conditions similar to those of the present. Modern sands of the outer shelf in the western Ross Sea have been related to strong bottom currents [Anderson and Smith, 1988].

The glacial marine sediments in cores DF 87-6 and DF 87-7 are interpreted as correlative to the transitional glacial marine sediments in cores DF 87-29 and DF 87-30, and to the subglacial tills in cores DF

80-176 and EL 52-8 (Figure 10). Radiocarbon dates from core DF 87-6 yield an age of >35,510 years B.P. for the interval from 189 to 190 cm and an age of $17,390 \pm 500$ years B.P. for the interval between 25 and 40 cm (Figure 10). These dates have been corrected for the carbon reservoir error using a value of ~1200 years [Stuiver *et al.*, 1981]. These dates are consistent with the results of Stuiver *et al.* [1981], who cite evidence for retreat of a lobe of the "Ross Ice Sheet" from Taylor Valley, 500 km to the south, beginning 17,000 years B.P. The thin sand that overlies these glacial marine sediments is, in essence, a condensed section and represents sedimentation since the ice sheet retreated from this region approximately 17,000 years ago.

The vast majority of piston cores from the central and eastern Ross Sea contain diamictites overlain directly by diatomaceous muds and oozes (Figure 8). A sharp contact separates these units, indicating that the change from subglacial sedimentation to hemi-

pelagic sedimentation occurred rapidly. Grain size analysis of surface sediments has shown a pattern of lateral size grading in which sediments decrease in grain size and become more diatomaceous to the south [Anderson *et al.*, 1984; Dunbar *et al.*, 1985]. This is believed to result from an increase in water depth and a decrease in marine current energy in that direction [Dunbar *et al.*, 1985]. No evidence of lateral grading exists in the sediments that directly overlie diamictites, offering further support for a rapid retreat of grounded ice from the shelf.

Ledford-Hoffman *et al.* [1986] obtained ^{210}Pb sedimentation rates for diatomaceous sediments overlying diamictites in the Ross Sea. These rates vary from less than 1 mm to 2.7 mm per year, but the thickness of these deposits varies from less than 10 cm to over 2 m. If pelagic sedimentation began soon after the ice sheet withdrew from this portion of the shelf, and if these rates have remained relatively constant, only a few thousand years have passed since the ice sheet re-

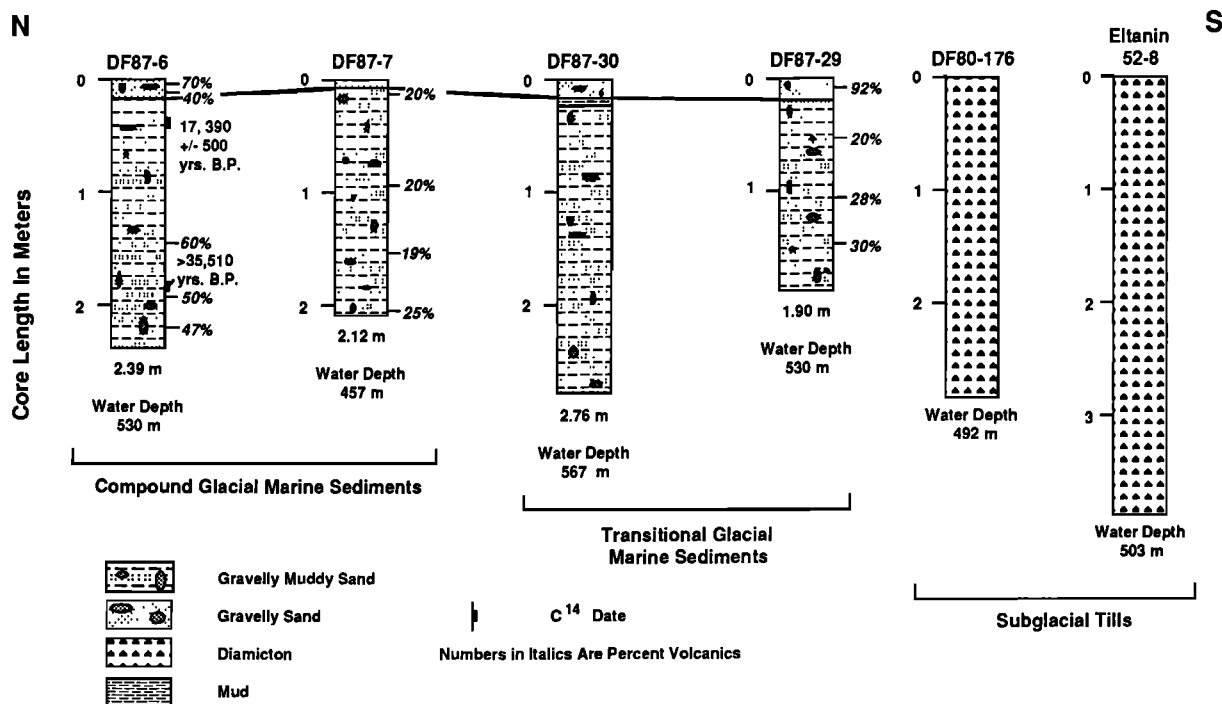


Fig. 10. Lithologies and interpretations of cores DF 80-176, DF 87-6, DF 87-7, DF 87-29, DF 87-30, and EL 52-8. Cores DF 80-176 and EL 52-8 penetrated subglacial tills. Cores DF 87-6 and DF 87-7 penetrated sandy units resting on compound glacial marine sediments [Anderson *et al.*, 1991], and cores DF 87-29 and DF 87-30 penetrated transitional glacial marine deposits overlain by sand. The percentage of volcanic debris and radiocarbon dates are presented with the cores.

treated from the inner shelf. This implies either that the grounding line retreated slowly from the shelf or that it was stabilized for some time at a position somewhere between Coulman Island and 75°S.

Piston cores from McMurdo Sound penetrated glacial marine sediments, diatomaceous muds, and a variety of sediment gravity flow deposits [Bartek and Anderson, 1991]. The latter group consists of sediments derived from Ross Island and the McMurdo Dry Valleys. Subglacial tills were not collected in McMurdo Sound, although Stuiver *et al.* [1981] and Kellogg *et al.* [1990] argue that an ice sheet was grounded there between 20,000 and 7750 years B.P.

Piston cores from the shelf offshore of Pennell Coast (Figure 3) also failed to penetrate subglacial tills [Brake, 1982]. This area is located adjacent to the northern limit of the Transantarctic Mountains (Figure 3), and glacial drainage is limited to valley glaciers which flow to the sea from the mountains. Diamictites, possibly subglacial tills, were collected farther west where Rennick Glacier flows into the sea. Rennick Glacier is a large outlet glacier flowing from East Antarctica (Figure 3). These diamictites were acquired in only a few cores, and the depth of penetration was not sufficient to allow detailed petrographic work.

CONCLUSIONS

Bathymetric maps of the Ross Sea show troughs associated with ice streams and outlet glaciers. Seismic records display widespread glacial erosional surfaces, which in places correspond to seafloor unconformities, and morphologic features interpreted as morainal banks, till tongues, and glacial deltas. A series of north-northeast to south-southwest troughs and depositional ridges, most prominent in the eastern Ross Sea, has been interpreted to represent the erosional remnant of ice streams. The ridges mark sites of sediment accumulation at the boundaries of ice streams; troughs denote the positions of the ice streams.

The most recent glacial erosional surface in the Ross Sea is draped by a seismic unit characterized by discontinuous reflectors and hyperbolic returns [Karl, 1989]. Piston cores penetrated diamictites covered by a thin layer of either diatomaceous glacial marine sediment (inner shelf) or sandy glacial marine sediment (outer shelf). The diamictites are overcompacted and massive, contain rare reworked microfossils, and display textural and mineralogic homogeneity within individual units. These properties have led various workers to interpret them as subglacial tills [Kellogg *et al.*, 1979; Anderson *et al.*, 1980, 1984]. However, with the exception of overcompaction,

which is a difficult property to measure, these properties are probably shared by glacial marine sediments deposited beneath ice shelves [Anderson *et al.*, 1991]. This being the case, detailed petrologic analyses of diamictites were conducted to further evaluate their origin and to reconstruct paleodrainage for the last glacial maximum.

Diamictites from the Ross Sea have rock and mineral compositions that allow them to be grouped

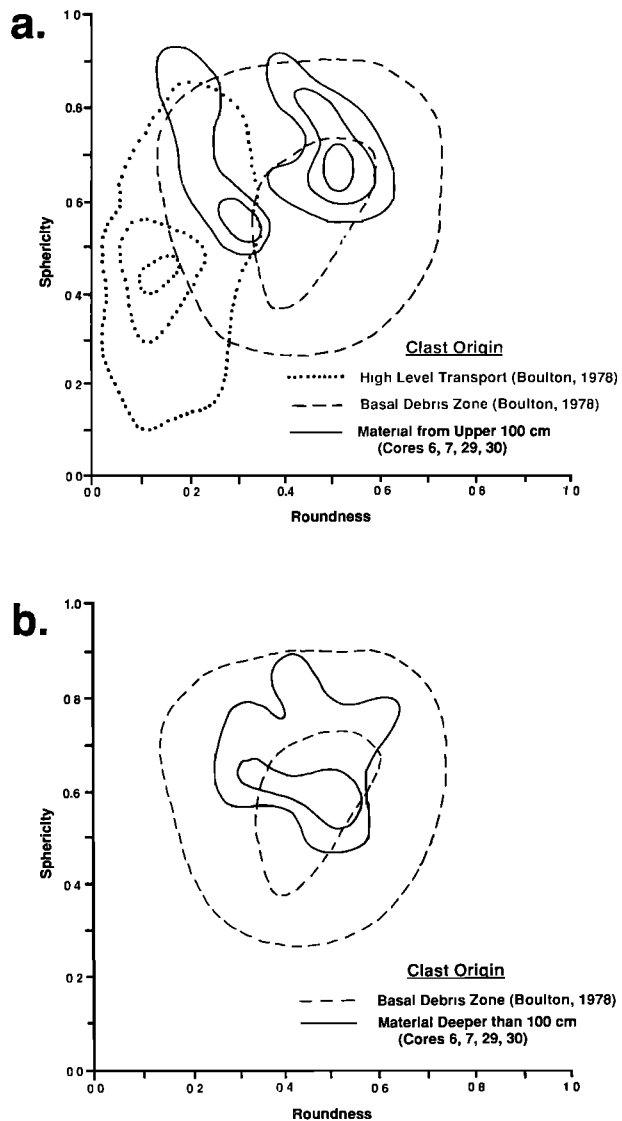


Fig. 11. Shape analyses of pebbles from cores DF 87-6, DF 87-7, DF 87-29, and DF 87-30, indicating a change from basal to a mixture of englacial and basal transport that corresponds to the sedimentary contact between transitional glacial marine sediments and surficial sand units.

into petrologic suites. These suites, in turn, occur within well-defined geographic zones or petrologic provinces. This implies deposition from the basal debris zones of either a marine ice sheet or an ice shelf. Individual diamicton provinces are widespread. Since ice shelves supposedly deposit their debris close to their grounding line, ice sheets must have grounded some distance out onto the continental shelf. The petrographic data also indicate that both the EAIS and the WAIS grounded on the continental shelf. The paleodrainage of the ice sheet was reconstructed from petrographic data and conforms reasonably well with the paleodrainage models constructed independently by *Stuiver et al.* [1981] and *Denton et al.* [1989] for the western Ross Sea. The results are inconclusive for the eastern Ross Sea but seem to best fit the maximum ice sheet expansion model of *Denton et al.* [1989].

The age of subglacial tills on the western shelf is extrapolated from radiocarbon dates of correlative glacial marine units. These ages range from >35,510 to 17,390 years B.P. The ice sheet is believed to have retreated from the outer shelf shortly after 17,000 years B.P., and seasonally open marine conditions were established soon after retreat. The sharp contact between the subglacial tills and the diatomaceous glacial marine sediments that overlie them is indicative of rapid retreat of the ice sheet and establishment of seasonally ice-free seas.

Acknowledgments. The authors thank R. D. Powell and G. M. Ashley for their helpful reviews of this paper. This research was funded by grants from the National Science Foundation's Division of Polar Programs (grants DPP-8516908 and DPP-8818523). We wish to thank Dennis Cassidy of the United States Antarctic Marine Geology Research Facility for providing assistance in acquiring sediment samples. Deep Freeze 87 was the final leg of the U.S. Coast Guard's *Icebreaker Glacier*; we are indebted to her officers and crew who assisted us during this cruise.

REFERENCES

- Alley, R. B., West Antarctic collapse—How likely?, *Episodes*, 13, 231–237, 1990.
- Alley, R. B., D. D. Blankenship, S. T. Rooney, and C. R. Bentley, Sedimentation beneath ice shelves—The view from ice stream B, *Mar. Geol.*, 85, 101–120, 1989.
- Alonso, B., J. B. Anderson, J. I. Diaz, and L. R. Bartek, Pliocene-Pleistocene seismic stratigraphy of the Ross Sea: Evidence for multiple ice sheet grounding episodes, this volume.
- Anderson, J. B., and L. R. Bartek, Preliminary results of a high-resolution seismic reflection survey of the Ross Sea continental shelf, *Antarct. J. U. S.*, 25, 61–63, 1990.
- Anderson, J. B., and L. R. Bartek, Cenozoic glacial history of the Ross Sea revealed by intermediate resolution seismic reflection data combined with drill site information, in *The Antarctic Paleoenvironment: A Perspective on Global Change*, part 1, *Antarct. Res. Ser.*, vol. 56, edited by J. P. Kennett and D. A. Warnke, pp. 231–263, AGU, Washington, D.C., 1992.
- Anderson, J. B., and M. J. Smith, Formation of modern sand-rich facies by marine currents on the Antarctic continental shelf, in *Shelf Sedimentation, Shelf Sequences, and Related Hydrocarbon Accumulation*, edited by R. Morton and D. Nummedal, pp. 41–52, Earth Enterprises, Austin, Tex., 1988.
- Anderson, J. B., D. D. Kurtz, E. W. Domack, and K. M. Balshaw, Glacial and glacial marine sediments of the Antarctic continental shelf, *J. Geol.*, 88, 399–414, 1980.
- Anderson, J. B., C. Brake, and N. Myers, Sedimentation on the Ross Sea continental shelf, Antarctica, *Mar. Geol.*, 57, 295–333, 1984.
- Anderson, J. B., E. W. Domack, D. Kennedy, and M. Smith, Sedimentary facies associated with Antarctica's floating ice masses, in *Paleoclimatic Interpretation from Glacial Marine Deposits*, edited by J. B. Anderson and G. M. Ashley, *Geol. Soc. Am. Spec. Publ.*, 1–26, 1991.
- Balshaw, K. M., Antarctic glacial chronology reflected in the Oligocene through Pliocene sedimentary section in the Ross Sea, Ph.D. dissertation, 140 pp., Rice Univ., Houston, Tex., 1981.
- Bartek, L. R., and J. B. Anderson, Facies distribution resulting from sedimentation under polar interglacial climatic conditions within a high latitude marginal basin, McMurdo Sound, Antarctica, in *Paleoclimatic Interpretation from Glacial Marine Deposits*, edited by J. B. Anderson and G. M. Ashley, *Geol. Soc. Am. Spec. Publ.*, 27–49, 1991.
- Bartek, L. R., P. R. Vail, J. B. Anderson, P. A. Emmet, and S. Wu, The effect of Cenozoic ice sheet fluctuations in Antarctica on the stratigraphic signature of the Neogene, *J. Geophys. Res.*, 96, 6753–6778, 1991.
- Bentley, C. R., and K. C. Jezek, RISS, RISP, and RIGGS: Post-IGY glaciological investigations of the Ross Ice Shelf in the U.S. programme, *J. R. Soc. N. Z.*, 11, 355–372, 1981.
- Boulton, G. S., Boulder shapes and grain-size distributions of debris as indicators of transport paths through a glacier and till genesis, *Sedimentology*, 25, 773–799, 1978.
- Brake, C. F., Sedimentology of the North Victoria Land continental margin, M. A. thesis, Rice Univ., Houston, Tex., 1982.
- Chriss, T., and L. A. Frankes, Glacial marine sedimentation in the Ross Sea, in *Antarctic Geology and Geophysics*, edited by R. J. Adie, pp. 747–762, Universitetsforlaget, Oslo, 1972.
- Clark, J. A., W. E. Farrel, and W. R. Peltier, Global changes in postglacial sea level: A numerical calculation, *Quat. Res.*, 9, 265–287, 1978.
- Davey, F. J., Geophysical studies in the Ross Sea region, *J. R. Soc. N. Z.*, 11, 477–479, 1981.
- David, T. W. E., and G. E. Priestley, Glaciology, physiography, stratigraphy, and tectonic geology of South Victoria Land: British Antarctic Expedition, 1907–1909: Reports of the Scientific Investigations, *Geology*, 1, 319 pp., 1914.

- Davis, J. C., *Statistics and Data Analysis in Geology*, 550 pp., John Wiley, New York, 1973.
- Debenham, F., Recent and local deposits of McMurdo Sound region: Natural history report, British Museum, British Antarctic Expedition, 1910, *Geology*, 1,(3), 63–90, 1921.
- Denton, S. C., and S. C. Wilson, Late Quaternary geology of the Rennick Glacier Area, northern Victoria Land, *Antarct. J. U.S.*, 17, 49–51, 1982.
- Denton, G. H., J. G. Bockheim, S. C. Wilson, and M. Stuiver, Late Wisconsin and early Holocene glacial history, inner Ross Embayment, Antarctica, *Quat. Res.*, 3, 151–182, 1989.
- Domack, E. W., Sedimentology of glacial and glaci-marine deposits on the George V-Adelie continental shelf, East Antarctica, *Boreas*, 11, 79–97, 1982.
- Domack, E. W., J. B. Anderson, and D. D. Kurtz, Clast shape as an indicator of transport and depositional mechanisms in glacial marine sediments: George V continental shelf, Antarctica, *J. Sediment. Petrol.*, 50, 813–820, 1980.
- Drewry, D. J., Late Wisconsin reconstruction for the Ross Sea region, Antarctica, *J. Glaciol.*, 24, 231–244, 1979.
- Drewry, D. J., Antarctica: Glaciological and geophysical folio, 9 sheets, Scott Polar Res. Inst. Univ. of Cambridge, Cambridge, England, 1983.
- Dunbar, R. B., J. B. Anderson, E. W. Domack, and S. S. Jacobs, Oceanographic influences on sedimentation along the Antarctic continental shelf, in *Oceanology of the Antarctic Continental Shelf*, *Antarct. Res. Ser.*, vol. 43, edited by S. S. Jacobs, pp. 291–312, AGU, Washington, D. C., 1985.
- Duphorn, K., Physiographical and glaciological observations in North Victoria Land Expedition 1979/90, *Geol. Jahrb., Reihe B*, 41, 89–109, 1981.
- Edwards, B. D., H. J. Lee, H. A. Karl, E. Reimnitz, and L. A. Timothy, Geology and physical properties of Ross Sea, Antarctica, continental shelf sediment, in *The Antarctic Continental Margin: Geology and Geophysics of the Western Ross Sea*, *Earth Sci. Ser.*, vol. 5B, edited by A. K. Cooper and F. J. Davey, pp. 191–216, Circum-Pacific Council for Energy and Mineral Resources, Houston, Tex., 1987.
- Fillon, R. J., Late Cenozoic paleo-oceanography of the Ross Sea, Antarctica, *Geol. Soc. Am. Bull.*, 86, 839–845, 1975.
- Gair, H. S., The geology of the upper Rennick Glacier to the coast of Northern Victoria Land, Antarctica, *N. Z. J. Geol. Geophys.*, 10, 309–344, 1967.
- Galehouse, J. S., Point counting, in *Procedures in Sedimentary Petrology*, edited by R. E. Carver, pp. 385–407, Wiley-Interscience, New York, 1971.
- Hamilton, W., The Hallett Volcanic Province, Antarctica, *U.S. Geol. Surv. Prof. Pap.*, 456-CC, 56 pp., 1972.
- Harrington, H. J., B. L. Wood, I. G. McKellar, and G. J. Lensen, Topography and geology of the Cape Hallett District, Victoria Land, Antarctica, *Bull. N. Z. Geol. Surv.*, 80, 1–100, 1967.
- Hollin, J. T., Origin of ice ages: An ice shelf theory for Pleistocene glaciation, *Nature*, 202, 1099–1100, 1962.
- Hughes, T. J., Is the West Antarctic ice sheet disintegrating?, *J. Geophys. Res.*, 78, 7884–7910, 1973.
- Hughes, T. J., West Antarctic ice streams, *Rev. Geophys.*, 15, 1–46, 1977.
- Hughes, T. J., Deluge II and the continent of doom: Rising sea level and collapsing Antarctic ice, *Boreas*, 16, 89–99, 1987.
- Karl, H. A., High resolution seismic-reflection interpretations of some sediment deposits, Antarctic continental margin, *Mar. Geol.*, 85, 205–223, 1989.
- Karl, H. A., E. Reimnitz, and B. D. Edwards, Extent and nature of Ross Sea unconformity in the western Ross Sea, Antarctica: in *The Antarctic Continental Margin: Geology and Geophysics of the Western Ross Sea*, *Earth Sci. Ser.*, vol. 5B, edited by A. K. Cooper and F. J. Davey, pp. 77–92, Circum-Pacific Council for Energy and Mineral Resources, Houston, Tex., 1987.
- Kellogg, T. B., and R. S. Truesdale, Late Quaternary paleoecology and paleoclimatology of the Ross Sea: The diatom record, *Mar. Micropaleontol.*, 4, 137–158, 1979.
- Kellogg, T. B., R. S. Truesdale, and L. E. Osterman, Late Quaternary extent of the West Antarctic Ice Sheet: New evidence from Ross Sea cores, *Geology*, 7, 249–253, 1979.
- Kellogg, T. B., D. E. Kellogg, and M. Stuiver, Late Quaternary history of the southwestern Ross Sea: Evidence from debris bands on the McMurdo Ice Shelf, Antarctica, in *Contributions to Antarctic Research I*, *Antarct. Res. Ser.*, vol. 50, pp. 25–56, AGU, Washington, D. C., 1990.
- Kennedy, D. S., and J. B. Anderson, Quaternary glacial history of Marguerite Bay, Antarctic Peninsula, *Quat. Res.*, 31, 1–22, 1989.
- King, L. H., and G. B. J. Fader, Wisconsinan glaciation of the Atlantic continental shelf of southeast Canada, *Geol. Surv. Bull., Geol. Soc. Can.*, 363, 72 pp., 1986.
- King, L. H., K. Rokoengen, G. B. J. Fader, and T. Gunleiksrud, Till-tongue stratigraphy, *Geol. Soc. Am. Bull.*, 103, 637–659, 1991.
- Krumbein, W. C., Measurement and geological significance of shape and roundness of sedimentary particles, *J. Sediment. Petrol.*, 11, 64–72, 1941.
- Ledford-Hoffman, P. A., D. J. DeMaster, and C. A. Nittrouer, Biogenic-silica accumulation in the Ross Sea and the importance of Antarctic continental-shelf deposits in the marine silica budget, *Geochim. Cosmochim. Acta*, 50, 2099–2110, 1986.
- Lingle, C. S., and J. A. Clark, Antarctic ice-sheet volume at 18,000 years B. P. and Holocene sea level changes at the West Antarctic margin, *J. Glaciol.*, 24, 213–230, 1979.
- Mayewski, P. A., Glacial geology and late Cenozoic history of the Transantarctic Mountains, Antarctica, *Rep. 56*, 168 pp., Inst. of Polar Stud., Ohio State Univ., Columbus, 1975.
- Mayewski, P. A., Upper Rennick Glacier ice mass fluctuation study, *Antarct. J. U.S.*, 17, 51–52, 1982.
- Myers, N. C., Petrology of Ross Sea basal tills, *Antarct. J. U.S.*, 17, 123–124, 1982.
- Priestley, R. E., *Physiography (Robertson Bay and Terra Nova Bay Regions): British Antarctic (Terra Nova)*

- Expedition, 1910-1913*, Harrison and Sons, London, 1923.
- Reid, D. E., Late Cenozoic glacial-marine, carbonate, and turbidite sedimentation in the northwestern Ross Sea, Antarctica, Master's thesis, 178 pp., Rice Univ., Houston, Tex., 1989.
- Scott, R. F., *The Voyage of the Discovery*, vol. 1, 556 pp., Charles Scribner's Sons, New York, 1905a.
- Scott, R. F., *The Voyage of the Discovery*, vol. 2, 508 pp., Charles Scribner's Sons, New York, 1905b.
- Stuiver, M., G. H. Denton, T. J. Hughes, and J. L. Fastook, History of the marine ice sheet in West Antarctica during the last glaciation: A working hypothesis, in *The Last Great Ice Sheets*, edited by G. H. Denton and T. J. Hughes, pp. 319-439, John Wiley, New York, 1981.
- Thomas, R. H., and C. R. Bentley, A model for Holocene retreat of the West Antarctic Ice Sheet, *Quat. Res.*, 10, 150-170, 1978.
- Truswell, E. M., and D. J. Drewry, Distribution and provenance of recycled palynomorphs in surficial sediments of the Ross Sea, Antarctica, *Mar. Geol.*, 59, 187-214, 1984.
- Whillans, I. M., Radio-echo layers and the recent stability of the West Antarctic Ice Sheet, *Nature*, 264, 152-155, 1976.
- Wong, H. K., and D. A. Christoffel, A reconnaissance seismic survey of McMurdo Sound and Terra Nova Bay, Ross Sea, in *Dry Valley Drilling Project, Antarct. Res. Ser.*, vol. 33, edited by L. D. McGinnis, pp. 37-62, AGU, Washington, D. C., 1981.

(Received January 31, 1992;
accepted May 26, 1992.)

**LATE QUATERNARY GLACIAL HISTORY OF THE NORTHERN ANTARCTIC
PENINSULA'S WESTERN CONTINENTAL SHELF:
EVIDENCE FROM THE MARINE RECORD**

PETER G. POPE

Hall Southwest Corporation, Austin, Texas 78752

JOHN B. ANDERSON

Department of Geology and Geophysics, Rice University, Houston, Texas 77251

Piston and gravity cores and bottom profiler records from the northern Antarctic Peninsula's western continental shelf were examined to reconstruct the glacial setting of this region during the last glacial maximum. The precision depth records (PDR) reveal evidence of subglacial scouring within Marguerite Bay and the inner portions of the continental shelf, with the exception of Biscoe Trough, whose bed is scoured partially onto the outer shelf. Piston cores reflect a modern depositional setting typical of the Antarctic continental shelf; terrigenous sediments are deposited as ice-raftered debris (IRD) in a marine environment where currents sweep fine sediments from the shallow banks of the shelf, leaving sandy lags, and deposit these fines in shelf depressions. Piston cores recovered basal till only from the inner shelf and from the floor of Biscoe Trough. Transitional glacial marine sediments are most prevalent in the southern portion of the study area near Marguerite Bay. These deposits are indicative of sub-ice shelf conditions; they grade upward into modern diatomaceous muds. In the northern portion of the study area, modern diatomaceous muds are in sharp contact with glacial marine deposits. The dominant sediments on the outer continental shelf are terrigenous gravelly muds, which display a gradual increase in marine component and degree of sorting toward the northern part of the study area. Pebbles and coarse sands from these sediments display significant petrogenic variability, and pebble shapes indicate high level (englacial and supraglacial) as well as basal transport. These combined data indicate that these sediments were deposited by icebergs. Our reconstruction for the last glacial maximum places a marine ice sheet in Marguerite Bay and on the inner shelf. Glacial ice retreated rapidly from the northern regions. Concurrently, offshore of Marguerite Bay an ice tongue (or small ice shelf) and associated pack ice canopy slowly retreated, yielding to open marine sedimentation during the early Holocene. Carbon 14 data indicate that the ice shelf retreated from Marguerite Bay sometime after 12,430 years B.P.

INTRODUCTION

Stuiver et al. [1981] and *Denton et al.* [1989] have reconstructed the Antarctic ice sheet during the last glacial maximum. These models call for expansion of the East and West Antarctic ice sheets onto the continental shelf. Marine geological studies on the Ross Sea [Kellogg et al., 1979; Anderson et al., 1980], Weddell Sea [Anderson et al., 1980, 1991; Elverhoi and Maisey, 1983], and Wilkes Land continental shelves [Domack, 1982] have added support to these models, at least for these areas.

Glaciologists and glacial geologists recently have mathematically modeled the behavior of the Antarctic Peninsula ice caps during the last glacial maximum [*Stuiver et al.*, 1981; *Payne et al.*, 1989]. These models predict that during a glacial maximum, the Antarctic Peninsula region and portions of the western continental shelf would be occupied by significant thicknesses of glacial ice. The purpose of this study was to examine the sedimentological record from the portion of the western continental shelf between 63°S and 67°S to test these models.

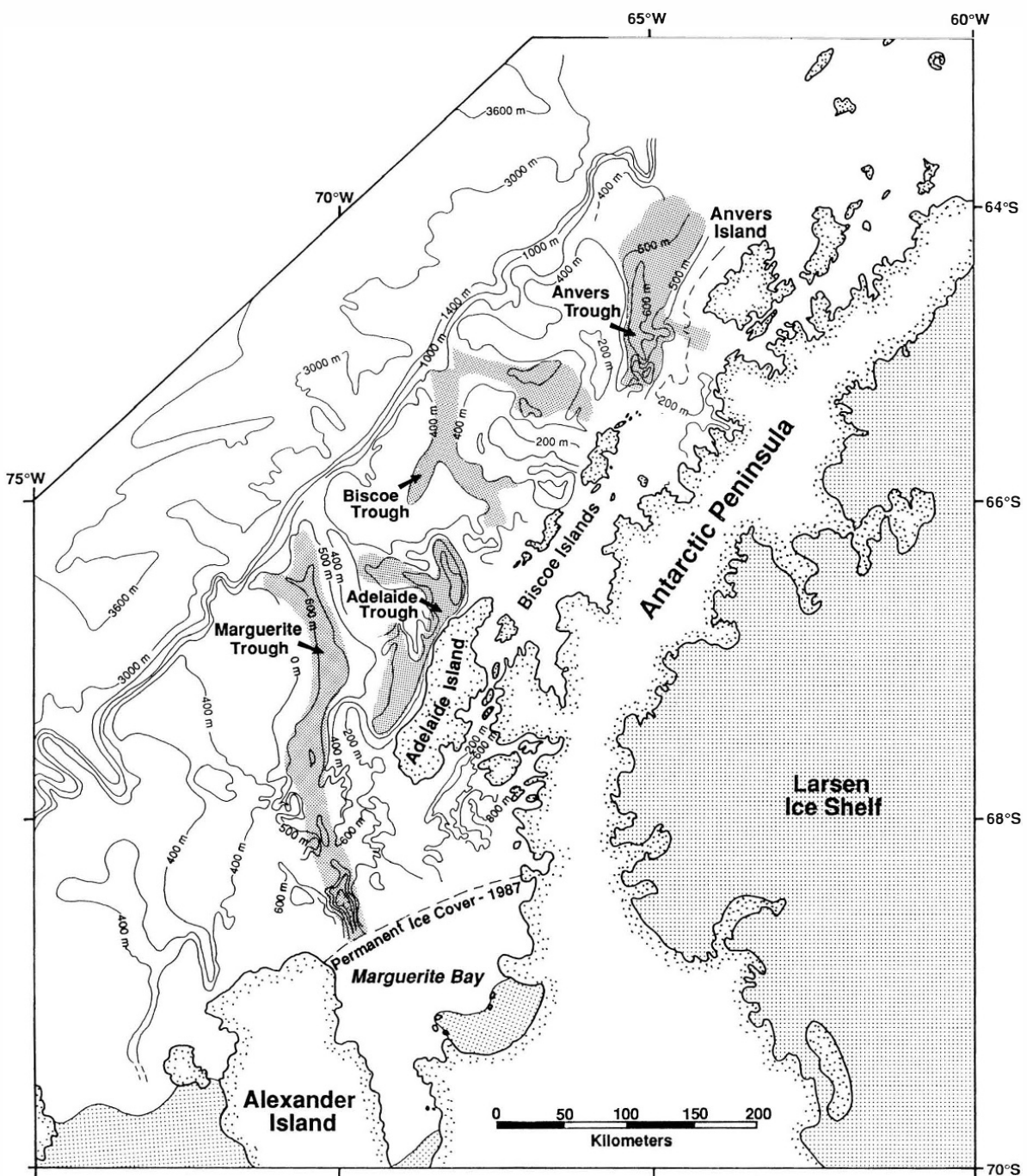


Fig. 1. Bathymetry and shelf physiography of the study area. Glacial troughs are indicated.

Shelf Physiography

Figure 1 presents the bathymetry of the study area. The continental shelf falls between 400 and 800 m in depth and slopes toward the continent. This deep,

foredeepened seafloor topography is typical of the Antarctic continental shelf and is due to isostatic depression caused by the weight of the ice sheet and by glacial erosion on the inner shelf [Anderson *et al.*, 1991]. In the Antarctic Peninsula there is no thick ice

sheet, so the deep, foredeepened topography there is attributed entirely to glacial erosion. The width of the shelf decreases northward, from more than 300 km wide near Marguerite Bay to less than 200 km north of Anvers Island.

The average depth of the shelf, excluding glacial troughs, also decreases northward, ranging from between 400 m and 500 m in the southern field area to less than 300 m at its northern portion. The inner shelf is rugged and relatively barren of sediment cover. The outer shelf consists of undulating plains with banks that are dissected by a series of troughs extending either parallel or perpendicular to the peninsula (Figure 1). One of the more prominent troughs is Marguerite Trough. It extends outward from Marguerite Bay, where it reaches depths in excess of 1000 m. Offshore of Adelaide Island, a second deep trough, referred to in this study as the Adelaide Trough, extends along the inner continental shelf parallel to the peninsula coast. Its trend is structurally controlled. Other troughs in the study area, including the Biscoe Trough and Anvers Trough, are shallower than the Marguerite and Adelaide troughs. These troughs are oriented toward the northeast, indicating paleodrainage in that direction.

Climate, Oceanography, and Glaciology

The Antarctic Peninsula is located in a region of strong temperature and precipitation gradients [Reynolds, 1981]. Isotherms parallel the axis of the peninsula, suggesting that there is a major orographic effect on the distribution of mean annual temperatures [Reynolds, 1981]. In fact, there are two distinct climatic regimes with a divide parallel to the peninsula's axis [Martin and Peel, 1978]. This divide separates the peninsula into a warmer, more maritime region along the Pacific coast and a cooler, more continental climate along the east coast in the Weddell Sea. Mean annual temperatures may differ by as much as 7°C between the west and the east coast at equivalent latitudes.

Published oceanographic data from this area are rare. However, the British Antarctic Survey (BAS) has compiled a large quantity of oceanographic data from George VI Sound in Marguerite Bay. Here, the water column consists almost entirely of warm (~+1°C) Circumpolar Deep Water (CPDW), responsible for the melting of the underside of George VI Ice Shelf [Potter and Paren, 1985].

Climatic and oceanographic conditions contribute to the great spectrum of glacial settings in the Antarctic Peninsula region, ranging from polar to subpolar. Ice shelves exist on the western coast only in protected regions where valley walls confine flow

(Figure 2). Within the study area the George VI Ice Shelf drains ice caps flowing northward from Palmer Land. This constitutes more than 90% of ice flowing into Marguerite Bay; the remainder drains from Alexander Island. Historically, another ice shelf, the Wordie Ice Shelf, was an outlet for ice flowing into Marguerite Bay. However, this ice shelf has virtually disappeared within the last two decades [Doake and Vaughan, 1992].

Iceberg calving is the primary source of ablation in the region today; basal melting of ice shelves is an important mechanism locally [Potter and Paren, 1985]. The base of the George VI Ice Shelf is melting at an average rate of 2 m/yr and is retreating at 1 km/yr [Potter and Paren, 1985]. The Wordie Ice Shelf had a similar retreat history. Locally, portions of the George VI Ice Shelf are thickening, probably in response to increased precipitation rates several hundred years ago; this results in uncertainties about the present mass balance of this glacial system [Potter and Paren, 1985].

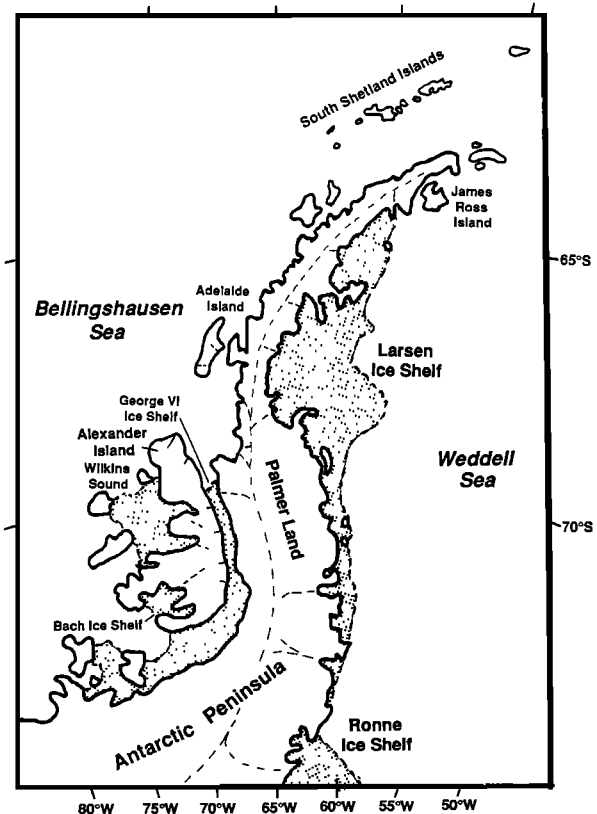


Fig. 2. Glaciological setting of the Antarctic Peninsula region, modified from Hughes [1981] and Kennedy [1988]. Stippled areas are ice shelves.

LATE QUATERNARY GLACIAL HISTORY

Evidence for a previously expanded marine ice sheet exists all along the Antarctic Peninsula. *Smith* [1985] showed that Larsen Ice Shelf once advanced far out onto the adjacent continental shelf; however, the timing of this event was not constrained by radiometric dating because of a lack of datable material.

Kennedy and Anderson [1989], on the basis of the presence of basal tills in Marguerite Trough, determined that ice grounded in Marguerite Bay, and perhaps even grounded out onto the adjacent continental shelf, presumably during Late Wisconsin time. Grounding at these depths requires an ice sheet nearly 1000 m thick. *Kennedy and Anderson* [1989] concluded that following the glacial maximum, Marguerite Bay was the site of a semipermanent ice shelf which slowly retreated as sea level rose and climate warmed. Again, the timing of these events was not constrained by radiometric dating because of a lack of datable material. Later work by *Harden* [1989] showed that the glacial marine unit that overlies subglacial and sub-ice shelf deposits was of Holocene age.

Clapperton and Sugden [1982] presented geomorphic evidence that separate ice domes existed on Alexander Island and Palmer Land during the last glacial maximum. The drainage from these ice domes was confluent in George VI Sound. Their reconstruction shows major drainage from the Alexander Island ice cap to the north into Marguerite Bay, and to the west into Bellingshausen Sea, with additional drainage into George VI Sound. The discovery of a shell-bearing moraine on Alexander Island suggests that the ice shelf may have disappeared from the bay and subsequently readvanced beyond its present configuration 6500 years B.P.

METHODS

During the austral summer of 1987–1988, a total of 43 piston and 18 gravity cores (Figure 3) and over 3500 km of single-channel seismic and precision depth record (PDR) data (Figure 4) were collected from the western continental shelf of the Antarctic Peninsula. These comprise the data set employed in this study.

All sediment cores were split at the Antarctic Core Facility at Florida State University and X-radiographed at Rice University to identify sedimentary contacts, sedimentary structures, pebble fabrics, and pebbles larger than 1 cm. Cohesive strengths of the sediments were measured using a TorVane to characterize the degree of sediment compaction. Selected cores were sampled at intervals

averaging 30 cm and sometimes at smaller intervals when significant downcore variations were observed. The biogenic fraction of these samples was described following the smear slide method used at the Antarctic Core Facility. The procedure was modified to describe the biogenic component as minor (10–15%), accessory (5–10%), or rare (1–5%). A 3- to 10-g sample was dried and weighed for settling tube analysis, and a small (0.1 to 0.5 g) sample was placed in water containing a dispersant (Calgon) for hydrometer analysis. The large sample was washed through a 38- μ m sieve to separate gravel, sand, and coarse silt from finer material. The sieved material was passed through a 2-mm sieve to separate gravel from sand and coarse silt. The latter component (2 mm to 38 μ m) was analyzed using an automated settling tube. Selected small samples were analyzed using a hydrometer for the medium and fine silt size distribution.

Pebbles greater than 1 cm were removed from selected cores for roundness and sphericity measurements, as outlined by *Krumbein* [1941], to aid in the determination of the mode of glacial transport. These pebbles were then examined for lithology using a binocular microscope. Select pebbles subsequently were thin sectioned and examined under a polarizing microscope for lithologic identification. A few samples were analyzed further for coarse sand lithology or mineralogy. Where possible, at least 200 to 300 grains were counted using the ribbon method of *Galehouse* [1971].

A number of samples contained foraminifera and, in some cases, other microfossils. The foraminifera and other carbonate materials (including bryozoans, pelecypods, and gastropods) were handpicked from the 63- μ m to 2-mm size fraction. Where planktonic forams were abundant, additional specimens were floated using carbon tetrachloride. All faunas were examined visually and described with respect to major, minor, and subordinate constituents. In selected samples, benthic foraminifera were identified to genus level, and to species level where possible, and counted to calculate the reciprocal of the diversity index [Simpson, 1949]. Abundances of foraminifera were quantified in terms of number per gram of sample. Abundances were low, typical of Antarctic glacial marine sediments; thus the number of specimens counted for diversity calculations ranged from 14 to more than 100. Bulk carbonate samples (~35 and 60 mg of carbonate) from four of these samples were sent to the National Science Foundation–University of Arizona tandem accelerator mass spectrometer (TAMS) facility for ^{14}C dating. Additional samples of *Cibicides* spp. and *Neogloboquadrina pachyderma* were analyzed for $\delta^{18}\text{O}$ and $\delta^{13}\text{C}$ values at the Rice University's Stable Isotope Laboratory.

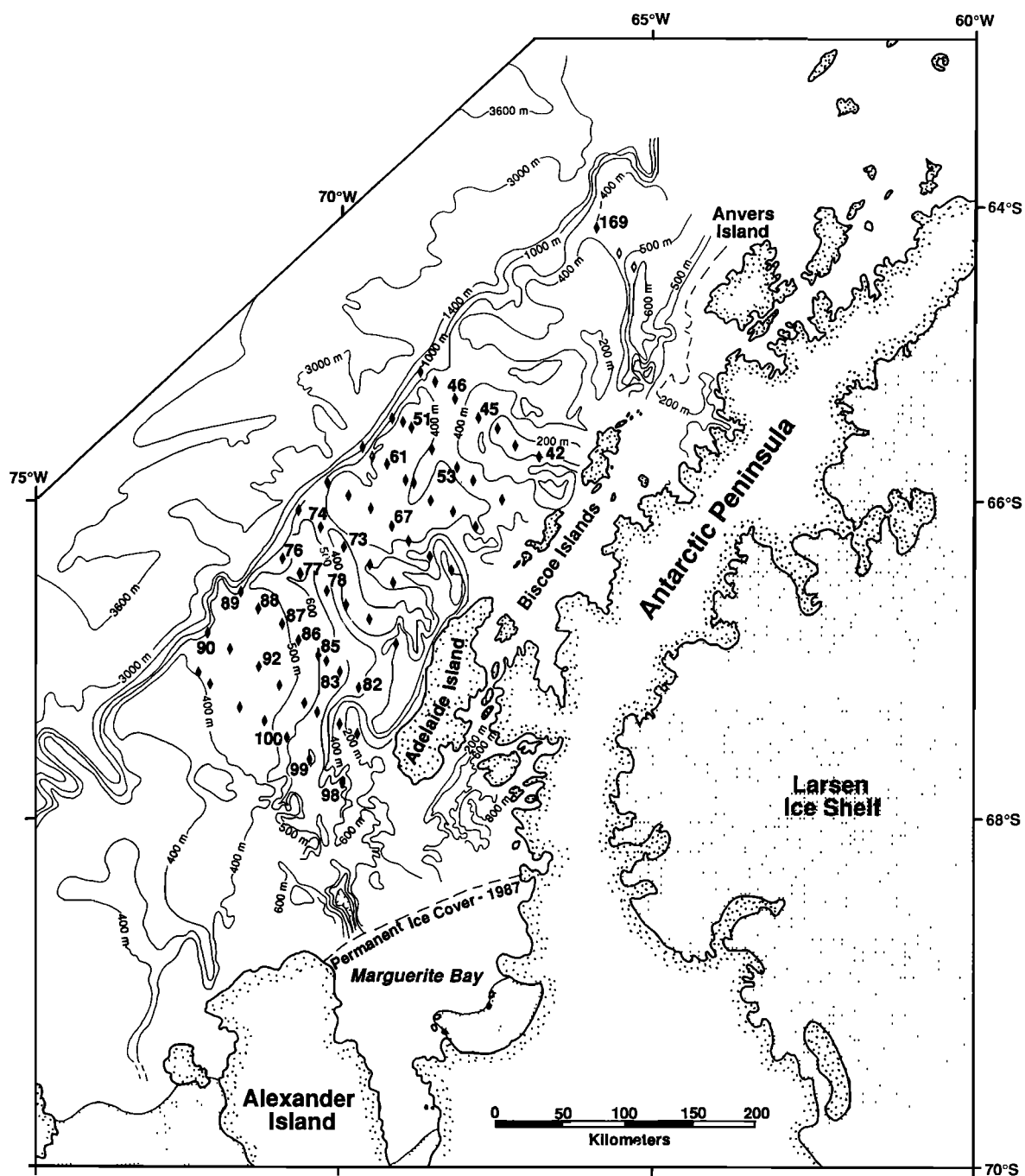


Fig. 3. Piston core locations. Diamonds with associated numbers are cores referred to in text.

MORPHOLOGICAL EVIDENCE OF GROUNDED ICE ON THE CONTINENTAL SHELF

Scientists have long been aware of the unique physiography of high-latitude continental shelves

[Holtedahl, 1929; Shepard, 1931]. Early studies focused primarily on the effects of subglacial processes on the development of large-scale shelf morphologies. More recently, workers have been able to conduct more detailed studies of seafloor morphol-

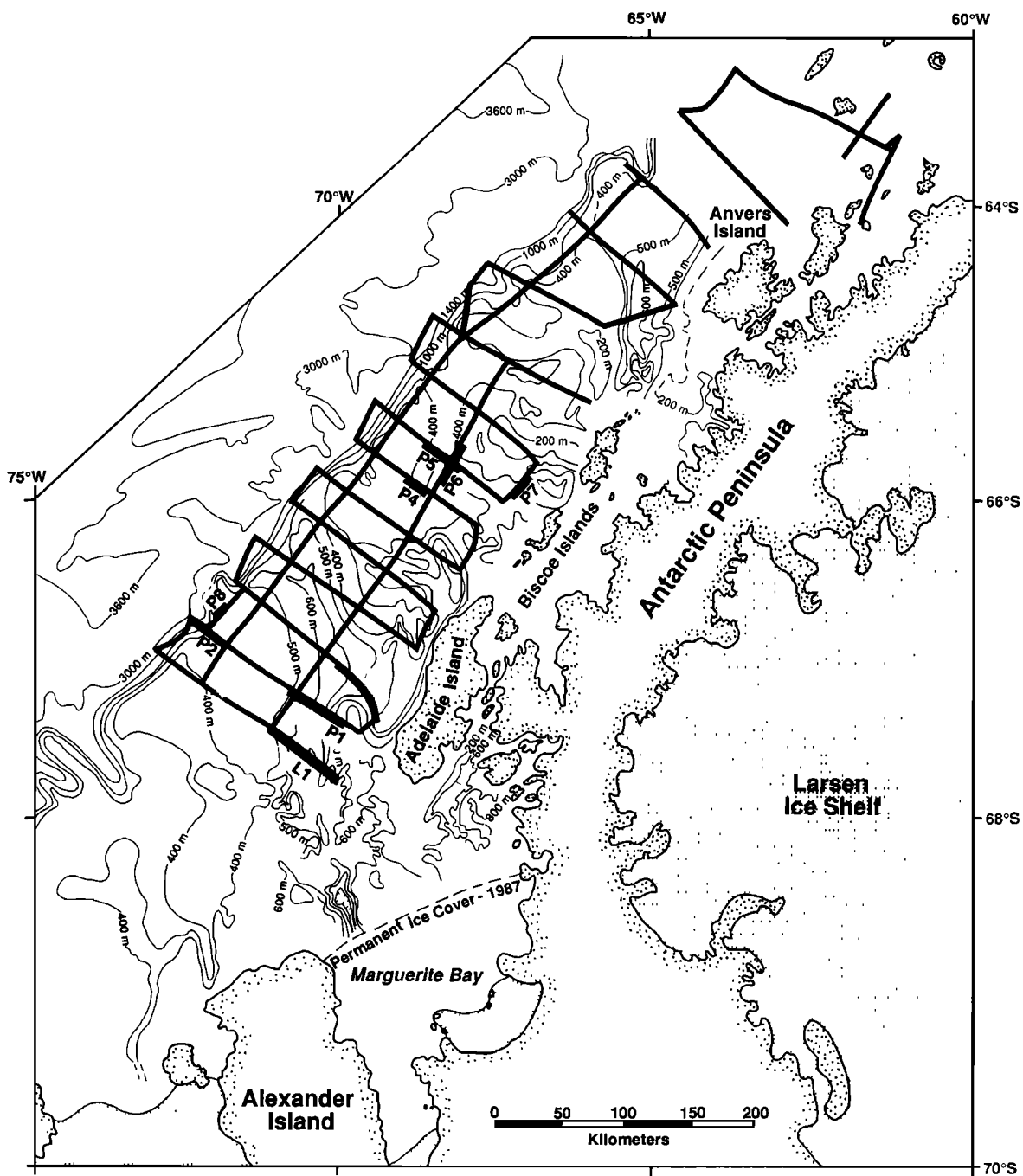


Fig. 4. USAP seismic and PDR track lines. Profiles referred to in text are labeled.

ogy utilizing high-resolution seismic, depth-sounding, and side scan sonar data [Barnes, 1987; Solheim et al., 1990].

Features such as flutes and transverse ridges can be related to the activity of grounded, sliding glaciers

[Boulton, 1976; Solheim et al., 1990]. Iceberg gouges have been observed on the Wilkes Land [Barnes, 1987] and Weddell Sea [Lien, 1981] continental shelves and indicate ice cover thin enough to allow icebergs to drift through these areas. Barnes showed

that icebergs play a significant role in reworking sediments on the Antarctic continental shelf.

Kennedy [1988] examined seismic data from Marguerite Bay and noted a strikingly thin sediment cover resting on crystalline bedrock or older glacial sediments. Sediment cores from the bay penetrated a relatively thin diatomaceous unit resting on glacial marine sediments. Seismic records from the inner shelf of the study region also show little sediment cover [*Anderson et al.*, 1991], and piston cores from the shelf, like those of Marguerite Bay, penetrated relatively thin "postglacial" deposits. Thus it is likely that geomorphic features produced during the last glacial maximum have not been completely buried by Holocene sediments.

Side scan sonar records acquired on the continental shelf in the northern portion of the study area display glacial flutes on the inner shelf and iceberg furrows on the outer shelf [*Barker et al.*, 1989]. These records (provided by Peter Barker, BAS) augmented the analysis of bottom profiler records from the area. Other examples were drawn from the literature [*Shepard*, 1931, 1948; *Barnes*, 1987; *Solheim et al.*, 1990]. From this analysis, bed forms were ranked as either glacially scoured or iceberg furrowed. Figure 5 shows several examples of these categories. The defining criteria for these two categories are as follows: Glacially scoured bed forms (1) occur in wide, deep troughs; (2) display a rugged surface with localized relief of the order of tens of meters; and (3) have ridges that appear to be parallel and that are spaced hundreds of meters apart. Iceberg-furrowed bed forms (1) usually appear on shallower banks of the shelf; (2) exhibit hummocky surfaces; and (3) have furrows that are spaced closely with relief of the order of a few meters and that show no preferred orientation.

The inner shelf floor characteristically is rugged and sediment barren. In contrast, the midshelf to outer shelf is smooth and draped by sedimentary deposits (Figure 5a). PDR records that cross troughs on the inner shelf show relatively large scale relief with ridges that are hundreds of meters apart. Profiles taken along the trough axes show much smoother beds, indicating that the ridges trend parallel to the trough axes (Figure 5b). In contrast, PDR records from shallower portions of the middle and outer shelf show relatively small scale bed forms indicative of iceberg scouring (Figure 5c). Iceberg furrows are prominent on banks shallower than 400 m.

On the basis of results of the geomorphologic analysis an initial model of ice sheet expansion was developed. This model calls for an ice sheet grounding on the inner shelf near Marguerite Bay and extending onto the outer shelf in the northeastern portion of the

study area (Figure 6). Although Marguerite Trough extends to the shelf edge, there is no good morphological evidence that an ice sheet occupied the outer portion of the trough during the last glacial maximum (Figure 6).

STRATIGRAPHY

Diatomaceous Muds

The generalized stratigraphy of cored sediments is illustrated using a series of core transects (Figures 7 and 8). The following discussion is based on these transects.

Many cores from the shelf are capped with a diatomaceous mud unit. This unit consists primarily of silt- and clay-sized material and a marine biogenic component, including diatom frustules and sponge spicules. An unsorted sand fraction is present but rarely exceeds 2% of the total sediment. Coarse sand counts of ice-raftered debris (IRD) reveal a diverse petrologic assemblage (Figure 9).

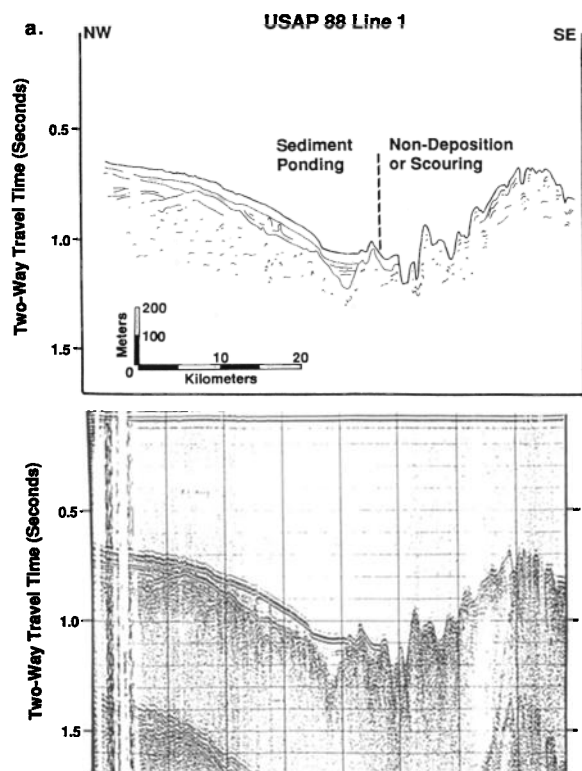


Fig. 5a. Line drawing of seismic profile USAP 88-1 and uninterpreted section.

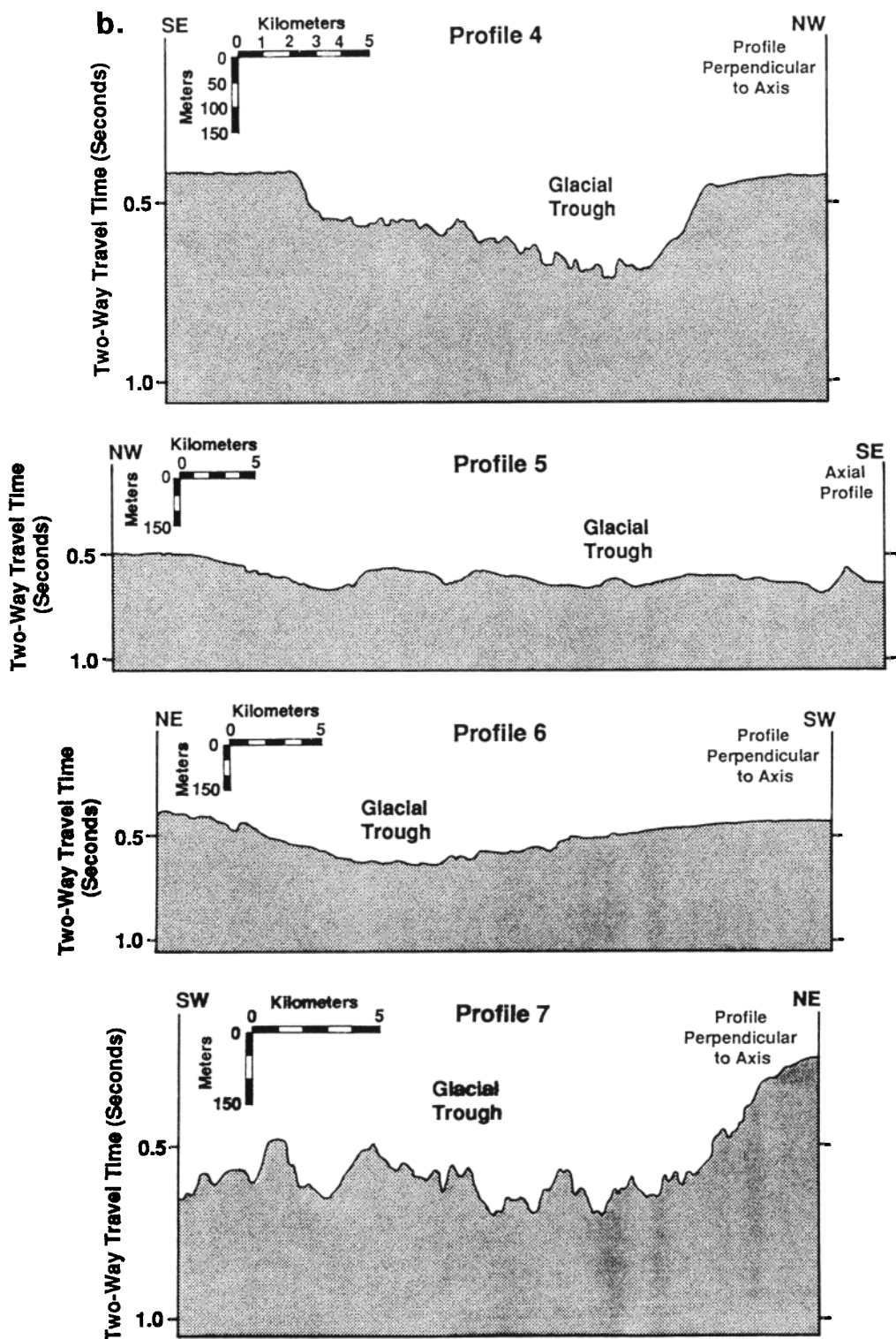


Fig. 5b. PDR records from glacial troughs. Profiles 4 and 7 cross the axis of the troughs, and profiles 5 and 6 are axial profiles.

Foraminifera in this unit were examined in some detail in piston core (PC) 99. Here the core top contains a benthic foraminiferal fauna which consists entirely of arenaceous foraminifera (predominantly *Miliammina* spp.). Calcareous foraminifera increase in abundance downcore. Planktonic foraminifera, exclusively *Neogloboquadrina pachyderma*, first appear at ~60 cm and increase in abundance downcore in this unit.

Diatomaceous muds are thickest in shelf depressions and are thin to absent on the outer shelf. This

distribution is similar to that in other areas (Ross Sea, George V Coast), where it has been related to impinging currents which sweep the outer shelf of fines and deposit them in inner shelf depressions.

Terrigenous Muds

In shelf depressions, terrigenous muds underlie the diatomaceous mud unit. These terrigenous muds fall into two general groups: (1) a distinct, thin, stratified

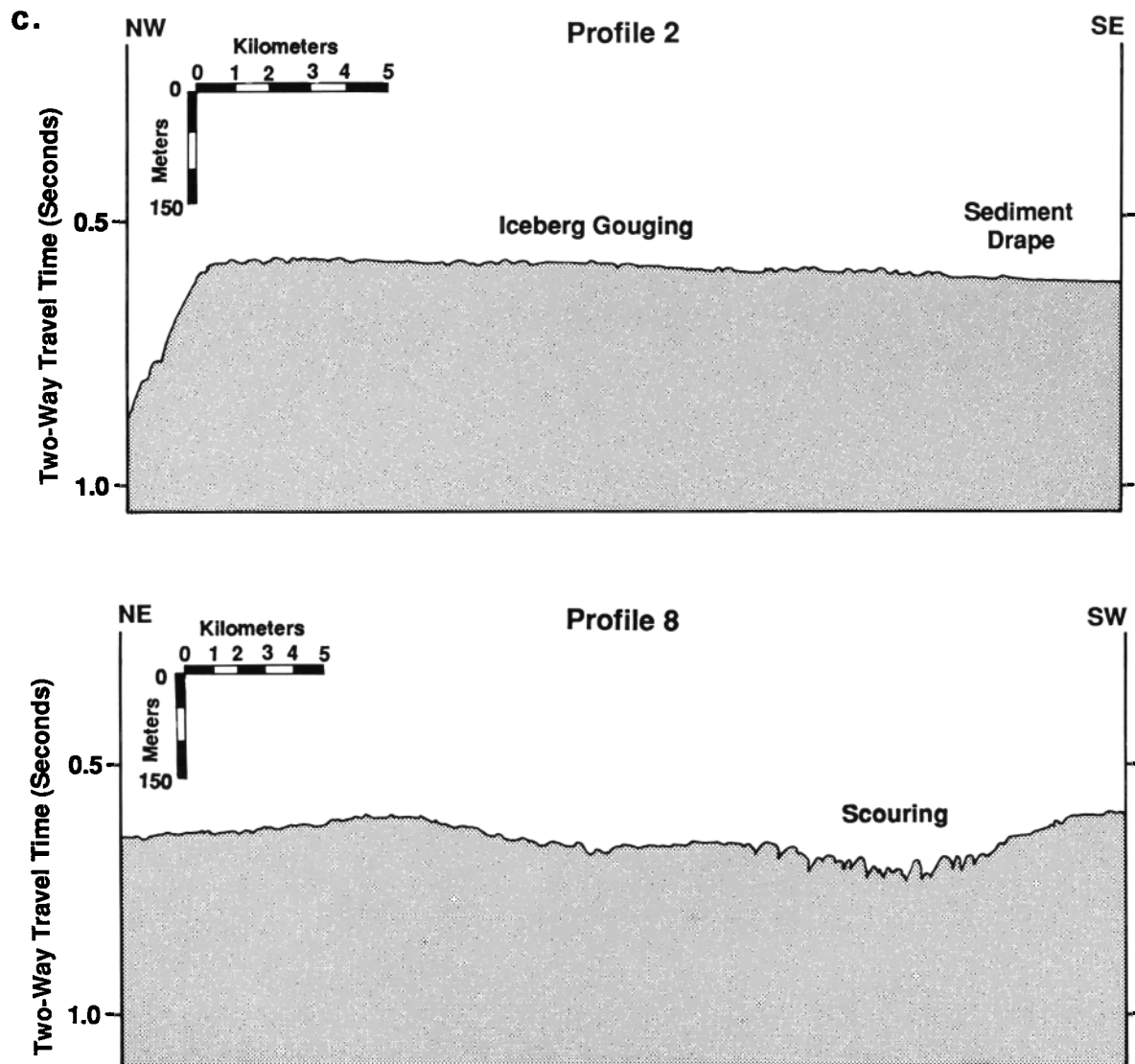


Fig. 5c. PDR profiles 2 and 8 from the outer shelf showing small-scale relief attributed to iceberg gouging.

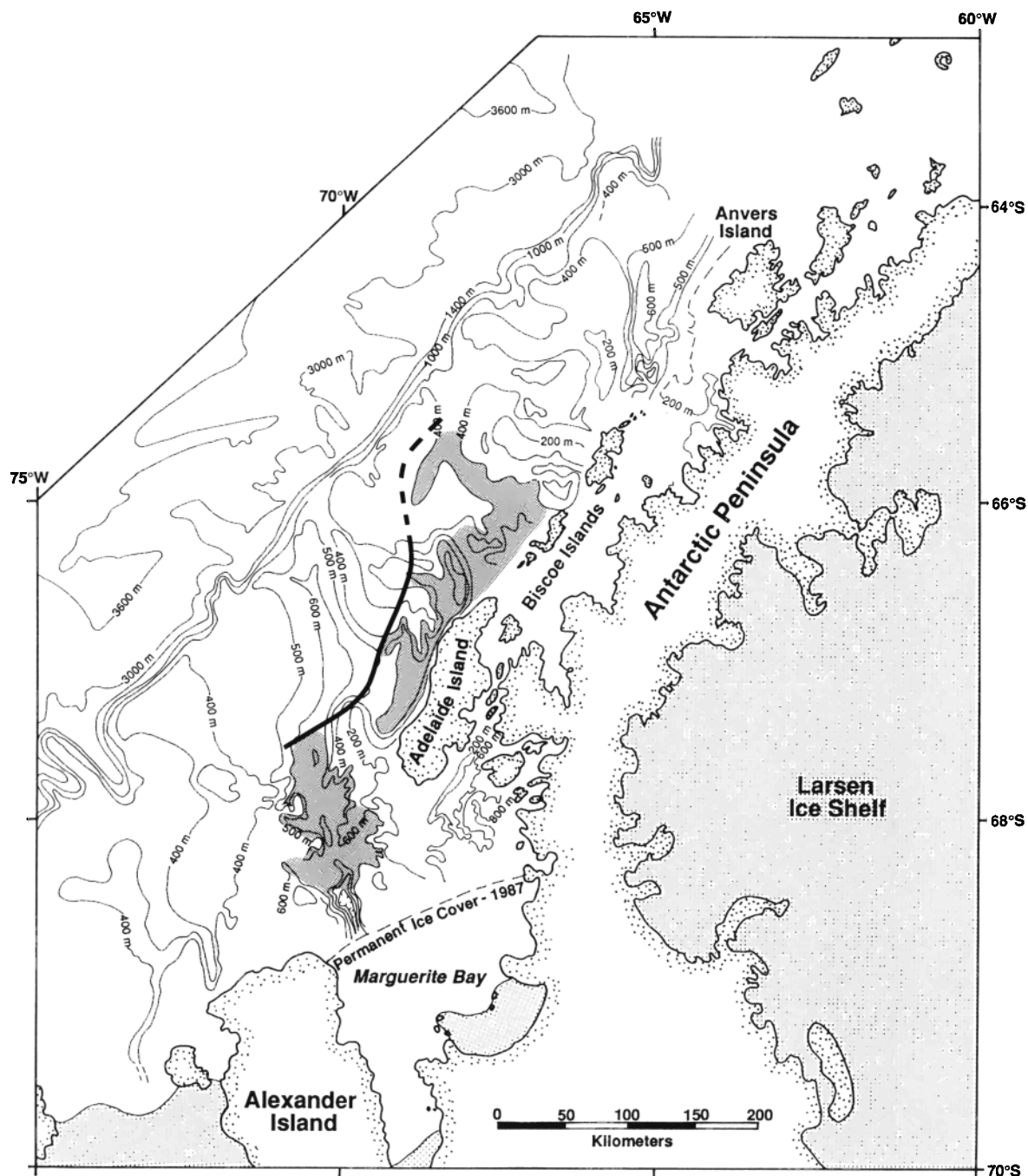


Fig. 6. Proposed grounding line of ice sheet during the last glacial maximum based on morphologic features on the shelf.

unit and (2) a unit that is gradational and overlying diatomaceous mud. The first group may be subdivided further into two subunits: (a) a terrigenous mud with a generally unsorted sand component and (b) a laminated silt and fine sand unit.

Groups 1a and 1b are found only in PC 99, where

they are interbedded with a sand and gravel unit. Texturally, group 1a mud consists primarily of fine silt with a significant (up to 40%) clay-sized fraction. Additionally, the uppermost group 1a terrigenous mud contains broken and complete *Neogloboquadrina pachyderma*. Group 1b mud exhibits significant

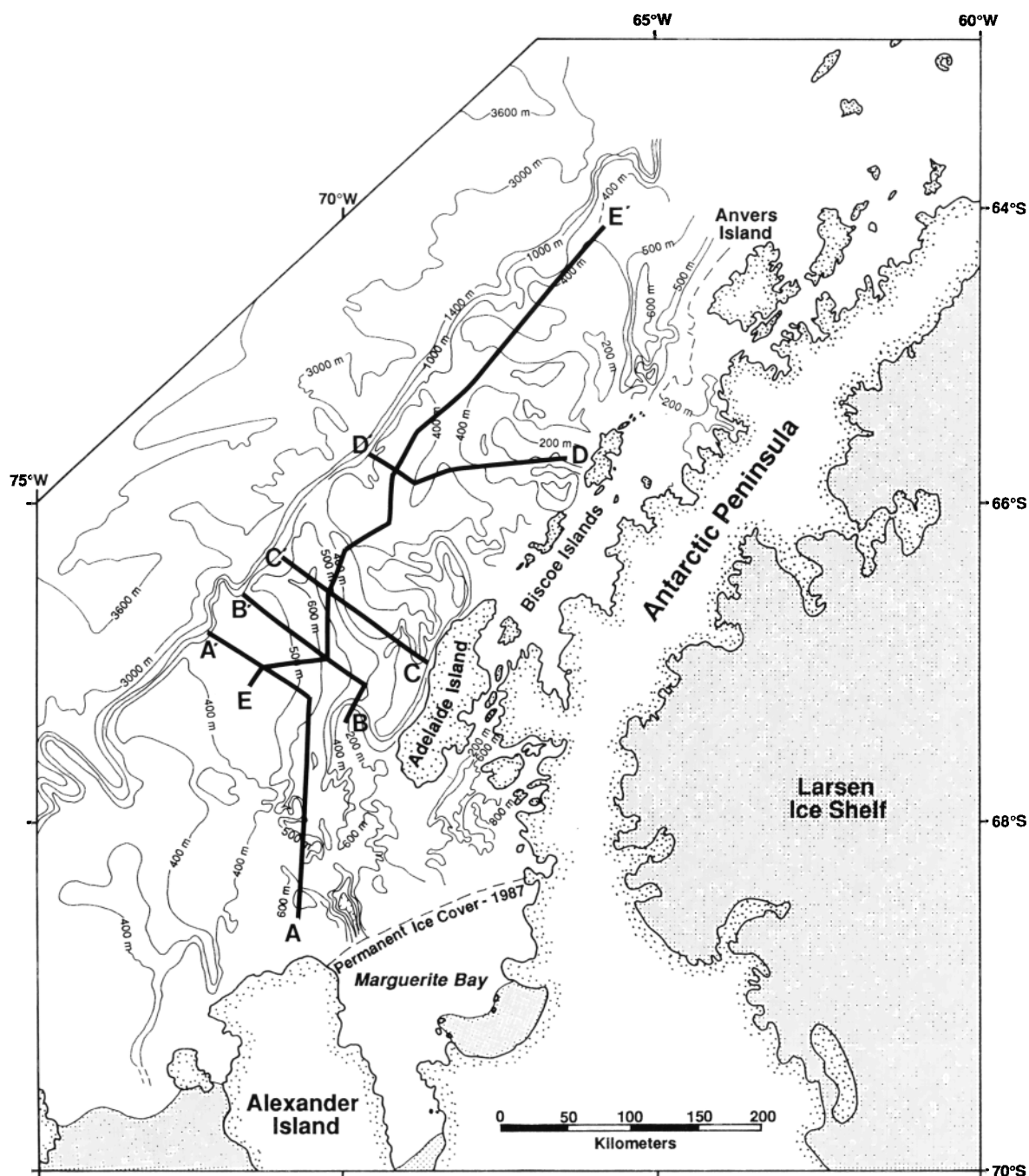


Fig. 7. Locations of piston core transects presented in Figure 8.

sorting within the fine sand and silt range. The X radiograph of this mud reveals a distinctly laminated unit with laminae of the order of millimeters thick. Group 2 terrigenous muds are indistinct texturally

from diatomaceous muds. These muds are, however, gradational in terms of color and texture, and they contain a much smaller marine biogenic component than diatomaceous muds.

Muddy Sands and Gravelly Sands

Sandy units are present in some cores. These may be divided into three groups. Seemingly discontinuous, thin muddy sands capping cores collected from the shallow banks offshore Marguerite Bay (PC 74, PC 78, GC 78, and PC 88) comprise a group hereafter called group 1 muddy sands. Diatoms and planktonic foraminifera are present but usually in

minor amounts. Particle size analyses indicate that sand content varies from 43% to 57% by weight. Weight percent of clay-sized material is low, ranging from 4% to 10%; the fine fraction is comprised predominantly of silt-sized material.

Group 2 muddy sands also are found in the tops of cores collected from shallow banks. Unlike group 1 muddy sands, they thicken toward the northern part of the study area where, in some cases (e.g., PC 46), 2–3

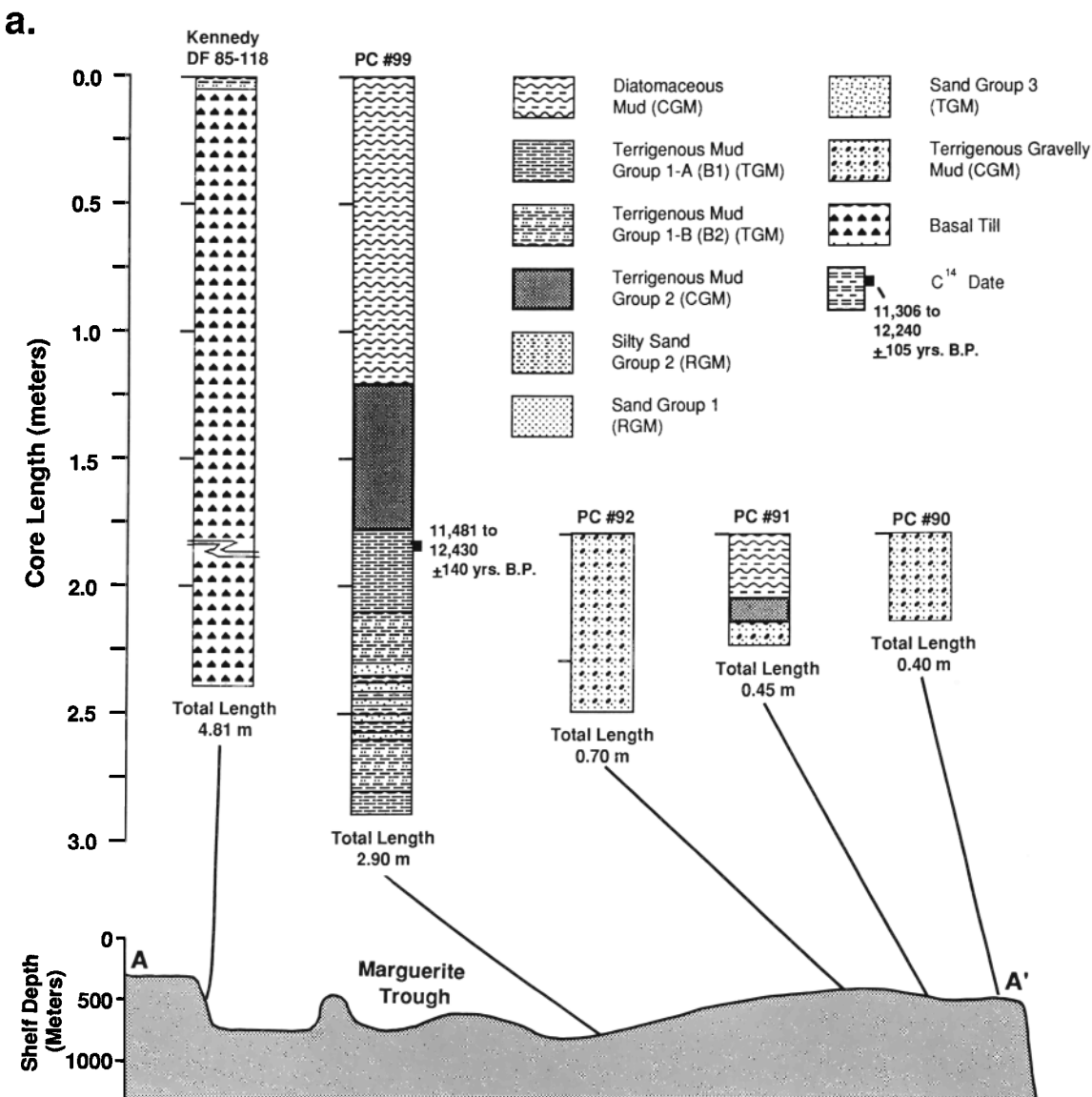


Fig. 8. Locations and lithologic logs of piston cores acquired along several shelf transects and illustrating facies relationships. Radiocarbon dates are included. A legend of sediment types described in this study is presented in Figure 8a.

m of pebbly, muddy sand was recovered. This unit was examined in detail in cores PC 42, PC 46, GC 51, PC 61, GC 67, and PC 169. A marine biogenic component, including diatoms, radiolarians, and foraminifera, is present. Sand content varies between 40% and 60%, and the modal size and sorting are variable, both laterally and downcore (Figure 10). A relatively high weight percent of clay-sized particles, ranging from 10 to 20%, helps distinguish this sediment type from group 1 muddy sand.

Group 3 gravelly sands were encountered only in

PC 99 and PC 85, collected from the deepest reaches of Marguerite Trough. In PC 85 this unit is 45 cm thick and defines the boundary between an upper terrigenous mud unit and a lower terrigenous gravelly mud unit. In PC 99 this unit is 30 cm thick and is enclosed within laminated terrigenous muds. Texturally, this unit consists of stratified gravelly sands, with a dominant mode of 0.5ϕ , and sandy muds, with a dominant mode finer than 6.0ϕ . In PC 99 the gravelly sands contain a significant (>10%) clay-sized fraction.

b.

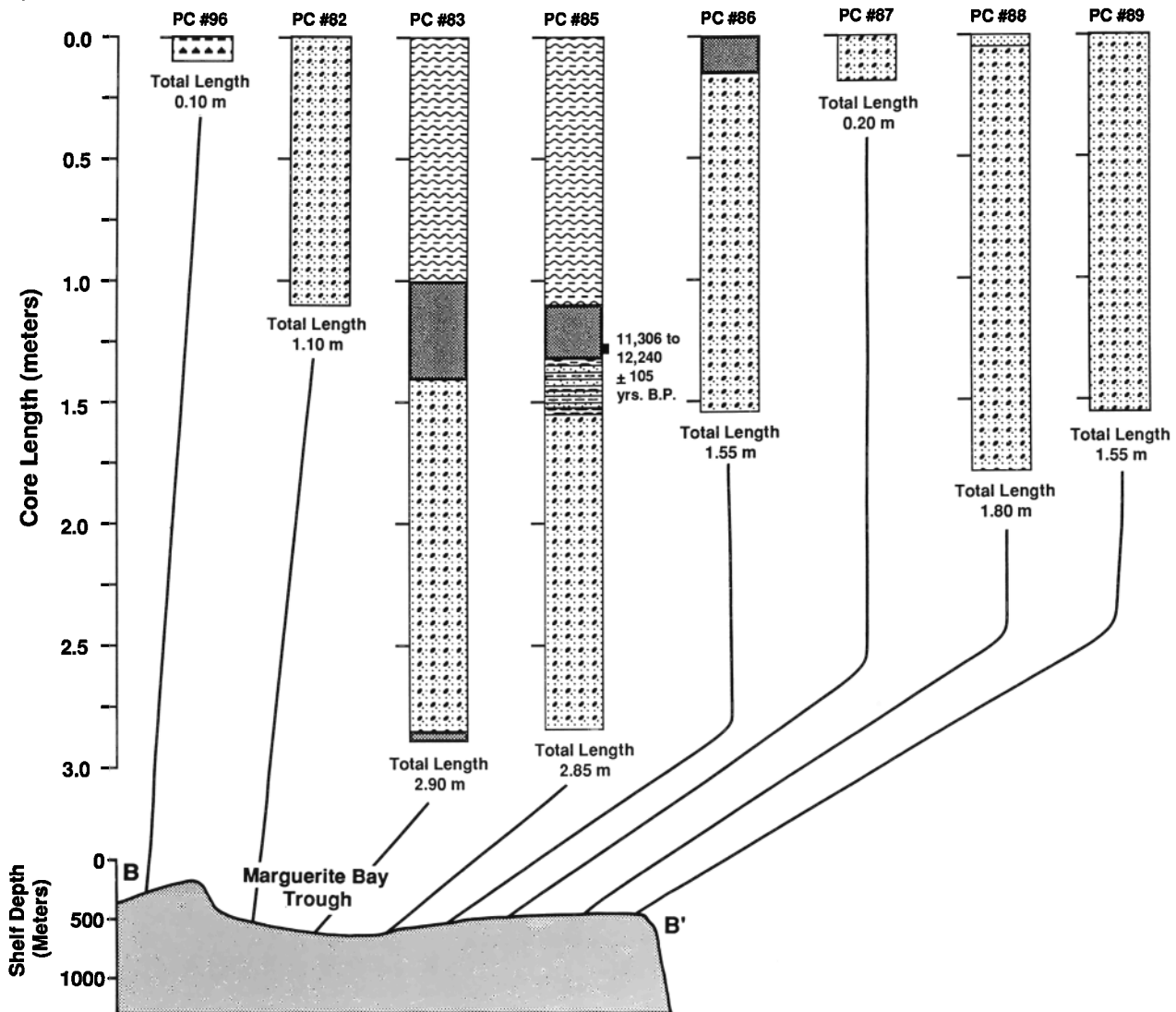


Fig. 8. (continued).

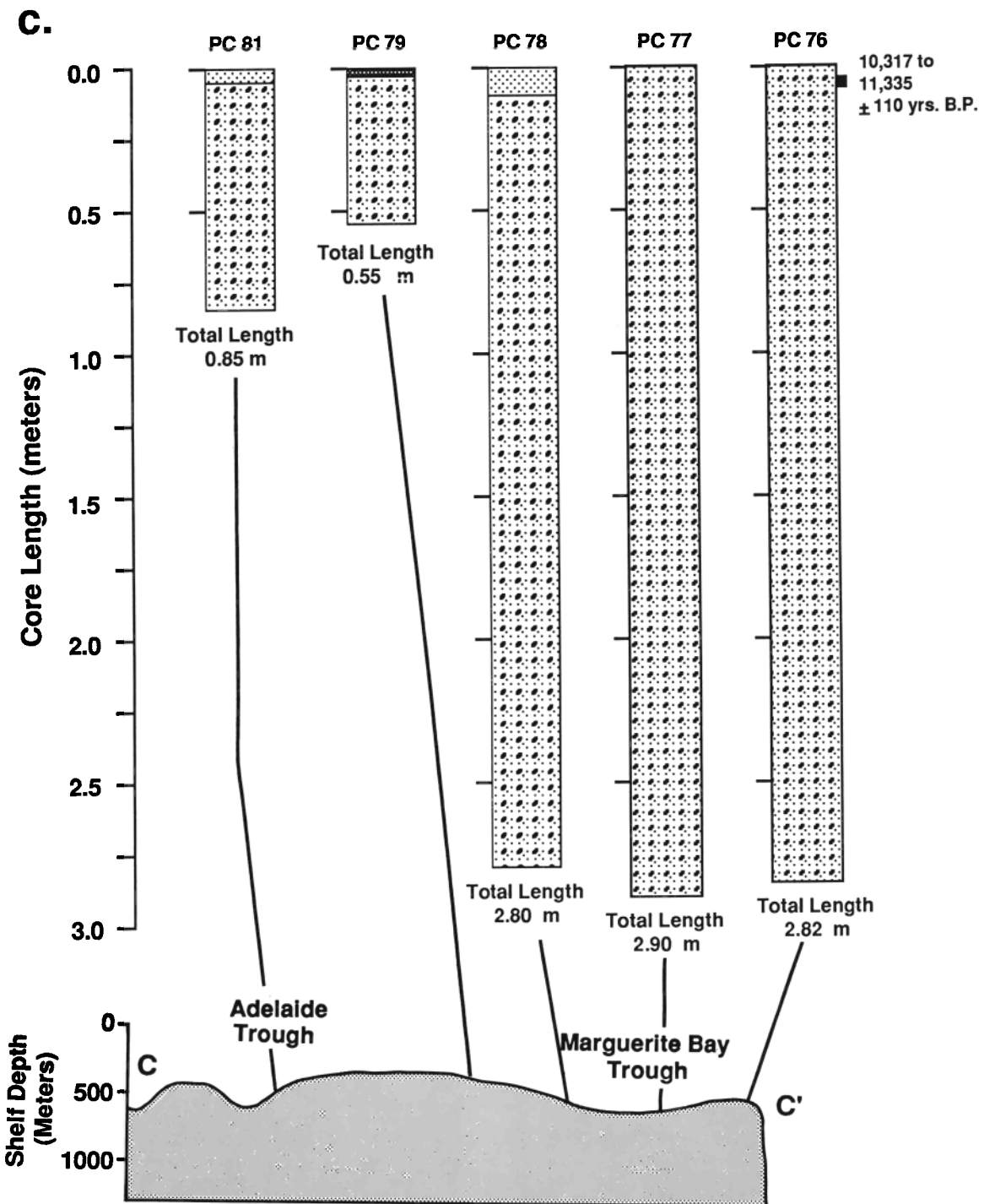


Fig. 8. (continued).

Terrigenous Gravelly Muds

Terrigenous gravelly muds (diamictites) dominate the sedimentary record of the study area. Initial visual examination of core X radiographs reveals little

distinction between these deposits. As a whole, these muds appear texturally homogeneous, with the exception of very subtle preferred pebble orientations and occasional size grading within the gravel fraction. No internal contacts are apparent. These sediments

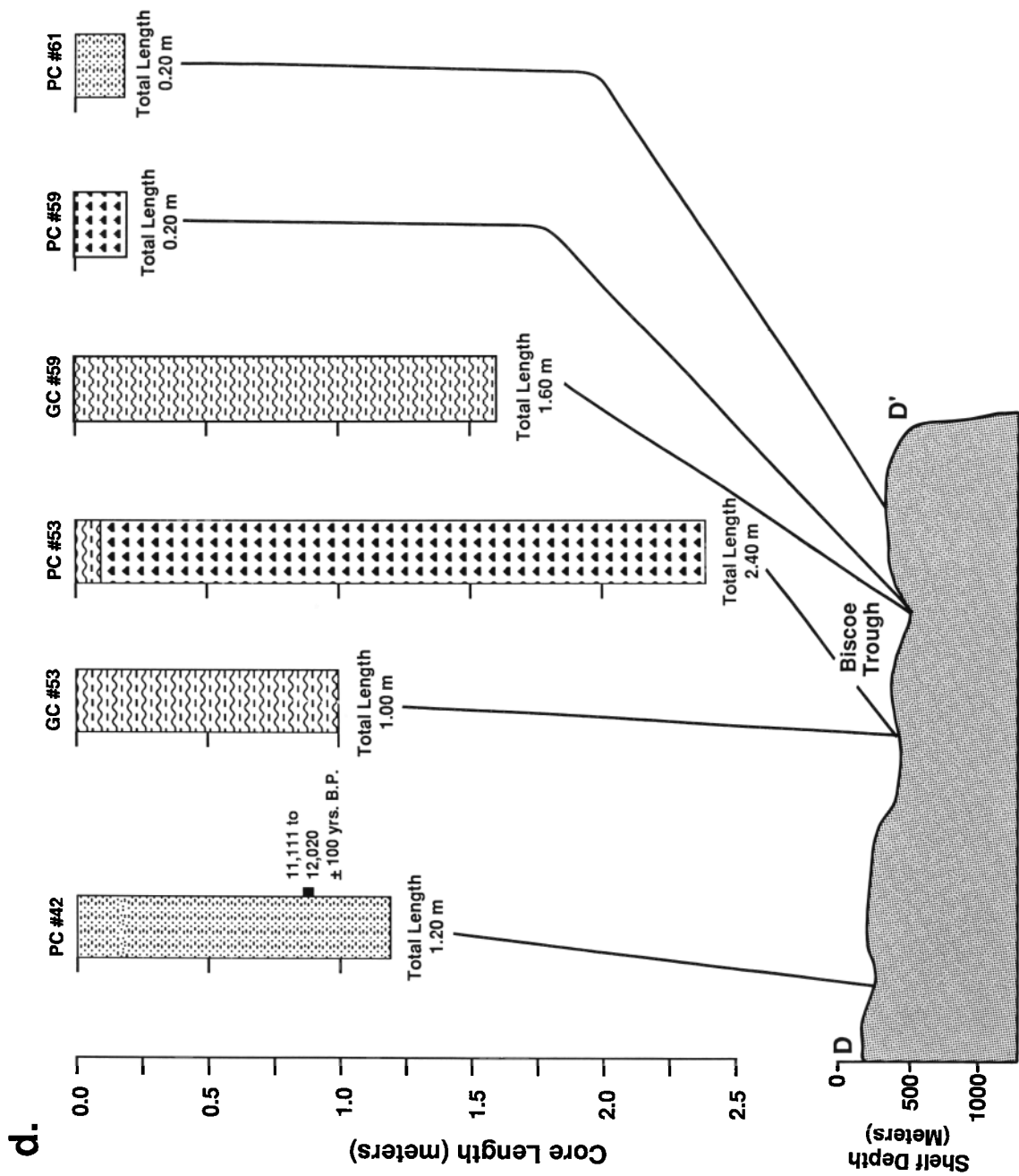


Fig. 8. (continued).

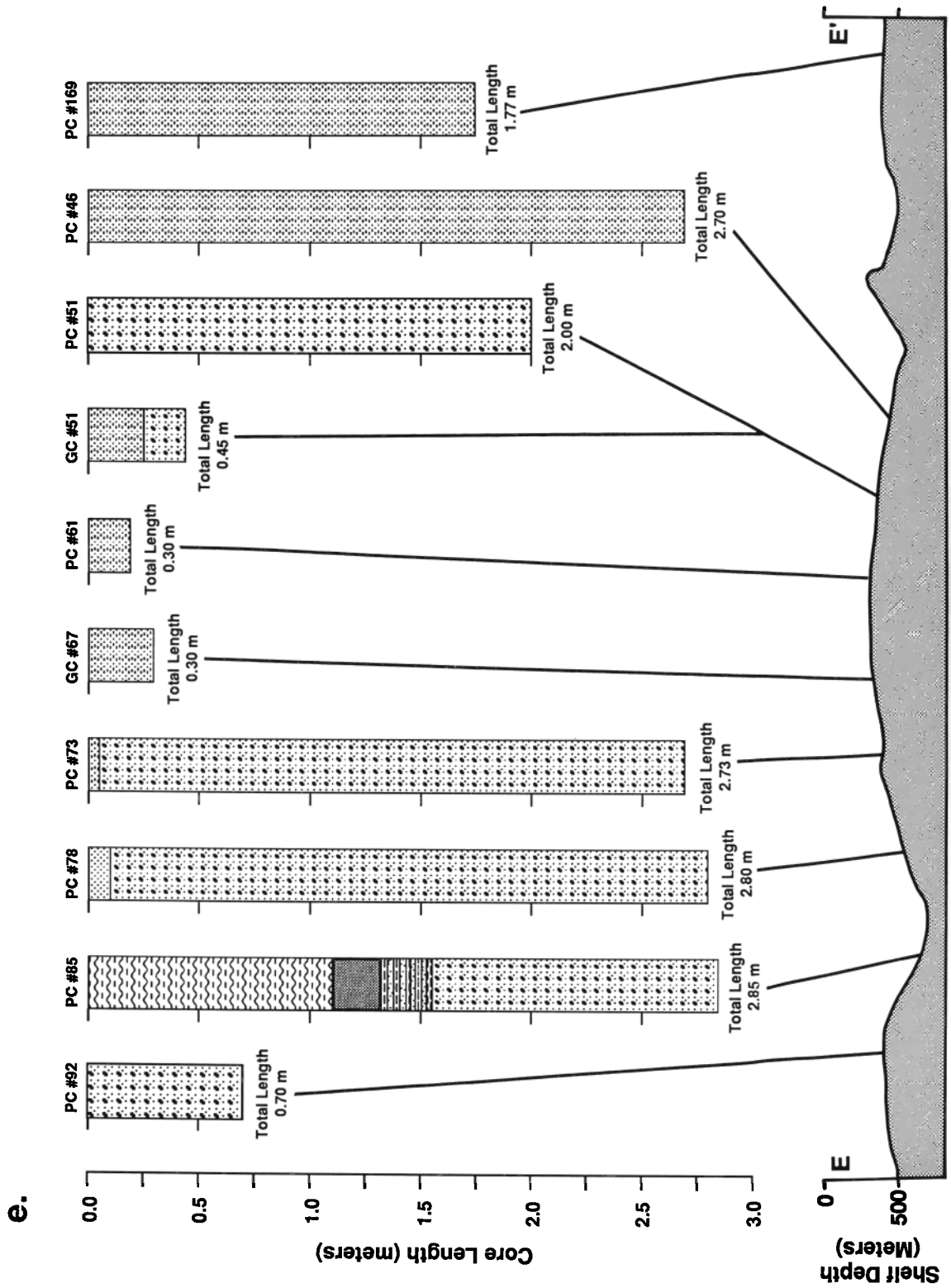


Fig. 8. (continued).

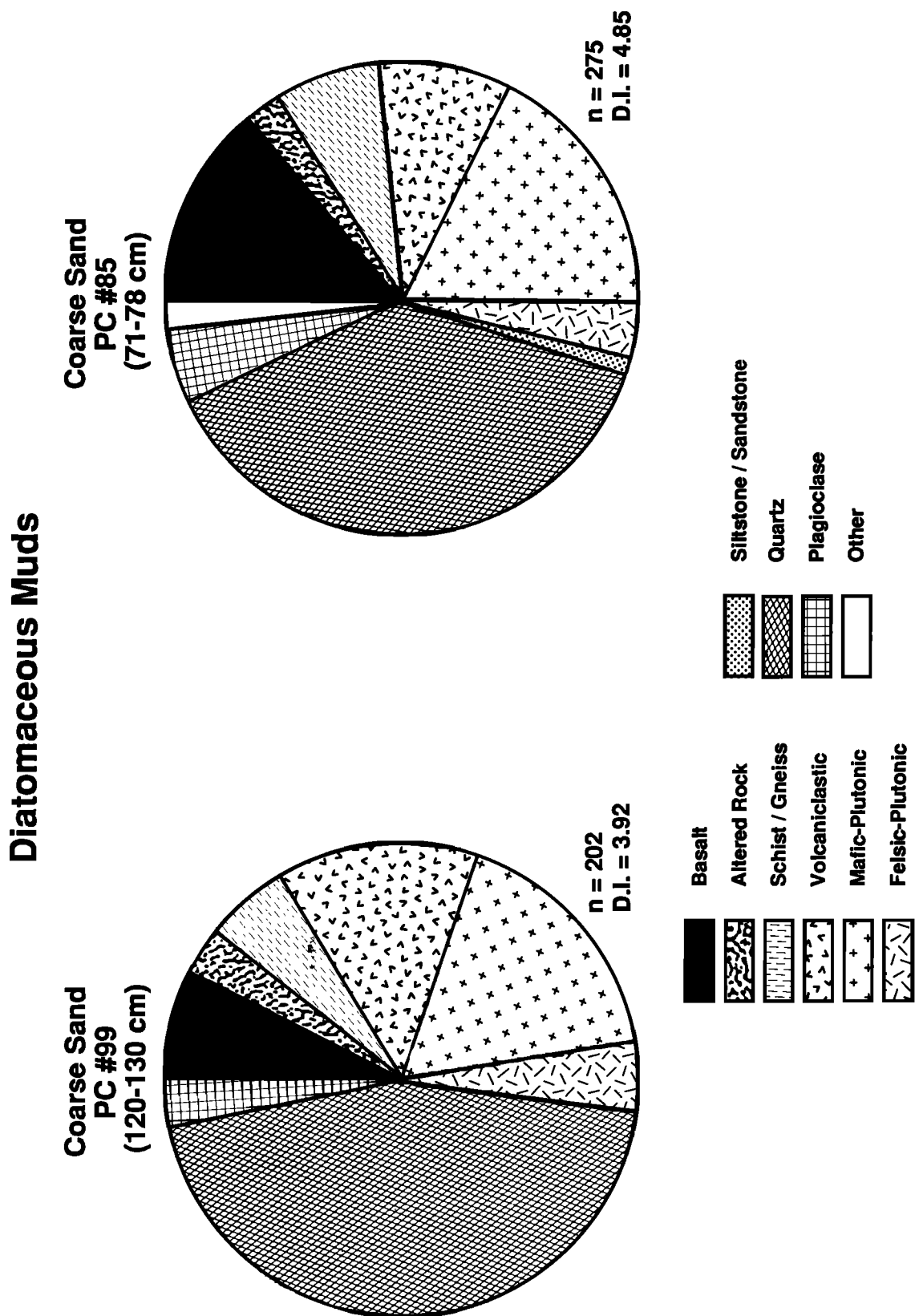


Fig. 9. Summary figure of coarse sand point counts from diatomaceous muds collected near Marguerite Bay.

typically are very poorly sorted, with an average percent sand/silt/clay ratio of 40/40/20. However, the sand fraction sometimes exhibits a strong medium sand mode within an otherwise unsorted mud (Figure 11). TorVane measurements indicate normal compaction, with the exception of PC 96, which yielded a shear strength in excess of 4 kg/cm².

A low-diversity benthic foraminiferal fauna and low abundances of *Neogloboquadrina pachyderma* are present only in cores collected near the shelf edge. Diatoms and sponge spicules are rare and appear to be predominantly reworked fragments.

Petrologic analyses of different pebbles shows significant differences between cores and a high

diversity of rock types in each unit. Shape analyses of pebbles from cores acquired in and near Marguerite Trough show two populations, one with relatively high roundness and sphericity and a second with lower roundness and sphericity values (Figure 12). Pebbles from cores collected on nearby banks reveal a uni-modal shape distribution (PC 90 and PC 92, Figure 12), plotting within the basal transport field of Boulton [1978].

Point counts also were completed on selected coarse sand samples from PC 85, and PC 87. These were compared to point counts of coarse sand samples from basal tills in Marguerite Bay [Kennedy and Anderson, 1989]. The results show greater petrographic variability for ter-

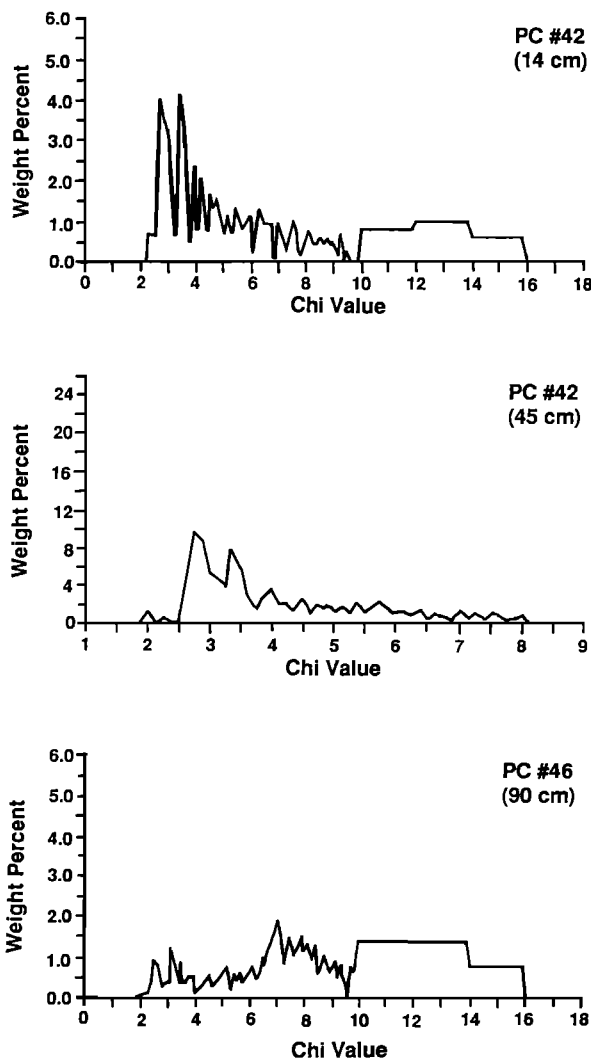


Fig. 10. Representative grain size distribution curves for group 2 sands showing differences in grain size and sorting.

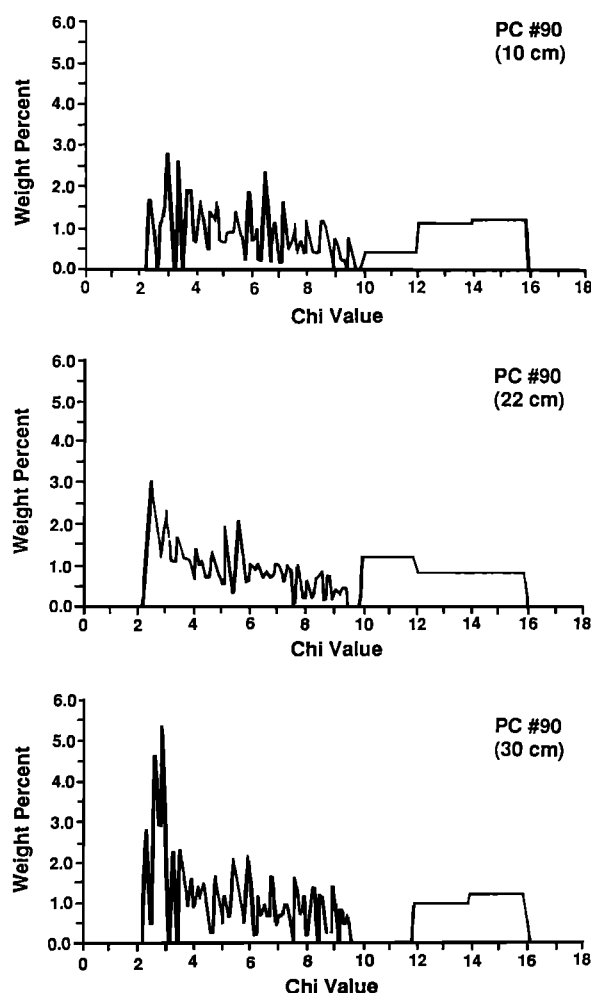


Fig. 11. Representative grain size curves for terrigenous gravelly muds.

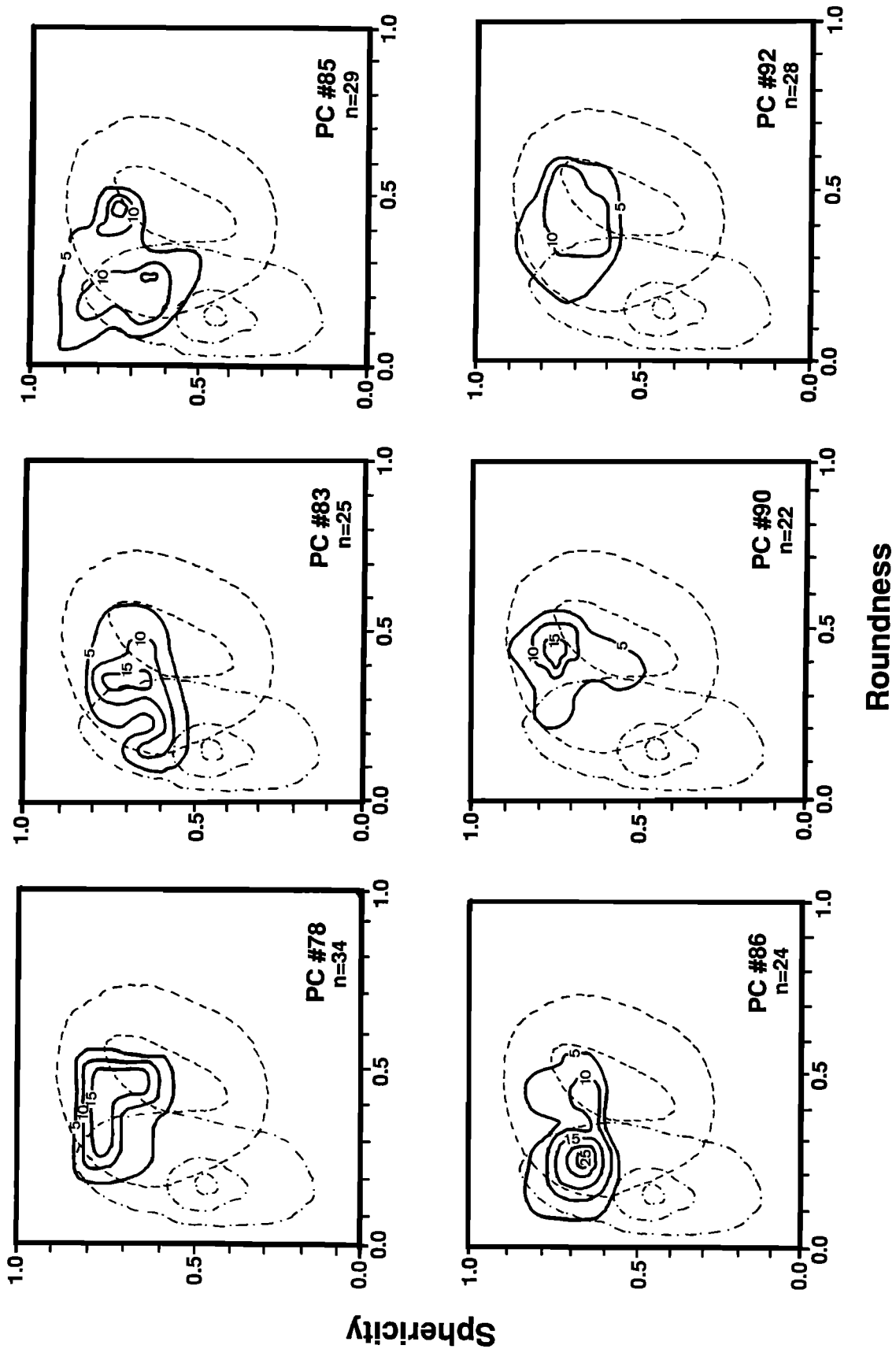
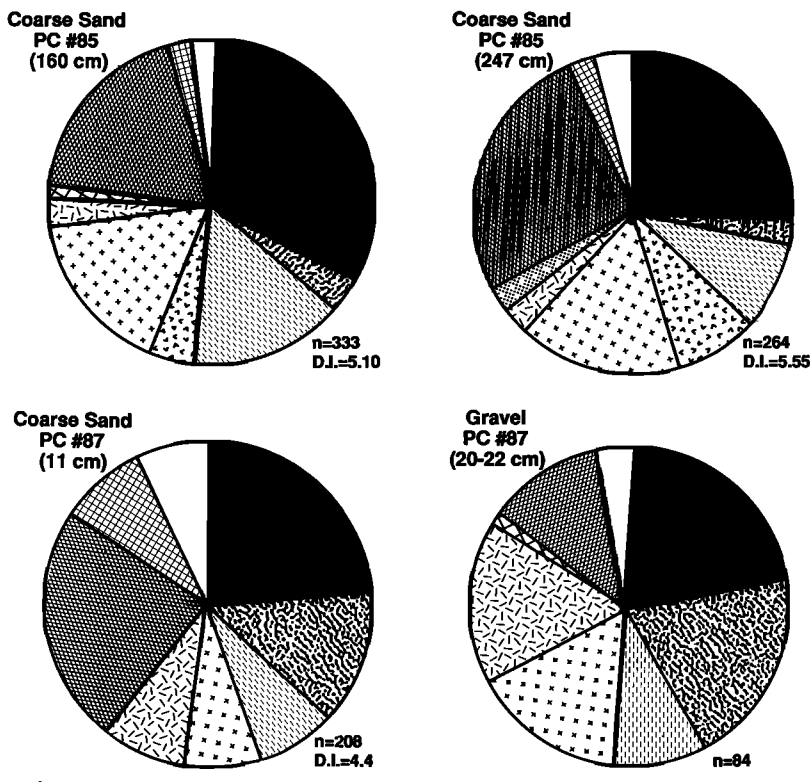


Fig. 12. Results of pebble shape analyses for terrigenous gravelly muds. The dashed curves represent Boultion's [1978] field for pebbles transported in the basal debris zone of a glacier. The dashed-dotted curves represent Boulton's field for englacial transport. Solid curves contour percent of data points per 1% area.

Terrigenous Gravely Muds



Marguerite Bay Basal Tills (from Kennedy, 1988)

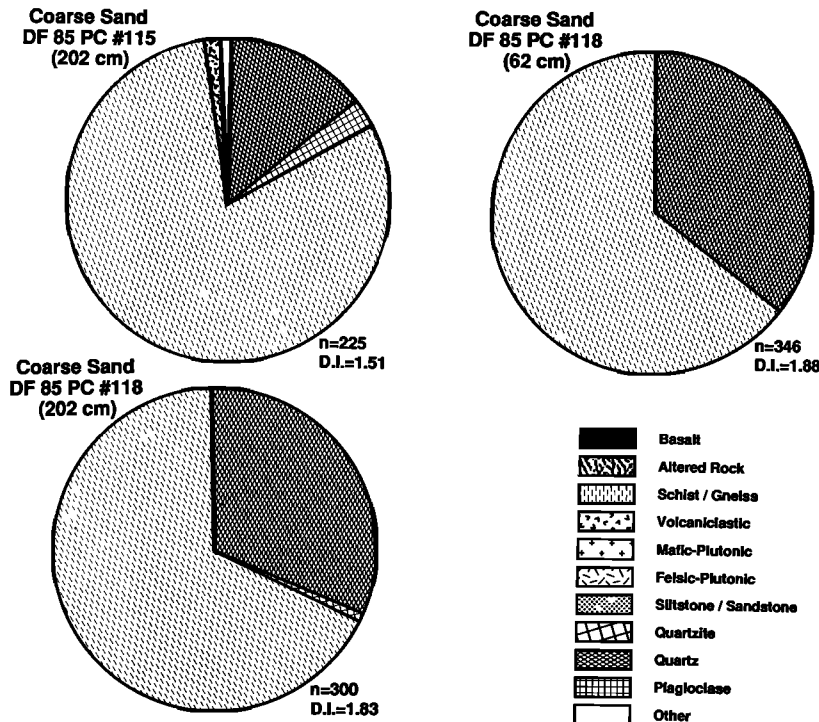


Fig. 13. Results of coarse sand point counts from terrigenous gravelly muds collected offshore of Marguerite Bay compared to basal tills from the bay [from Kennedy, 1988].

riginous gravelly muds of the shelf relative to basal tills from the bay (Figure 13).

FACIES MODEL

Sediments of the study area may be classified with respect to depositional setting using the model for Antarctic glacial marine sedimentation developed by Anderson *et al.* [1980, 1991].

Basal Tills

Kennedy and Anderson [1989] described basal tills from the northwest quadrant of Marguerite Bay which consisted primarily of schistose pebbles. Very few of the terrigenous gravelly muds examined in this study possess properties characteristic of basal tills. There are two exceptions, PC 96 and PC 53. The former diamictite unit is overcompacted, and its coarse sand and pebble fraction consists almost entirely of basalts and volcaniclastics. The latter is poorly sorted, and its coarse sand and pebble fraction consists primarily of schist and quartz. Unlike the unit in PC 96, this unit is normally compacted.

In PC 53 the upper contact of the gravelly mud is relatively sharp, with a thin (<3 cm) interval of group 2 terrigenous mud resting on top, suggesting that the source for coarse terrigenous material was removed rapidly. Furthermore, this gravelly mud exhibits a striking downcore mineralogic homogeneity and contains highly rounded schistose pebbles. For these reasons this unit is interpreted to have been deposited from the basal debris zone of an ice shelf, proximal to the grounding line, and perhaps under grounded ice if a mechanism for mobilization of this till can be established. Thus deposition beneath or near the grounding line of an ice sheet occurred in Marguerite Bay and in the inner portions of Adelaide and Biscoe troughs. Petrographic data indicate that the glacial sediments in these two areas were deposited by ice draining two different source areas, one comprised of volcaniclastic rocks and basalts and the other consisting of mostly metamorphic (schistose) rocks.

Compound Glacial Marine Sediments

Compound glacial marine (CGM) sediments reflect a depositional setting where fine-grained sediments are deposited along with ice rafted debris in a relatively low energy marine setting [Anderson *et al.*, 1980, 1991]. They typically occur in depressions deeper than 400 m. Diatomaceous muds and terrigenous muds of the study area fall into this category.

Most terrigenous gravelly mud units acquired on the shelf also fall within this category and are

characterized by the following properties: (1) textural homogeneity with the exception of weak to mild stratification and preferred (near horizontal) pebble orientations; (2) a foraminiferal fauna of low diversity and low abundance; (3) sand fractions exhibiting varying degrees of sorting within an otherwise unsorted particle size distribution; (4) petrogenic diversity laterally and vertically within the sand and pebble fractions; (5) medial to low roundness values and medial to high sphericity values in the pebble fraction; and (6) normally compacted and often water-saturated sediment.

These sediments resemble CGM sediments of the northwestern Weddell Sea continental shelf [Anderson *et al.*, 1991]. The diatoms in these sediments generally are larger, dissolution resistant forms and may have been transported into the depositional setting by marine currents (R. B. Dunbar, personal communication, 1991). This supports the presence of a permanent floating ice canopy, either sea ice or a thin ice shelf. Deposition from the base of a thick ice shelf is eliminated on the basis of pebble shape and composition.

Sediment derived from the basal debris zone should reflect the petrologic homogeneity seen in basal tills. Basal tills described in this area consist primarily of schists and basalts. Minor amounts of exotic material may be present, sourced by englacial debris and increasing in importance with distance from the ice shelf grounding line. The frequent occurrence of exotic clasts, including plutonic rocks and altered rocks, and the lack of a distinct pattern of distribution do not satisfy this criterion. Furthermore, these glacial sediments contain a sand population even more diverse in rock types than the IRD deposited in modern CGM sediments of the region. This implies that these CGM sediments were deposited from icebergs.

Complete diatoms were identified from the terrigenous mud underlying this facies in core PC 83. *Nitzschia* spp. dominated the diatom flora, indicating sea ice cover. This also is not consistent with the presence of a semipermanent ice shelf, although these diatoms could be transported beneath the ice shelf by impinging CPDW [Shemesh *et al.*, 1989].

In summary, the depositional setting for the CGM facies is believed to occur beneath permanent pack ice or thin fringing ice shelves, which would limit any significant marine biogenic production but would not restrict icebergs from moving through the area. Glacial drainage from the mountainous terrain of the peninsula should allow for the entrainment of ample englacial and superglacial debris into the ice, thus feeding large quantities of sediment into the surrounding waters via ice streams and outlet glaciers [Ander-

son *et al.*, 1991]. Angular pebble shapes support this aspect of the proposed depositional model.

Residual Glacial Marine Sediments

Group 1 and 2 muddy sands are comparable to residual glacial marine (RGM) sediments. They are indicative of sedimentation in an open marine environment where currents are able to winnow fines. This facies is thickest north of Adelaide Island and thins southward, where it exists as a thin cover on top of glacially derived gravelly muds.

Group 3 gravelly sands differ from typical RGM sediments in that they lack any biogenic component, other than reworked foraminifera and diatom frustules. These sediments are stratified distinctly in X radiographs, indicating alternating current energy. They are localized within the deepest portions of Adelaide Trough and are associated with a transition from terrigenous gravelly muds to CGM sediments. An interesting feature of the sandy lags within this unit is the presence of a residual silt- and clay-sized fraction. This suggests that the sands, though winnowed, were deposited in a silt- and clay-rich environment.

Sediment Gravity Flows

Several terrigenous gravelly mud units show evidence of transport by sediment gravity flow. These units occur in PC 98 and PC 45. PC 45 is topped with a well-sorted sand resting sharply on a poorly sorted gravelly mud. This unit is interpreted as a turbidite.

Transitional Glacial Marine Sediments

Transitional glacial marine (TGM) sediments are deposited near the grounding line of an ice shelf [Anderson *et al.*, 1991]. These were cored only in the northwestern part of Marguerite Bay (PC 99).

Ice Turbates

Although ice turbates, described by Vorren *et al.* [1983] and Barnes [1987], are not conspicuous on the continental shelf in the study area, one would expect to see them in the regions where iceberg gouges are prevalent. PC 83, for example, sampled an interval of terrigenous gravelly mud which contains a variable amount of diatoms and rests on a terrigenous mud unit. This is overlain by modern diatomaceous mud. The lower terrigenous gravelly mud and terrigenous mud units may be the products of iceberg reworking. These units have since been draped with diatomaceous mud. An apparent lack of modern ice turbates in the

study area suggests that iceberg furrowing occurred during the last glacial maximum when sea level was lower or when thicker icebergs traversed the shelf.

CHRONOSTRATIGRAPHY

Antarctic sediments are notoriously difficult to date because they contain very little carbonate. Thus it is important to exhaust every means of acquiring age information. In this study, radiocarbon dates were supported by $\delta^{18}\text{O}$ isotopic analyses. The $\delta^{13}\text{C}$ data showed no definable pattern and were not used for chronostratigraphic purposes, although some of the data are shown to illustrate this. The following is a brief discussion of the techniques used and the results.

Carbon 14 Age Dating

Four ^{14}C dates were obtained in order to constrain the timing of glacial events (Table 1). Calcareous foraminifera were collected for TAMS radiocarbon analysis from cores PC 42, PC 85, PC 99, and PC 76 (Figure 3). All samples were a mixture of benthonic and planktonic calcareous foraminifera.

Four sedimentary units were targeted. Group 1a (TGM) and group 2 terrigenous muds (CGM) were selected to constrain the timing of transition from glacially dominated to open marine conditions. The terrigenous gravelly muds (CGM) and group 2 sands (RGM) were chosen to determine if these are late Pleistocene or Holocene in age. Radiocarbon dates were corrected for the carbon reservoir effect using Harden's [1989] correction value of 1200 to 2818 years, which was established for this region.

Analysis of foraminifera from group 1a terrigenous mud from the interval of 180 to 190 cm in PC 99 yielded a corrected ^{14}C age of $11,481 \pm 12,430 \pm 140$ years B.P. Foraminifera from group 2 terrigenous mud from the interval of 125 cm to 135 cm in PC 85 yielded a corrected ^{14}C age of $11,306 \pm 12,240 \pm 105$ years B.P.

These dates provide temporal control over the decline of glacially dominated conditions in the region

TABLE 1. Carbon 14 Ages of Glacial Marine Sediments, Northern Antarctic Peninsula

Sample	Core	Depth, cm	Uncorrected ^{14}C age, years B. P.
AA-5684	PC 99	180–190	$13,490 \pm 140$
AA-7324	PC 85	125–135	$13,335 \pm 105$
AA-5685	PC 76	1–6	$12,425 \pm 110$
AA-7323	PC 42	80–90	$13,120 \pm 100$

near Marguerite Bay following the glacial maximum. The unit of group 1a terrigenous mud from PC 99 reflects a transitional glacial marine facies (B1 [Kennedy and Anderson, 1989]) that in part defines an ice shelf recessional setting. The group 2 terrigenous muds described in this study are also transitional. These muds are gradational with the overlying diatomaceous muds, thus indicating an apparent gradual change from a glacially dominated to an open marine (lacking a permanent ice canopy) depositional setting for the region near Marguerite Bay. A similar relationship of rock flour grading upward into diatomaceous mud is also observed, and radiocarbon dated, by Harden *et al.* [1992] in a core from northeastern Marguerite Bay (PC-112 [Harden *et al.*, 1992, p. 90]). Their uncorrected (conventional) date of ~10,800 years B.P. compares well with our dates. The discrepancy (500 to 330 years) may be due to the variance of the carbon reservoir but probably indicates that the outer shelf regions became ice free at an earlier date. All dates suggest a late Pleistocene to early Holocene timing for this transition to open marine conditions.

Additionally, foraminifera were removed from the upper 6 cm of PC 76, which included a relatively abundant, low-diversity fauna. Some bryozoan material also was included in this sample. A corrected date of 10,317 to 11,335 ± 110 years B.P. was determined for this near-surface sample. The fact that this surface sample is so old raises some questions. It may be the product of iceberg keels gouging and reworking the upper few meters of sediment on the shallow shelf edge. However, the carbonate material sampled for this radiocarbon date was removed from several centimeters of a gravelly lag which was presumably the result of currents winnowing sediments near the shelf edge. Therefore this date may demonstrate that very little sediment has accumulated during Holocene time at this location. Given the uncertainties, however, this date is, at best, tenuous.

Finally, analyses of foraminifera from PC 42 at 80–90 cm depth yielded a radiocarbon age of 11,111 to 12,020 ± 100 years B.P. These data verify a late Pleistocene to early Holocene timing for the deposition of sediments sampled in this study.

Values of $\delta^{18}\text{O}$ as a Chronostratigraphic Tool

The $\delta^{18}\text{O}$ of benthic foraminifera may be considered a reliable indicator of variations in global ice volumes and temperatures, although the relative influence of these factors remains controversial [Anderson and Arthur, 1983]. However, the ice volume effect is formidable, so that the glacial to interglacial transition appears as a negative shift (on a

profile of glacial age to recent values) of 0.8 to 1.3 ‰ [Anderson and Arthur, 1983]. With respect to the oxygen isotope record, the late Wisconsinan glacial maximum, as referred to in this study, should correspond to oxygen isotope stage 2.

Although those factors influencing surface water $\delta^{18}\text{O}$ values (and the $\delta^{18}\text{O}$ of planktonic foraminifera) should exhibit little impact on benthic foraminifera in the deep sea, the benthic foraminifera living at the sediment/water interface of the shallow banks of the inner Antarctic continental shelf may be influenced significantly, especially if the water column on the continental shelf is sufficiently mixed to transfer surface waters to depth. Additional physical controls may influence the waters near the Antarctic continent. For example, the $\delta^{18}\text{O}$ -salinity relationships break down near the continent because of sea ice formation, which increases salinity while leaving $\delta^{18}\text{O}$ values the same, or because of glacier ice input, which may introduce water with anomalous $^{18}\text{O}/^{16}\text{O}$ values [Charles and Fairbanks, 1990].

Upon consideration of the above factors, one may conclude that the isotopic signal recorded by planktonic and benthic foraminifera will be the product of an environment influenced by a complex relationship among temperature, salinity, glacial meltwater input, and seafloor diagenesis of carbonate material. This relationship will vary significantly around Antarctica, and the relative influences may be difficult, if not impossible, to discern. Furthermore, the signal will be superimposed over a larger-scale ice volume/glacial-interglacial signal. Whether or not the local influences are significant enough to wipe out the ice volume signal is not known for certain.

Charles and Fairbanks [1990] demonstrated that the temperature effect, theoretically, should swamp the effect of salinity on $\delta^{18}\text{O}$ values of surface waters over a critical latitudinal range. They also showed that the isotopic signal of the planktonic foraminifera *Neogloboquadrina pachyderma* reflects sea surface temperatures predictably. A latitudinal profile of $\delta^{18}\text{O}$ values from these foraminifera indicates a very strong gradient across the Antarctic Polar Front (APF). Over a 10° range of latitude, the $\delta^{18}\text{O}$ variation is roughly 3 times that expected for full glacial-interglacial cycles [Charles and Fairbanks, 1990]. The APF is significantly distant to the north of the study area. As it is unlikely that the APF was farther south during the last glacial maximum, the temperature variations should be minimized, and it may be argued that the $\delta^{18}\text{O}$ values predominantly reflect changes in ice volume. Nevertheless, benthic foraminifera from shallow banks of the continental shelf near Antarctica may be influenced by surface water temperatures, especially if mixing of waters in the water column is sufficient to transfer surface water temperature effects to depth.

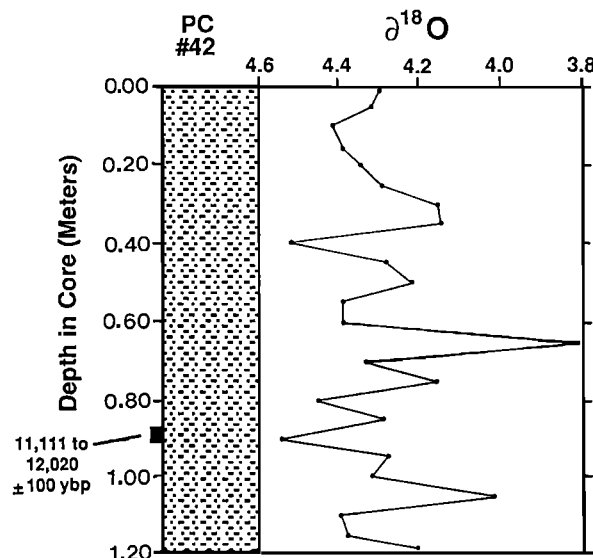


Fig. 14. Oxygen isotope curve with radiocarbon control for PC 42.

A $\delta^{18}\text{O}$ curve was generated from benthic (*Cibicides* sp.) foraminifera removed from PC 42, which contains 120 cm of RGM sediments. This core was chosen because it contains an abundant benthic fauna and exhibits evidence of winnowing, yet it contains no obvious hiatuses. Thus it was predicted that this core may represent a condensed section of open marine sedimentation that would include the most recent glacial to interglacial transition.

It is apparent that $\delta^{18}\text{O}$ values did not vary significantly during the time period of deposition represented by core PC 42. Values range from $4.02\text{\textperthousand}$ to $4.52\text{\textperthousand}$, with the exception of sample 42-65 cm, where a value of $3.81\text{\textperthousand}$ was measured. The value of the maximum negative shift is $0.73\text{\textperthousand}$, and above this the $\delta^{18}\text{O}$ values become more positive (heavier) again. Therefore one may reasonably conclude that deposition of these RGM sediments began in the late Pleistocene or early "postglacial" time following the transition to low $\delta^{18}\text{O}$ values in southern ocean waters. This conclusion is supported by the radiocarbon date of 1111 to $12,020 \pm 100$ years B.P. from foraminifera at a depth of 80–90 cm in this core (Figure 14). In addition, glacial age $\delta^{18}\text{O}$ values in this region are expected to be greater than $5.00\text{\textperthousand}$ (R. B. Dunbar, personal communication, 1991). Thus it appears that the latest Pleistocene to Holocene signal, at least as recorded by benthic foraminifera on the continental shelf, varies between 3.80 and $4.60\text{\textperthousand}$. These fluctuations are probably a function of temperature variations and glacial ice input, as temperature alone will shift $\delta^{18}\text{O}$ values by $0.50\text{\textperthousand}$ per 2°C .

Other than those found in the RGM sediments in the northern part of the study area, *N. pachyderma* specimens were found only in terrigenous gravelly muds (CGM) near the shelf edge (PCs 76, 88, 89, 90) and in the group 2 terrigenous muds and modern diatomaceous muds (CGM) collected in shelf depressions. Individual samples were collected from

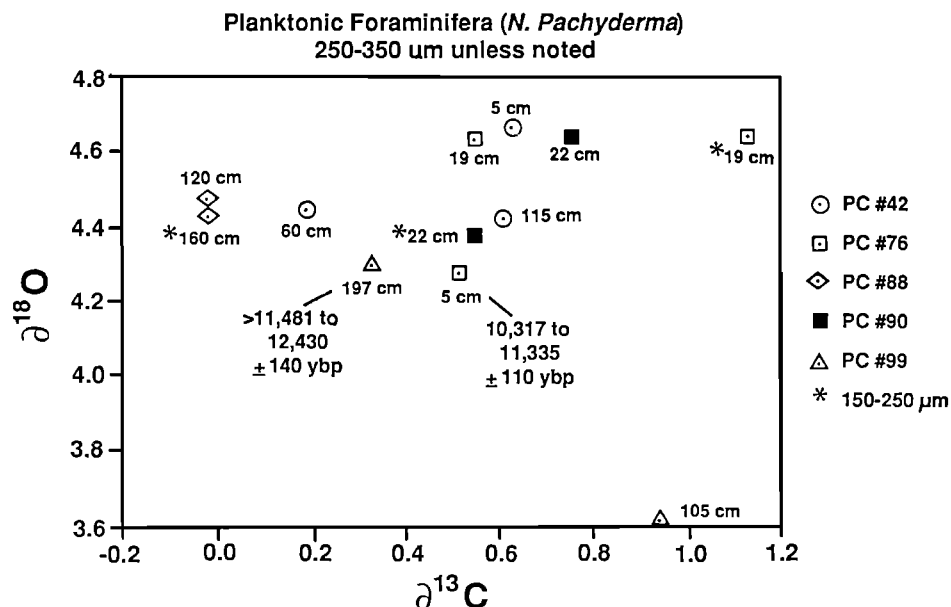


Fig. 15. Summary of stable isotope data from PC 42, PC 76, PC 88, PC 90, and PC 99.

some of these different sediments to obtain "interglacial" sediments. The results are summarized in Figure 15.

Two samples especially are significant since they represent intervals which have been radiocarbon dated. The PC 99, 197-cm sample was collected 2 cm below an interval of terrigenous mud that yielded a corrected date of 11,481 to 12,430 ± 140 years B.P., and sample PC 76 at 5 cm from a terrigenous gravelly mud (CGM) yielded a corrected date of 10,317 to 11,335 ± 110 years B.P. The $\delta^{18}\text{O}$ values for these samples are 4.30 and 4.28 ‰, respectively. A number of other samples yielded similar isotopic values (Figure 15), indicating an early postglacial to early Holocene age. Therefore, in terms of planktonic foraminifera, the $\delta^{18}\text{O}$ signal for latest Pleistocene to Holocene sediments ranges between 3.62 and 4.67 ‰.

GLACIAL RECONSTRUCTION

The presence of basal till indicates that glacial ice grounded in Marguerite Bay during the last glacial maximum [Kennedy and Anderson, 1989]. No sedimentary evidence was found to indicate that glacial ice in Marguerite Trough advanced beyond the inner shelf. Features indicative of glacial scouring and a lack of sediment cover suggest that an ice sheet was grounded in Adelaide and Biscoe troughs. Basal till also was collected in a single core from Biscoe Trough, but the age of this deposit is not known. Otherwise, geomorphologic features indicate that the ice sheet grounding line was located on the inner shelf of the study area (Figure 6). It should be noted that piston cores from the outer shelf apparently did not penetrate sediments deposited during the glacial maximum. Thus the extent of grounded ice on the outer continental shelf remains problematic.

Thick and laterally extensive glacial marine sediments with a subordinate or nonexistent marine component were sampled in numerous piston cores taken on the continental shelf south and west of Adelaide Island. The $\delta^{18}\text{O}$ data from planktonic foraminifera indicate that these sediments were deposited during the early Holocene and perhaps during the glacial-interglacial transition. Petrogenic diversity of pebbles and coarse sands from these sediments, a paucity of diatoms, and pebble shapes indicate that they were deposited under thick pack ice or a thin fringing ice shelf.

During the glacial-interglacial transition the glacial setting of the study area perhaps resembled that of the northwestern Weddell Sea continental shelf today. A large fringing ice shelf, perhaps similar to the present Larsen Ice Shelf, efficiently distributed sediment, in the form of englacial debris, onto the continental shelf

(Figure 16c). Unlike Larsen Ice Shelf, which receives most of its mass from smaller outlet glaciers [Anderson *et al.*, 1991], the George VI ice stream contributed a significant portion of the ice draining into this ice shelf. This system produced a succession of glacial marine sediments that are generally lacking in a marine biogenic component, but which display a gradual increase in marine influence from Marguerite Bay to the shelf edge. The ice shelf withdrew from the shelf after 12,430 years B.P., as is evident from PC 99. Northward along the shelf, these facies grade into RGM sediments offshore of the Biscoe Islands, indicating a stronger marine influence in that area (Figure 16a).

The transition from glacial to interglacial conditions occurred during the latest Pleistocene to early Holocene. During this episode of glacial retreat the shelf setting was highly depositional, leaving widespread terrigenous gravelly muds covering the shelf near Marguerite Bay. This flux of sediments to the outer shelf may reflect enhanced glacial drainage for a short period of time following the glacial maximum.

Near Marguerite Bay the evidence is strongly in support of a gradual transition from a glacially dominated to an open marine (seasonal sea ice) depositional system [Kennedy and Anderson, 1989]. In contrast, sedimentary changes in cores from the open shelf indicate a rapid retreat of the floating ice canopy (Figure 17). This may be related to a rapid retreat of glacial ice from the inner shelf.

Within Marguerite Bay the retreat of this ice shelf was slow enough to allow for the development of discrete sub-ice shelf depositional environments as described by Kennedy and Anderson [1989]. These sub-ice shelf facies are stacked in PC 99, such that a grounding line proximal-distal-proximal-distal-proximal relationship is apparent. These transitions occur over an interval encompassing only 1.1 m; therefore it is not certain if this reflects repeated grounding line advances or lateral grounding line shifts during a single advance/retreat.

Historically, the George VI Ice Shelf and Wordie Ice Shelf have melted in response to warmer CPDW flowing beneath them [Doake, 1982]. Conceivably, retreat of the marine ice sheet and ice shelf was triggered by incursion of this relatively warm water mass onto the shelf. There is some evidence for this in the form of RGM sediments in the tops of cores collected from the banks of the outer continental shelf where CPDW occupies the entire shelf water column. The presence of winnowed sands in cores PC 99 and PC 85 at the transition from glacial to interglacial deposits could reflect the influence of CPDW. Alternatively, variations in sediment texture may reflect meltwater pulses from near the ice shelf

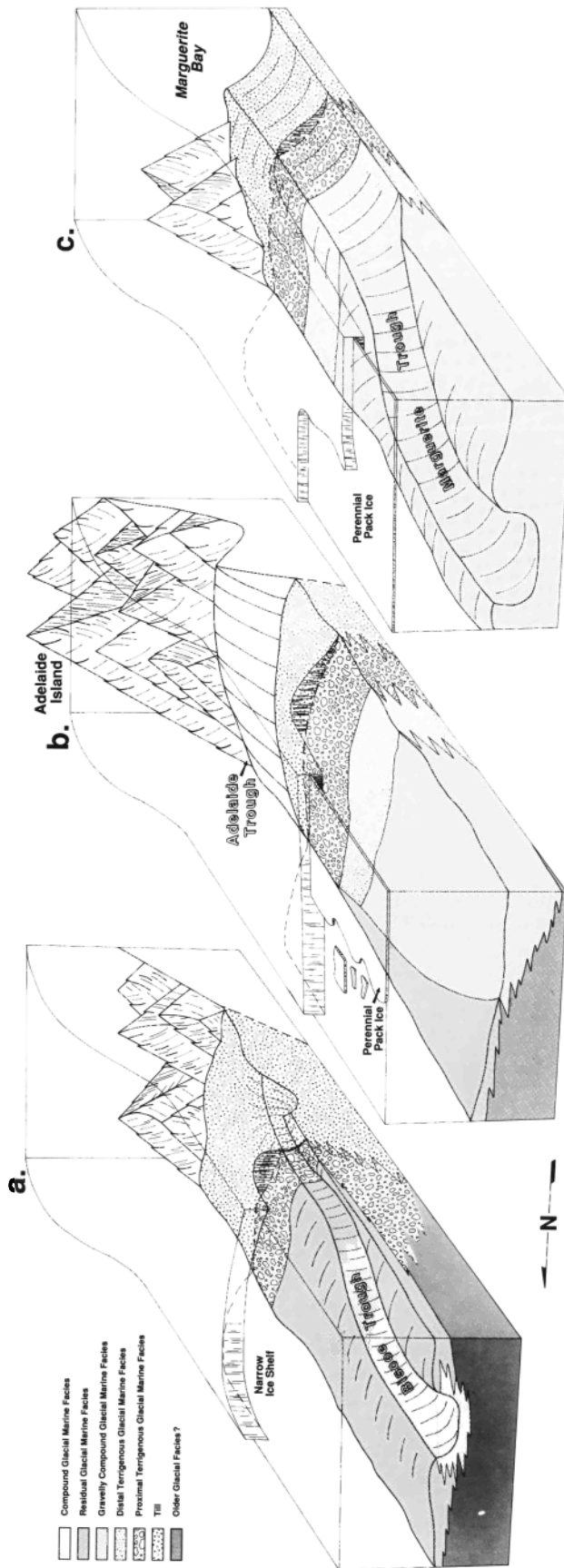


Fig. 16. Reconstruction of glacial conditions at the onset of the glacial-interglacial transition: (a) offshore of the Biscoe Islands, (b) offshore of Adelaide Island, and (c) offshore of Marguerite Bay.

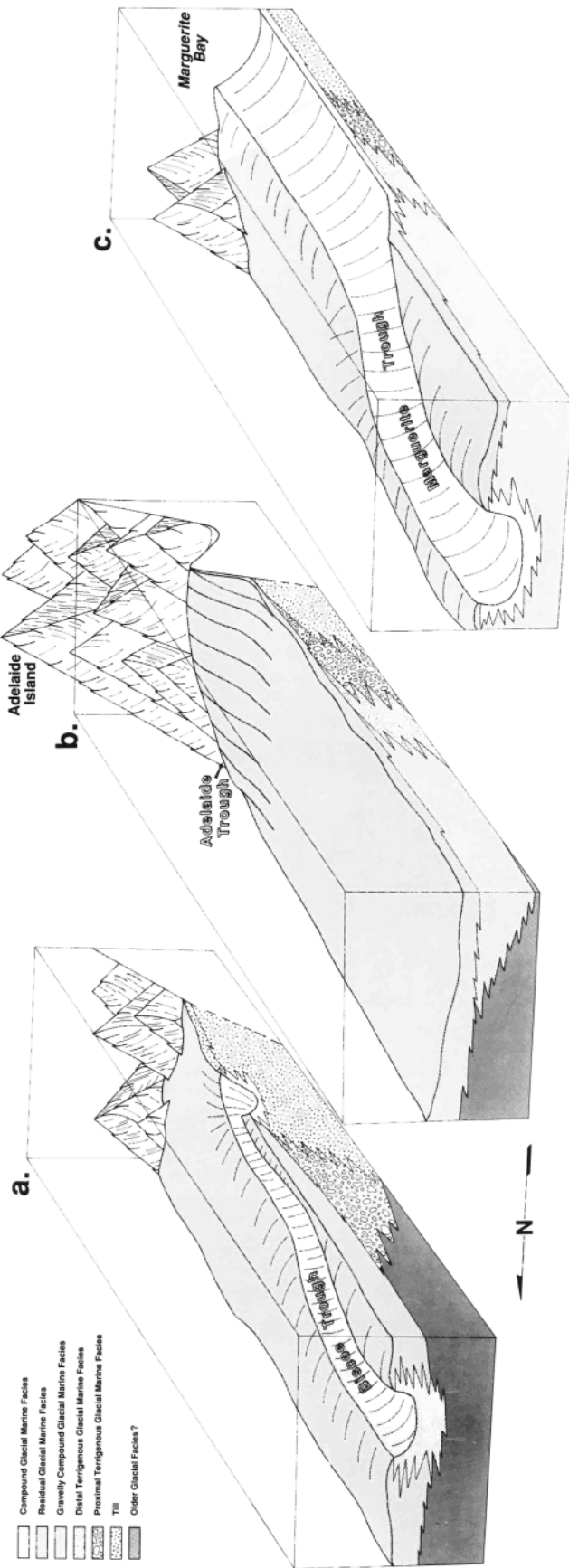


Fig. 17. Facies distribution during present interglacial.

grounding line and have nothing to do with impinging warm deep waters. There also is a decrease in carbonate upward in core PC 99; the top of this core contains only benthic foraminifera. In Weddell Sea, CPDW is associated with arenaceous foraminifera, and this is interpreted as being due to dissolution effects [Anderson, 1975]. Whether this impinging CPDW was the cause or the effect of ice sheet retreat remains problematic.

CONCLUSIONS

The sedimentary history of the study area deduced from piston cores is consistent with the reconstruction based upon seafloor morphology. This study uncovered little direct evidence for a major grounding event on the outer continental shelf of the study area during the last glacial maximum. It should be noted that glacial age (late Wisconsinian) sediment may not have been recovered. However, basal tills in Marguerite Bay reflect the presence of an ice sheet which must have been close to 1 km thick [Kennedy and Anderson, 1989]. The ice sheet also was grounded on the inner shelf of the study area. The middle shelf and outer shelf were covered by a perennial canopy of ice, either thick sea ice or a thin fringing ice shelf.

It is apparent that the latest Pleistocene to early Holocene was a period of dramatic transition throughout the study area. Offshore of Marguerite Bay, glacially sourced terrigenous material continued to dominate the sediments deposited on the continental shelf throughout the glacial-interglacial transition and into the early Holocene. This glacially dominated system gradually gave way to seasonally open marine conditions and deposition of diatomaceous glacial marine sediments sometime during the Holocene.

The present depositional setting reflects seasonally open marine sedimentation in a polar setting. Primary productivity is high, terrigenous sediments are transported to the shelf by ice rafting, and the primary influences on sediment distribution are marine currents which sweep fine sediment from the shallow banks and subsequently deposit it in shelf depressions.

Acknowledgments. This research was supported by a grant from the National Science Foundation (NSF-DPP-8818523). Carbonate samples were dated at the NSF TAMS Facility at the University of Arizona and were funded partially by NSF grant EAR85-12761. The authors wish to thank Scott Ishman for his helpful comments and suggestions, Tom Hobbs for his assistance in the construction of the bathymetric map, and Stephanie Staples Shipp for her help in figure drafting and editing. Peter Barker of the British Antarctic Survey kindly provided side scan survey records of the study region. We also are grateful to Dennis Cassidy of the Antarctic Core Storage Facility for his

assistance in obtaining and sampling the cores used in this study. We thank the crew of the R/V *Polar Duke* for their enthusiastic support during the 1988 Deep Freeze Cruise.

REFERENCES

- Anderson, J. B., Factors controlling CaCO_3 dissolution in the Weddell Sea from foraminiferal distribution patterns, *Mar. Geol.*, 19, 315–332, 1975.
- Anderson, J. B., D. D. Kurtz, E. W. Domack, and K. M. Balshaw, Glacial and glacial marine sediments of the Antarctic continental shelf, *J. Geol.*, 88, 399–414, 1980.
- Anderson, J. B., D. S. Kennedy, M. J. Smith, and E. W. Domack, Sedimentary facies associated with Antarctica's floating ice masses, in *Glacial Marine Sedimentation: Paleoclimatic Significance*, edited by J. B. and G. M. Ashley, *Spec. Pap. Geol. Soc. Am.*, 261, 1–25, 1991.
- Anderson, T. F., and M. A. Arthur, Stable isotopes of oxygen and carbon and their application to sedimentological and paleoenvironmental problems, in *Stable Isotopes in Sedimentary Geology, SEPM Short Course*, 10, 1–151, 1983.
- Barker, P. F., R. D. Larter, C. J. Pudsey, A. M. Conway, I. W. Hamilton, and J. B. Anderson, Glacial history and subduction-related processes along Antarctic Peninsula margin, (abstract), 28th International Geology Congress, vol. 1, pp. 1-87–1-88, 1989.
- Barnes, P. W., Morphological studies of the Wilkes Land continental shelf, Antarctica—glacial and iceberg effects, in *The Antarctic Continental Margin: Geology and Geophysics of Offshore Wilkes Land, Earth Sci. Ser.*, vol. 5A, edited by S. L. Eittreim and M. A. Hampton, pp. 175–194, Circum-Pacific Council for Energy Resources, Houston, Tex., 1987.
- Boulton, G. S., The origin of glacially fluted surfaces, observations and theory, *J. Glaciol.*, 17, 287–309, 1976.
- Boulton, G. S., Boulder shape and grain-size distributions of debris as indicators of transport paths through a glacier and till genesis, *Sedimentology*, 25, 773–799, 1978.
- Charles, C. D., and R. G. Fairbanks, Glacial to interglacial changes in the isotopic gradient of southern ocean surface waters, in *Geological History of the Polar Oceans: Arctic vs. Antarctic*, edited by U. Bleil and J. Theide, pp. 519–538, Kluwer Academic, Boston, Mass., 1990.
- Clapperton, C. M., and D. E. Sugden, Late Quaternary glacial history of George VI Sound area, West Antarctica, *Quat. Res.*, 18, 243–267, 1982.
- Denton, G. H., J. G. Bockheim, S. C. Wilson, and M. Stuiver, Late Wisconsin and early Holocene glacial history, inner Ross Embayment, Antarctica, *Quat. Res.*, 31, 151–182, 1989.
- Doake, C. S. M., State of balance of the ice sheet in the Antarctic Peninsula, *Ann. Glaciol.*, 3, 77–82, 1982.
- Doake, C. S. M., and D. G. Vaughan, Rapid disintegration of the Wordie Ice Shelf in response to atmospheric warming, *Nature*, 350, 328–329, 1992.

- Domack, E. W., Sedimentology of glacial and glacial marine deposits on the George V-Adelie continental shelf, East Antarctica, *Boreas*, 11, 79–97, 1982.
- Elverhoi, A., and G. Maisey, Glacial erosion and morphology of the eastern and southeastern Weddell Sea shelf, in *Antarctic Earth Science*, edited by R. L. Oliver, P. R. James, and J. B. Jago, pp. 483–487, Australian Academy of Science, Canberra, Australia, 1983.
- Galehouse, J. S., Point counting, in *Procedures in Sedimentary Petrology*, edited by R. E. Carver, pp. 385–407, Wiley-Interscience, New York, 1971.
- Harden, S. L., Establishing rates of sediment accumulation on 100-year and 1000-year time scales for glacial-marine deposits of the continental shelf of the western Antarctic Peninsula: A radiochemical approach, Master's thesis, 87 pp., N. C. State Univ., Raleigh, 1989.
- Harden, S. L., D. J. DeMaster, and C. A. Nittrouer, Developing sediment geochronologies for high-latitude continental shelf deposits: A radiochemical approach, *Mar. Geol.*, 103, 69–97, 1992.
- Holtedahl, O., On the geology and physiography of some Antarctic and sub-Antarctic islands: Scientific results of the Norwegian Antarctic expeditions, 1927–1928 and 1928–1929, *Rep. 3*, 172 pp., Nor. Videnskaps Akad., Oslo, 1929.
- Hughes, T. J., Numerical reconstruction of paleo-ice sheets, in *The Last Great Ice Sheets*, edited by G. H. Denton and T. J. Hughes, pp. 222–260, Wiley-Interscience, New York, 1981.
- Kellogg, T. B., R. S. Truesdale, and L. E. Osterman, Late Quaternary extent of the West Antarctic ice sheet: New evidence from Ross Sea cores, *Geology*, 7, 249–253, 1979.
- Kennedy, D. S., Modern sedimentary dynamics and Quaternary glacial history of Marguerite Bay, Antarctic Peninsula, Master's thesis, 203 pp., Rice Univ., Houston, Tex., 1988.
- Kennedy, D. S., and J. B. Anderson, Glacial-marine sedimentation and Quaternary glacial history of Marguerite Bay, Antarctic Peninsula, *Quat. Res.*, 31, 255–276, 1989.
- Krumbein, W. C., Measurements and geological significance of shape and roundness of sedimentary particles, *J. Sediment. Petrol.*, 11, 64–72, 1941.
- Lien, R., Sea bed features in the Blaaenga area, Weddell Sea, Antarctica, paper presented at Sixth International Conference on Port and Ocean Engineering under Arctic Conditions, Univ. Laval, Laval Quebec, Can., July 27–31, 1981.
- Martin, P. J., and D. A. Peel, The spatial distribution of 10m temperatures in the Antarctic Peninsula, *J. Glaciol.*, 20, 311–317, 1978.
- Payne, A. J., D. E. Sugden, and C. M. Clapperton, Modeling the growth and decay of the Antarctic Peninsula ice sheet, *Quat. Res.*, 31, 119–134, 1989.
- Potter, J. R., and J. G. Paren, Interaction between ice shelf and ocean in George VI Sound, Antarctica, in *Oceanology of the Antarctic Continental Shelf*, *Antarct. Res. Ser.*, vol. 43, edited by S. S. Jacobs, pp. 35–58, AGU, Washington, D. C., 1985.
- Reynolds, J. M., The distribution of mean annual temperatures in the Antarctic Peninsula, *Br. Antarct. Surv. Bull.*, 54, 123–133, 1981.
- Shemesh, A., L. H. Burckle, and P. N. Froelich, Dissolution and preservation of Antarctic diatoms and the effect on sediment thanatocoenses, *Quat. Res.*, 31, 288–308, 1989.
- Shepard, F. P., Glacial troughs of the continental shelves, *J. Geol.*, 39, 345–360, 1931.
- Shepard, F. P., *Submarine Geology*, 348 pp., Harper and Row, New York, 1948.
- Simpson, E. H., Measurement of diversity, *Nature*, 163, 688, 1949.
- Smith, M. J., Marine geology of the northwestern Weddell Sea and adjacent coastal fjords and bays: Implications for glacial history, Master's thesis, 250 pp., Rice Univ., Houston, Tex., 1985.
- Solheim, A., L. Russwurm, A. Elverhoi, and M. N. Berg, Glacial geomorphic features in the northern Barents Sea: Direct evidence for grounded ice and implications for the pattern of deglaciation and late glacial sedimentation, in *Glacimarine Environments: Processes and Sediments*, edited by J. A. Dowdeswell and J. D. Scourse, *Geol. Soc. Spec. Publ. London*, 53, 253–268, 1990.
- Stuiver, M., G. H. Denton, T. J. Hughes, and J. L. Fastook, History of the marine ice sheet in West Antarctica during the last glaciation: A working hypothesis, in *The Last Great Ice Sheets*, edited by G. H. Denton and T. J. Hughes, pp. 319–439, Wiley-Interscience, New York, 1981.
- Vorren, T. O., M. Hald, M. Edværset, and O. Lind-Hansen, Glacigenic sediments and sedimentary environments on continental shelves: General principals with a case study from the Norwegian Shelf, in *Glacial Deposits of Northwest Europe*, edited by J. Ehlers, pp. 61–73, A. A. Balkema, Rotterdam, Netherlands, 1983.

(Received February 29, 1992;
accepted May 26, 1992.)

PLIOCENE-PLEISTOCENE SEISMIC STRATIGRAPHY OF THE ROSS SEA: EVIDENCE FOR MULTIPLE ICE SHEET GROUNDING EPISODES

BELÉN ALONSO,¹ JOHN B. ANDERSON,² JOSÉ I. DÍAZ,¹ AND LOUIS R. BARTEK³

The distribution, morphology, and thickness of Pliocene-Pleistocene deposits on the Ross Sea continental shelf were mapped using high-resolution seismic reflection data acquired during the U.S. Antarctic Program 1990 cruise. Chronostratigraphic control is provided by Deep Sea Drilling Project (DSDP) leg 28 drill sites on the shelf. In the western Ross Sea, the Pliocene-Pleistocene section is relatively thin and is restricted mainly to the outer shelf. However, the Eastern Basin contains a relatively thick (up to 600 ms) and widespread Pliocene-Pleistocene section that has been subdivided into seven seismic units. On the basis of the original biostratigraphic work on core from DSDP site 271, the three lower units are Pliocene in age, and the youngest unit is Pleistocene in age. The age of the three middle units was not determined; the aggradational stacking pattern of these units indicates a Pleistocene age. The seismic units are separated by relatively smooth erosional surfaces and differ in thickness, lateral extent, and seismic reflection character. Numerous erosional surfaces, tens of kilometers wide and tens of meters deep, are interpreted as glacial troughs; these are similar in scale to modern troughs on the shelf that were carved by large ice streams. The troughs typically are filled with acoustically massive, wedge-shaped sedimentary bodies interpreted as subglacial deposits (till tongues). A variety of other seismic facies are recognized, and these are mainly attributed to glacial marine sedimentation. During the Pliocene the growth pattern of the continental shelf shifted from progradational to aggradational. This change was due to an increase in the frequency of grounding events and a corresponding decrease in accommodation space, resulting from higher-frequency sea level changes. The seven units reflect multiple ice sheet grounding events during which the ice sheet extended to the shelf break, followed by retreat from the shelf. These fluctuations in grounding line position indicate extreme variations in the Antarctic climate and sea level. Ice sheet grounding events do not require a polar climate; they could reflect subpolar to temperate shifts in climate.

INTRODUCTION

During Deep Sea Drilling Project (DSDP) leg 28, several drill sites were occupied on the Ross Sea continental shelf for the purpose of acquiring a record of the Antarctic's glacial history. Unfortunately, recovery at these sites was so poor that a detailed paleoclimatic reconstruction was not possible. This was true especially for the Pliocene-Pleistocene section because drilling took place in areas where the younger section is thin; leg 28 objectives focused on the older Tertiary section. The only other offshore sites in the Ross Sea region are the MSSTS 1 and

CIROS 1 and 2 sites in McMurdo Sound [Barrett and McKelvey, 1989]. These cores yielded a valuable record of East Antarctic glaciation; they did not provide information about the West Antarctic Ice Sheet glacial record.

The primary objective of the U.S. Antarctic Program 1990 (USAP 90) cruise was to augment the DSDP leg 28 sites by acquiring intermediate-resolution seismic reflection profiles through these sites. It was hoped that these profiles would provide direct evidence for or against ice sheet advance and retreat on the shelf and for or against temperate interglacial episodes. The timing of these events could then be constrained by the drill sites. A second objective of the cruise was to identify areas where future drilling might recover a relatively complete Pliocene-Pleistocene section that would allow detailed study of relationships between waxing and waning ice sheets on the continental shelf and global sea level changes. This paper provides a summary of the results

¹Instituto de Ciencias del Mar, CSIC, Paseo Nacional s/n, 08039 Barcelona, Spain.

²Department of Geology and Geophysics, Rice University, Houston, Texas 77251.

³Department of Geology, University of Alabama, Tuscaloosa, Alabama 35487.

of a detailed investigation of the Pliocene-Pleistocene portion of this record.

REGIONAL SETTING AND DRILL SITES

Ross Sea is a large marine embayment bound on one margin by the Transantarctic Mountains of East Antarctica and on the other by Marie Byrd Land of West Antarctica (Figure 1a) [Davey *et al.*, 1982]. Approximately 50% of the ice draining West Antarctica flows into the Ross embayment. As the ice flows toward the sea, it converges into a series of rapidly flowing ice streams (Figure 1a). Ross Ice Shelf, the world's largest ice shelf, lies seaward of the ice sheet grounding line.

The main physiographic features of the Ross Sea continental shelf are its great depth (average 500 m), rugged topography, and landward gradient. Three distinct rift basins, Victoria Land Basin, Central Trough, and Eastern Basin, occur on the shelf. Ross Ice Shelf covers the inner portion of the shelf, but the topography of this area has been revealed by airborne radar imaging [Bentley, 1969; Drewry, 1983]. A series of north-south oriented basins and ridges characterize the bathymetry of the shelf [Hayes and Frakes, 1975]. These features extend beneath the Ross Ice Shelf where they have a more northwest-southeast orientation [Drewry, 1983]. Hughes [1977] observed that the linear basins of the inner shelf correspond to the locations of modern ice streams. From this he inferred that the seaward continuations of these basins represent the former positions of ice streams during glacial maxima.

DSDP leg 28 occupied four drill sites. Three of these sites (sites 270, 271, and 272) were drilled along the southwestern edge of the Eastern Basin (Figure 1b). The total composite sedimentary section drilled at all three sites was about 1200 m. The oldest sedimentary deposits drilled include shallow marine glauconitic sandstone of late Oligocene age (25–26 Ma), based on K/Ar dates derived from glauconites. These deposits rest on continental basement rocks [Hayes and Frakes, 1975]. The sampled interval consists predominantly of poorly sorted glacial and glacial marine deposits which range in composition from massive diamictites to diatomaceous pebbly mudstones [Hayes and Frakes, 1975; Balshaw, 1981]. Site 271 is the only site where the expanded Pliocene section was sampled, so this site provides the only biostratigraphic control for seismic stratigraphic analysis. It should be noted that the biostratigraphic zonations designated during DSDP leg 28 were crude compared to present-day zonations; this site needs to be reexamined using more recent zonations. Such an analysis hopefully would provide better biostratigraphic detail so that the timing of events described in this paper could be better constrained.

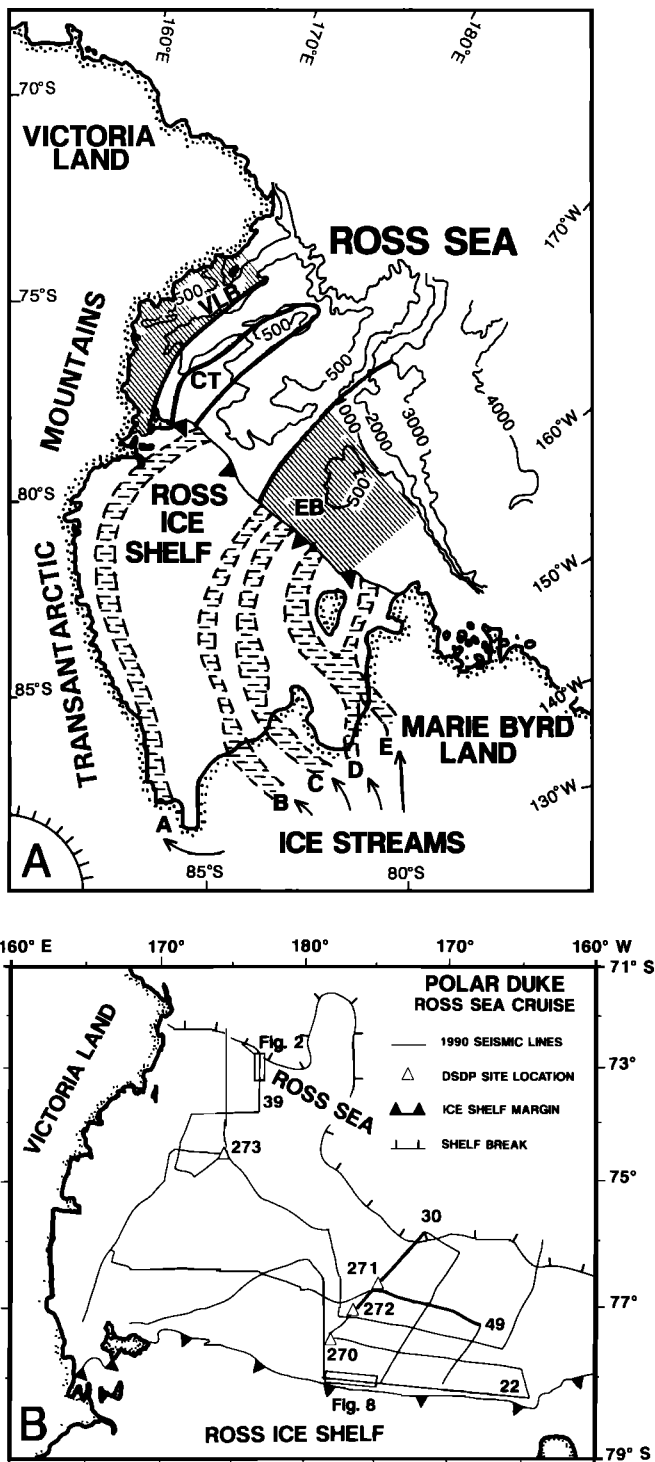


Fig. 1. Location of the study area: (a) generalized bathymetry of the Ross Sea (in meters), locations of ice streams [from Hughes, 1977], and the locations of major sedimentary basins [from Davey *et al.*, 1982] and (b) track lines of seismic reflection profiles and locations of DSDP leg 28 drill sites. The line segments highlighted are those referred to in other figures.

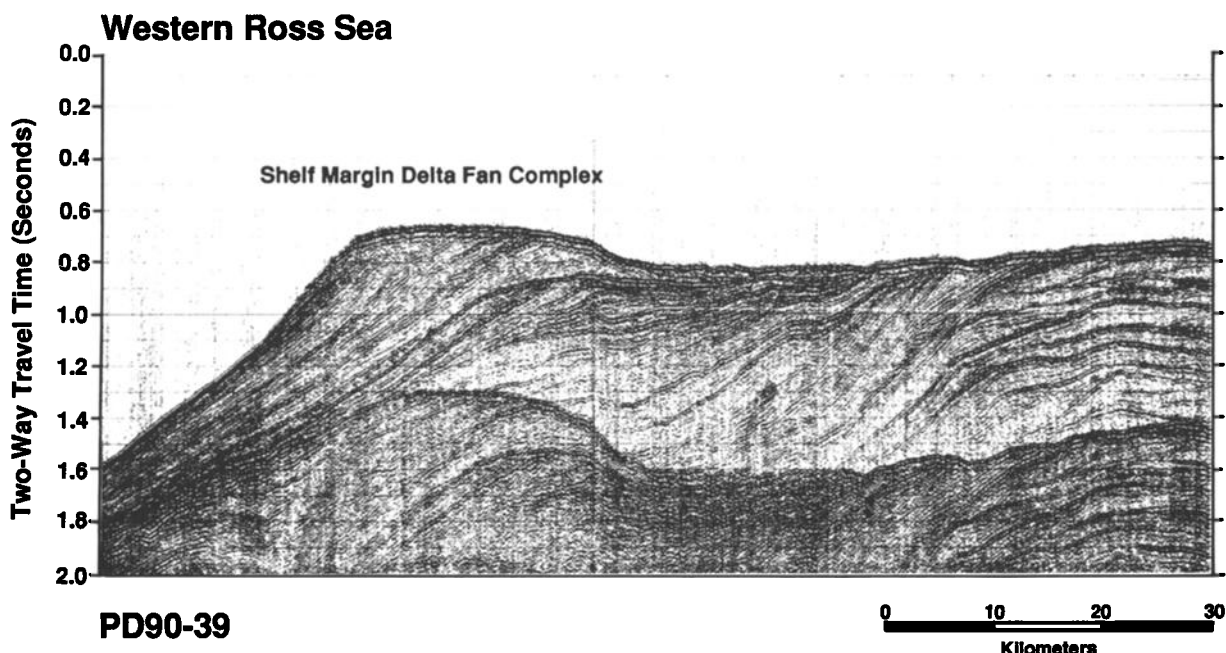


Fig. 2. Seismic profile PD 90-39 from the western Ross Sea (see Figure 1b for profile location) showing the abrupt seaward thickening of Pliocene-Pleistocene strata near the shelf break. This sequence is the product of erosion of late Miocene and younger deposits on the inner shelf.

Site 273, drilled on the outer shelf of western Ross Sea (Figure 1b), penetrated a thin (42.5 m) Pliocene-Pleistocene sequence. At this site a massive diamicton rests on a major unconformity and is overlain by diatomaceous glacial marine sediments. An unconformity within the Pliocene-Pleistocene section spanning approximately 2.8 to 0.65 Ma was reported by *Savage and Ciesielski* [1983].

METHODS

The data base for this study consists of approximately 6000 km of intermediate-resolution, single-channel seismic reflection profiles collected mainly with a 150-inch³ bubble-free air gun (Figure 1b). A 100-inch³ water gun was used during a brief period when the air gun was being serviced, but the two guns provided similar results in terms of stratigraphic resolution (5 to 8 m); the air gun provided subbottom penetration between 1.5 and 2.0 s, compared to 1.0 s for the water gun. The National Science Foundation chartered research vessel *Polar Duke* was used to acquire the data. Navigation was by the global positioning system (GPS) for approximately 20 hours per day and by transit satellite for the remaining time.

SEISMIC UNITS

Previous seismic records from Ross Sea record a widespread unconformity, the Ross Sea Unconformity (RSU), that was thought to mark the first advance of an ice sheet onto the continental shelf [*Houtz and Meijer*, 1970; *Houtz and Davey*, 1973; *Hayes and Davey*, 1975]. *Anderson and Bartek* [1992] now argue that ice sheets grounded on and eroded the continental shelf much earlier (late Oligocene to early Miocene). The age of the RSU has been a subject of controversy [*Hayes and Frakes*, 1975; *Kellogg et al.*, 1979]; the most recent work [*Savage and Ciesielski*, 1983] suggests that it represents an erosional event in the western Ross Sea that ended approximately 4.0 Ma. *Anderson and Bartek* [1992] demonstrate that the RSU is an amalgamation of several erosional surfaces and that the amount of erosion associated with this surface increases in an updip direction on the shelf.

Seismic data from western Ross Sea (west of approximately 180°) show that the Pliocene-Pleistocene section is very thin to absent, generally less than 0.1 s [*Karl et al.*, 1987; *Karl*, 1989] (this study), on the inner to middle shelf. On the outer shelf, north of DSDP site 273, the section thickens to 0.4 s (Figure 2). Given the

limited distribution of Pliocene-Pleistocene strata in the region, it is not possible to distinguish individual units.

The thickest Pliocene-Pleistocene section occurs within the Eastern Basin. Seismic records acquired during USAP 90 reveal seven seismic units within the Pliocene-Pleistocene section (Figure 3). On the basis of the biostratigraphic zonations for site 271, units VII, VI, and V are Pliocene in age and unit I is Pleistocene in age. Units IV, III, and II were sampled at site 271 but yielded few microfossils from which to establish their age. Units V through VII are progradational, whereas the four youngest units (I-IV) are aggradational (Figure 3). This change from progradation to aggradation possibly corresponds to a similar sequence stratigraphic change seen in other regions. The change is associated with higher-order sea level fluctuations of the Pleistocene [Haq *et al.*, 1987; Bartek *et al.*, 1991]. On the basis of this, a tentative age of Pleistocene has been assigned to units I through IV.

Smooth unconformities and semiregional, continuous high-amplitude reflectors generally define the boundaries between these units; however, these surfaces may be weaker, or occasionally absent, for limited distances (Figure 4). In most cases the boundaries between units are planar to subhorizontal when viewed in a dip section (Figure 3). Strike sections show broad erosional surfaces (tens of kilometers wide), similar in scale to the modern troughs of the region (Figure 4). The unconformities display both downlap terminations and a shift in onlap terminations. These combined characteristics imply that the hiatuses are of glacial origin.

Using the terminology defined by Mitchum *et al.* [1977], three main seismic reflection configurations can be discerned within the units: semitransparent (T), stratified (S), and chaotic (C) (Figure 5). The semitransparent configuration (T) is characterized by poorly defined or absent reflectors. The stratified configuration was subdivided into (1) planed parallel (S1), with flat, relatively high amplitude and regularly spaced reflectors; (2) divergent (S2), with reflectors commonly filling depressions; and (3) oblique (S3), with prograding clinoforms displaying steep-dipping strata terminated updip by toplap at a nearly flat surface. The chaotic seismic reflection configuration displays hyperbole (C1) or discontinuous and randomly oriented reflectors (C2) that commonly have a high-amplitude signal (Figure 5).

Figure 6 is an isopach map of the Pliocene-Pleistocene deposits in the eastern Ross Sea. The thickest strata occur in the Eastern Basin and on the outer shelf. This implies that the availability of accommodation space controls the distribution of these strata.

Unit VII, the oldest unit, is confined to the outer shelf (Figure 7). It is acoustically semitransparent and interfingers seaward with discontinuous stratified internal reflectors that display prograding clinoforms at the paleoshelf break. Unit VII has a maximum thickness of 60 ms near the shelf break (Figure 3).

Units V and VI are basinal in extent and together reach a thickness of 200 ms at the paleoshelf break. These units display a complex seismic signature, including chaotic, semitransparent, continuous/discontinuous stratified, oblique stratified, and sigmoid stratified reflector patterns (Figure 5). The chaotic and discontinuous reflector patterns are associated with, and occur within, broad channels (Figure 8).

Seismic units IV, III, and II are confined to the western sector of the Eastern Basin (Figure 7). Units IV and III display similar acoustic signature patterns, consisting of chaotic reflectors in the western portion of the basin that grade laterally into continuous reflectors in the eastern portion of the basin. Both units have a maximum thickness of 40 ms at the paleoshelf break. Unit II, reaching a 50-ms thickness, displays semitransparent to faintly chaotic reflection patterns. Troughs within this unit display chaotic and discontinuous reflection patterns, are U-shaped, and range from 1.0 to 6.0 km in width.

Unit I is basinal in extent (Figure 7). It is characterized by high-amplitude and continuous coherent reflection patterns; individual reflectors are traceable over distances of many tens of kilometers. The thickness of the unit (average 30 ms) varies only slightly across the basin. Unit I has broad erosional surfaces (glacial troughs), massive wedges (till tongues) and wedge-shaped units with clinoforms (subglacial deltas). A prominent, north-south oriented ridge, 50 to 75 ms thick and extending for a distance of 190 km, occurs within this unit near the center of the basin (Figure 4, inset). The ridge displays a complex reflector pattern with chaotic, stratified continuous/discontinuous and oblique stratified reflectors.

DISCUSSION

The genetic interpretation of seismic units is based on their acoustic signature, external shape, and limited lithological data from DSDP site 271. Individual units display features such as complex internal reflector patterns, discontinuous and often hyperbolic reflector patterns, erosional surfaces, and massive, wedge-shaped intervals that are characteristic of subglacial deposits [King and Fader, 1986; Karl *et al.*, 1987; Stoker, 1990; Vorren *et al.*, 1990; Solheim *et al.*, 1990; Belknap and Shipp, 1991; King *et al.*, 1991]. The broad erosional surfaces seen in strike lines (Figure 4) and associated massive units imply glacial

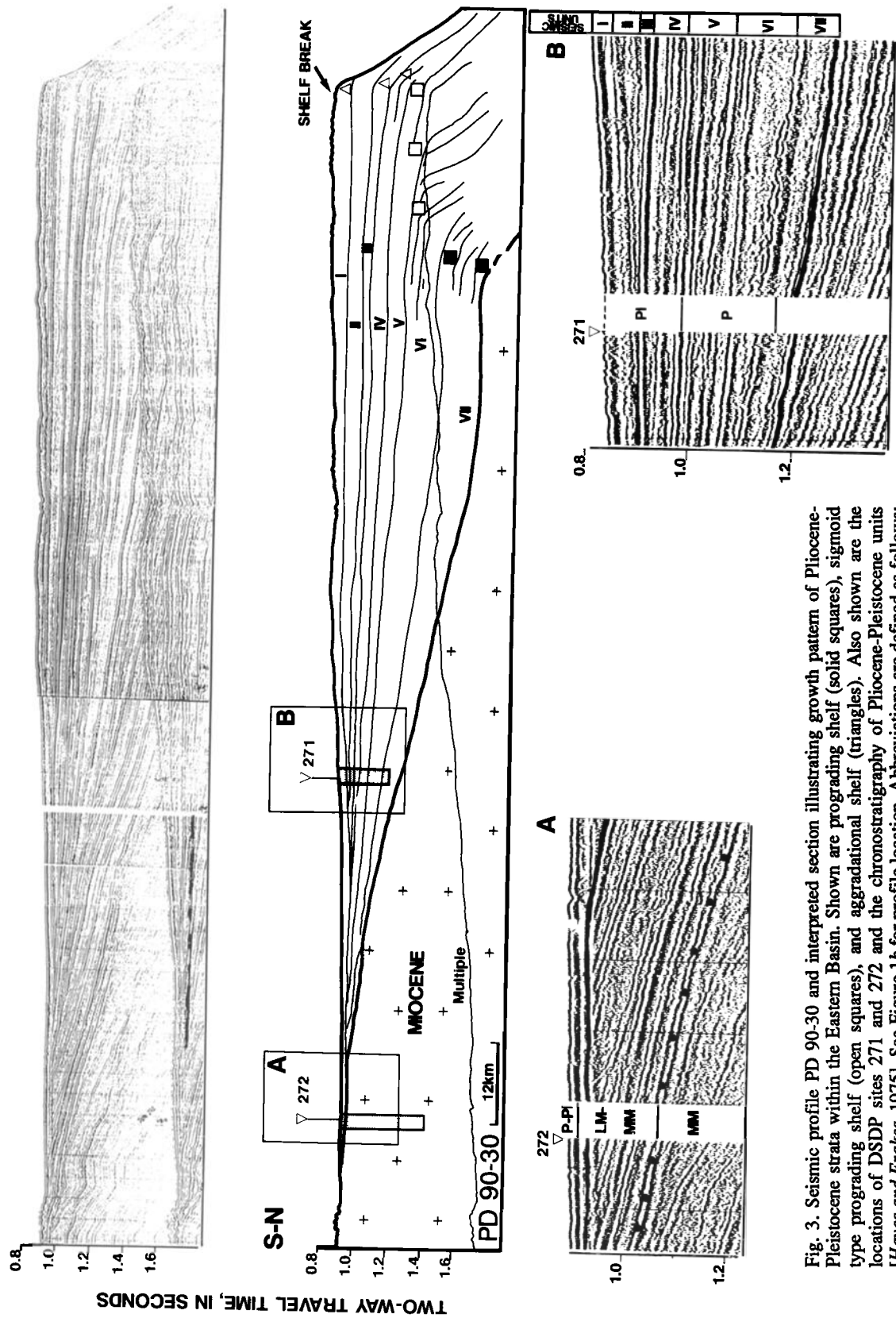


Fig. 3. Seismic profile PD 90-30 and interpreted section illustrating growth pattern of Pliocene-Pleistocene strata within the Eastern Basin. Shown are prograding shelf (solid squares), sigmoid type prograding shelf (open squares), and aggradational shelf (triangles). Also shown are the locations of DSDP sites 271 and 272 and the chronostratigraphy of Pliocene-Pleistocene units [Hayes and Frakes, 1975]. See Figure 1b for profile location. Abbreviations are defined as follows: L.M., late Miocene; M.M., mid-Miocene; P, Pliocene; P-P1, Pliocene-Pleistocene; and P1, Pleistocene. The heavy line marks the Miocene-Pliocene boundary.

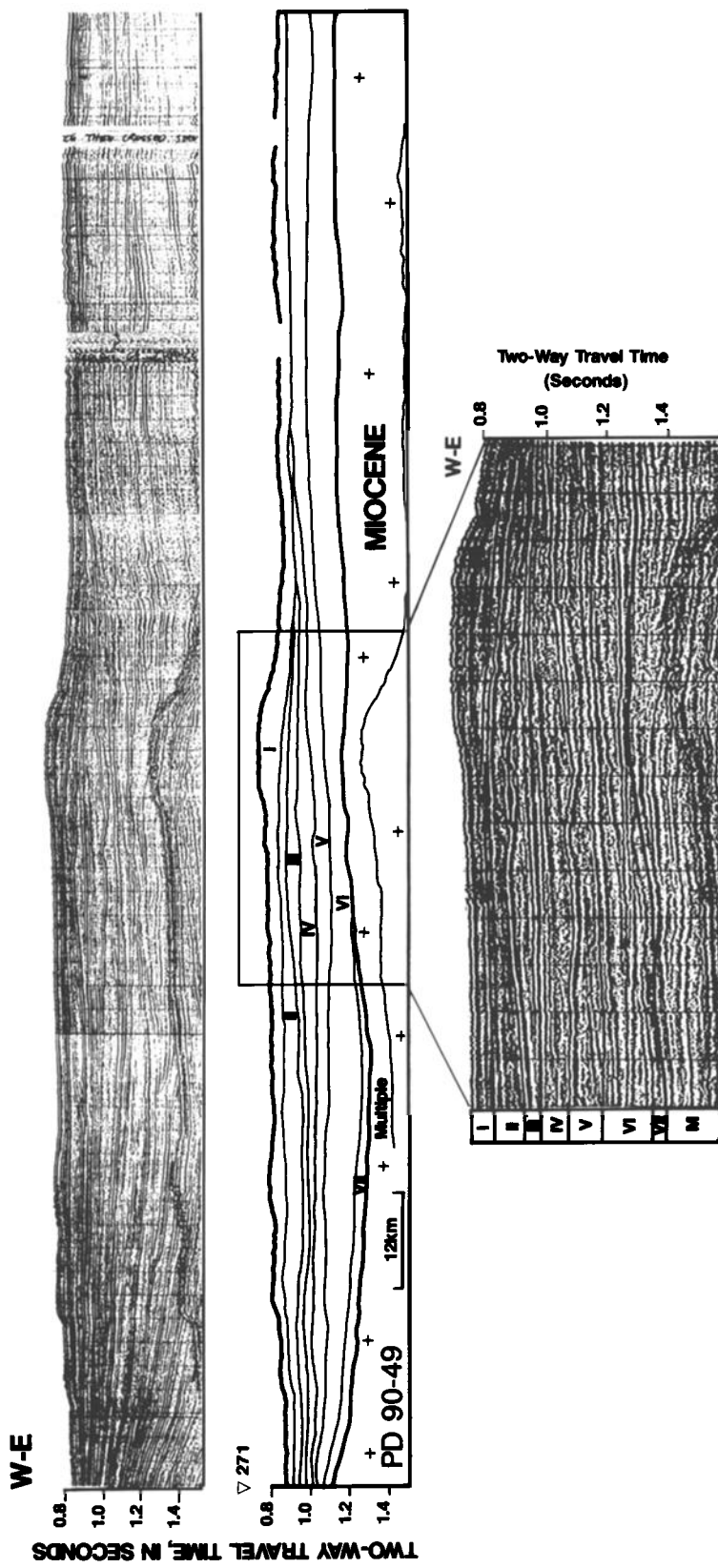


Fig. 4. Seismic profile PD 90-49, a strike line from the outer shelf, and interpreted section. This profile shows the regional erosional surfaces between Pliocene-Pleistocene seismic units. Note the sedimentary ridge within unit 1. Inset shows both the complex internal structure of the sedimentary ridge and the erosional surfaces within this feature. Letter M designates the Miocene section. See Figure 1b for profile location.

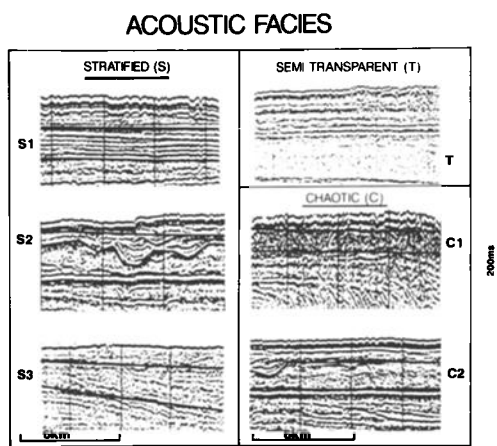


Fig. 5. Three main types of acoustic signatures identified in the study area: S, stratified (S1, continuous parallel; S2, continuous divergent; S3, oblique); T, semitransparent; C, chaotic (C1, hyperbolic; C2, lacking hyperbole).

erosion and deposition by ice masses that were similar in scale to modern ice streams of the region. The U-shaped channels in units V and VI (Figure 8) are thought to result from erosion by subglacial meltwater streams as indicated by the presence of crosscutting comparable to subglacial channel deposits described by Armentrout [1983] and Ashley *et al.* [1985].

Units I, II, and III contain massive seismic facies interpreted to be subglacial deposits. The massive facies grade laterally into well-stratified reflectors that have onlap terminations. The stratified units are interpreted to be glacial marine deposits. A prominent sedimentary ridge within unit I (Figure 4) possibly is a morainal ridge that developed parallel to ice flow and formed at the confluence of ice streams C and D during the last glacial maximum.

DSDP site 271 is the only location where an expanded Pliocene-Pleistocene section was sampled (Figure 3). Unfortunately, recovery at this site was poor (7% [Hayes and Frakes, 1975]). Thus few correlations between lithologic and seismic units could be made. The boundary between seismic unit V and seismic unit VII corresponds to a diatomaceous bed resting on massive diamictite, which indicates a glacial to interglacial transition [Balshaw, 1981]. The interval of seismic units V and IV was not sampled. The base of unit III correlates with a semilithified, massive diamictite at site 271, which supports a subglacial origin for this unit. Unit II was not sampled. The top of seismic unit I, penetrated by numerous piston cores, is composed of overcompacted diamictite that is interpreted as till [Kellogg *et al.*, 1979; Anderson *et al.*, 1980].

The smooth erosional surfaces between the different seismic units in the Eastern Basin are very widespread, implying a glacial origin and representing several ice sheet advances onto the continental shelf [Alonso *et al.*, 1991]. A similar stratal pattern exists in the Barents Sea, where erosion surfaces have been correlated with sudden increases in shear strength of cored deposits caused by expansion of the Baltic Ice Sheet [Vorren *et al.*, 1990].

The restricted distribution of units II, III, IV, and VII (Figure 7) implies deposition from a point source, possibly the convergence of ice streams B and C (Figure 1a). Similar geometry has been described by Kuvaas and Kristoffersen [1990] for glaciogenic sediments of Crary Fan on the southern Weddell Sea margin. In contrast, units I, V, and VII are of basinal extent and are thickest at the shelf break (Figure 7). This implies a line source for sediments comprising these units. Erosion also has played an important role in regulating the distribution of Pliocene-Pleistocene strata on the shelf.

During the time the sediments of units V, VI, and VII were deposited, the shelf prograded some 25 km (Figure 3). A period of shelf aggradation (units I through IV) followed. By comparison with the Cenozoic sedimentary sequences on other Antarctic continental margins, the Pliocene-Pleistocene strata of the Eastern Basin are equivalent to the type I progradational sequence of Cooper *et al.* [1990]. However, the seismic records show that the growth pattern of the Ross Sea strata shifted from progradational to aggradational, even though the ice sheet continued to ground on the continental shelf (Figure 9). We concur with Bartek *et al.* [1991], who argue that the overall stacking pattern of these strata has been influenced

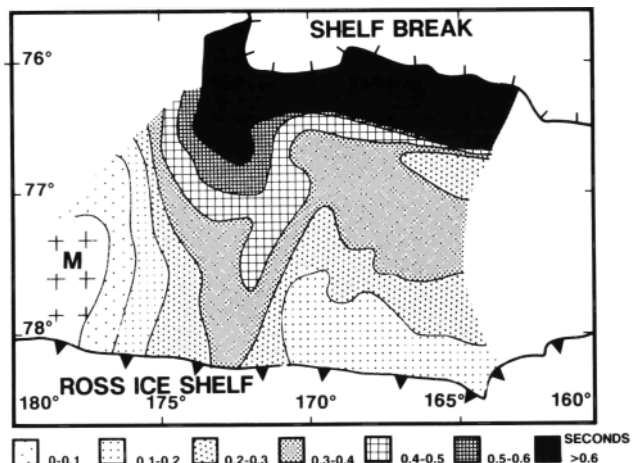


Fig. 6. Isopach map of Pliocene-Pleistocene strata in the Eastern Basin. M refers to Miocene outcrop.

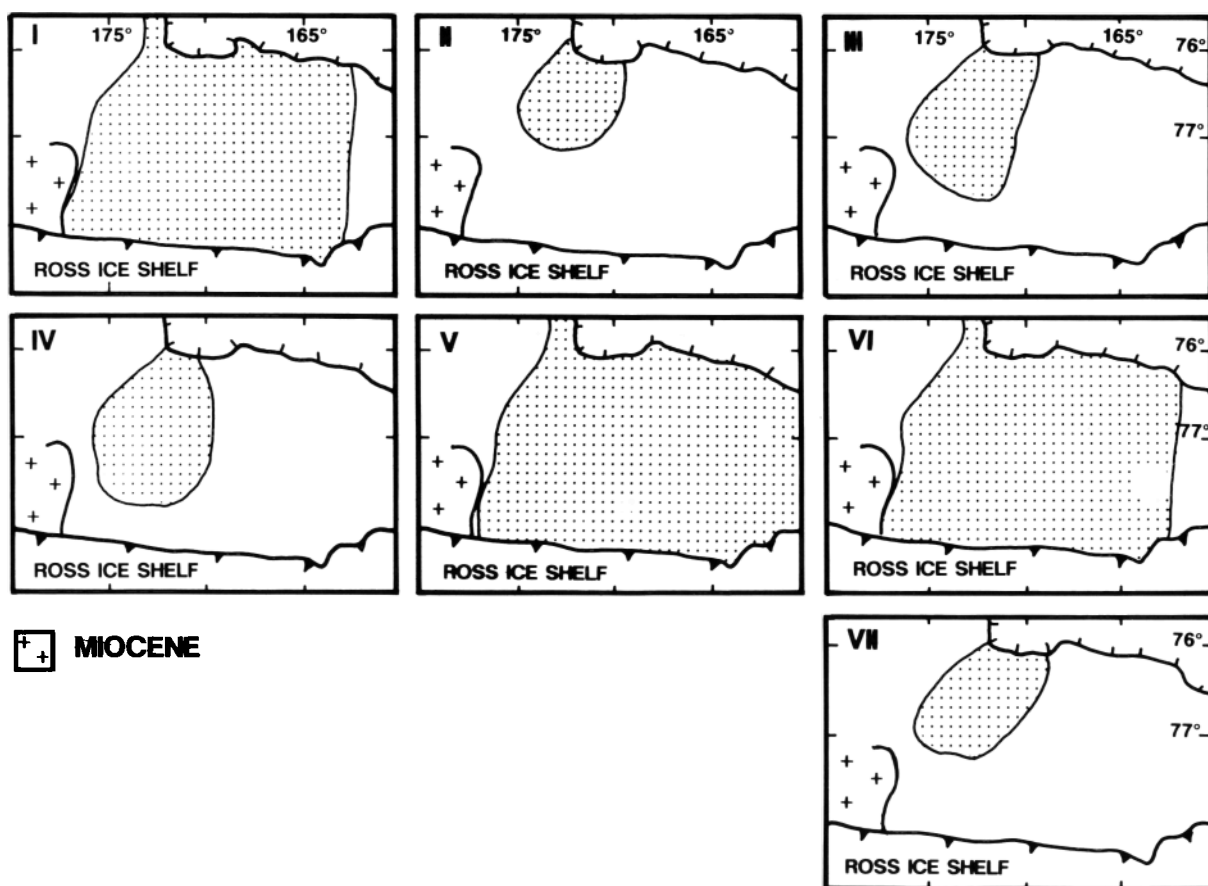


Fig. 7. Areal distribution of each of the seven Pliocene-Pleistocene seismic units in the Eastern Basin from youngest (I) to oldest (VII).

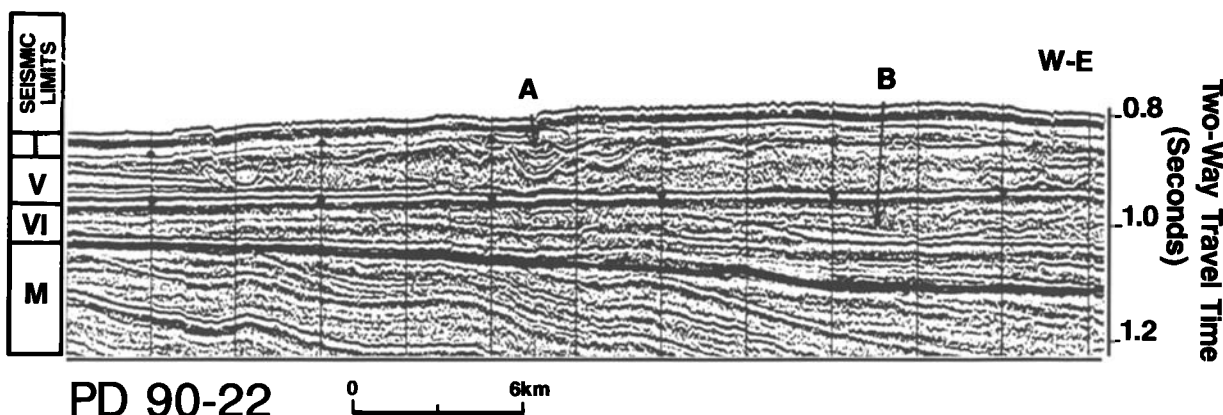


Fig. 8. Two types of incised valleys on the shelf. The first type (A) is characterized by U-shaped profiles and is infilled with strongly reflective units. These are perhaps subglacial tunnel valleys. The second type (B) is broader than the first and is infilled with acoustically massive and chaotic units. These are interpreted as small glacial troughs. See Figure 1b for profile location.

predominantly by changes in the frequency of eustatic cycles. It is well established that marine ice sheets are sensitive to rising and falling sea level. As the rate of sea level rise and fall increased in the Pleistocene [Haq *et al.*, 1987], the longevity of ice sheet grounding events diminished and delivery of sediment to the outer shelf and slope significantly decreased, resulting in the observed change from a progradational to an aggradational shelf.

There is mounting evidence that the Pliocene was a time of extreme climatic variability in Antarctica, based on the discovery of East Antarctic-derived marine diatoms and *Nothofagus* plant fossils in

Pliocene tills of the Sirius Group [Webb and Harwood, 1991]. The evidence presented in this paper is strongly in favor of multiple ice sheet advance and retreat phases during the Pliocene-Pleistocene. Grounding of ice sheets on the continental shelf does not require a polar climate and is not inconsistent with climates warmer than the present day during the Pliocene. During the last glacial maximum, grounded ice sheets existed on the Pacific and Atlantic margins of North America, as far south as the Puget Lowlands of Washington on the west coast [Domack, 1983; Booth, 1987] and the Gulf of Maine on the east coast [Belknap and Shipp, 1991], but these areas are not

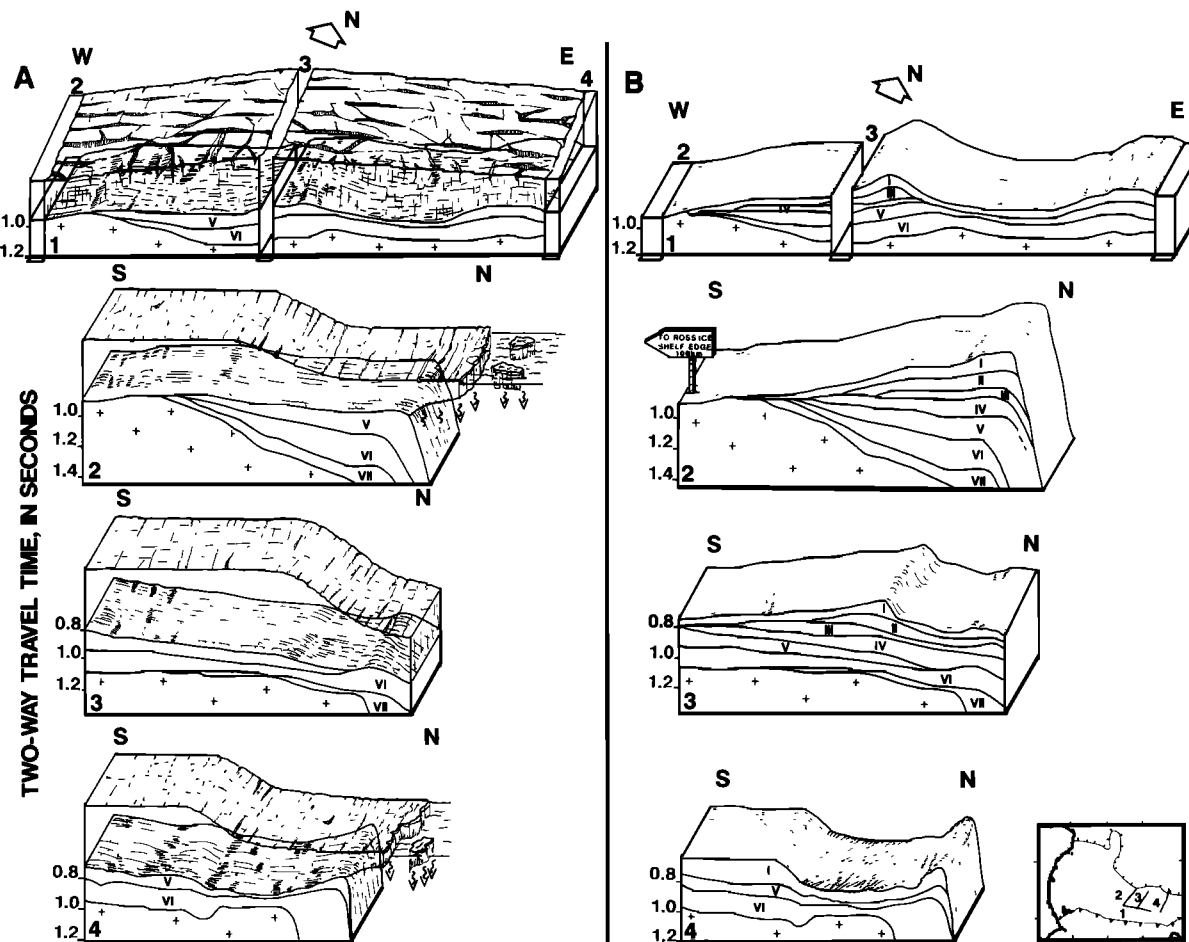


Fig. 9. Block diagrams showing how glacial erosion and deposition resulted in observed stacking order of seven seismic units in the Eastern Basin. The three sections cutting block diagrams 1A and 1B and labeled 2, 3, and 4 are illustrated by the block diagrams 2, 3, and 4, respectively. (a) Late Pliocene to early Pleistocene model for the advance of the Ross Ice Sheet to the continental shelf edge (glacial maximum) and (b) model showing the distribution of seismic units on the shelf following the most recent retreat of the ice sheet from the continental shelf.

believed to have experienced polar climate conditions. However, little direct evidence of a warm (temperate) interglacial climate during the Pliocene-Pleistocene has been recovered (i.e., low-stand incised fluvial valleys, shelf margin deltas, high-stand deltas).

CONCLUSIONS

Pliocene-Pleistocene strata of the eastern Ross Sea are interpreted to be the product of multiple (at least seven) ice sheet grounding episodes. During these events the West Antarctic Ice Sheet extended to the shelf edge. The thickest strata occur in the Eastern Basin and on the outer shelf. Pliocene-Pleistocene strata are much thinner on the western shelf where ice sheets eroded more deeply, removing most of the mid-Miocene and younger section and redepositing these sediments on the shelf edge and slope.

Within the Eastern Basin the older seismic units are mainly progradational, whereas the younger sequences are aggradational. This change in stratal geometry is believed to have resulted from an increase in the frequency of sea level rise and fall, which prompted more frequent, but short-lived, episodes of ice sheet grounding on the shelf. This record of ice sheet expansion and contraction during the Pliocene-Pleistocene is consistent with models calling for extreme climatic variability during that period. It does not require that the climate was as cold (polar) as at present. Our data provide no direct evidence (i.e., low-stand incised fluvial valleys, shelf margin deltas, and high-stand fluvial deltas) for warm (temperate) interglacial conditions during the Pliocene-Pleistocene.

A rich history of West Antarctica's climatic and glacial history resides in the northern sector of the Eastern Basin and awaits future drilling. Also, more detailed biostratigraphic work on DSDP site 271 could provide better age constraints on the events described in this paper.

Acknowledgments. We would like to thank R. D. Powell and E. W. Domack for helpful reviews of this paper. This research was funded by the National Science Foundation, Division of Polar Programs, under grant NSF-DPP 88-18523 to J.B.A. We wish to thank the crew of the R/V *Polar Duke* for their enthusiastic support during the USAP 90 cruise. Participation of B.A. and J.I.D. in the cruise was funded by the Comision Interministerial de Ciencia y Tecnologia of Spain under grant ANT 89-0817-E.

REFERENCES

- Alonso, M. B., J. B. Anderson, J. I. Diaz, and L. R. Bartek, Plio-Quaternary seismic stratigraphy of Ross Sea Eastern Basin (Antarctica): Implications to glacial history and basin evolution (abstract), Annual Meeting, Am. Assoc. of Pet. Geol., Tulsa, Okla. 1991.
- Anderson, J. B., and L. R. Bartek, Cenozoic glacial history of the Ross Sea revealed by intermediate resolution seismic reflection data combined with drill site information, in *The Antarctic Paleoenvironment: A Perspective on Global Change*, *Antarct. Res. Ser.*, part 1, vol. 56, A, edited by J. P. Kennett and D. Warnke, pp. 231-263, AGU, Washington, D. C., 1992.
- Anderson, J. B., D. D. Kurtz, E. W. Domack, and K. M. Balshaw, Glacial and glacial marine sediments of the Antarctic continental shelf, *J. Geol.*, 88, 399-414, 1980.
- Armentrout, J. M., Glacial lithofacies of the Neogene Yakataga Formation, Robinson Mountains, southern Alaska Coast Range, in *Glacial-Marine Sedimentation*, edited by B. F. Molnia, pp. 629-665, Plenum, New York, 1983.
- Ashley, G. M., J. Shaw, and N. D. Smith, Glacial sedimentary environments, *Short Course Notes 16*, 245 pp., Society of Paleontologists and Mineralogists, Tulsa, Okla., 1985.
- Balshaw, K. N., Antarctic glacial chronology reflected in the Oligocene through Pliocene sedimentary section in the Ross Sea, Ph.D. dissertation, 140 pp., Rice Univ., Houston, Tex., 1981.
- Barrett, P. J., and B. C. McKelvey, Stratigraphy, in *Antarctic Cenozoic History from the MSSTS-1 Drillhole, McMurdo Sound*, edited by P. J. Barrett, *Bull. 237*, pp. 9-51, Sci. and Inf. Cent., Dep. of Sci. and Ind. Res., Wellington, N. Z., 1989.
- Bartek, L. R., P. R. Vail, J. B. Anderson, P. A. Emmet, and S. Wu, Effect of Cenozoic ice sheet fluctuations in Antarctica on the stratigraphic signature of the Neogene, *J. Geophys. Res.*, 96, 6753-6778, 1991.
- Belknap, D. F., and C. R. Shipp, Seismic stratigraphy of glacial marine units, Maine inner shelf, in *Glacial Marine Sedimentation: Paleoclimatic Significance*, edited by J. B. Anderson and G. M. Ashley, *Spec. Pap. Geol. Soc. Am.*, 261, 137-158, 1991.
- Bentley, C. R., Ice thickness and physical characteristics of the Antarctic Ice Sheet, *Antarct. Map Folio Ser.*, folio 2, Am. Geogr. Soc., New York, 1969.
- Booth, D. B., Timing and processes of deglaciation along the southern margin of the Cordilleran ice sheet, in *The Geology of North America*, vol. K-3, *North America and Adjacent Oceans During the Last Deglaciation*, edited by W. F. Ruddiman and H. E. Wright, Jr., pp. 71-90, Geological Society of America, Boulder, Colo., 1987.
- Cooper, A. K., P. J. Barrett, V. V. Traube, K. Hinz, and H. Stagg, Prograding sedimentary sequences of the Antarctic continental margin, *U.S. Geol. Surv. Open File Rep.*, 90-309, 109-118, 1990.
- Davey, F. J., D. J. Bennett, and R. E. Houtz, Sedimentary basins of the Ross Sea, Antarctica, *N. Z. J. Geol. Geophys.*, 25, 245-255, 1982.
- Domack, E. W., Facies of late Pleistocene glacial-marine sediments on whidbey Island, Washington: An isostatic glacial-marine sequence, in *Glacial-Marine Sedimentation*, edited by B. F. Molnia, pp. 535-570, Plenum, New York, 1983.

- Drewry, D. J., Antarctica: Glaciological and geophysical folio, 9 sheets, Scott Polar Res. Inst., Univ. of Cambridge, Cambridge, England, 1983.
- Haq, B. L., J. Hardenbol, and P. R. Vail, Chronology of fluctuating sea levels since the Triassic, *Science*, 235, 1156–1167, 1987.
- Hayes, D. E., and F. J. Davey, Textural characteristics of Cenozoic preglacial and glacial sediments at site 270, Ross Sea, Antarctica, *Initial Rep. Deep Sea Drill. Proj.*, 28, 757–767, 1975.
- Hayes, D. E., and L. A. Frakes, General synthesis: Deep Sea Drilling Project 28, *Initial Rep. Deep Sea Drill. Proj.*, 28, 919–942, 1975.
- Houtz, R. E., and F. J. Davey, Seismic profiler and sonobuoy measurements in the Ross Sea, Antarctica, *J. Geophys. Res.*, 78, 3448–3468, 1973.
- Houtz, R. E., and R. Meijer, Structure of the Ross Sea shelf from profiler data, *J. Geophys. Res.*, 75, 6593–6597, 1970.
- Hughes, T., West Antarctic ice streams, *Rev. Geophys.*, 15, 1–46, 1977.
- Karl, H. A., High-resolution seismic-reflection interpretations of some sediment deposits, Antarctic continental margin: Focus on the western Ross Sea, *Mar. Geol.*, 85, 205–223, 1989.
- Karl, H. A., E. Reimnitz, and B. D. Edwards, Extent and nature of Ross Sea unconformity in the western Ross Sea, Antarctica, in *The Antarctic Continental Margin: Geology and Geophysics of the Western Ross Sea*, Earth Sci. Ser., vol. 5B, edited by A. K. Cooper and F. J. Davey, pp. 77–92, Circum-Pacific Council for Energy and Mineral Resources, Houston, Tex., 1987.
- Kellogg, T. B., R. S. Truesdale, and L. E. Osterman, Late Quaternary extent of the West Antarctic Ice Sheet: New evidence from Ross Sea cores, *Geology*, 7, 249–253, 1979.
- King, L. H., and G. Fader, Wisconsinan glaciation of the continental shelf, southeast Atlantic, Canada, *Geol. Surv. Bull. Geol. Soc. Can.*, 363, 72 pp., 1986.
- King, L. H., K. Rokoengen, G. B. J. Fader, and T. Gunleiksrud, Till-tongue stratigraphy, *Geol. Soc. Am. Bull.*, 103, 637–659, 1991.
- Kuvaas, B., and Y. Kristoffersen, The seismic stratigraphy of glaciogenic sediments along the Weddell Sea margin, *U. S. Geol. Surv. Open File Rep.*, 90-309, 171–176, 1990.
- Mitthem, R. M., Jr., P. R. Vail, and J. B. Sangree, Seismic stratigraphy and global changes of sea level, 6, Stratigraphic interpretation of seismic reflection patterns in depositional sequences, *AAPG Mem.*, 26, 117–133, 1977.
- Savage, M. L., and P. F. Ciesielski, A revised history of glacial sedimentation in the Ross Sea region, in *Antarctic Earth Science, Proceedings of the Fourth International Symposium on Antarctic Earth Science*, edited by R. L. Oliver, P. R. James, and J. B. Jago, pp. 555–559, Australian Academy of Science, Canberra, Australia, 1983.
- Solheim, A., L. Russwurm, A. Elverhoi, and B. Nyland, Glacial geomorphic features in the northern Barents Sea: Direct evidence for grounded ice and implications for the pattern of deglaciation and late glacial sedimentation, in *Glacimarine Environments: Processes and Sediments*, edited by J. A. Dowdeswell and J. D. Scourse, *Geol. Soc. Spec. Publ. London*, 53, 253–268, 1990.
- Stoker, D. M., Glacially-influenced sedimentation in the Hebridean slope, northwestern United Kingdom continental margin, in *Glacimarine Environments: Processes and Sediments*, edited by J. A. Dowdeswell and J. D. Scourse, *Geol. Soc. Spec. Publ. London*, 53, 349–362, 1990.
- Vorren, T. O., E. Lebesbye, and K. B. Larsen, Geometry and genesis of the glaciogenic sediments in the southern Barents Sea, in *Glacimarine Environments: Processes and Sediments*, edited by J. A. Dowdeswell and J. D. Scourse, *Geol. Soc. Spec. Publ. London*, 53, 269–288, 1990.
- Webb, P. N., and D. M. Harwood, Late Cenozoic glacial history of the Ross embayment, Antarctica, *Quat. Sci. Rev.*, 10, 215–223, 1991.

(Received December 27, 1991;
accepted June 16, 1992.)

AN ANALYSIS OF GRAVITY MEASUREMENTS ON THE ROSS ICE SHELF, ANTARCTICA

LAWRENCE L. GREISCHAR,¹ CHARLES R. BENTLEY, AND LARRY R. WHITING²

Geophysical and Polar Research Center, University of Wisconsin-Madison, Madison, Wisconsin 53706

During the Ross Ice Shelf Geophysical and Glaciological Survey (RIGGS) field program, between 1973 and 1978, gravity measurements were made at 181 sites on a 55-km grid covering the Ross Ice Shelf and along 350 km of profile lines at base camps. These data and earlier gravity observations on the ice shelf have been reduced using the gravity datum International Gravity Standardization Net 1971 and Geodetic Reference System 1967. Marine gravity data, which have been approximately adjusted to the new datum and reference system, have been used to extend coverage to the edge of the Ross Sea continental shelf. Free-air, Bouguer, and Airy isostatic anomaly maps reveal linear anomalies paralleling the Transantarctic Mountains as a dominant feature. Block faulting due to extension between East Antarctica and West Antarctica is a likely tectonic source for these features. Modeling of local gravity observations made at the five RIGGS base camps revealed probable faulting at every camp. Since location of base camps was not based upon any knowledge of geological structure, the implication is that the seafloor beneath the entire Ross Ice Shelf has been tectonically affected. The correspondence of modeled local structures to regional trends suggests that they are the result of regional tectonic activity. A spectral analysis technique applied to the free-air anomaly, Bouguer anomaly, and bathymetry maps of the Ross embayment revealed that relatively short wavelength (<500 km) topographic loads appear isostatically uncompensated. For these features, which reflect the dominant ridge-trough submarine topography of the embayment, this presumably means that rifting has produced lower crustal densities under the troughs than under the ridges. An apparently negative overcompensation at the longer wavelengths, we believe, is due to glacio-isostatic imbalance. Regional free-air gravity anomalies in the Ross embayment are everywhere negative: they decrease (numerically) from a minimum of -28 mGal along the Siple Coast to -18 mGal in the grid easternmost Ross Sea. The observed field is even more negative than the low-order terms of the satellite-derived free-air anomaly field; the difference increases with distance into the Ross embayment. We interpret this as reflecting the mass deficit left by the Holocene retreat of a more extended grounded ice sheet. A simple exponential model of crustal rebound has been used to derive isochrons of ice retreat. The result generally agrees both spatially and temporally with retreat models based on ice sheet dynamics.

CONTENTS

Introduction	106
Description of the RIGGS program	106
Other gravity measurements on and near the	
Ross Ice Shelf	106
Data Collection and Reduction	106
Field procedures	106
Measurement of gravity and ancillary data	108
Computation of gravity anomalies	112
Gravity anomaly maps	114

Local gravity gradients	123
Modeling of Local Gravity Anomalies	124
Gravity modeling programs	124
Local gravity modeling	124
Discussion of local gravity models	137
Analysis of Isostasy in the Ross Embayment	138
Spatial frequency spectra of gravity and bathymetry	138
Gravity admittance function	141
Speculations on glaciological implications of	
isostatic gravity	143
Isostatic equilibrium grounding line between the West	
Antarctic inland ice sheet and the Ross Ice	
Shelf	151
Summary	151
Appendix	153

¹Now at Department of Meteorology, University of Wisconsin-Madison, Madison, Wisconsin 53706

²Now at P.O. Box 1021, Pocatello, Idaho 83204.

INTRODUCTION

The Ross Sea and Ross Ice Shelf together with the adjacent part of interior West Antarctica between Marie Byrd Land and the Transantarctic Mountains form the Ross embayment, which penetrates more than 1000 km into the Pacific sector of the Antarctic continent. The Ross embayment is a boundary zone between the old continental craton of East Antarctica and the geologically younger mountains of Marie Byrd Land. Study of this area is integral to understanding the evolution of the whole Antarctic plate. In this work we report on gravity studies on the Ross Ice Shelf and integrate the results with other work in the Ross embayment.

Unless otherwise specified, grid coordinates are used throughout this paper. In grid coordinates, meridians are parallel to the prime meridian, and grid north is toward Greenwich, England, i.e., toward the top of an Antarctic map with standard orientation. All our maps have that same orientation.

Description of the RIGGS Program

The Ross Ice Shelf Geophysical and Glaciological Survey (RIGGS) program was an airlifted survey supported by Twin Otter aircraft. Flight operations were carried out over four austral summer seasons (RIGGS I: 1973–1974; RIGGS II: 1974–1975; RIGGS III: 1976–1977; and RIGGS IV: 1977–1978) from four base camps (BC, RI, Q13, and C-16) strategically located on the ice shelf (see Figure 1). In addition, local experiments were carried out at J9DC, the site of the Ross Ice Shelf Project drilling through the ice shelf. Camp J9DC was one of three seasonal camps within 2 km of each other at RIGGS station J9 [Bentley, 1984]. Measurements at a typical geophysical field station comprised radar soundings of ice thickness, seismic soundings of water depth, and gravity measurements. Gravity measurements were made at 181 sites spread at intervals of approximately 55 km (one half of a grid degree) across the Ross Ice Shelf (for specifics, see Bentley [1984]).

Other Gravity Measurements on and Near the Ross Ice Shelf

Several oversnow traverses have crossed parts of the Ross Ice Shelf since the beginning of the International Geophysical Year (see the map in the work of Bentley [1984]). Between 1957 and 1960, the Ross Ice Shelf Traverse (1957–1958), the first Victoria Land Traverse (1985–1959), and the Discovery Deep Traverse (1960) were completed; each included gravity measurements on the ice shelf. Results from

these traverses were given for the ice shelf by Crary *et al.* [1962]. Bennett [1964] further analyzed the gravity data from these traverses and also considered data collected along the Little America Station to Byrd Station Trail. Gravity profiles across eight outlet glaciers through the Transantarctic Mountains at their junction with the ice shelf were presented by Giovinetto *et al.* [1966].

During the austral summers of 1961–1962 and 1962–1963, geophysical studies were carried out on Roosevelt Island (Figure 1), a large ice rise in the grid southwestern part of the ice shelf. Roosevelt Island is 120 km long and 70 km wide, nearly oval in shape, and rises to 500 m above the floating ice that surrounds it. Geophysical studies were part of a program to study the ice flow of this small ice cap. Gravity, magnetic, and seismic measurements made along traverse lines covering Roosevelt Island are summarized in an unpublished manuscript by C. R. Bentley and M. Hochstein (1965).

Marine gravity data were collected in the Ross Sea on cruises 32, 51, and 52 of the USNS *Eltanin* [Hayes *et al.*, 1972, 1978] (Figure 1). Extensive additional data in the grid easternmost Ross Sea (the Victoria Land basin) [Cooper and Davey, 1987] have not been incorporated into our study because the minor effect they would have on the overall gravity picture of the Ross embayment did not seem to us to warrant the large additional computational effort that would have been required to redo all our analyses.

DATA COLLECTION AND REDUCTION

Field Procedures

Two LaCoste and Romberg model G geodetic gravimeters (G-1 and G-19) were used during all four RIGGS seasons. The power required by these meters to maintain a constant internal temperature and to operate the reading light was provided by 12-V rechargeable nickel-cadmium batteries. In addition, jumper cables were used for connection to storage

Fig. 1. (opposite) Map of the Ross embayment showing the locations of gravity measurements and tracks of cruises of the USNS *Eltanin* in the Ross Sea. RIGGS stations are denoted by small solid circles; large solid circles are base camps. Station J9 is a composite station that includes J9DC. Open circles and crosses indicate points of previous surveys. Free-air and Bouguer anomalies have been calculated at all points shown. Cruise tracks are from Hayes *et al.* [1972, 1978]. Names of geographic features referred to in the text are also shown. The grid coordinate system in this and all subsequent maps has its origin at the south pole; the 0° longitude line runs toward Greenwich, England.

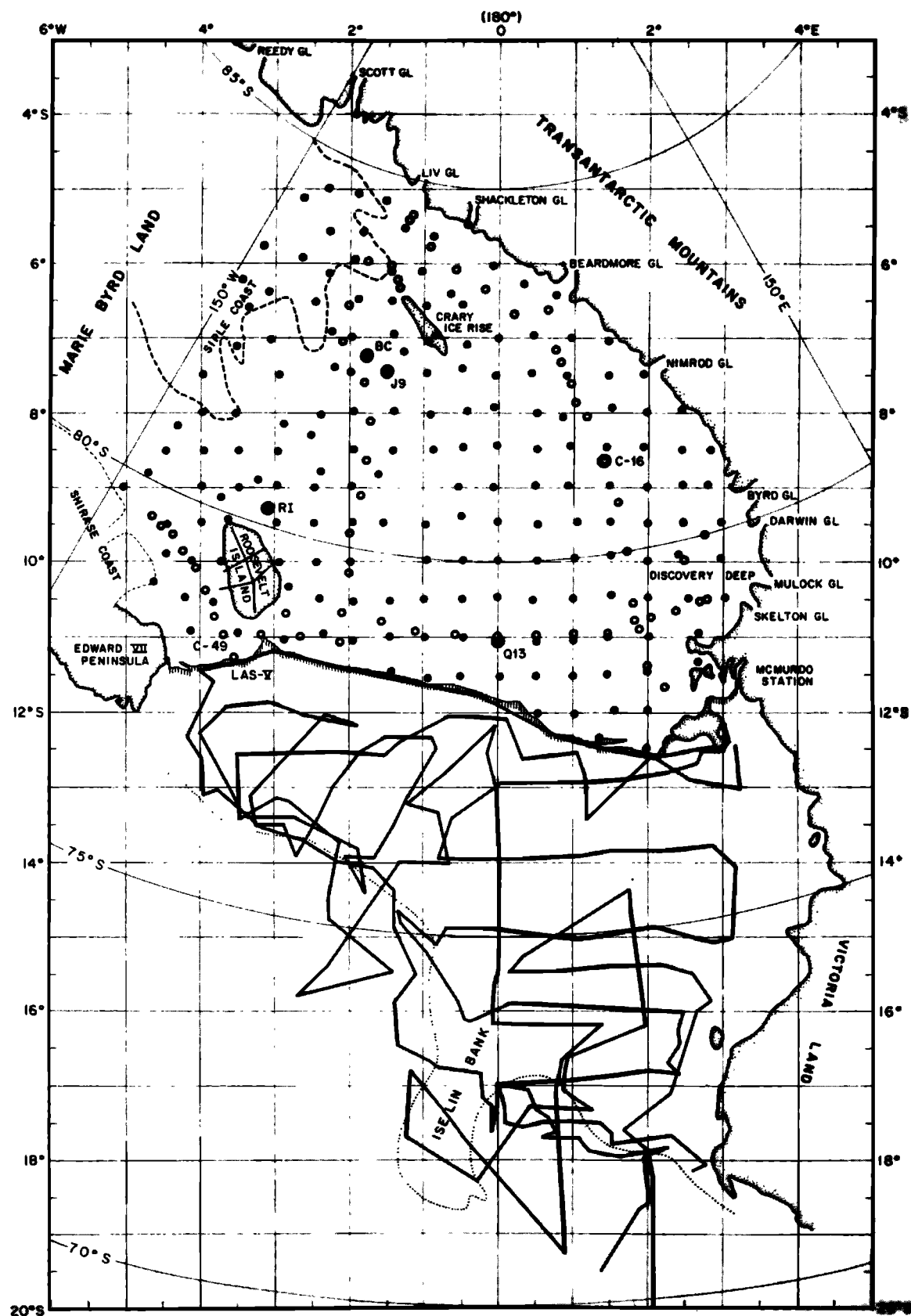


TABLE 1. Absolute Gravity Values at RIGGS Base Camps (Based on McMurdo)

Base Camp	Meter	Date	Gravity Value	Adopted Value
BC	G-1	Dec. 17, 1973	983 085.50	
	G-19	Dec. 17, 1973	085.52	983 085.64 ± 0.16
	G-1	Feb. 3, 1974	983 085.885	
	G-19	Feb. 3, 1974	975.68	
	G-1	Dec. 5, 1974	983 011.05	
RI	G-19	Dec. 16, 1974	001.09	983 001.13 ± 0.25
	G-1	Jan. 27, 1974	983 000.96	
	G-19	Jan. 27, 1975	000.97	
	G-19	Dec. 5, 1976	983 001.59*	983 001.57 ± 0.03
	G-19	Dec. 23, 1976	001.55	
C-16	G-1	Dec. 1, 1976	983 029.90*	
	G-19	Jan. 26, 1977	029.66*	983 029.75 ± 0.13
	G-19	Feb. 8, 1977	029.69	
	G-1	Jan. 17, 1978	983 003.01*	
	G-1	Jan. 23, 1978	029.61	
Q-13	G-1	Jan. 27, 1978	029.79	983 029.76 ± 0.16
	G-19	Jan. 17, 1978	029.63*	
	G-19	Jan. 27, 1978	029.78	
	G-19	Dec. 26, 1976	982 989.24	983 989.26 ± 0.03
	G-19	Jan. 26, 1977	989.28*	
	G-1	Dec. 23, 1977	982 989.24	
	G-1	Jan. 17, 1978	989.02*	982 989.18 ± 0.12
	G-19	Dec. 23, 1977	989.16	
	G-19	Jan. 17, 1978	989.30*	

*Indirect tie.

batteries during extended field operations. Thus except for occasional mishaps, both meters were continuously on heat throughout each season in Antarctica.

A gravity observation at a station consisted of at least two consecutive readings made within a few minutes. Near the ice front, where vertical movements of the ice shelf caused gravity oscillations, many readings were averaged in order to make a satisfactory observation [see Bennett, 1964]. Every series of observations formed a closed loop. A base station at the base camp was occupied at the beginning and end of each day's loop of remote field stations. Meter drift and tares (if any) during each loop were thus determined. The first and last observations for each season were made at the McMurdo base station, part of the International Gravity Standardization Net 1971 (IGSN 71) (see the next subsection).

Transportation to remote field sites was by Twin Otter aircraft. Gravity observations were made upon arrival and just before departure from each field site; as many as five sites were occupied during a day of field operations. At 63% of the stations occupied during RIGGS I and II there was sufficient time to determine gravity gradients by taking readings at the points in a "strain rosette" set up to determine strain rates in the ice [Thomas *et al.*, 1984].

Ice thicknesses and water depths were measured by radar and seismic soundings [Robertson and Bentley,

1990; Albert and Bentley, 1990]. Station positions were determined by a variety of methods including satellite Doppler positioning by geoceivers, sunshots, the inertial navigation system on the Twin Otter, and sighting of landmarks [Bentley, 1984].

When weather conditions precluded flying to remote field sites, gravity measurements were made as part of local surveys around the base camps. Gravity readings were routinely made at all points surveyed for glaciological or other geophysical measurements. In addition, a few lines were surveyed solely to provide data needed to fill in a local gravity map. Station spacings varied from 0.5 to 2.0 km. The terrain surrounding each of the base camps was relatively flat, and elevation differences between adjacent stations probably did not exceed 1 m. Base ties generally were made within about 6 hours so that tidal variations could be approximately removed.

Measurement of Gravity and Ancillary Data

Gravity bases. All RIGGS gravity values are based on the International Gravity Standardization Net 1971, which has both a relative and an absolute accuracy of ±0.1 mGal or better [Morelli, 1971; Hammond and Iliff, 1978; Harrison and LaCoste, 1978]. The primary base station was the McMurdo U.S. Antarctic Research Program (USARP) garage (B) base station

(IGSN 59676D), which is one of a group of gravity bases in McMurdo Sound tied to the world gravity net. It has a value of 982,973.45 mGal relative to IGSN 71.

At base camps BC and RI, piers that consisted of a platform mounted on four 4 × 4 in. posts each extending 3 m into firm were constructed inside small Jamesways. These platforms served both as tie points for field measurements and as bases for a recording gravity meter used to measure the tidal variation of gravity [Williams and Robinson, 1980]. Reading points at C-16 and Q13 were located on the snow surface just outside a Jamesway. Table 1 lists the gravity ties to RIGGS base camps and the adopted gravity values.

The base camps at RI, C-16, and Q13 were used in two different seasons. The movement of the ice shelf is large enough to change the geographic positions of these stations significantly over a 12-month period. However, only at RI, where 2 years passed between occupations, did the gravity value change significantly (Table 1).

Since readings at RI were made on the same pier in both seasons, the 0.44 ± 0.25 mGal increase in the base gravity value between 1974–1975 and 1976–1977 was presumably due to a combination of ice shelf movement and a decrease in elevation. Ice shelf movement at RI is 360 m yr^{-1} in a direction approximately 170° magnetic [Thomas et al., 1984]. The free-air anomaly gradient in that direction is $\sim 0.25 \text{ mGal km}^{-1}$ (Figures 14 and 15); so the movement in 2 years would increase observed gravity at RI by about 0.18 mGal (the latitudinal change is negligible). The surface accumulation rate is 0.15 m yr^{-1} of ice [Thomas et al., 1984], corresponding to about 0.4 m yr^{-1} of snow. Thus Sorge's Law ($\partial p/\partial t = 0$, where p is the density of the firm) would imply a 2-year decrease in elevation of 0.8 m, causing an additional gravity increase of 0.24 mGal. Added together, these two factors essentially match the observed change.

The gravity bases at C-16 and Q13 were on successive snow surfaces, so the elevation change is unknown, although an elevation decrease like that inferred for RI is not to have been expected. Camp Q13 moves along 188° grid at nearly 1 km yr^{-1} [Thomas et al., 1984]; it is difficult to estimate the free-air anomaly change in that direction from the free-air anomaly map (Figure 17), but there is a latitudinal gradient of $-0.31 \text{ mGal km}^{-1}$. The fact that the observed gravity changes only by -0.08 ± 0.12 mGal (Table 1) suggests that the free-air anomaly actually increases by about 0.2 mGal between the successive positions of Q13. At C-16, where the ice movement is 0.5 km yr^{-1} to the grid south [Thomas et al., 1984], the corresponding free-air anomaly and latitudinal gradients are about 1 mGal km^{-1} (Figure

26) and $-0.25 \text{ mGal km}^{-1}$, respectively. The absence of an increase in observed gravity of a few tenths of a milligal in one year at C-16 may reflect the canceling effect of an increase in elevation of the reading point, owing to the buildup of a snow drift hill around the camp buildings between field seasons.

Meter drift and calibration. Corrections for meter drift were computed from differences in base station readings. The drift was assumed to be linear except for cases where jarring the gravity meter caused a tare. In such cases a step variation was introduced into the drift curve. Figure 2 shows drift curves for gravimeter G-1 at C-16 and gravimeter G-19 at Q13, illustrating ocean tidal effects (surface elevation changes), instrumental drift, and tares. It can be seen that long-term instrumental drift is negligible and that the measured tidal effect is less than about 0.3 mGal. Since the tidal gravity variations are smaller than the uncertainty introduced by elevation errors, a theoretical tidal curve was not calculated, nor were observed tidal gravity data, which were sometimes available, applied. The largest tidal variation measured by Williams and Robinson [1980] was approximately 0.5 mGal at spring tide.

Only three tares occurred during the entire RIGGS program, all in the 1976–1977 season. Tare A (~ 0.7 mGal) resulted from rough handling of gravimeter G-19 at McMurdo. Tare B (~ 1.9 mGal) occurred when gravimeter G-19 fell from a snowmobile during the return trip from the magnetic south end of line A at Q13. Tare C (~ 4.8 mGal) occurred from a fall with gravimeter G-1 while deplaning at station N12. Stations in base loops containing tares could be referred to the proper base reading because it was known when each tare occurred. Hence the net effect of the tare on field gravity readings was minimized, although no drift corrections could be applied to stations read in a base loop containing a tare.

Calibrations of gravity meters G-1 and G-19 were checked by a tie between the USARP garage (McMurdo B) base and Christchurch A base (IGSN 71, number 48732A) at the close of the RIGGS III field season in February 1977. Comparison of this tie with the accepted IGSN 71 gravity difference revealed the following:

1. The manufacturer's calibration for gravimeter G-1 (dated 1960) yields an error of about 1.04 mGal over the 2479.16-mGal difference between the bases (McMurdo B: 982,973.45 mGal; Christchurch A: 980,494.29 mGal).

2. The calibration of gravimeter G-19 made by the Army Map Service in 1964 over 46 stations of the North American Calibration Line from Point Barrow, Alaska, to Paso de Cortez, Mexico, leads to agreement with the IGSN 71 difference between McMurdo and Christchurch to within 0.1 mGal.

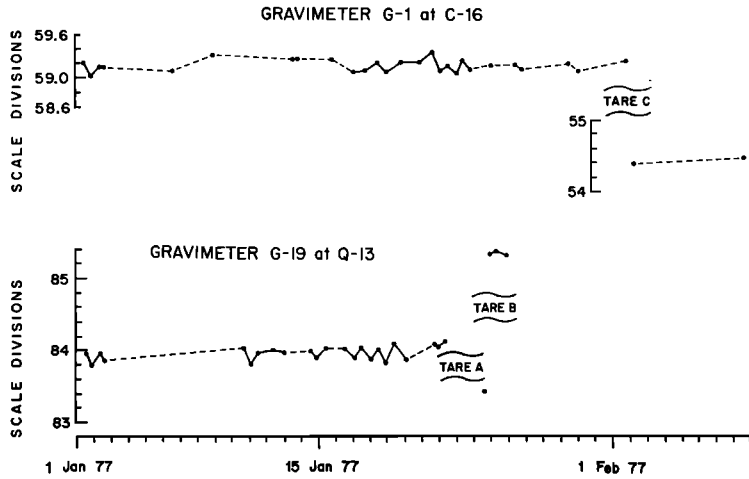


Fig. 2. Gravimeter drift curves during January 1977 (RIGGS III). Ordinates are in scale divisions on the gravimeter dials; one scale division very nearly equals one milligal. Tares are described in the text.

Gravity ties between McMurdo and South Pole stations made during each RIGGS field season as part of a long-term program of measuring the secular change of gravity at South Pole Station showed good agreement between gravimeters G-1 and G-19, after the adjustment determined in point 1 was applied to readings with gravimeter G-1. The largest disagreement over the 661-mGal difference between the two stations was 0.07 mGal. The secular change in gravity at "new" South Pole Station measured during the RIGGS program (0.10 ± 0.03 mGal/yr $^{-1}$) between February 1974 and October 1978 agrees with the change measured at "old" South Pole Station during the period December 1957 to November 1967 (0.10 ± 0.01 mGal/yr $^{-1}$) [Behrendt, 1967; Bentley, 1971]. Thus it appears that the calibrations for gravity meters G-1 and G-19 are stable and that it is valid to use these calibrations throughout the RIGGS program, particularly over the relatively small range (~216 mGal) of gravity values measured on the Ross Ice Shelf.

Determination of positions, elevations, and thicknesses. Geographic positions of RIGGS stations were determined by four different methods [Bentley, 1984]. Approximately two thirds of the RIGGS station positions were determined by satellite Doppler fixes, with an accuracy of better than ± 10 m [Thomas *et al.*, 1984]. Most of the remaining stations were fixed by sunshots to an accuracy of about 1 km. At 13 stations where neither a satellite fix nor a sunshot position was available, the position indicated by the inertial navigation system (INS) of the Twin Otter aircraft was used; the estimated accuracy for these positions is ± 3 km. Finally, at seven stations near the end of the RIGGS IV field season where the INS on the Twin Otter failed to operate, positions were determined by

sights taken on Mount Erebus, Mount Terror, Mount Discovery, and the tip of Minna Bluff (see Figure 1). These positions are estimated to be accurate to within ± 5 km [Greischar *et al.*, 1978].

Surface elevations e at RIGGS stations on floating ice were calculated by assuming the ice to be floating in hydrostatic equilibrium with seawater according to the following equation:

$$e = \frac{(\rho_w - \bar{\rho}_i)}{\rho_w} h_i + \frac{\bar{\rho}_i}{\rho_w} \delta \quad (1)$$

where $\delta = h_i (1 - \bar{\rho}_i/\rho_w)$, h_i is ice thickness, ρ_i and ρ_w are densities of ice and water, respectively, and $\bar{\rho}_i$ is the vertically averaged density in the ice shelf; δ is a correction value to be subtracted from e and h_i to reduce them to equivalent values for solid ice [Shabtaie and Bentley, 1982].

Direct measurements and seismic determinations of densities in the upper 100 m of the ice shelf both have been reported [Crary *et al.*, 1962; Robertson and Bentley, 1990; Langway, 1975; Chiang and Langway, 1978; Kirchner and Bentley, 1990; Albert and Bentley, 1990]. Table 2 shows average densities to 100 m, $(\bar{\rho}_i)_{100}$, calculated by using seismic determinations down to the maximum depth of wave penetration, z_{\max} (54–70 m), and assuming a linear increase in density below z_{\max} to an assumed value of 0.910 Mg m $^{-3}$ at 100 m (rounded off from a density of 0.908 Mg m $^{-3}$ at 101 m at Little America Station [Gow, 1963]). Also listed in Table 2 are values of $(\bar{\rho}_i)_{100}$ calculated from measurements on ice cores from Little America Station and RIGGS station J9DS (a substation of station J9). 16 seismically determined values of $(\bar{\rho}_i)_{100}$ range from 0.763 Mg m $^{-3}$ to 0.794 Mg m $^{-3}$ with a

TABLE 2. Densities in the Upper Ross Ice Shelf, From Seismic and Core Studies

Station	z_{\max} , m	Density at z_{\max} , Mg m^{-3}	Average Density Surface to z_{\max} Mg m^{-3}	Average Density, Upper 100 m, Mg m^{-3}	Source
BC	70	0.905	0.736	0.787	a
H7	70	0.901	0.727	0.781	a
H11S	70	0.889	0.708	0.765	a
J7S	70	0.904	0.730	0.783	a
J9DS	70	0.890	0.721	0.775	a
K11	70	0.889	0.728	0.779	a
P5	70	0.890	0.704	0.763	a
RI	70	0.909	0.722	0.778	a
C16	55	0.883	0.692	0.784	b
J9DC	54	0.902	0.699	0.794	b
H13	56	0.868	0.675	0.770	b
M14	54	0.893	0.699	0.792	b
Q13	56	0.892	0.691	0.783	b
O11	56	0.888	0.688	0.781	c
O19	57	0.889	0.696	0.784	c
R16	56	0.882	0.684	0.778	c
LAS	ice core			0.763	d
J9DS	ice core			0.774	e

Sources: (a) Robertson and Bentley [1990]; (b) Kirchner and Bentley [1990]; (c) Albert and Bentley [1990]; (d) Gow [1963]; (e) Langway [1975].

mean of 0.780 Mg m^{-3} and a standard deviation of 0.009 Mg m^{-3} . The agreement with the average of directly measured densities at the one common station, J9DS, is excellent [Kirchner and Bentley, 1990].

Using $\rho_i = 0.910 \text{ kg m}^{-3}$, $\rho_w = 1.029 \text{ kg m}^{-3}$ (at a temperature of -2°C and a salinity of 35% [Crary, 1961a]), and $\delta = 14.3$ (average for the 16 stations in Table 2) in equation (1) for e and h_i in meters gives

$$e = 0.116h_i + 12.6 \quad (2)$$

Elevations computed for lower bound and upper bound ice thicknesses of 200 m and 900 m, respectively, and lower bound and upper bound average densities for the upper 100 m of ice (Table 3) show that the uncertainty in elevation arising from the adoption of a single mean value of δ is no more than 2 m. There is also an elevation error due to uncertainties in the ice thickness given simply by $de/dh_i = 0.116$.

The uncertainty in ice thickness is about ± 10 m [Robertson and Bentley, 1990; Albert and Bentley, 1990]; so the total uncertainty in surface elevation is about ± 3 m. A comparison of elevations computed as above and satellite elevations computed in relation to the GEM 10C geoid at RIGGS stations where at least two satellite-determined elevations were available (S. Shabtaie, personal communication, 1990) yielded a mean difference (hydrostatic minus satellite) insignificantly different from zero: -1.2 ± 4.3 m for 60 stations.

One check point on the ice shelf is available: the hole through the ice at station J9DC [Clough and Hansen, 1979]. The surface height there was determined to be 59.6 m above sea level [Shabtaie and Bentley, 1987], close to the value of 60.7 m calculated from equation (2) for $h_i = 415$ m [Albert and Bentley, 1990].

Elevations at grounded stations F7, I10S, J4, and KL7 were determined by satellite observations to an

TABLE 3. Variation of Elevation With Average Density of Upper 100 m of Ice Shelf

Ice Thickness, m	Average Density, Upper 100m, Mg m^{-3}	Average Density, Ice Shelf, Mg m^{-3}	Surface Elevation, m
200	0.763	0.836	37.5
200	0.794	0.852	34.4
900	0.763	0.894	118.1
900	0.794	0.897	115.5

accuracy of about ± 5 m. Measurements of the elevation at the other three grounded stations (F10, I10, and Q18) were made only with altimeters. Both a hand-carried altimeter and the altimeter of the Twin Otter were used to measure elevation differences between those stations and either the base camp or the nearest floating station. Altimetry errors are difficult to determine; we will follow Bentley [1964] and take ± 10 m for instrument error and 0.1 m per kilometer distance from the reference point for the pressure gradient effect. That distance was of the order of 100 km, giving another ± 10 -m elevation error. We will take the sum of these two factors, ± 20 m, as a reasonable estimate of the elevation error at those stations.

Evaluation of satellite elevations by Shabtaie and Bentley [1987] revealed that seven RIGGS stations grid northwest of Crary Ice Rise previously believed to be floating were actually on grounded ice. Elevations for these stations were interpolated from the contour map of Shabtaie and Bentley [1987, Figure 10, p. 1324] to an estimated accuracy of ± 10 m.

The thickness of the water layer at RIGGS stations was measured either by seismic reflections alone or by seismic echoes from the seafloor combined with ice thicknesses determined by radar. The error in water layer thickness was estimated to be ± 5 m [Robertson and Bentley, 1990; Albert and Bentley, 1990]. Combining this with the error in ice thickness determination gives ± 15 m for the uncertainty in the depth of the seafloor.

Computation of Gravity Anomalies

The gravity anomaly at a point on the Earth's surface is the difference between the value of gravity observed at that point and a corresponding theoretical gravity value computed there. In this paper we calculate and examine the free-air, Bouguer, and Airy isostatic anomalies (listed in the appendix).

Theoretical gravity. The theoretical gravity at an observation point at latitude ϕ is the value at that latitude on an ideal equipotential surface (reference ellipsoid) given by a standard gravity formula. The formula that approximates the Earth's gravitational field has been modified several times since the turn of the century as the amount and precision of gravity and geodetic information have increased. We used the gravity formula adopted by the International Union of Geodesy and Geophysics in 1967 [Morelli, 1971] known as the Geodetic Reference System (GRS) 1967 [Woollard, 1979]. Data from RIGGS and all data used in this paper were reduced using the GRS 1967:

$$\gamma = 978031.85 [1 + 0.0053024 \sin^2(\phi) - 0.0000059 \sin^2(2\phi)] \quad (3)$$

where γ is the gravity value (in milligals) on the reference ellipsoid and ϕ is the latitude.

Differentiating (3) yields, for the latitude correction to gravity, $0.815 \sin 2\phi$ mGal km $^{-1}$. This varies from 0.15 to 0.35 across the range of latitudes of RIGGS stations; at a nominal latitude of 80° it is 0.28 mGal km $^{-1}$.

Free-air anomaly. The free-air (elevation) correction is $0.3086e$ mGal (e is in meters), whence the free-air anomaly, Δf_{fa} , becomes $\Delta f_{fa} = g_{obs} + 0.3086e - \gamma$ where g_{obs} is the observed gravity value.

Bouguer anomaly. The effect of the mass between the observation point and sea level is generally approximated by the Bouguer correction for an infinite horizontal slab, δg_B :

$$\delta g_B = 2\pi G\rho e = 0.0419\rho e \quad (4)$$

where ρ is the density of the material in the slab (in megagrams per cubic meter), i.e., between the observation point and sea level. The Bouguer correction is subtracted to remove the effect of the intervening mass in adjusting g_{obs} to sea level. The application of both the Bouguer and the free-air corrections to g_{obs} gives the simple Bouguer anomaly ("simple" means "without terrain corrections").

At sea level on land, since both corrections are zero, the free-air and Bouguer anomalies are the same. On the ocean, however, it is standard practice to extend the Bouguer correction to the mass deficit between the ocean water and crustal rock: in equation (4) e becomes d_w , the ocean depth (in meters), and ρ becomes $\rho_r - \rho_w$, the density difference between water and rock, and the correction is now added. Bouguer anomalies were calculated in this way for the RIGGS measurements made on the ice shelf. (Note that on ice floating in hydrostatic equilibrium, $\delta g_B = 0.0419(\rho_r - \rho_w)d_w$ independent of the surface elevation.) Taking $\rho_r = 2.67$ Mg m $^{-3}$ and $\rho_w = 1.028$ Mg m $^{-3}$, we then have for the Bouguer anomaly on the ice shelf, δg_B ,

$$\delta g_B = g_{obs} + 0.3086e + 0.0687d_w - \gamma$$

For consistency, Bouguer anomalies at grounded RIGGS stations were also calculated by replacing ice below sea level with rock.

A terrain correction, which is sometimes applied to correct for the deviation of the real Earth from a flat Bouguer slab, was not included in our data reduction. The ice shelf is very flat and local sea bottom slopes, measured beneath seismic spreads of the order of 1 km in length, are mostly less than 1°; only 7 of the 56 observed local slopes are larger than that [Crary *et al.*, 1962; Robertson, 1975]. Furthermore, since the RIGGS gravity observations were made on the surface of the ice shelf which is hundreds of meters above the

seafloor, the gravitational effects of local submarine topographic highs and lows tend to cancel, thereby diminishing the terrain effect.

Airy isostatic anomaly. An isostatic gravity correction attempts to account for the gravitational effects of the masses associated with isostatic compensation. For topographic features that are large in comparison with depths of compensation, the Bouguer and isostatic corrections are nearly equal, so that the combined correction approaches zero. On the other hand, for topographic features that are small in comparison with depths of compensation, the gravitational effect of the compensating mass is relatively small; so the combined Bouguer-isostatic correction approaches the Bouguer correction.

An idea of the magnitude of the gravity disturbance due to compensated surface masses can be obtained from a model composed of one or more circular disks [Nettleton, 1976, Figure 7A-8, p. 232]. For compensation at a depth of 30 km, the combined Bouguer-isostatic correction for a circular topographic feature 40 km across is 83% of the simple Bouguer correction, but it drops to only 35% of the simple Bouguer correction for features 160 km across (Table 4). A topographic feature as large as the Ross embayment would retain a combined Bouguer-isostatic correction equal to about 5% of the simple Bouguer correction. Taking an average water depth of 600 m in the Ross embayment, the combined Bouguer-isostatic correction would be approximately 2 mGal.

The Airy mechanism of perfect local isostatic compensation, whereby topographic features are balanced by crustal roots (antiroots in oceanic regions) in the mantle, has been assumed for our calculations. Isostatic corrections were computed using the three-dimensional Talwani procedure [Talwani and Ewing, 1960]. A constant crustal thickness of 30 km throughout the Ross embayment was assumed. That value was based on data available at the time of RIGGS [Bentley, 1973]; the crust is now believed to be about 5 km thinner [Cooper et al., 1991]. As explained below, changing the assumed thickness by 5 km would change the average isostatic anomaly only

by about 1 mGal; anomalies were therefore not recalculated. Densities of 2.67 Mg m^{-3} for the upper crust, 2.95 Mg m^{-3} for the lower crust, and 3.32 Mg m^{-3} for mantle material were used. For 243 gravity stations on the Ross Ice Shelf, the mean isostatic correction was -42.02 mGal .

The Airy isostatic gravity anomaly, δg_A , is given by

$$\Delta g_A = g_{\text{obs}} + 0.3086e + 0.0687d_w + \delta g_A - \gamma$$

where δg_A , the computed Airy isostatic correction, is negative everywhere on floating ice.

The isostatic correction is insensitive to changes in the choice of density, since the mass of the isostatic compensation remains fixed. Furthermore, particularly in a region of subdued submarine topography such as the Ross embayment, the isostatic anomalies are insensitive to a change in isostatic model. Kososki [1972] calculated both Pratt-Hayford and Airy-Heiskanen average isostatic anomalies for one-degree ($111 \text{ km by } 111 \text{ km}$) squares for West Antarctica and found that differences between individual anomalies rarely exceeded 2 mGal, even in the mountainous interior. Similarly, the crustal thickness assumed for the Airy model is unimportant. For a typical feature in the Ross embayment with a linear dimension of approximately 160 km and relief of the order of 200 m, corresponding to a simple Bouguer correction of 14 mGal, the isostatic correction would change only 2 mGal for a 10-km change in crustal thickness (Table 4).

Errors in gravity anomalies. The various contributions to the estimated errors for free-air and Bouguer anomalies at field stations are listed in Table 5. Errors from uncertainty in latitude were evaluated at a latitude of 80° . At the 94% of the RIGGS stations located on the floating ice shelf, gravity anomalies are accurate to about $\pm 2 \text{ mGal}$. For grounded stations the error ranges from 2 mGal to 6 mGal, depending on the method of elevation determination.

Bennett [1964] estimated the accuracy of pre-RIGGS gravity stations on the ice shelf to be $\pm 6 \text{ mGal}$ for both free-air and Bouguer values; the larger errors in his work stem from larger uncertainties in surface elevations, which were determined by altimetry alone.

TABLE 4. Magnitude of Combined Airy-Isostatic and Bouguer Correction Relative to Bouguer Correction Alone for Cylindrical Disks

Diameter, km	Crustal Thickness, %		
	20 km	30 km	40 km
40	71	83	90
160	23	35	46
320	11	17	23
800	4	7	9
1600	2	3	4

TABLE 5. Estimated Errors in Gravity Anomalies

Measurement	Method or Source	Error, mGal	
		Free-Air Anomaly	Bouguer Anomaly
Elevations (surface and bed)			
Floating stations	hydrostatic balance	0.9	1.9
Grounded stations	satellite	1.6	2.6
	map [<i>Shabtaie and Bentley, 1987</i>]	3.1	3.4
	altimetry	6.2	6.1
Latitude	satellite	0	0
	sunshot	0.3	0.3
	INS	0.8	0.8
	landmark	1.4	1.4
Earth and ocean tides	<i>Williams and Robinson [1980]</i>	0.5	0.5
Base station value	<i>Morelli [1971]</i>	0.1	0.1
Total error (rms)	floating stations	1.0–1.8	2.0–2.4
	grounded stations	1.7–6.4	2.6–6.3

Gravity Anomaly Maps

Figures 3a and 4a show the free-air and Bouguer gravity anomaly maps of the Ross embayment, respectively. Versions of the same maps filtered to remove wavelengths less than ~160 km are shown in Figures 3b and 4b. The data in the Ross Sea were approximately adjusted to the new reference system and datum (GRS 67 and IGSN 71) by applying a constant correction of ~10 mGal [*Bentley and Robertson, 1982*]. The bathymetric map of the Ross embayment (reproduced in Figure 5a; the filtered version is in Figure 5b), prepared by *Albert et al. [1978]* and published in the work of *Albert and Bentley [1990]*, was used to compute the Airy isostatic gravity anomaly map.

Aliasing is sure to be present in the maps, since the measurement points are approximately 55 km apart over most of the ice shelf and the distance between ship's tracks in the Ross Sea was mostly even more. There are some clues to the magnitude of the resulting error. As discussed below, 65% of the 57 gravity gradients measured in the grid western part of the Ross Ice Shelf agree in direction (within $\pm 60^\circ$) with the regional gradient of the free-air anomaly map. All the local gravity surveys at RIGGS base camps (see below) showed considerable variation in gravity over distances of a few tens of kilometers (30 mGal at Q13 and C-16, 9 mGal at J9DC, 16 mGal at RI, and 14 mGal at BC), but the local variations are generally consistent with the regional anomaly field. Departures of the gravity anomaly values at Q13, C-16, J9DC, BC, and RI from the average gravity anomaly values estimated from the local coverage at these stations are approximately +6, -4, -5, +4, and -3 mGal, respectively. From those

figures we estimate ± 5 mGal for the error in using station anomaly values to represent the mean anomaly for the 0.5° square surrounding each station. This error, combined with the errors in the anomalies themselves, is large enough to suggest that any features on the following maps defined by only one 10-mGal contour interval are of questionable significance.

We base the following discussion on the unfiltered maps, to which the specific positions cited refer, but most of the features can be seen, many of them more clearly, on the filtered maps, to which we direct the reader also.

Free-air anomaly map. Except for a few isolated anomalies, free-air gravity values in the Ross embayment (Figure 3) are negative. Several of the free-air anomalies are clearly related to bottom topography (Figure 5); several more are not. Most notable of the former are the linear high-low gravity anomalies over the ridge-trough topography of the grid northwestern area of the ice shelf, the gravity high on Roosevelt Island, the low directly grid southwest of Roosevelt Island (grid 11°S , 3.5°W), the gravity low over Discovery Deep (grid 10.6°S , 2.7°E), and the gravity lows adjacent to Ross Island (grid 12°S , 2°E). Anomalies not clearly associated with submarine topography include the gravity low directly grid southeast of Roosevelt Island (grid 10.7°S , 2.8°W), the large gravity high trending grid north-south in the Ross Sea between 1°E and 2°E (grid), and gravity lows roughly paralleling the continental shelf edge in the Ross Sea. *Bennett [1964]* suggested that the gravity low grid southeast of Roosevelt Island may be due to a low-density granitic intrusion, and *Hayes and Davey [1975]* postulate a similar source for the gravity lows near the edge of the

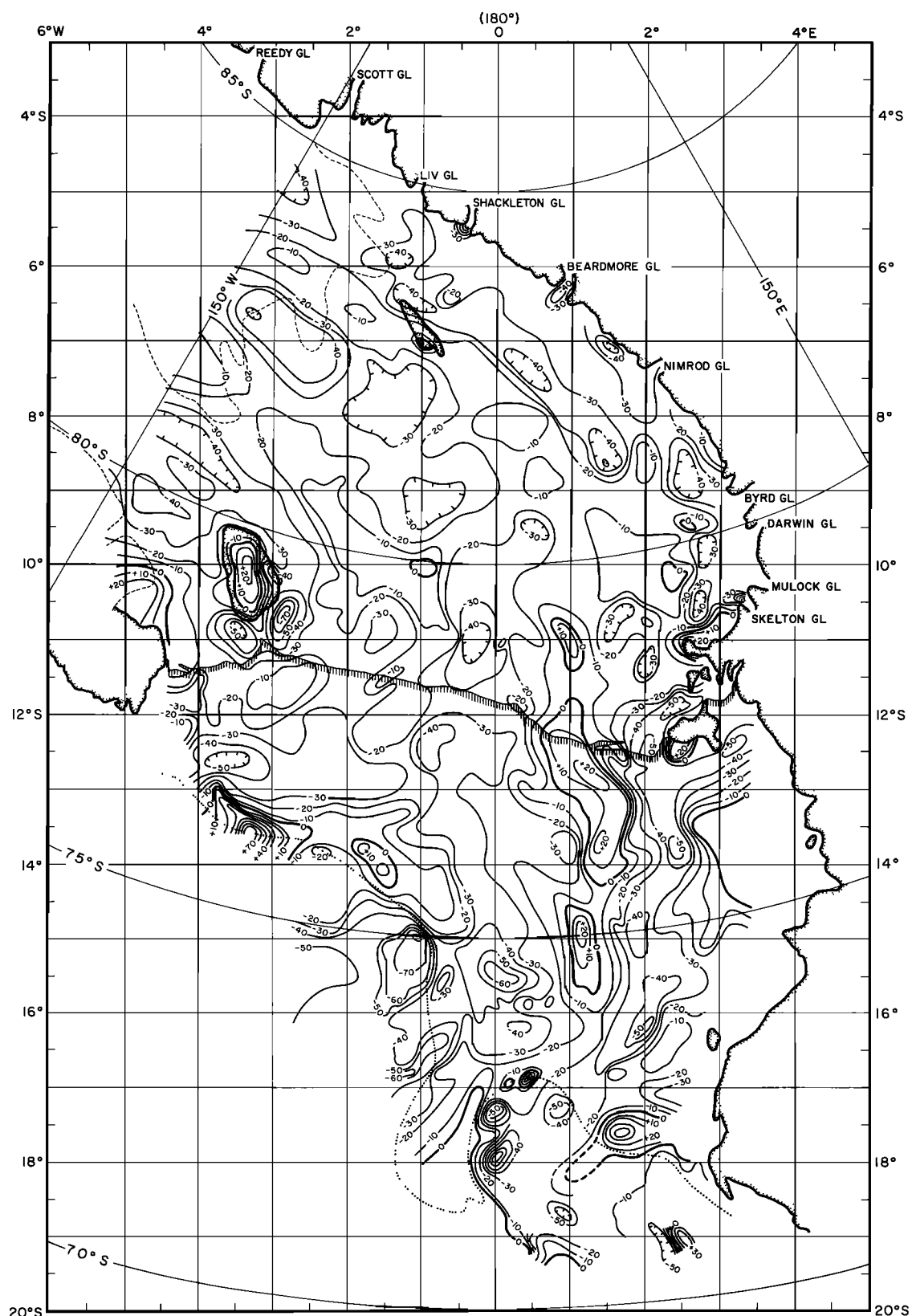


Fig. 3a. Map of free-air anomalies in the Ross embayment. The contour interval is 10 mGal. A heavy line marks the 0-mGal contour.

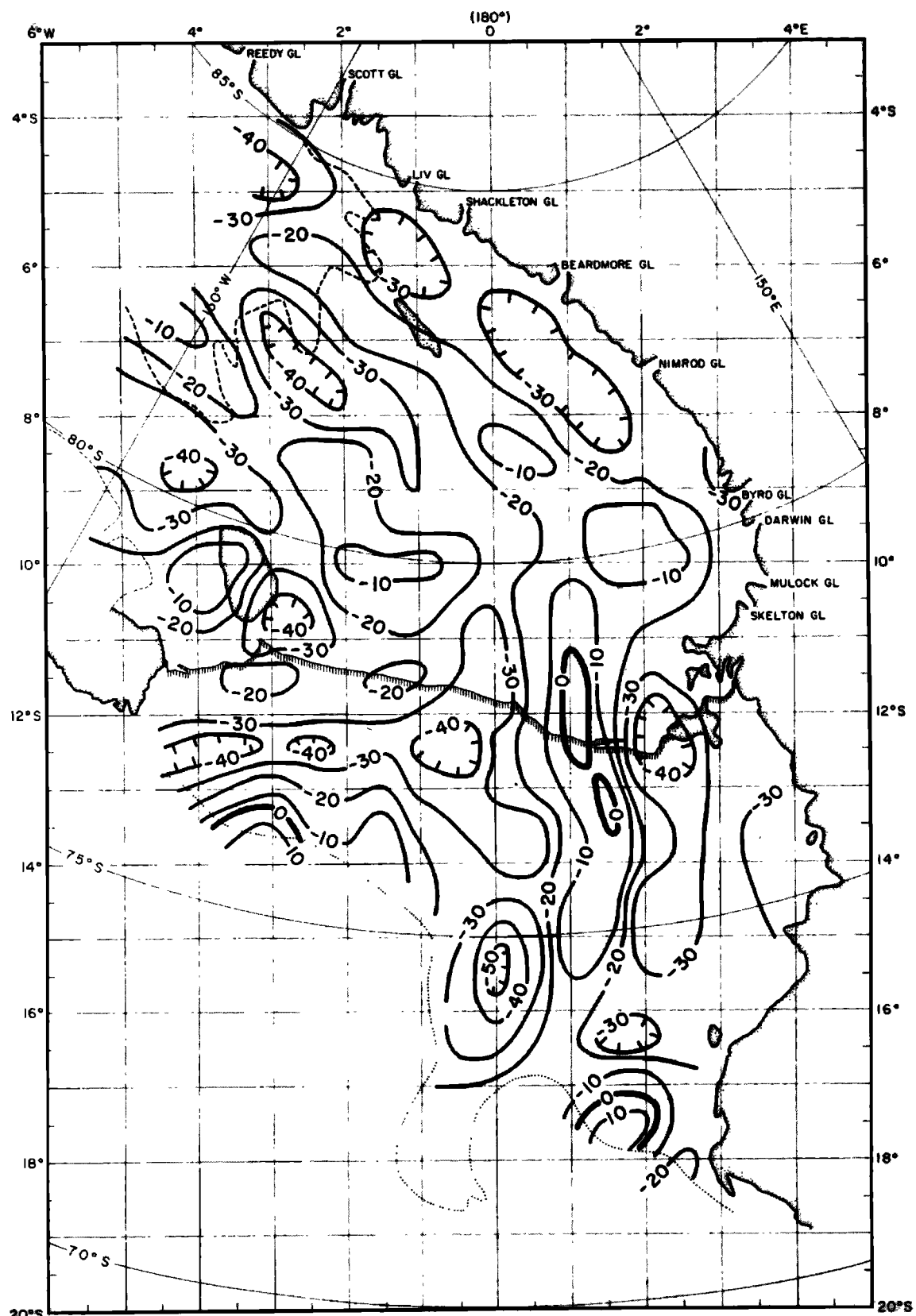


Fig. 3b. Map of free-air anomalies in the Ross embayment, filtered to remove wavelengths less than 160 km. The contour interval is 10 mGal. A heavy line denotes the 0-mGal contour.

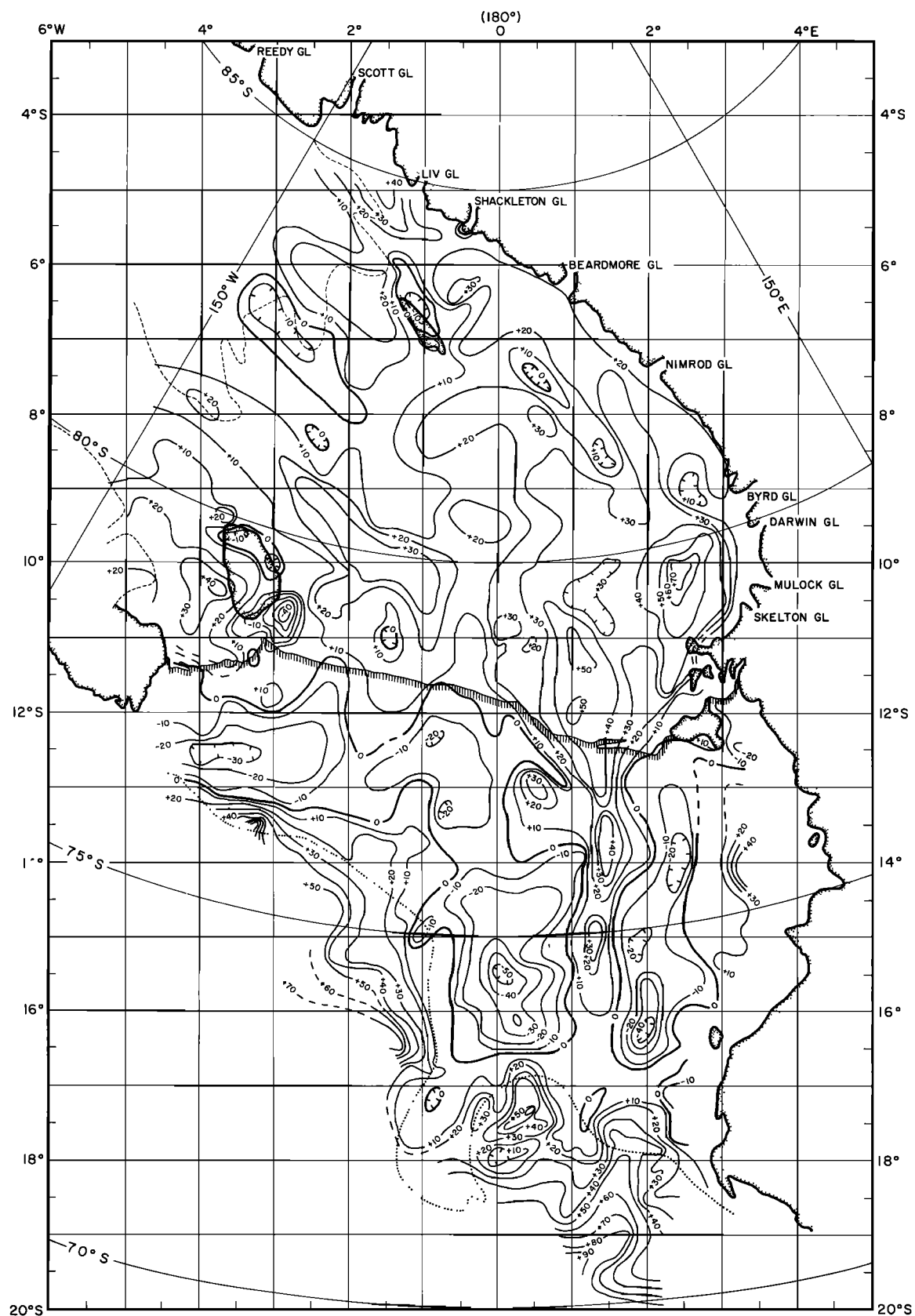


Fig. 4a. Map of Bouguer anomalies in the Ross embayment. The contour interval is 10 mGal. A heavy line marks the 0-mGal contour. RIGGS base camps are denoted by black circles.

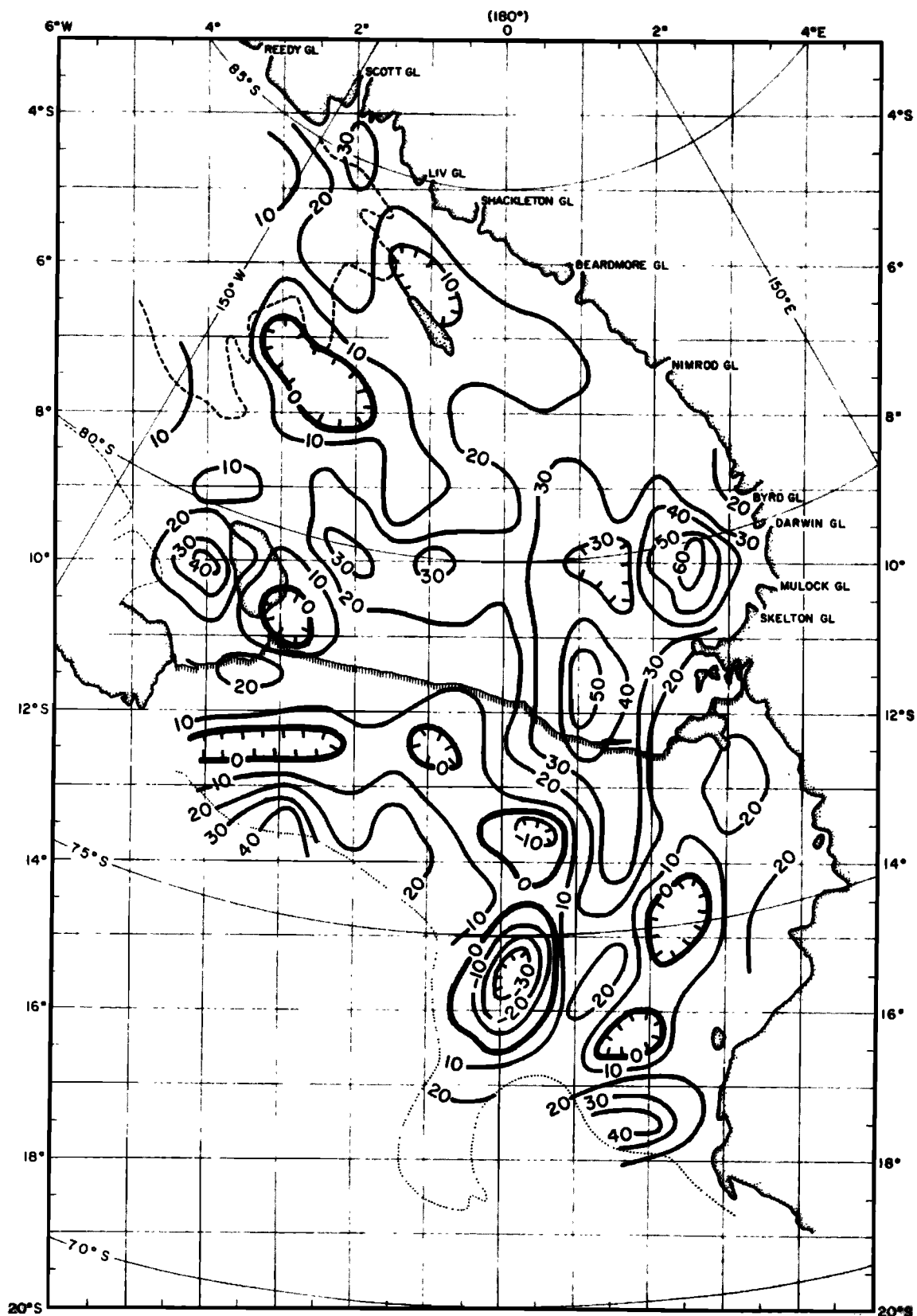


Fig. 4b. Map of Bouguer anomalies in the Ross embayment, filtered to remove wavelengths less than 160 km. The contour interval is 10 mGal. A heavy line denotes the 0-mGal contour.

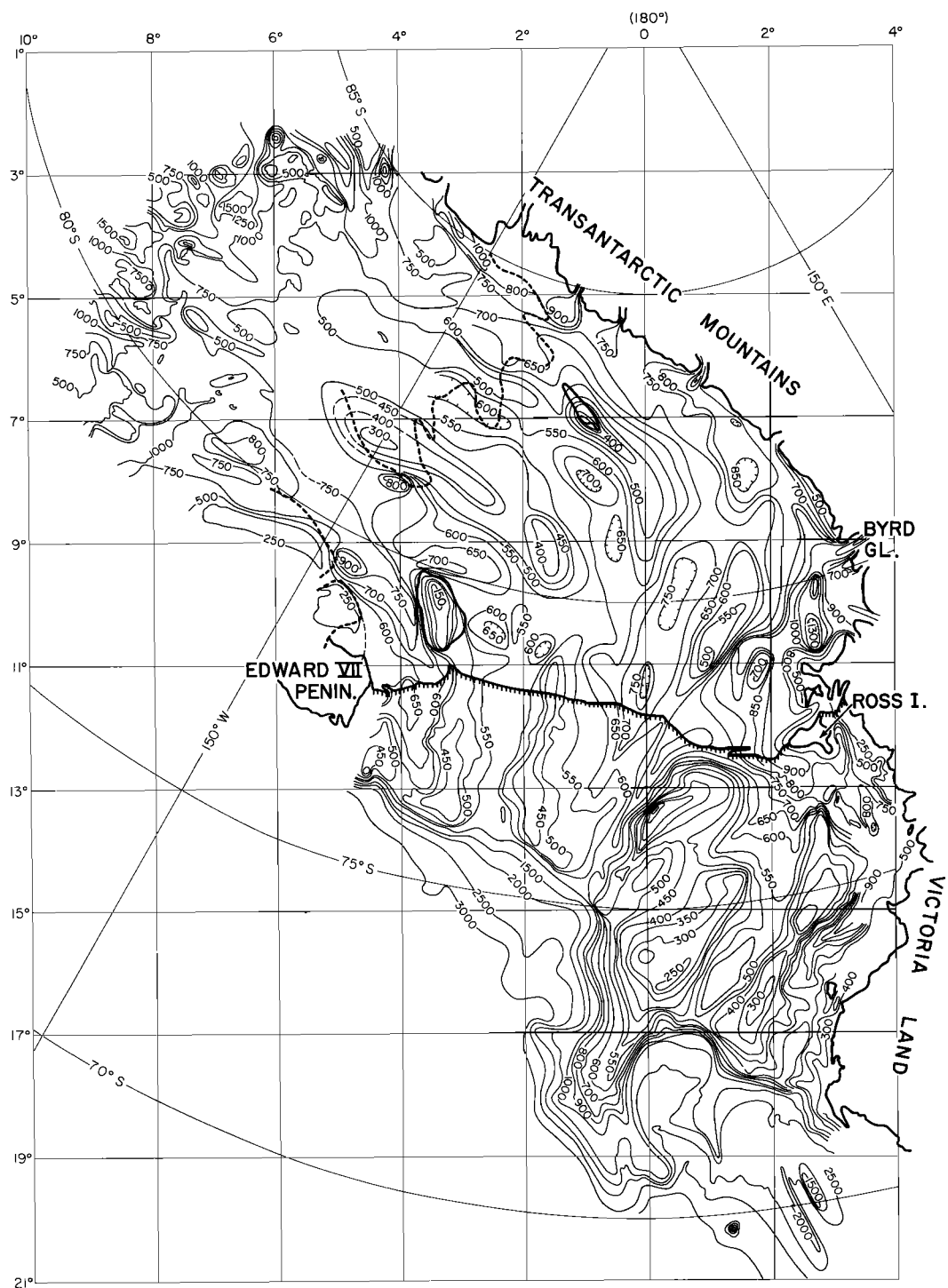


Fig. 5a. Map of submarine topography in the Ross embayment. The contour interval is 50 m beneath the Ross Ice Shelf and in the Ross Sea and 250 m under the inland ice in the grid northwest. RIGGS base camps are denoted by black circles.

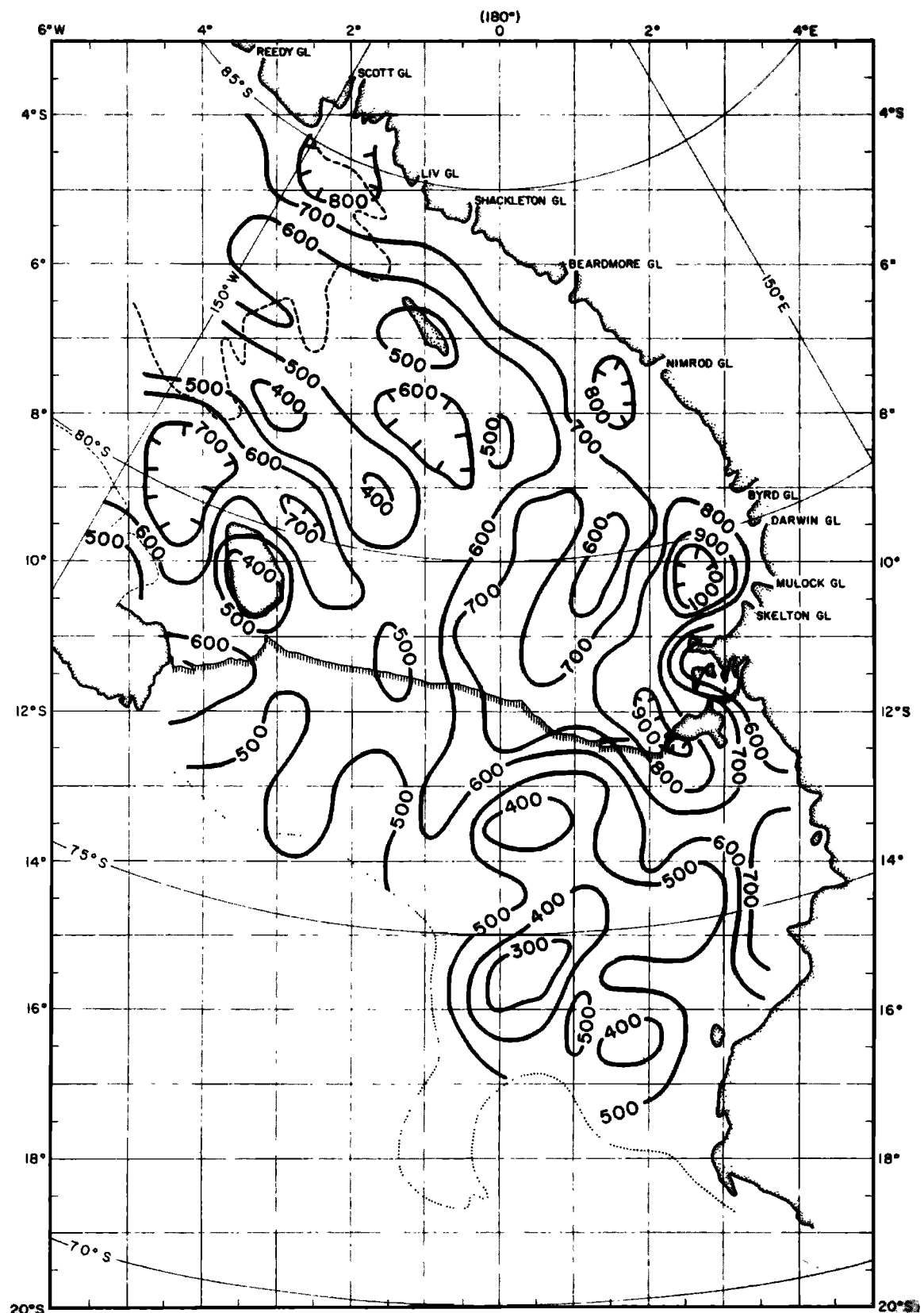


Fig. 5b. Map of submarine topography anomalies in the Ross embayment, filtered to remove wavelengths less than 160 km. The contour interval is 50 m.

continental shelf at grid 15.5°S , 0°W and grid 12.5°S , 3.5°W . Hayes and Davey [1975] modeled the large north-south trending gravity high in the central Ross Sea as a high-density intrusion into the upper crust, probably the result of crustal rifting. For a comprehensive discussion of the relationship between gravity anomalies and upper crustal structure on the Ross Sea continental shelf that includes many new data, particularly for the grid eastern Ross Sea, see Davey and Cooper [1987].

Bouguer gravity anomaly map. The Bouguer gravity anomaly map (Figure 4) emphasizes density contrasts beneath the seafloor including those due to masses compensating topographic loads. Correlation with bottom topography is largely removed except where topographic loads are extensive enough to be isostatically compensated.

The Bouguer gravity anomaly map can be divided into three regions based on anomaly amplitudes and trends. The first, around and grid south of Roosevelt Island, is characterized by roughly circular Bouguer anomalies with one anomaly as negative as -40 mGal (grid 10.3°S , 3.7°W) and one as large as $+40$ mGal (grid 10.6°S , 2.7°E). These anomalies may be related to low-density and high-density intrusions associated with Marie Byrd Land (see the paragraph on Roosevelt Island anomalies below).

The linearly trending anomalies over the ridges and troughs in the second region, between Roosevelt Island and the Transantarctic Mountains, range from -10 to $+40$ mGal. They are generally supposed to arise from horst and graben structures that have resulted from rifting between the Transantarctic Mountains and Marie Byrd Land [Elliot, 1980; Davey, 1987; Cooper et al., 1991; Behrendt et al., 1991]. Vertical crustal displacements of 1 or 2 km could easily account for these anomalies.

Grid southeast of a curved line extending from Byrd Glacier to the edge of the continental shelf grid west of Iselin Bank is the third region, characterized by grid north-south trending anomalies ranging from -50 to $+70$ mGal. The association of these anomalies with basins and highs beneath the shelf is discussed by Davey and Cooper [1987].

Airy isostatic gravity anomaly map. The isostatic anomalies (Figure 6) generally are intermediate between the free-air and Bouguer anomalies: as was pointed out above, the isostatic anomaly map approximates the Bouguer anomaly map over local topographic features, and the free-air anomaly map, over regional features. It is important to note that nonzero isostatic anomalies do not necessarily imply lack of isostatic equilibrium, particularly in regions of lateral density variations [Simpson et al., 1986]. However, it is unlikely that a region with a small isostatic anomaly is greatly out of balance.

It appears from Figure 6 that large areas of the seafloor below the ice shelf are in isostatic equilibrium. In particular, free-air anomalies at Discovery Deep (grid 10.6°S , 2.7°E), on Roosevelt Island, and on Crary Ice Rise have been removed by the isostatic correction, which implies that these features are isostatically equilibrated.

Several regions of pronounced isostatic anomalies remain, however. An elongated isostatic anomaly low reaching -40 mGal is centered over and parallel to the grid eastern edge of Roosevelt Island. This low extends grid north-northwest from the large closed low (-77 mGal) directly grid southeast of Roosevelt Island to grid 8.5°S , 4.0°W . Grid west of Roosevelt Island, however, the isostatic anomaly is small, which implies isostatic equilibrium of the topographic trough there (Figure 5a) as well as of Roosevelt Island.

The linear free-air anomalies that extend grid southeast from the West Antarctic grounding line remain on the isostatic map. Particularly pronounced, and scarcely smaller here than on the free-air map, is the anomaly of -30 to -40 mGal that runs parallel to the Transantarctic Mountains from grid northwest of Crary Ice Rise at 150°W longitude (grid 5°S , 3°W) to base station C-16. Grid northeast of Crary Ice Rise (grid 6.5°S , 0.5°W) left-lateral displacement of this low trend is suggested.

The negative anomaly is bounded to the grid northeast by a linear isostatic anomaly high that is even more pronounced than the corresponding free-air anomaly. The occurrence of this relative high over the submarine trough adjacent to the Transantarctic Mountains argues against the presence beneath the ice shelf of a thick sedimentary section such as the one (the Victoria Land basin) modeled by Stern and ten Brink [1989] for the East Antarctic/West Antarctic boundary in the Ross Sea. Also, the linear high that parallels the Transantarctic Mountains about 200 km offshore which, in the Ross Sea, Stern and ten Brink [1989] interpret as being linked with downward flexure at the western margin of the Ross embayment, is seen here (grid 6°S , 3°W to grid 10°S , 2°E), farther into the embayment, to be the middle one of three similar highs.

The low that trends from the Siple Coast at grid 6.5°S , 3°W to grid 9°S , 1°W is narrower and less continuous on the isostatic map than on the free-air map. In the extreme grid western part of the survey area, the anomaly is not centered on the topographic trench (grid 6.7°S , 3°W ; Figure 5a), but it instead lies over the flank of the topographic ridge to the grid north of it. The pinching of the anomaly in the center of the survey area (grid 8°S , 1°W) appears to be associated with a crosscutting trend that runs grid northeastward to near the Transantarctic Mountains. The positive trend running from the grid southern

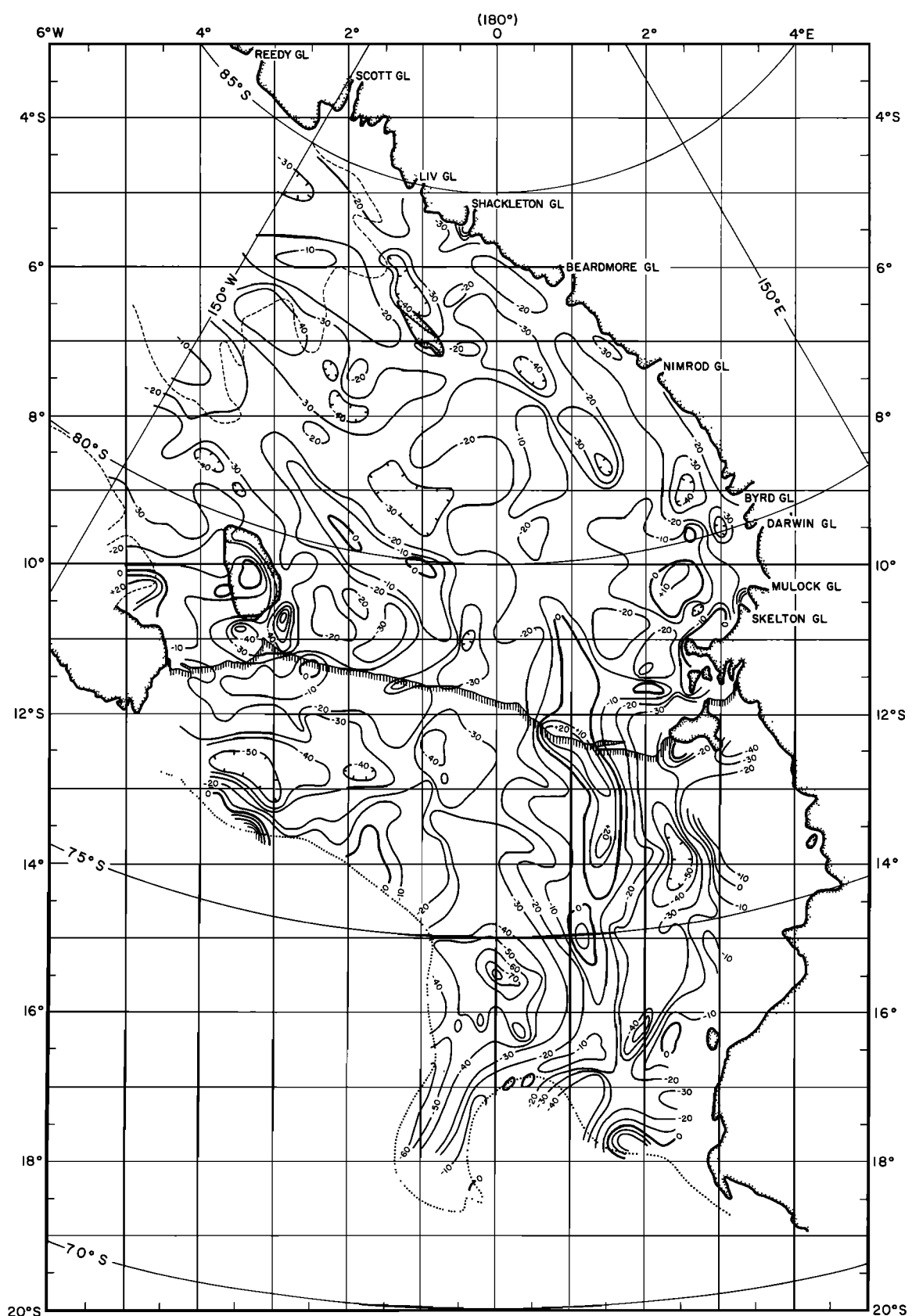


Fig. 6. Map of Airy isostatic anomalies in the Ross embayment. The contour interval is 10 mGal. A heavy line marks the 0-mGal contour. RIGGS base camps are denoted by black circles.

Siple Coast (grid 7.5°S , 4°W) to grid 10°S , 1°W , which overlies a topographic ridge, is little changed from the free-air to the isostatic map. The central Ross Sea gravity high is relatively unchanged by the isostatic correction.

Since the three principal negative-isostatic-anomaly trends are approximately parallel to each other and to the troughs and ridges in the ocean bottom topography, are directly associated with topographic troughs at least along the grounding line, and are of about the same magnitude, it appears likely that the three arise from the same geologic cause. Likely causes are (1) thick sequences of low-density sediments in the areas of negative anomalies or (2) infolding or downdropping of metasediments and/or felsic intrusives of upper crustal density into the lower crust.

An uncompensated, 1-km-thick, flat slab of glacial-marine sediments with a density of 2.0 Mg m^{-3} sitting in continental crust ($\rho = 2.67 \text{ Mg m}^{-3}$) produces a gravity anomaly of -28 mGal , about the right magnitude to account for the three observed negative anomalies. At J9DC and RI, both of which have an isostatic anomaly of -35 mGal , the estimated sediment thicknesses are about 1350 m and 850 m [Robertson and Bentley, 1990]. The gravity anomalies there could be reduced to less than 10 mGal by including uncompensated layers of low-density sediments of the proper thicknesses in the model. However, the 500-m difference in sediment thickness between those two stations should lead to an anomaly difference of about 14 mGal . Similarly, the seismic sections at Little America V (grid 11.25°S , 3.62°W) [Crary, 1961b] and I10S (grid 7.05°S , 0.95°W) [Robertson and Bentley, 1990] also contain large but different thicknesses of sediment (1325 m and 750 m, respectively), yet the isostatic anomalies at these sites, -16 mGal and -14 mGal , respectively, are nearly the same. On the other hand, at station C-49 (grid 10.98°S , 3.71°W) the thickness of the sediment layer is the same as at I10S, yet the isostatic anomaly is 14 mGal less. It is likely, in fact, that thick glacial-marine sediment layers underlie most parts of the RIGGS survey area and that the primary source of the isostatic anomalies is deeper. Supporting this conclusion is the fact that negative anomalies do not appear in areas where one would expect sediments to be thick, such as the trench next to the Transantarctic Mountains, the trench south of Crary Ice Rise, and the trough between Roosevelt Island and the Rockefeller Mountains.

From seismic evidence, Robertson and Bentley [1990] suggest that the basement beneath the ice shelf consists of metasedimentary and felsic intrusive rocks. Modeling calculations indicate that an uncompensated 3-km penetration of metasedimentary and felsic intrusive rocks into the lower crust is sufficient to

produce a -30-mGal anomaly. We conclude that the sea bottom topography is tectonically controlled and that the associated isostatic anomalies are associated with crustal faulting. Robertson *et al.* [1982] reached a similar conclusion from an examination of the Bouguer anomalies.

Local Gravity Gradients

General. Where gravity was measured on a strain rosette (Figure 7), a small free-air anomaly map of the rosette area was drawn, from which the direction and magnitude of the gravity increase were estimated (Figure 8; tabulated values are in the appendix). The relative error in anomaly between the points in the

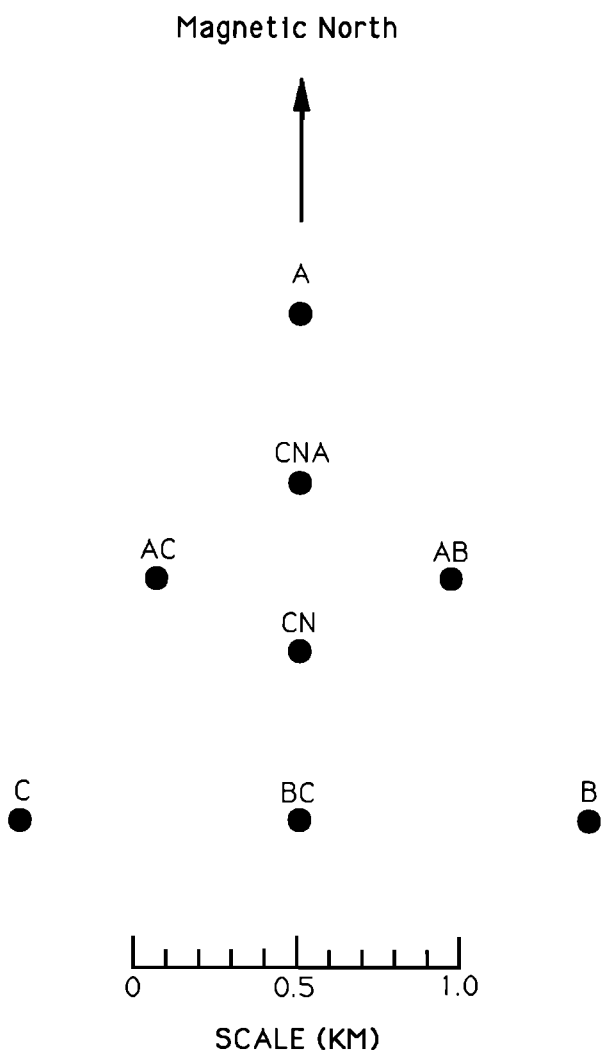


Fig. 7. Layout of a typical strain rosette at a RIGGS station [Thomas *et al.*, 1984].

strain rosettes was taken to be 0.6 mGal, corresponding to an uncertainty in elevation of 2 m, a conservative figure on the flat ice shelf. For eight stations in a rosette, this leads to an estimated error for the gradients of $\pm 0.2 \text{ mGal km}^{-1}$ in magnitude and $\pm 20^\circ$ in direction.

Of the 57 gradients measured, 38 (67%) agree in direction (within $\pm 60^\circ$) with the free-air map. Agreement does not depend upon size of the gradients: when only the 40 largest gradients are considered, the agreement rate increases only an insignificant 1%. About one third of local sources would agree in direction ($\pm 60^\circ$) just by coincidence; so we can say generally that about half of the local gradients have principally regional sources.

Regional bathymetric control also is suggested, most strongly in the region around Roosevelt Island, where eight of the nine gradients are in good agreement with both the free-air and the bathymetric maps.

Local gravity anomalies around Roosevelt Island. The large positive free-air anomaly centered on Roosevelt Island clearly is caused by the several-hundred-meter increase in bottom elevation, as shown by the fact that the feature disappears from the Bouguer anomaly map. In contrast, the large negative free-air anomaly located at the grid southeastern edge of the ice rise is also pronounced on the Bouguer anomaly map. A positive magnetic anomaly of more than 200 γ was also found in this area [Bennett, 1964]. The gravity and magnetic anomalies both can be modeled by a sialic body with a density of 2.6 Mg m^{-3} intruding 5 km into the high-density subbasement [Bennett, 1964]. Bennett [1964] also calculated that the difference in Bouguer anomalies between Roosevelt Island and the center of the negative anomaly could be explained by a sediment thinning of 1.2 km or by a reduction in the vertical extent of the intrusion under Roosevelt Island. A similar, possibly connected intrusion is the likely source of the lesser but still pronounced free-air and Bouguer anomaly lows grid south by west of Roosevelt Island.

MODELING OF LOCAL GRAVITY ANOMALIES

The local gravity fields around station J9DC and the four RIGGS base camps can be taken as a random sampling of short-wavelength fields on the Ross Ice Shelf. In fact, strong anomaly gradients are present in all five of those local fields. To obtain a quantitative measure of the significance of those anomalies, we have calculated models that could explain each of them. Because there is insufficient control on various parameters, the models must be considered as representative rather than definitive. They show the types and magnitude of structures that must be called upon to produce the observed anomalies (see "discussion of local gravity models").

Gravity Modeling Programs

Computer programs were used to compute the gravitational effects of two- and three-dimensional bodies. Two-dimensional models were computed using the method of *Talwani et al.* [1959]. The computer program, POLYGON V, was originally written by A. G. Smith of Princeton University and later revised by E. Higgins, J. D. Robertson, and the authors in order to meet changing requirements. Three-dimensional models were computed by a program using the algorithm of *Talwani and Ewing* [1960] that approximates the gravitational effect of source bodies by numerical integration of polygonal laminae approximating the shape of the body. The computer program implementing the Talwani-Ewing algorithm is called THREED and was supplied by J. D. Robertson.

Local Gravity Modeling

Two-dimensional models of the local free-air anomaly fields at J9DC and the four RIGGS base camps were calculated. The free-air anomaly fields at BC and J9DC are particularly close to being two dimensional. At Q13, two dimensionality must be assumed, since the areal extent of gravity measurements is insufficient to define a three-dimensional pattern. Both two- and three-dimensional modeling was done at C-16, where areal coverage is good and two dimensionality is not a good approximation.

All local gravity models incorporated three layers: water (with a density of 1.03 Mg m^{-3}), sediment (2.0 Mg m^{-3}), and "basement" (2.7 Mg m^{-3}), lying upon a "subbasement" of density 3.0 Mg m^{-3} . This choice of layers was based principally on the seismic measurements of *Crary* [1961b] at Little America Station. Variations in water depth can potentially produce the largest gravitational effects because of the large density contrast at the seafloor. The water depth is poorly known near BC, RI, Q13 and J9DC, although the sediment thickness is approximately known from seismic long-refraction profiles. Conversely, at C-16, where the water depth is well known, the sediment thickness is not known. Additional information about the thickness of these layers can be inferred from models of the local gravity anomalies at these base camps.

Base camp BC (grid 7.2°S , 1.8°W). Profiles were completed along two lines. One line, 28 km long, lay on the magnetic north-south line that connects BC with J9; the second line was 24 km long perpendicular to the first. The magnetic north-south profile (Figure 9) looks like the classic example of a gravity anomaly caused by a nearly vertical fault. Its half width is 2.4 km, which implies a depth of 2.4 km to the center of the throw of the fault. For modeling, we assumed that

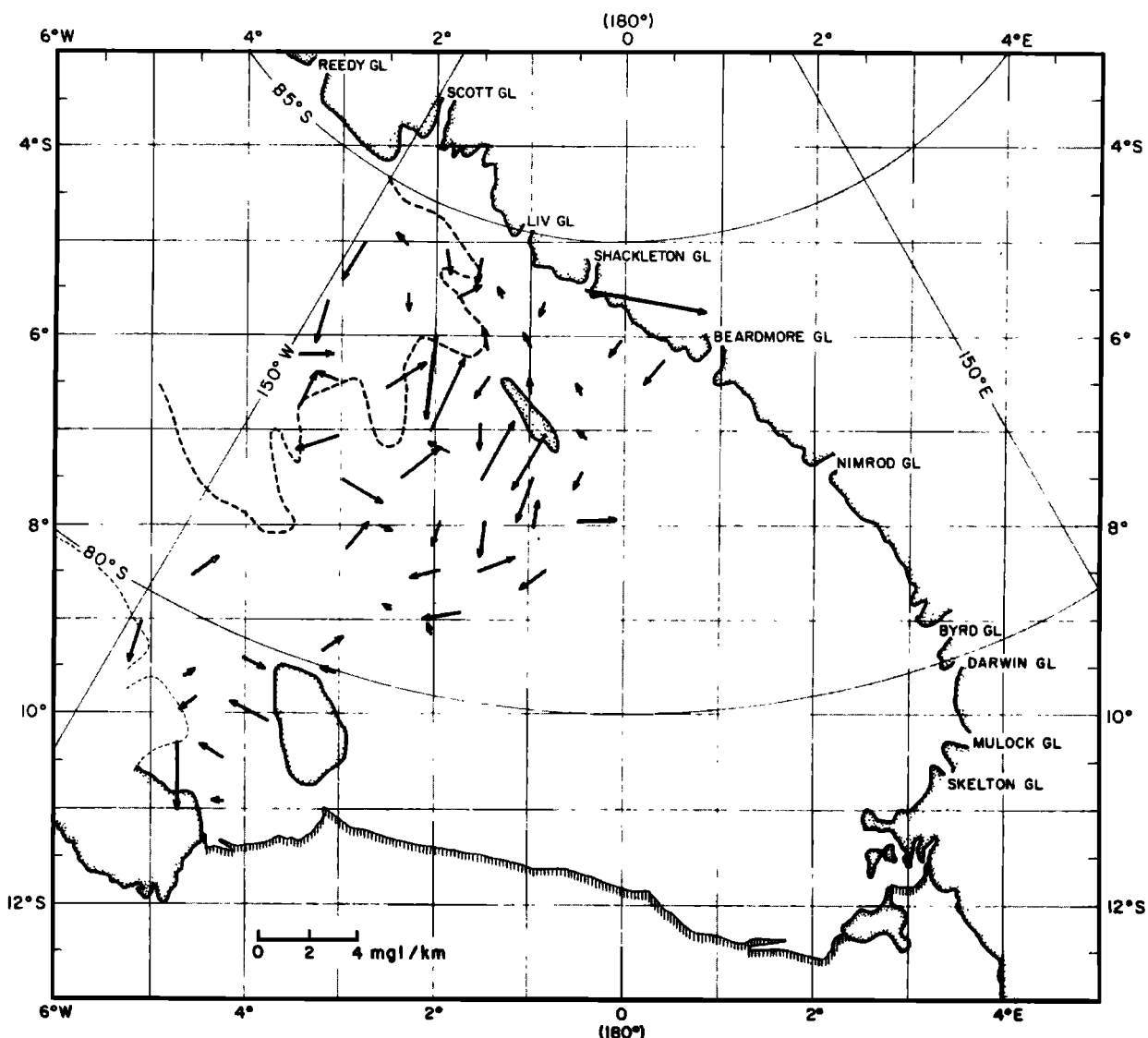


Fig. 8. Map of the Ross Ice Shelf showing the magnitude and direction of the local gravity gradients at RIGGS stations. The gradient scale is near the bottom of the figure.

the ice and water were infinite flat slabs (a discussion of why changes in water layer thickness are inadequate to explain the observed gravity gradients can be found in the section "base camp Q13"), with thicknesses as measured near camp. Two dimensionality is a good approximation here, as shown by the relatively small changes in anomaly on the cross profile (Figure 10). Assuming first a vertical fault, a model was found for which the calculated gravity agreed very well with the observed anomaly (Figure 9). Two additional models were calculated to determine the effect of thickening or thinning the sediment layer by 0.5 km. The slopes for those models were significantly

different from the observed slope, and the root-mean-square residuals increase from 0.20 mGal to 0.31 mGal and 0.49 mGal, respectively, which suggests that a depth estimate of 2.4 km for a vertical fault is accurate to within a few hundred meters. The best model has a sediment thickness ranging from 1.5 to 2.2 km (Figure 9), a range that includes the lower bound sediment thickness of 1.9 ± 0.4 km estimated by Robertson and Bentley [1990] for a seismic refraction path between BC and 20 km on the same line. The average thickness from the gravity model beneath the seismic shot and receiving points is 1.85 km. This agreement provides good support for

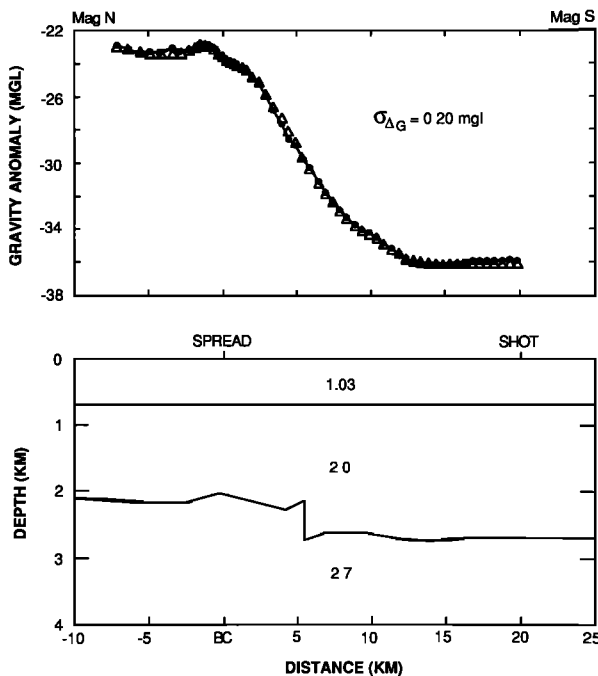


Fig. 9. (Top) Gravity profile and (bottom) modeled density structure along a magnetic north-south line at base camp BC. Dots indicate the observed free-air anomalies, and the triangles represent the modeled values. The standard deviation of the fit between the two is indicated by σ , in the top diagram in megagrams per cubic meters. Densities assumed for the modeling are shown in the bottom diagram, as are the locations of a seismic long-refraction shot and recording spread. Distances are measured from BC.

Robertson and Bentley's [1990] attribution of failure to record seismic arrivals through the bed to travel time delay by thick sediments.

Station J9DC (grid 7.5°S, 1.5°W). Local gravity observations at station J9DC (grid 7.5°S, 1.5°W) were made on a $2 \times 5 \text{ km}$ grid established for radar profiling (Figure 11). The center line, line P, was extended an additional 5 km to the grid northwest (magnetic north), and lines P and B both were

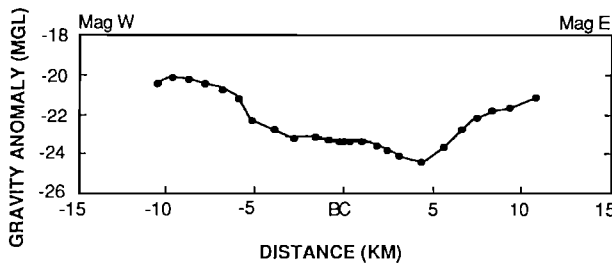


Fig. 10. Profile of free-air anomalies along a magnetic east-west line at base camp BC. Distances are measured from BC.

extended 5 km to the grid southeast (magnetic south). The free-air gravity map at J9DC (Figure 12) shows a steep anomaly increase to the grid northeast (9 mGal in less than 5 km). This gradient, where it is steepest (along the profile line indicated in Figure 12), can be modeled by a vertical step at the sediment-basement boundary 1.2 km grid northeast of J9DC (Figure 13). Also incorporated in the model is a 1° slope of the sea bottom toward the grid northeast. The top of the step was put 600 m below the seafloor to match the indicated sediment thickness found from refraction shooting at station I10S, 78 km grid northeast of J9 [Robertson and Bentley, 1990]. The thickness of the sediment over the bottom of the step, modeled at 1100 m, is essentially uncontrolled. The seismic refraction estimate of sediment thickness is $1700 \pm 300 \text{ m}$ [Robertson and Bentley, 1990]; this figure represents the average of thicknesses beneath J9DC and the seismic recording spread some 21 km to the grid northwest, i.e., only 1 or 2 km from the shot point on the BC refraction profile, where the modeled sediment thickness is 2000 m (Figure 9). That implies a sediment thickness beneath J9DC of $\sim 1400 \text{ m}$, which is compatible with the gravity model. There is, of course, the possibility that the locally steep gravity gradient reflects influences other than a simple fault, such as a three-dimensional effect (suggested by the curvature of the contours in Figure 12) or enhancement by deeper structures, but the necessity for a fault of some kind seems clear.

Base camp RI (grid 9.3°S, 3.1°W). Profiles were completed along two lines. One line, 32 km long, lay on a magnetic north-south line (azimuth 131° grid); the second line was 20 km long running magnetic east-west. Here the gravity anomaly pattern is decidedly not two dimensional. However, the magnetic

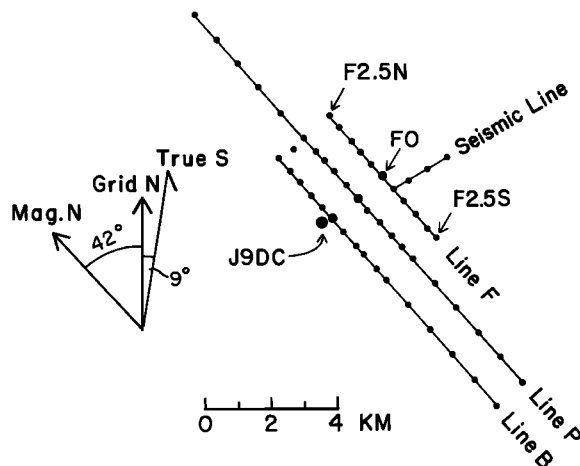


Fig. 11. Diagram of the local gravity survey net near base camp J9DC. Dots denote gravity reading sites.

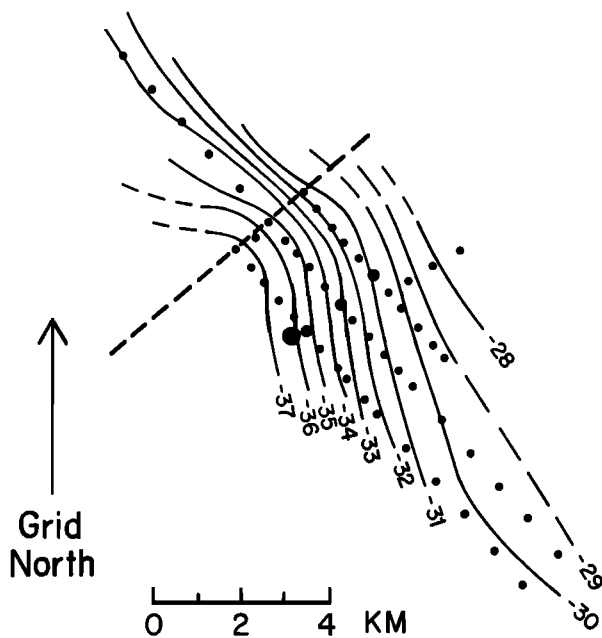


Fig. 12. Contour map of free-air anomalies near base camp J9DC. Dots denote gravity reading sites. The profile shown in Figure 13 is along the dashed line.

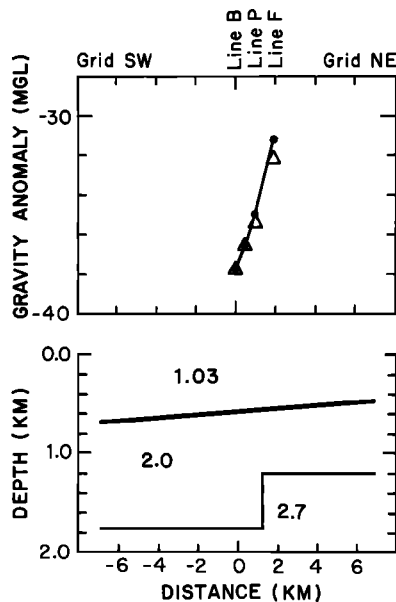


Fig. 13. (Top) Free-air anomaly profile and (bottom) modeled density structure near J9DC. Dots indicate the observed free-air anomalies, and triangles denote the modeled values. Locations of the survey lines shown in Figure 11 are indicated at the top of the diagram. Densities assumed for the modeling are shown in megagrams per cubic meter in the lower diagram. Distances are measured from line B.

north-south profile (Figure 14) can be fit to the first approximation by a simple linear slope; so we will assume that to arise from a sloping seafloor or sediment/basement interface and use two-dimensional modeling for the magnetic east-west profile (Figure 15). To get an estimate of the sediment thickness, the steepest portion of the profile, from -2.0 to 6.0 km, was assumed to reflect a vertical fault, and the half-width method was used to calculate a depth to the middle of the fault of 1.1 km and a throw of 0.3 km.

Again we assumed that the ice and water were infinite flat slabs, and we took their thicknesses to be as those measured near RI, but then the modeled sediment pinched out entirely before the west end of the profile. Moving the fault to a depth of approximately 1.3 km led to a model (Figure 15) that leaves some sediment at -10.0 km and still agrees very well with the observed anomaly.

The magnetic north-south profile suggests a thickening of the sediments and/or an increasing depth of water toward the magnetic north (grid northwest). Regionally, the seafloor shoals to the magnetic northeast (grid north) (Figure 5); so thickening sediments are the more likely cause. How much thickening is difficult to model because considerable isostatic compensation is likely on this scale. Qualitatively, our interpretation agrees with the increasing thickness of sediments inferred by *Robertson and Bentley* [1990]. Taken together, the gravity and seismic profiles indicate, surprisingly, a thinning of sediments going into the trough grid south of station RI.

Robertson and Bentley's [1990] refraction profile was made along the magnetic north-south gravity profile, with the shot at -24 km and receiving spreads at 0, 2, and 4 km. The sediment thickness obtained at 0 km from the gravity model is 0.71 km, which agrees well with *Robertson and Bentley's* [1990] mean thickness of 0.75 km and thickness at 0 km (24 km in their Figure 30) of 0.7 km.

Base camp Q13 (grid 11.0°S, 0.0°E). A total of 95 km of gravity profiling with station spacings of 1–2 km was done near base camp Q13 during the RIGGS III and IV field seasons. Figure 16 shows station locations. The longest gravity profile, line D, runs 46 km grid east-west through Q13 and is coincident grid west of Q13 with the RIGGS IV seismic long-refraction profile. Another long gravity profile, line A, runs through Q13 about 8° east of magnetic north-south coincident to the magnetic south with the RIGGS III seismic long-refraction line. Shorter gravity profiles are along line B, which extends magnetic east 7.6 km, and line C, which runs 11.0 km nearly along magnetic west. Additional data come from Ross Ice Shelf Traverse (RIST) stations [*Crary et al.*, 1962].

Figure 17 shows the free-air anomaly map of the Q13 area. Anomalies range from a high of +13.2

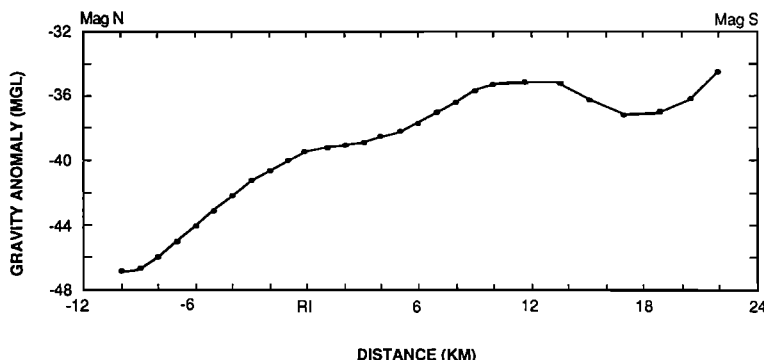


Fig. 14. Free-air anomaly profile along the magnetic north-south line near base camp RI. Distances are measured from RI.

mGal at the grid southeast end of line A to a low of -45.0 mGal approximately 21 km grid west of Q13. A local high of -20 mGal lies approximately 6 km grid east-southeast of Q13. The gravity gradient of approximately 3.5 mGal/km at the grid southeast end of line A is remarkable. Of the 57 gravity gradient measurements for RIGGS stations in the grid western portion of the Ross Ice Shelf, only two are as large as this value: one measurement (station F10; gradient 5 mGal km^{-1}) on Shackleton Glacier adjacent to the Transantarctic Mountains and one measurement (station G7; 3.5 mGal km^{-1}) near the Siple Coast grounding line. The locations of those two large gravity gradients suggest that they may be due to changes in bottom depths. Unfortunately, bottom depth control in the vicinity of Q13 is limited to three seismic reflection determinations: 732 m at Q13, 795 m at 9 km grid west of Q13, and 823 m at RIST station C-8.0 (Figure 16), approximately 14 km grid north-northeast of Q13.

The two seismic refraction profiles provide an indication of sediment layer thickness, although they are somewhat contradictory. These unreversed, one-shot profiles each involved two recording locations (Figure 16), at each of which there was a spread of 12 geophones. Signals were recorded in parallel with different gains on oscillograph channels 1-12 and 13-24. Seismograms from the shot at the end of line A (376 kg in a 15-m hole) are shown in Figure 18. The upper seismogram, recorded on a Texas Instruments model 7000B seismic system, shows fairly good arrivals on six of the twelve traces. Unfortunately, there are no timing lines on the record; a subsequent record with timing lines was used to give a time scale. The lower seismogram, recorded on a Southwest Industrial Electronics (SIE) seismic system, has only weak arrivals of uncertain onset time.

For the refraction recording along line D the charge was 475 kg of explosives located in a 100-m hole at Q13. Receiving spreads were located at 9.1 km and

30.7 km from the shot point (the former, too close to the shot point to record refracted energy from the seabed, was placed there in the unrealized hope of recording a Moho reflection). The seismogram recorded at 30.7 km (Figure 19) shows two different refracted arrivals with apparent velocities of 5.7 ± 0.3 km s^{-1} and 7.8 ± 0.2 km s^{-1} , respectively.

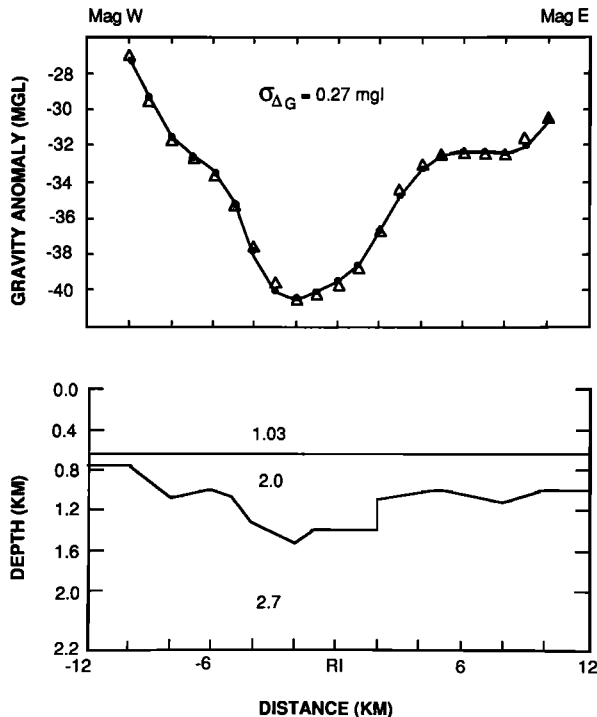


Fig. 15. (Top) Free-air anomaly profile and (bottom) density model along the magnetic east-west line near base camp RI. Observed values are denoted by circles, and modeled values are indicated by triangles; $\sigma_{\Delta G}$ is the standard deviation of the fit. Densities are given in megagrams per cubic meter. distances are measured from RI.

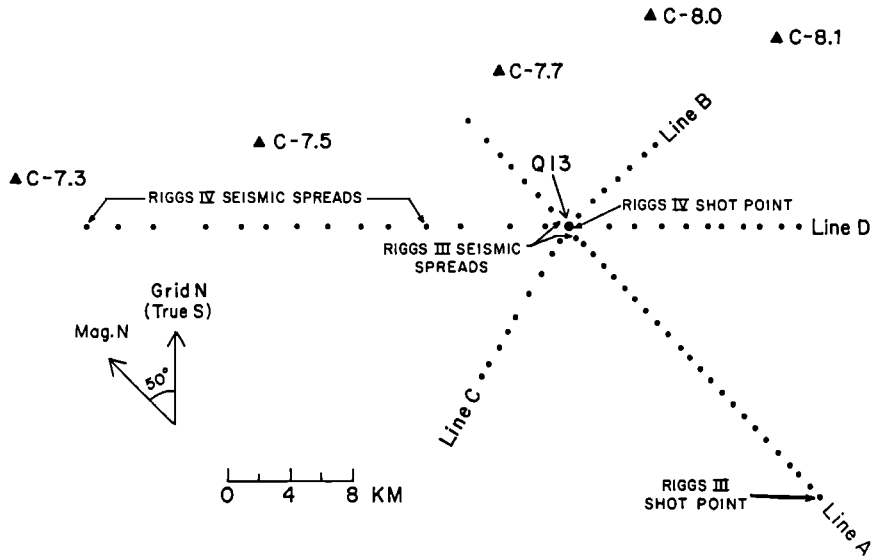


Fig. 16. Diagram of gravity sites, seismic shot points, and seismic spreads near base camp Q13. Circles mark RIGGS sites; triangles denote stations from the International Geophysical Year (IGY) survey of Crary *et al* [1962].

On the travel time plot for line A (Figure 20) a line between the arrivals from the two records yields an apparent velocity, 5.4 km s^{-1} , that agrees with that from the first peaks on record 7000B. If we use 5.4 km s^{-1} for v_4 , the wave speed in the seismic basement, wave speeds of $v_1 = 3.51 \text{ km s}^{-1}$ (vertical average), $v_2 = 1.44 \text{ km s}^{-1}$, and $v_3 = 2.4 \text{ km s}^{-1}$ in ice, seawater, and sediment, respectively, and the thicknesses of the ice and water layers, 328 m and 445 m, respectively, given by Albert and Bentley [1990] for Q13, we calculate a sediment layer thickness of 110 m. However, the strong free-air gravity gradient between the two recording spreads (-1 km to $+1 \text{ km}$ in Figure 22) suggests slopes (according to the model shown in Figure 22) on the seafloor and the sediment-basement contact of about 0.5° and 1° , respectively. These slopes would cause the apparent velocity to be too

small by about 0.3 km s^{-1} , which would imply that $v_4 \approx 5.7 \text{ km s}^{-1}$. That, in turn, leads to a sediment thickness of $\sim 370 \text{ m}$ that is increased further to $\sim 400 \text{ m}$ if the seafloor is shallower under the shot point than beneath Q13, as is implied by the gravity-derived map of seafloor topography (Figure 24).

This large sediment thickness is difficult to reconcile with the travel times for the earlier of the two arrivals along line D (Figure 21), which imply a minimum velocity of 5.6 km s^{-1} (taking the seafloor topography of Figure 24 into account) for no sediments at all. To accommodate 400 m of sediments would require that $v_4 \approx 6.0 \text{ km s}^{-1}$. This value not only does not agree with v_4 on line A, but is substantially higher than wave speeds generally found in the seismic basement in the Ross embayment: $5.5\text{--}5.7 \text{ km s}^{-1}$ beneath the ice shelf [Robertson and Bentley,

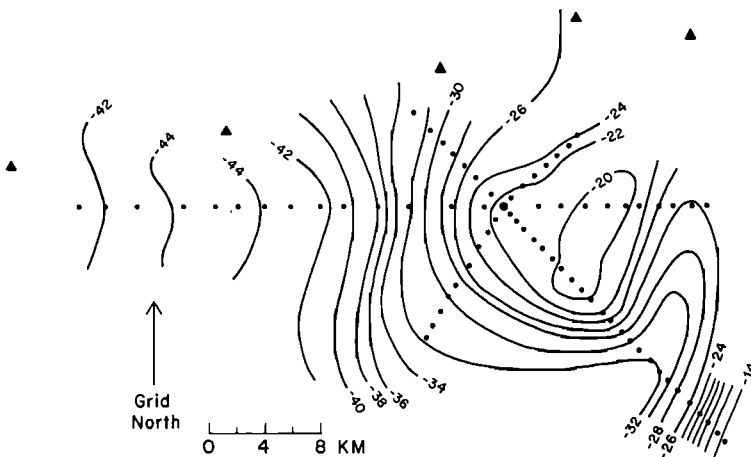
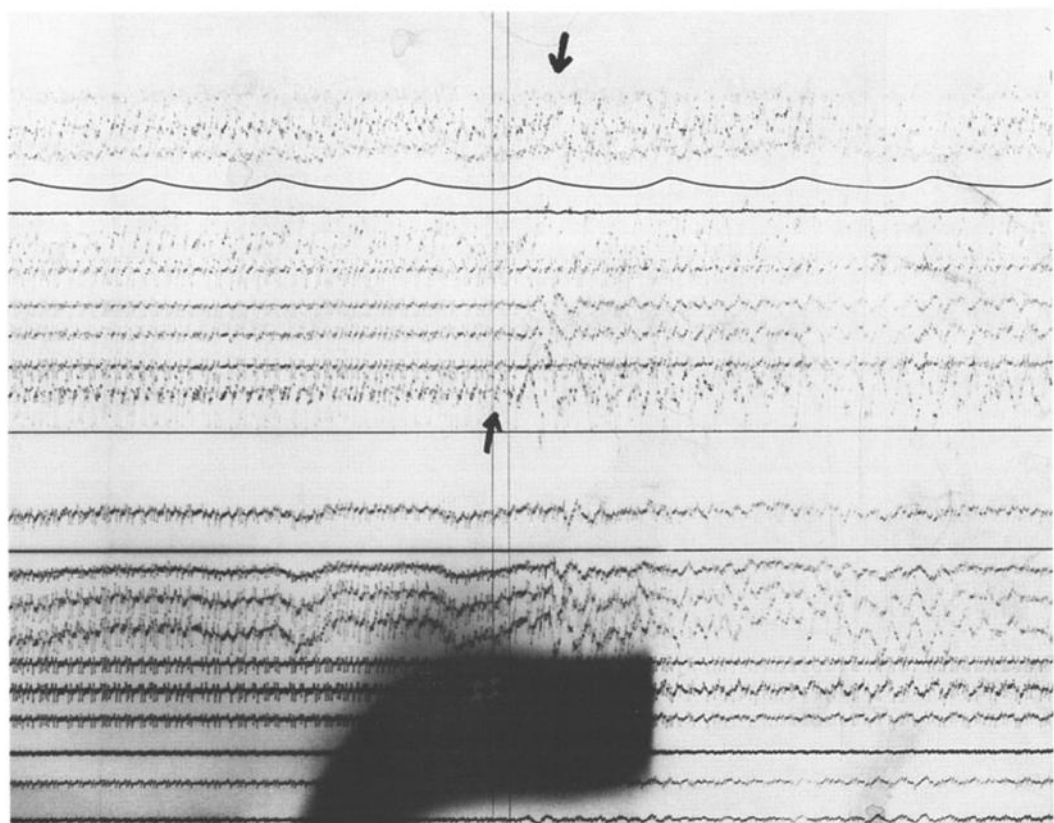
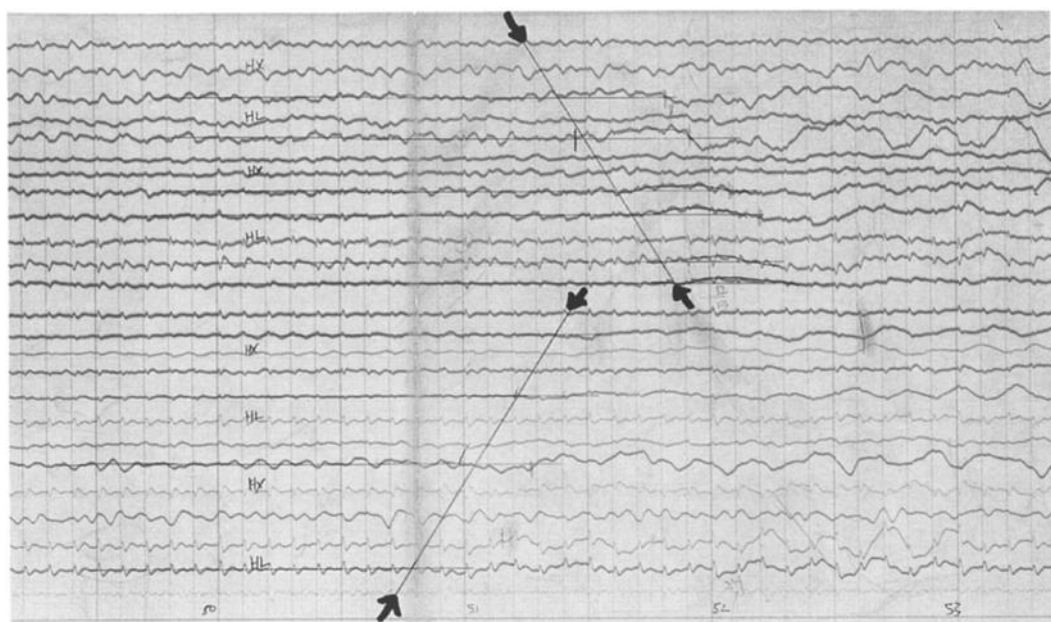


Fig. 17. Map of free-air anomalies near base camp Q13. The contour interval is 2 mGal.



a.



b.

Fig. 18 Portions of seismograms from the long-refraction shot (376 kg in a 15-m hole) on line A recorded near base camp Q13, showing arrivals through seismic basement (arrows). (a) Record 7000 B, recorded 23.4 km from the shot on a spread of 12 geophones 30 m apart recorded at different gain, on traces 1-12 and 13-24. Horizontal motion recorded on traces 7 and 19 (longitudinal) and 3, 10, 15, and 22 (transverse); vertical motion on all other traces. (b) Record 355 recorded 24.7 km from the shot on a spread of 12 geophones 30 m apart, recorded at different gain on traces 1-12 and 13-24. Horizontal motion recorded on traces 4, 10, 18, and 24 (longitudinal) and 2, 7, 15, and 21 (transverse); vertical motion on all other traces.

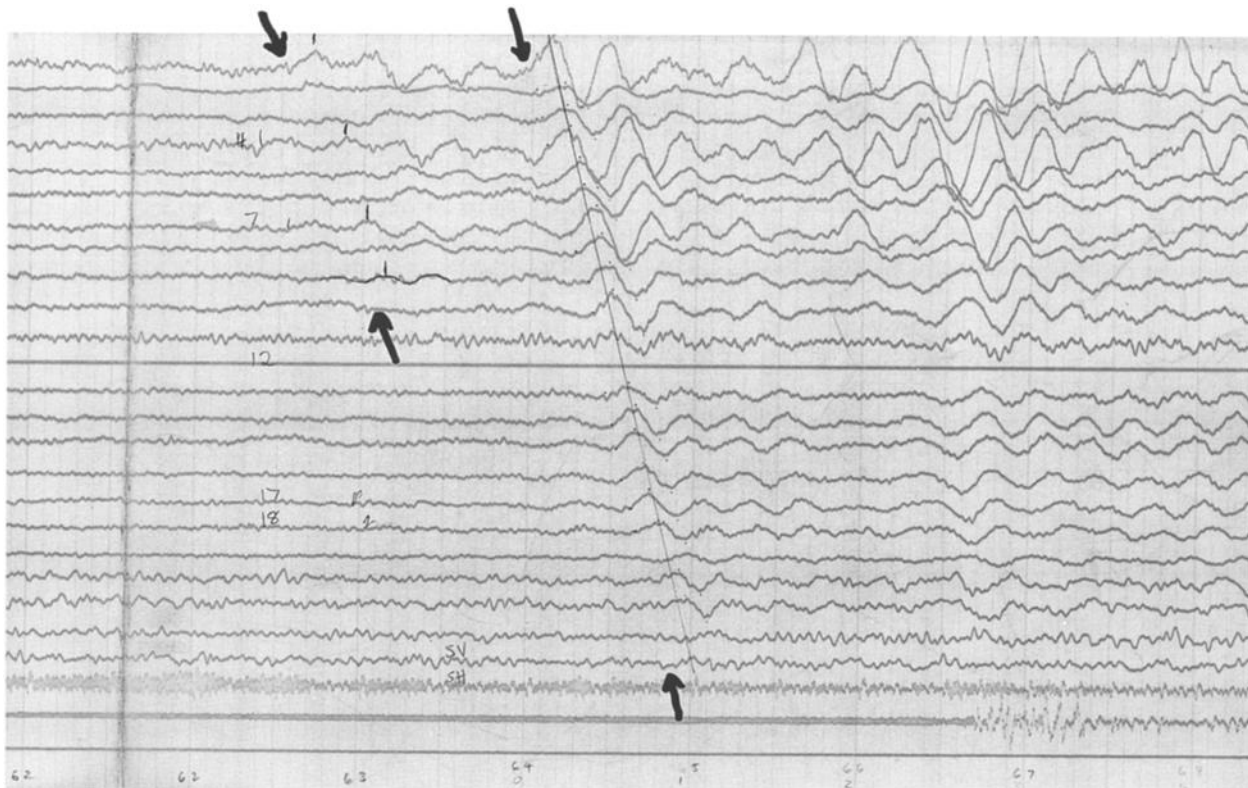


Fig. 19. Portion of the seismogram from the long-refraction shot (475 kg in a 100-m hole) on line D recorded near base camp Q13, showing arrivals through seismic basement, and through a deeper layer (two pairs of arrows). The spread comprised 24 geophones 30 m apart 30.7 km from the shot. Horizontal motion was recorded on traces 23 (longitudinal) and 24 (transverse); vertical motion on all other traces.

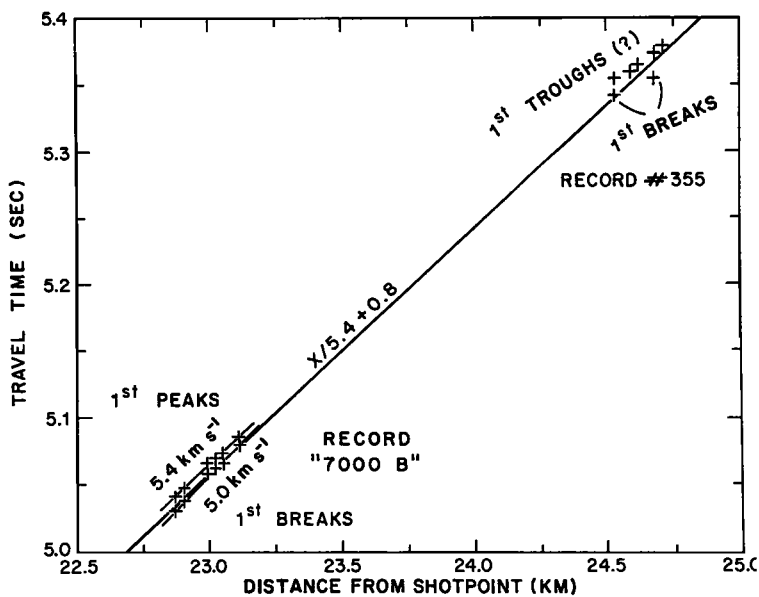


Fig. 20. Travel times from the long-refraction shot on line A recorded near base camp Q13. Apparent velocities from first breaks and first peaks on record "7000B" and a travel time equation for the line between records are shown.

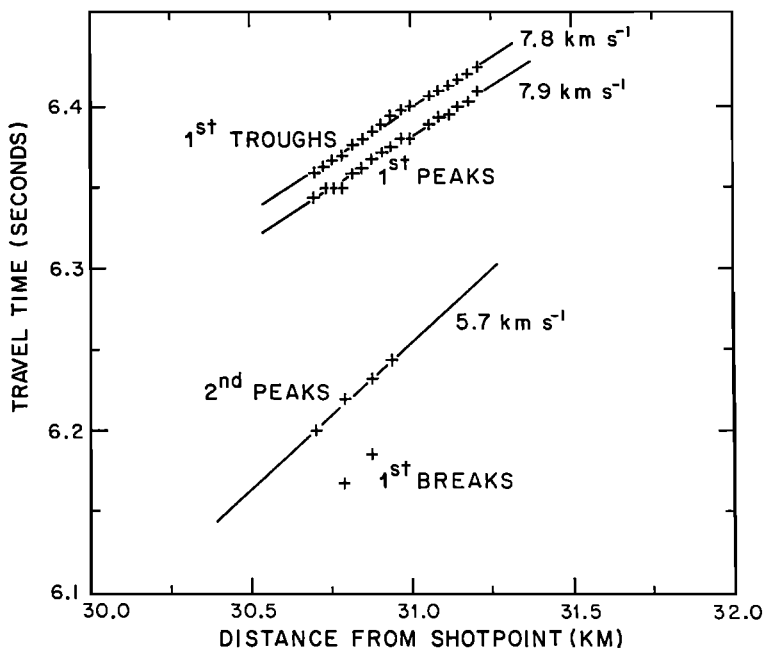


Fig. 21. Travel times from the long-refraction shot on line D recorded near base camp Q13. Apparent velocities for second peaks on the basement arrival and first peaks and troughs on the subbasement arrival are shown.

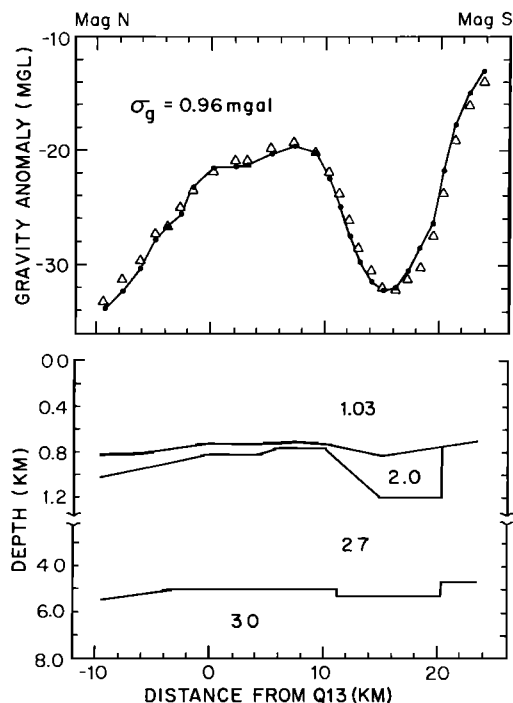


Fig. 22. (Top) Free-air anomaly profile and (bottom) density model along line A near base camp Q13. Observed values are denoted by circles, and modeled values are indicated by triangles; σ_g is the standard deviation of the fit. Densities are given in megagrams per cubic meter. Distances are measured from Q13.

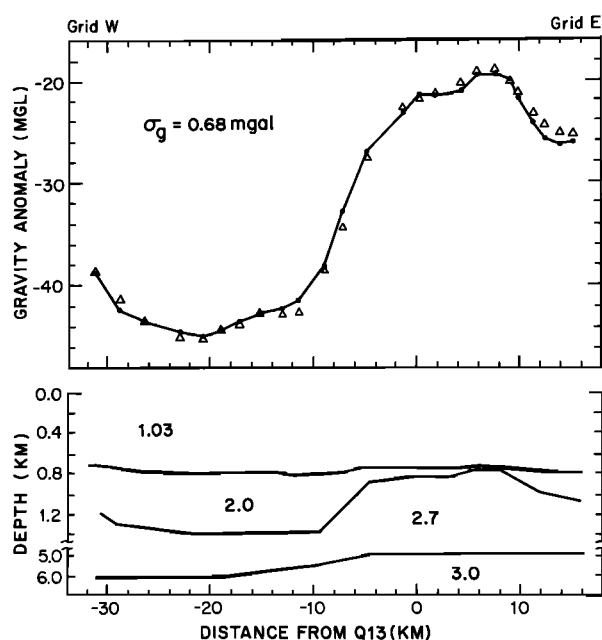


Fig. 23. (Top) Free-air anomaly profile and (bottom) density model along line D near base camp Q13. Observed values are denoted by circles, and modeled values are indicated by triangles; σ_g is the standard deviation of the fit. Densities are given in megagrams per cubic meter. Distances are measured from Q13.

1990] and an average 5.5 km s^{-1} in the Ross Sea [Houtz and Davey, 1973]. We conclude that in fact $v_4 \approx 5.7 \text{ km s}^{-1}$ and that the sediment thickness is highly variable. This variability also shows in the gravity models (Figures 22 and 23). The sketchy nature of the seismic evidence and the various sources of uncertainty in interpretation (absence of timing lines on record 7000B, weak arrivals on record 355, uncertain water depths) preclude more definite conclusions about thicknesses of sediments.

The strong secondary arrival along line D (Figure 19) shows an extremely high apparent wave speed (Figure 21) that cannot reasonably be the true wave speed, v_5 , in the deeper crustal layer. Crary [1961b] found $v_5 = 6.4 \text{ km s}^{-1}$ from a reversed profile near Little America. Several of the sonobuoy profiles in the Ross Sea discussed by Cooper *et al.* [1987] show wave speeds of around 6.4 km s^{-1} ; several others show wave speeds of around 7.4 km s^{-1} . Assuming successively that $v_5 = 6.4 \text{ km s}^{-1}$ and 7.4 km s^{-1} and that the sedimentary layer is thin leads to depths below the seafloor to the high-speed layer of 4.5 and 6 km, respectively.

Free-air anomalies along line A were fitted with a model (Figure 22) that consists of the seawater layer ($\rho_w = 1.03 \text{ Mg m}^{-3}$) and three rock layers with densities of 2.0, 2.7, and 3.0 Mg m^{-3} . The root-mean-square residual for this model of line A is 1.0 mGal. The modeled ocean bottom along line A passes through the measured depth of 732 m at Q13 and follows the trends established by the regional bathymetry with bottom slopes that never exceed 1° . Although bottom depth control along this line consists only of the single value at Q13, it appears likely from the modeling calculations that bottom depth variation can account for no more than approximately 50% of the gravity variation, since a larger contribution would imply excessively large sea bottom slopes. For example, a seafloor slope of almost 6° would be required at 20 km magnetic south to model the 4.3 mGal km^{-1} gravity gradient that occurs there. For comparison, only 7 of the 46 seismically estimated local seafloor dips reported by Crary *et al.* [1962] and none of the 9 reported by Robertson and Bentley [1990] are greater than 1° . Hayes and Davey [1975] report maximum sea bottom slopes of 1.6° for the Ross Sea from bathymetric profiling. Although one of the largest local sea bottom slopes reported by Crary *et al.* [1962], 6.5° over a distance of about 0.2 km, is near Q13 at RIST station C-8.0 (Figure 16), it is highly unlikely that a large dip would extend over distances of several kilometers in light of the generally smooth character of the observed bathymetry in the Ross embayment. A 6° bottom slope over 6 km would correspond to a 600-m change in ocean depth. Such a depth change would require the existence near

Q13 of an ocean deep comparable to Discovery Deep. A change in sediment thickness combined with limited variations in ocean depth appears to be a much more likely way to explain the gravity change at the south end of line A. Assuming a minimal seafloor slope between 15 and 21 km leads to a model with a nearly vertical fault truncating the sediments at 20.4 km (Figure 22). (Deeper structure is shown in the model but is not essential.)

The gravity model for line D is shown in Figure 23. As it is modeled, the 25-mGal range in free-air anomaly along the line principally reflects changes in sediment, from a minimum of 35 m at 8 km and east of Q13 to a nearly constant maximum of about 600 m between 10 km and 29 km grid west of Q13. The high-density layer is put at a depth of 5 to 6 km to accord with the seismic refraction results; the slight slope shown is not essential.

The bottom topography in the vicinity of Q13 was contoured (Figure 24) based upon the three seismic depths and the depths estimated from the gravity modeling. This local coverage suggests that Q13 lies on the grid northwest edge of a localized topographic high trending grid northeast-southwest. The length of this high is not clearly defined by these data or by the regional bathymetry. Its shape may be better defined by the gravity map (Figure 17), which suggests that it is more domelike than ridgelike. The gravity modeling shows that the topographic high reflects a more pronounced high in the subsediment basement.

Base camp C-16 (grid 8.7°S , 14°E). Figure 25 shows the locations of local gravity measurements made at RIGGS base camp C-16. Profile lines EP and DM, each approximately 24 km in length and centered at EP1, were oriented in the true north-south and east-west directions, respectively, whereas line G extends 11 km true southwest from EP1. A gravity reading was taken also at survey point DM107, located 36 km true east of C-16. RIST stations C-15.6, C-16.0, and C-16.1 provide additional isolated data points nearby. Additional gravity measurements were made 0.5 km apart in a $1.5 \times 5.0 \text{ km}$ grid near camp that was used for a radar survey.

Free-air anomaly values around C-16 (Figure 26) show a striking, partially closed low of -52 mGal . From this low, anomalies increase rapidly in all directions except possibly to the grid north, where data are lacking. Regionally, C-16 is located at the grid southeast end of a long linear trend of negative free-air anomalies (Figure 3), which suggests that the anomaly at C-16 may be part of a regional feature. Seismic reflection profiling of ocean depths along lines DM and EP made possible the contouring of the bottom topography near C-16 (Figure 27) and the construction of a Bouguer gravity anomaly map (Figure 28). The Bouguer correction modifies the

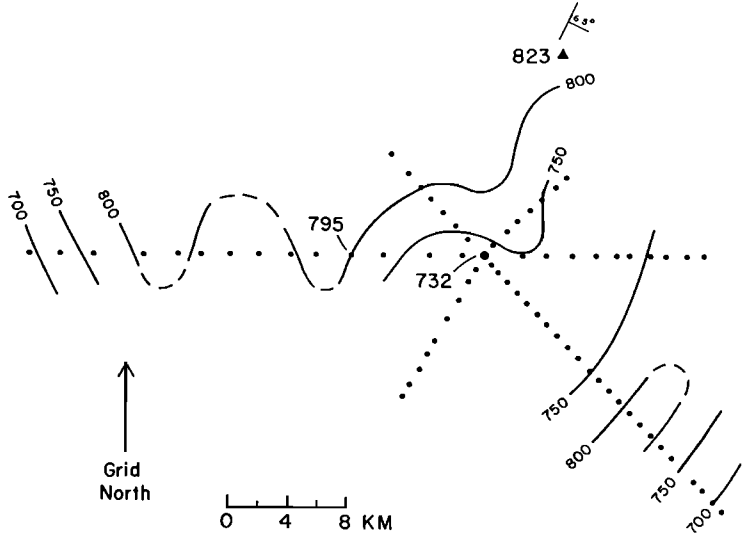


Fig. 24. Map of seafloor depths (meters below sea level) near base camp Q13. The contour interval is 50 m. The seafloor dip symbolized at the top of the figure was measured by Crary *et al.* [1962] from seismic reflections.

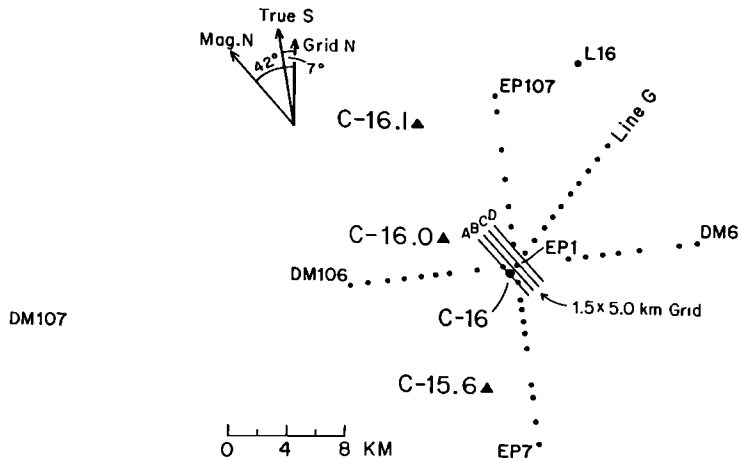


Fig. 25. Diagram of gravity sites near base camp C-16. Circles denote RIGGS sites; triangles denote stations from the IGY survey of Crary *et al.* [1962]. Measurements were made every 0.5 km along lines A, B, C, and D.

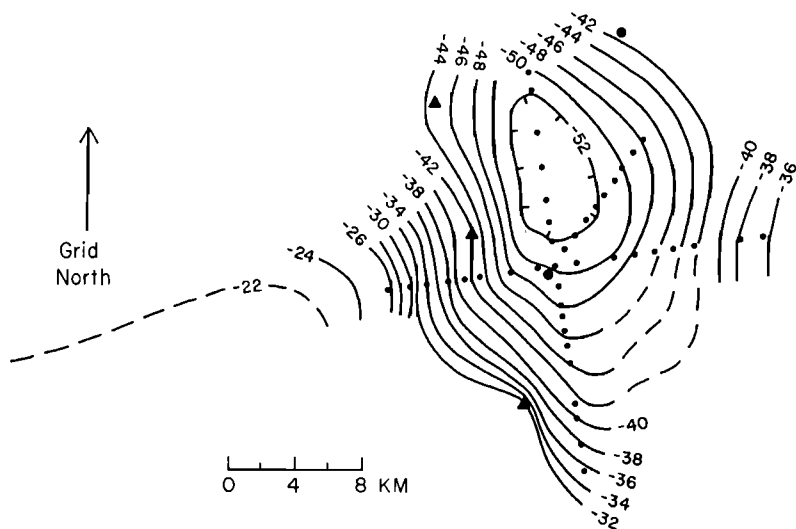


Fig. 26. Map of free-air anomalies near base camp C-16. The contour interval is 2 mGal.

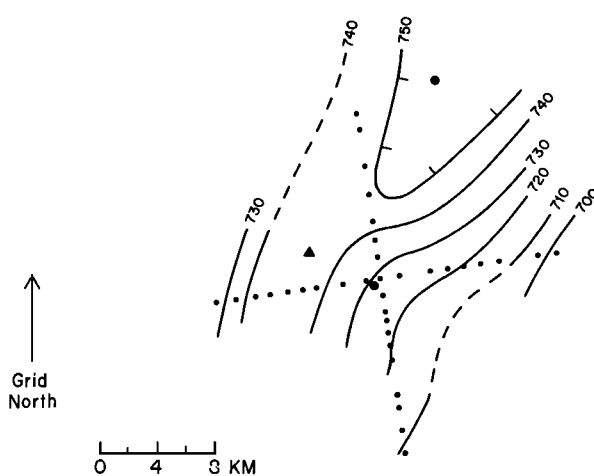


Fig. 27. Map of seafloor depths (meters below sea level) near base camp C-16. The contour interval is 50 m.

character of the free-air gravity map only by changing slightly the gravity gradients to the grid east and west of C-16.

Base camps C-16 and Q13 lie along the same submarine topographic low, which extends from Nimrod Glacier grid south-southwest into the Ross Sea (Figure 5a). The grid northeast-southwest trend of the local bottom topography near C-16 (Figure 27) fits this regional bathymetry well.

Seismograms from a long-refraction shot (295 kg in a 15-m hole) about 23 km grid south of C-16 along line EP are shown in Figure 29. The upper seismogram was recorded on the 7000B seismograph at EP1, 23.7 km from the shot, using a single spread of 12 geophones fed in parallel into channels 1–12 and 13–24. The lower seismogram was recorded on the SIE seismograph 2.6 km true south of EP1, 26.3 km from the shot, using all 24 channels. Both seismograms show good first arrivals on nearly all the traces with vertical geophones. Unfortunately, neither seismogram recorded the shot instant, so only relative travel times for these seismograms can be plotted (Figure 30). Picks of first breaks, first peaks, and first troughs on the 7000B seismograms give apparent velocities of 4.6, 5.4, and 5.0 km s^{-1} , respectively; the average is 5.0 km s^{-1} . Picks of first breaks and first peaks from the SIE seismogram both give apparent velocities of 4.3 km s^{-1} . Figure 31 shows an interpretation of these data in which it is assumed that the true basement velocity is 5.0 km s^{-1} . A 5° dip of the sediment-basement interface beneath the SIE spread is required to match the low apparent velocity observed there. (This section of the bed lies at the grid southern end of the -52-mGal contour in Figure 26.) The thickness of the sediment layer beneath C-16 is undetermined since total travel times were not recorded.

Even though the gravity anomaly is clearly three dimensional, we have fitted several two-dimensional models first for ease in comparing the effects of different structures. Line DM can be modeled entirely in terms of a sedimentary basin that is bounded by vertical faults on both sides (Figures 32 and 33, model a); according to this model, C-16 lies approximately over the center of a graben one side of which, 7 km grid west of C-16, has a throw of 1200 m and the other side of which, 8 km grid east of C-16, has a throw of 750 m. This model gives an estimate of the thickest sediment layer likely to occur at C-16 (2600 m), since the observed gravity gradients could not be produced by more deeply buried faults. Alternatively, the observations can be fitted by more gradual or lesser changes in sediment thickness by the inclusion of deeper structure (Figures 32 and 33, models b–d). It is even possible to fit the observed anomalies without any change in sediment thickness, but only with models that are geologically highly unlikely (for example, Figure 33, model e).

Only one three-dimensional model was fitted to the data. That model (Figure 34) includes a polygonal approximation to the sea bottom contours (Figure 27, solid lines) and a graben on the boundary between layer 3 and layer 4 (heavy dashed lines). A thick layer of low-density sediments in this model (~1750 m) coincides with the gravity low grid north of C-16. Thinning of these sediments to the grid south combined with the effect of approaching the upthrown high-density fault block causes the increasing gravity values at this end of line EP (Figure 35). A similar though smaller effect associated with the fault bounding the grid northeastern side of the graben occurs at the grid northern end of lines EP and G. The details of this model are, of course, subject to the

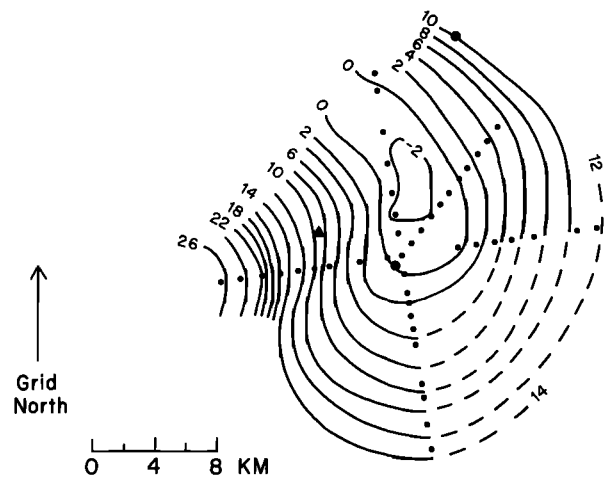


Fig. 28. Map of Bouguer anomalies near base camp C-16. The contour interval is 2 mGal.

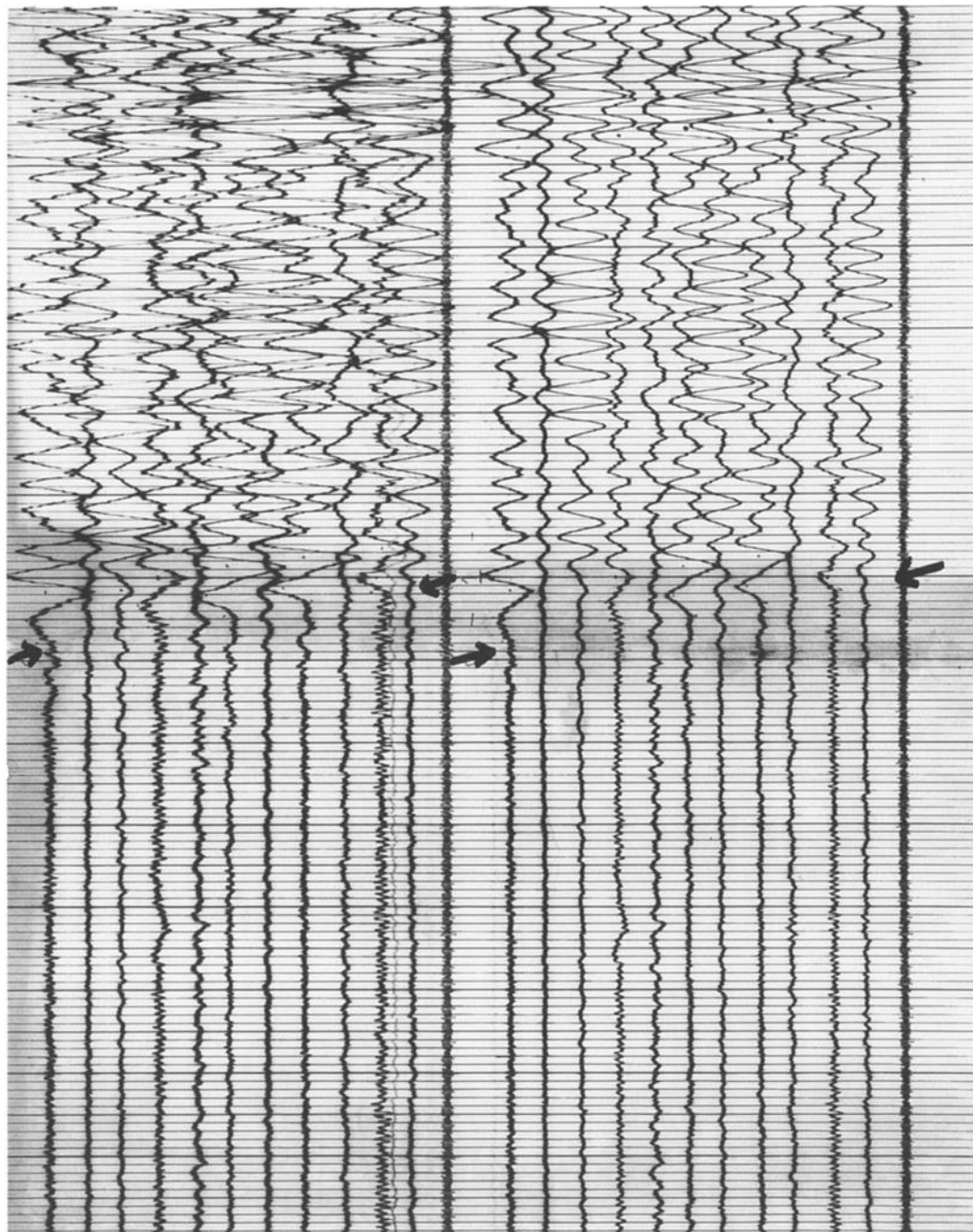


Fig. 29. Portions of seismograms from the long-refraction shot (295 kg in a 15-m hole) recorded near base camp C-16, showing arrivals through seismic basement (arrows). (a) Record 7000B, recorded 23.4 km from the shot on a spread of 12 geophones 30 m apart, recorded at different gain on traces 1-12 and 13-24. Horizontal motion recorded on traces 3, 7, 11, 15, 19, and 23 (longitudinal) and 5, 9, 17, and 21 (transverse); vertical motion on all other traces. (b) Record 174, recorded 26.3 km from the shot on a spread of 24 geophones 30 m apart. Horizontal motion recorded on traces 3, 7, 11, 15, 19, and 23 (longitudinal) and 5, 9, 17, and 21 (transverse); vertical motion on all other traces.

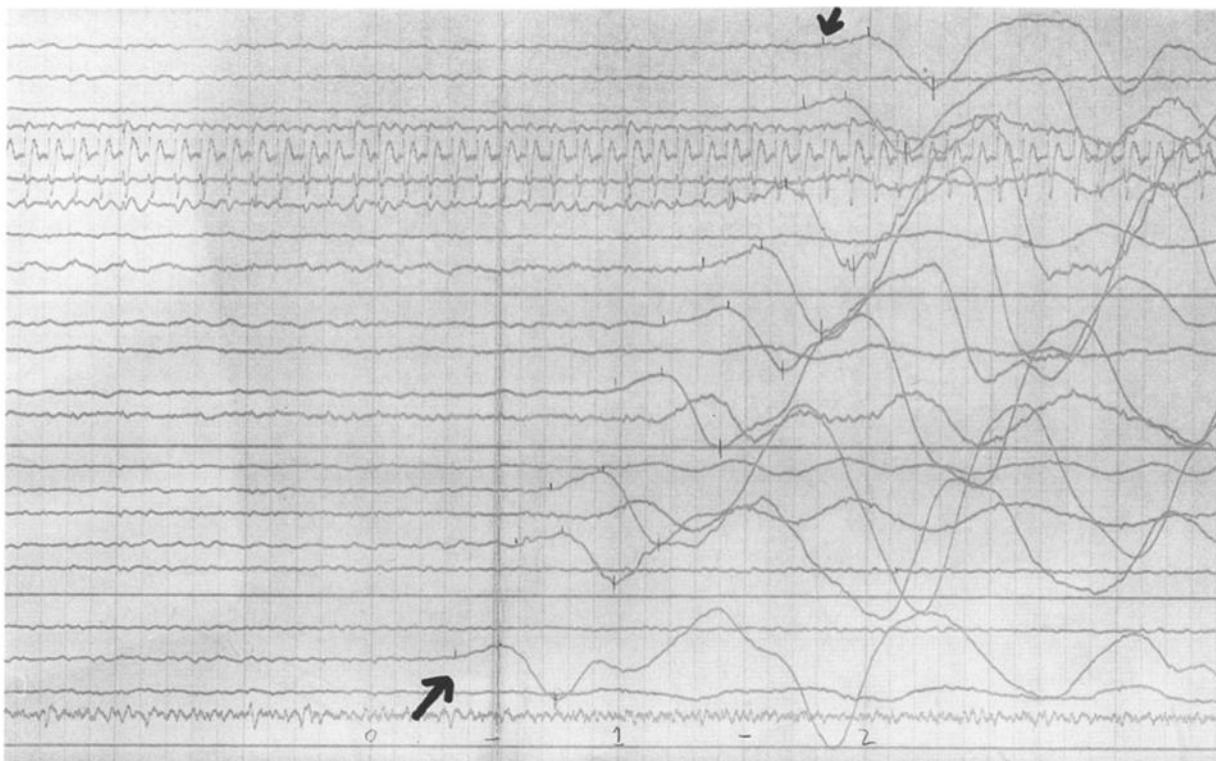


Fig. 29b

same kinds of ambiguities demonstrated by the two-dimensional modeling (Figure 33).

Discussion of Local Gravity Models

The configuration of the low-density sediments at J9DC and Q13 is controlled both by seismic refraction measurements and by the presence of steep gravity gradients that can be satisfactorily modeled only by shallow structure. Restricting sea bottom slopes to 1° or less constrains the gravitational effect of the water

depth to less than half of the total observed variation. At C-16, where the sea bottom is defined seismically, the observed gravity can be modeled satisfactorily by variations in sediment thickness, in basement thickness, or by a combination of the two. However, modeling entirely in terms of the basement/subbasement interface brings the high-density subbasement within 260 m of the seafloor, which is unlikely as no significant magnetic anomalies were observed near C-16 during the Ross Ice Shelf Traverse [Bennett, 1964]. If the basement/subbasement interface is

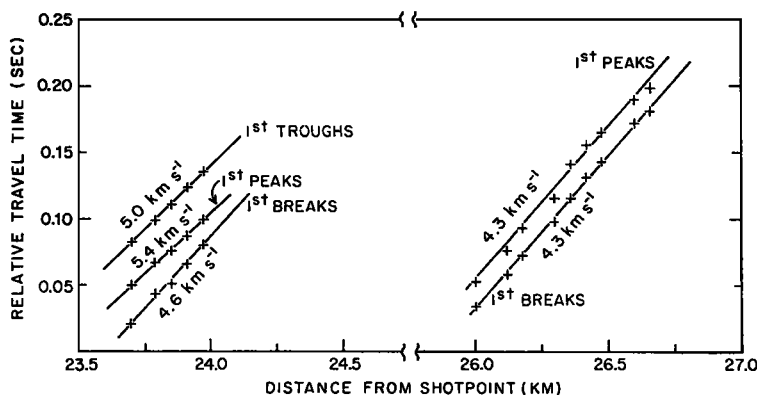


Fig. 30. Relative travel times from the long-refraction shot recorded near base camp C-16. Note the break in the distance scale. Travel times are only relative because no shot instant was recorded.

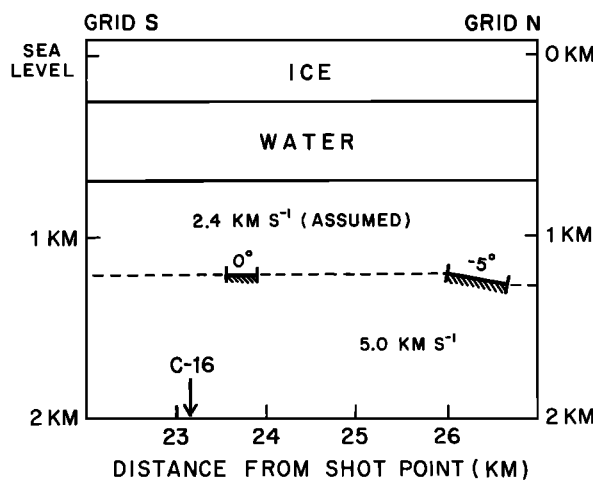


Fig. 31. Seismic section deduced from the travel time plot in Figure 30. Wave speeds in the sediments and the seismic basement and the dips indicated by the cross-spread apparent velocities are shown. The position of C-16 along the line is marked.

everywhere deeper than 5 km, as at Q13, then a decrease in sediment thickness of approximately 900 m to the grid west and 600 m to the grid east is required to fit the observed data. For these intermediate models, the total sediment thickness beneath C-16 can vary from approximately 2.5 km for vertical step changes (vertical faults) to approximately 1 km for gradual changes (slope of $\sim 5^\circ$). The configuration of the basement/subbasement interface is even less constrained, since it is modeled to fit the more "regional" variations of the observed gravity which actually could be due to gradual variations in sediment thickness.

Seismic long-refraction profiles and local gravity observations indicate that the "central high" in the Ross Sea, i.e., the basement ridge that runs along longitude 180° [Davey, 1987], probably extends to the grid north beneath the ice shelf at least as far as Q13. The best fitting two-dimensional gravity model at Q13 includes a vertical fault striking approximately along 030° grid with 450 m of vertical uplift on the grid southeast side.

The sedimentary basin beneath C-16 appears to be related to a regional feature extending grid northwest for several hundred kilometers. More generally, a grid northwest-southeast trend, probably associated with crustal rifting, is, as already discussed, a major feature of the gravity field on the Ross Ice Shelf. The faults modeled at J9DC and RI parallel this trend. However, the fault modeled at BC located only 43 km grid northwest of J9DC strikes approximately normal to this trend; it may be related to a secondary trend, running grid northeast-southwest to the grid northeast of Crary Ice Rise, that is evident in the Bouguer and isostatic gravity anomalies (Figures 4a and 6).

The correspondence of all these local structures to the regional trends in the Ross embayment suggests that they are the result of regional tectonic activity. Furthermore, as the siting of the five stations was not based on any geological knowledge, i.e., was geologically random, the occurrence of pronounced structures at each implies that most of the seafloor beneath the Ross Ice Shelf has been tectonically affected. These facts lend strong support to the concept of the Ross embayment as a zone of rifting [Davey, 1987; Tessensohn and Wörner, 1991; Behrendt et al., 1991].

ANALYSIS OF ISOSTASY IN THE ROSS EMBAYMENT

Spatial Frequency Spectra of Gravity and Bathymetry

Values of gravity and bathymetry were interpolated from the Ross embayment data onto a grid with spacing of 0.5° (55.5 km) extending from grid 5°W to 3.5°E and grid 3°S to 18.5°S (18×32 points). RIGGS stations were planned to be located every 0.5° and were generally placed very close to these grid locations. Over the Ross Sea continental shelf, shipborne coverage is sufficient for good interpolation to these grid points.

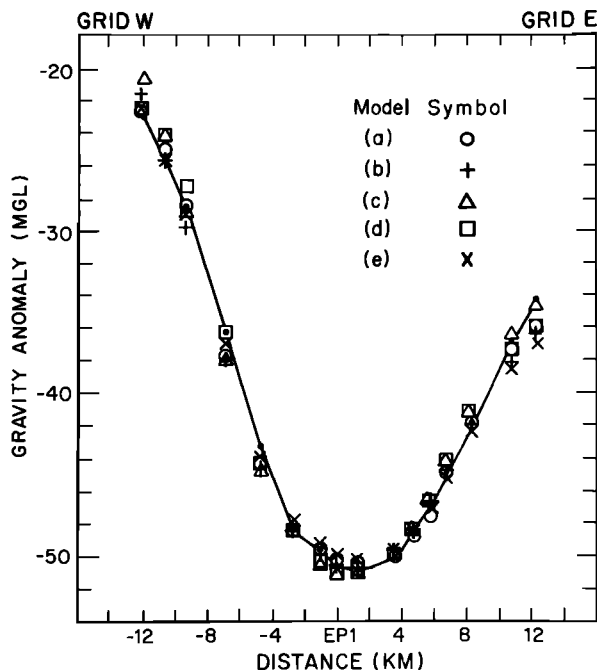


Fig. 32. Free-air anomaly profile along grid east-west line near base camp C-16. Observed values are denoted by solid circles; modeled values refer to the models in Figure 34. Distances are measured from survey point EP1 (Figure 25).

The corners of this rectangular grid extend beyond the edge of the continental shelf to the grid southwest and into the Transantarctic Mountains to the grid northeast. Although some gravity data exist for the Transantarctic Mountains area, no data cover the Ross

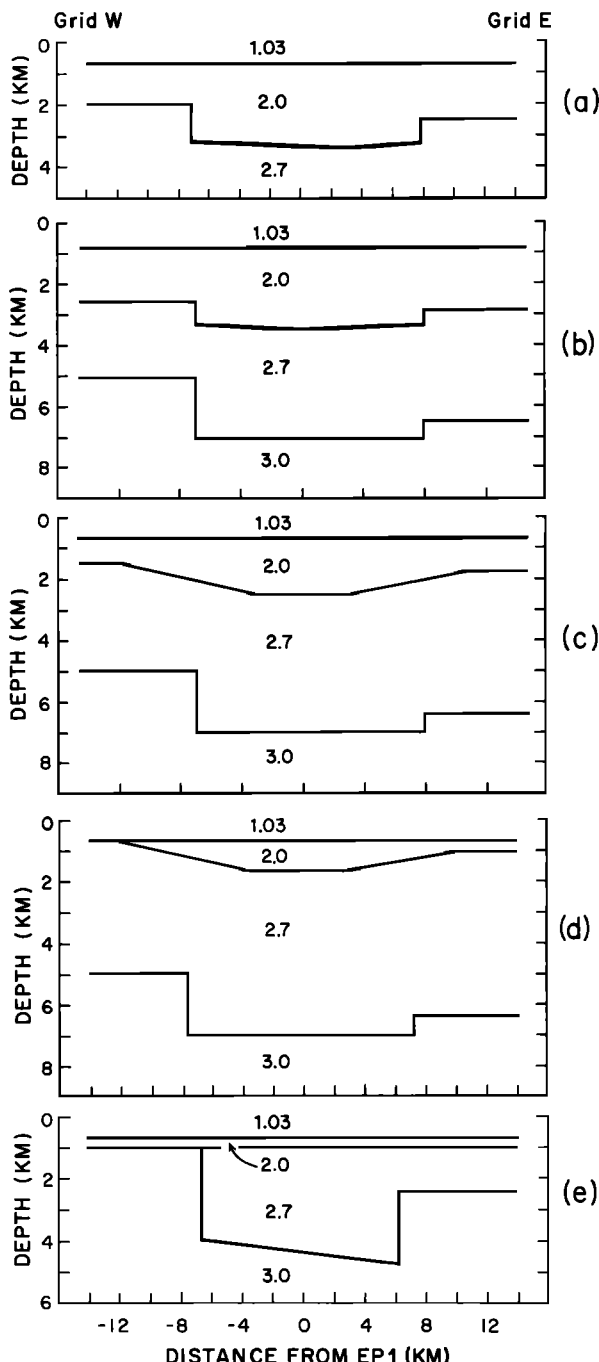


Fig. 33. Density models for the grid east-west profile through survey point EP1 (Figure 25) near base camp C-16. Densities are given in megagrams per cubic meter.

Sea in the grid southwestern corner of the rectangle. As the focus of our study is the Ross embayment, we made no attempt to fill in these corners with realistic estimates of gravity and bathymetry. A plane was fit by least squares to the real data in order to remove the mean and trend. This procedure is standard in time series analysis for minimizing distortions in the finite Fourier transform. Corner data points were then filled with zeroes. Frequency domain representations of the Bouguer and free-air gravity and the bathymetry were computed using MATLAB on an Apple McIntosh computer.

Spatial frequency spectra are generally presented as contour maps of amplitudes of spatial frequency components with the vertical and horizontal axes representing spatial frequencies in the conventional (here grid) map directions. The spectral amplitude at a point (f_x, f_y) on the spatial frequency spectrum represents the amplitude of a "corrugated" wavy surface whose crests and troughs strike normal to the line through the origin and that point. The angular spatial frequency of this corrugated surface $(f_x^2 + f_y^2)^{1/2}$ corresponds to the distance of the point from the origin. Since the original data are represented by real numbers, the spatial frequency spectrum is symmetric about the origin.

Figures 36 to 38 show the magnitudes of the spatial frequency components of the free-air anomaly, Bouguer anomaly, and bathymetry, respectively. The sampling interval of 55.5 km means that the shortest

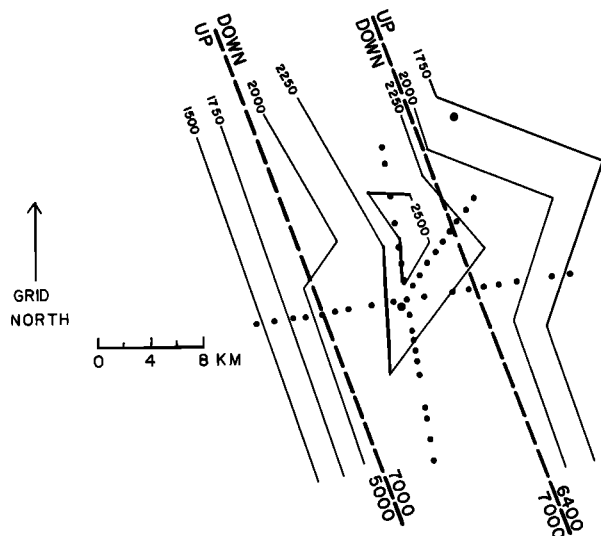


Fig. 34. Diagram of three-dimensional density model, base camp C-16. Solid contours show depths in meters to the base of the sediment layer (layer 2); dashed lines show faults on the boundary between layer 3 and layer 4 with depths to that boundary. Densities are the same as in Figure 33.

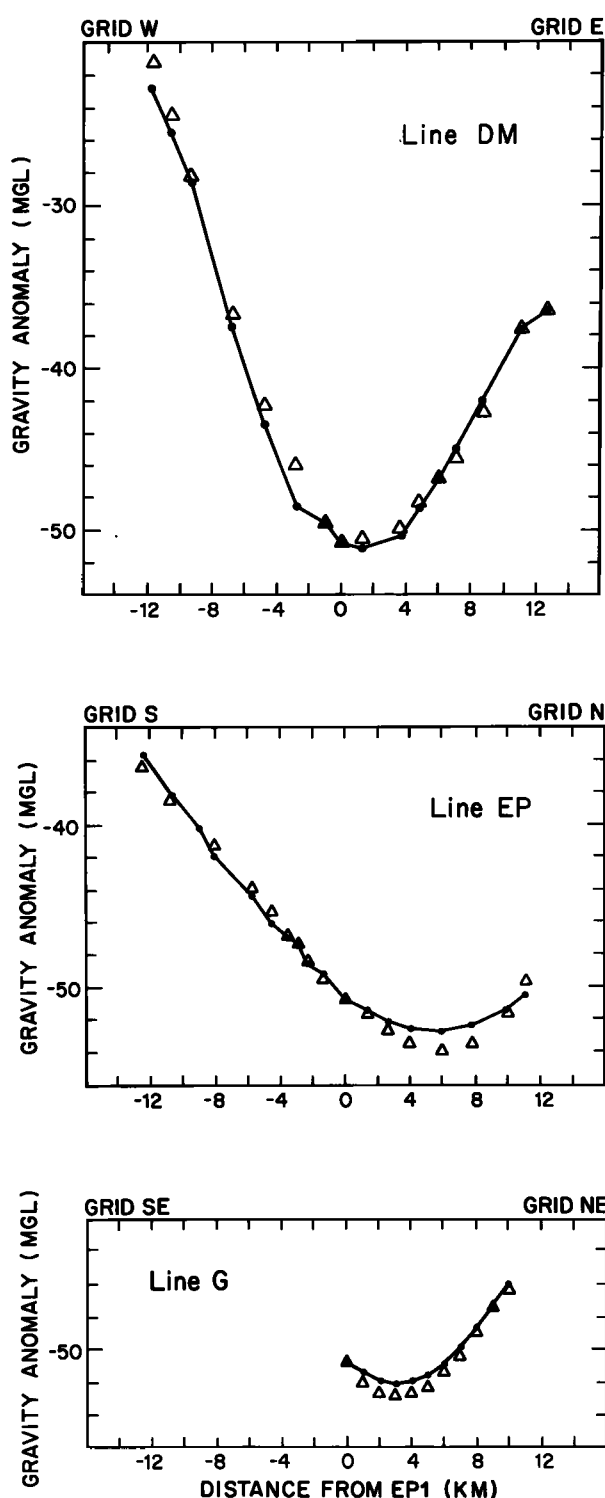


Fig. 35. Free-air anomaly profiles along three lines through survey point EP1 near base camp C-16 (compare Figure 25). Observed values are denoted by circles, and values from the three-dimensional model are shown by triangles.

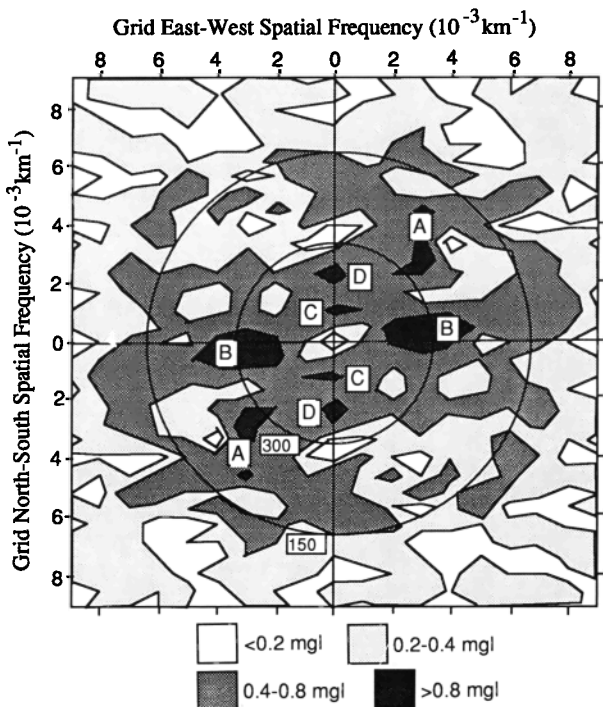


Fig. 36. Spectrum of free-air gravity anomalies in the Ross embayment. Spatial frequencies are in cycles per thousand kilometers. Circles denote wavelengths of 150 km and 300 km, as marked. Letters mark features referred to in the text.

wavelength sampled along each axis is 111 km. The longest wavelengths are 999 km (18×55.5 km) in the grid east-west direction and 1776 km (32×55.5 km) in the grid north-south direction. Circles corresponding to wavelengths of 300 and 150 km are drawn in each figure for reference.

The free-air anomaly (Figure 36) and bathymetric (Figure 38) spectral maps show high amplitudes (>0.8 mGal, >8 m) at wavelengths around 250 km in the grid northeast-southwest direction (labeled A in Figures 36 and 38, respectively) corresponding to spatial features aligned along grid NW-SE. These arise from the bathymetric ridges and troughs and associated free-air anomalies in the grid northwestern part of the embayment. The corresponding north-south features in the grid eastern embayment can be seen near wavelengths of 300 km along the east-west axes in all three spectra (labeled B in Figures 36–38). Both sets of features are prominent on the maps of gravity and bathymetry low-pass filtered at 160 km (Figures 3b, 4b, and 5b).

There are high spectral amplitudes at wavelengths of about 900 km along the grid north-south axis on all three spectral maps (labeled C in Figures 36–38). These correspond to alternating highs and lows that show up clearly on the maps filtered at 870 km (see

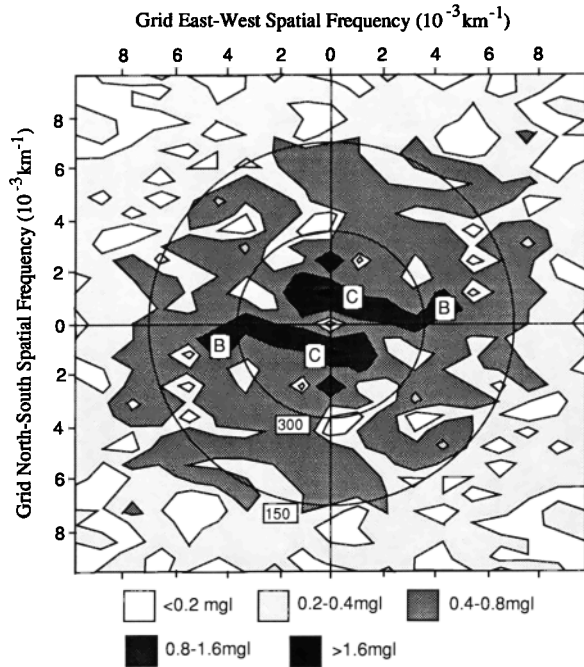


Fig. 37. Spectrum of Bouguer gravity anomalies in the Ross embayment. Spatial frequencies are in cycles per thousand kilometers. Circles denote wavelengths of 150 km and 300 km, as marked. Letters mark features referred to in the text.

Figures 41–43). The free-air anomalies contain an additional spectral maximum at around 500 km on the north-south axis (labeled D in Figure 36) whose origin is uncertain.

Gravity Admittance Function

Insight into the realization of isostasy can be obtained by analyzing the correlation between gravity and elevation [Lambeck, 1988, section 9.1.2]. The filter function or admittance, which relates gravity to bathymetry in the spatial frequency domain, is given by

$$G(f_n, \theta_i) = Z(f_n) \times B(f_n, \theta_i)$$

where Z is the complex admittance, G is the transform of the gravity observations, B is the transform of the bathymetry, f_n is the spatial frequency, and θ_i is the azimuth. We assume that Z is independent of azimuth so that the effects of noise can be reduced by averaging over all azimuths. Then $Z(f_n)$ is estimated by

$$Z(f_n) = \frac{\sum_{i=1}^N G(f_n, \theta_i) \times B^*(f_n, \theta_i)}{\sum_{i=1}^N B(f_n, \theta_i) \times B^*(f_n, \theta_i)} \quad (5)$$

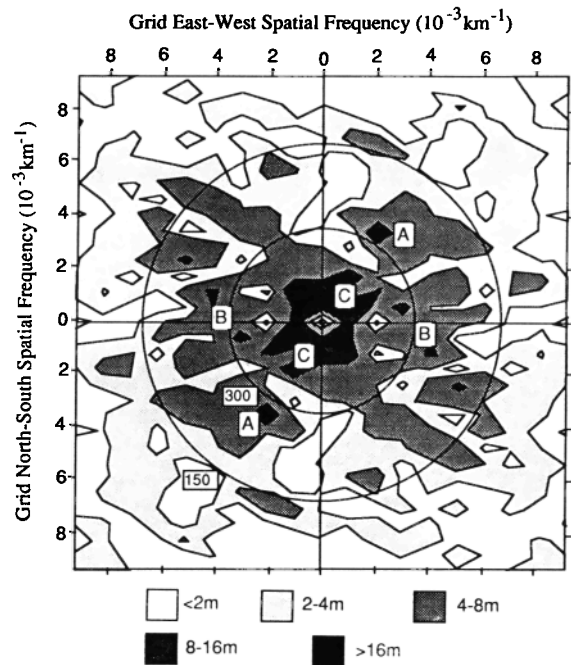


Fig. 38. Spectrum of submarine topography anomalies in the Ross embayment. Spatial frequencies are in cycles per thousand kilometers. Circles denote wavelengths of 150 km and 300 km, as marked. Letters mark features referred to in the text.

The asterisks denote the complex conjugates, and N , which depends upon f_n , is the number of azimuths.

An estimate of the fraction of the power spectrum of the gravity anomalies that results (directly or indirectly) from bathymetry, is given by the coherence $C(f_n)$, where

$$C^2(f_n) = \frac{\left[\sum_{i=1}^N G(f_n, \theta_i) \times B^*(f_n, \theta_i) \right]}{\left[\sum_{i=1}^N B(f_n, \theta_i) \times B^*(f_n, \theta_i) \right]} \cdot \frac{\left[\sum_{i=1}^N G(f_n, \theta_i) \times B^*(f_n, \theta_i) \right]^*}{\left[\sum_{i=1}^N G(f_n, \theta_i) \times G^*(f_n, \theta_i) \right]} \quad (6)$$

(see, e.g., McKenzie and Bowin [1976]).

The free-air gravity admittance and coherence functions were computed for the Ross embayment from equations (5) and (6) in spatial frequency bands $1/1776 \text{ km}^{-1}$ wide. Sixteen points were computed for spatial frequencies $n/1776 \text{ km}^{-1}$, $n = 1-16$; N

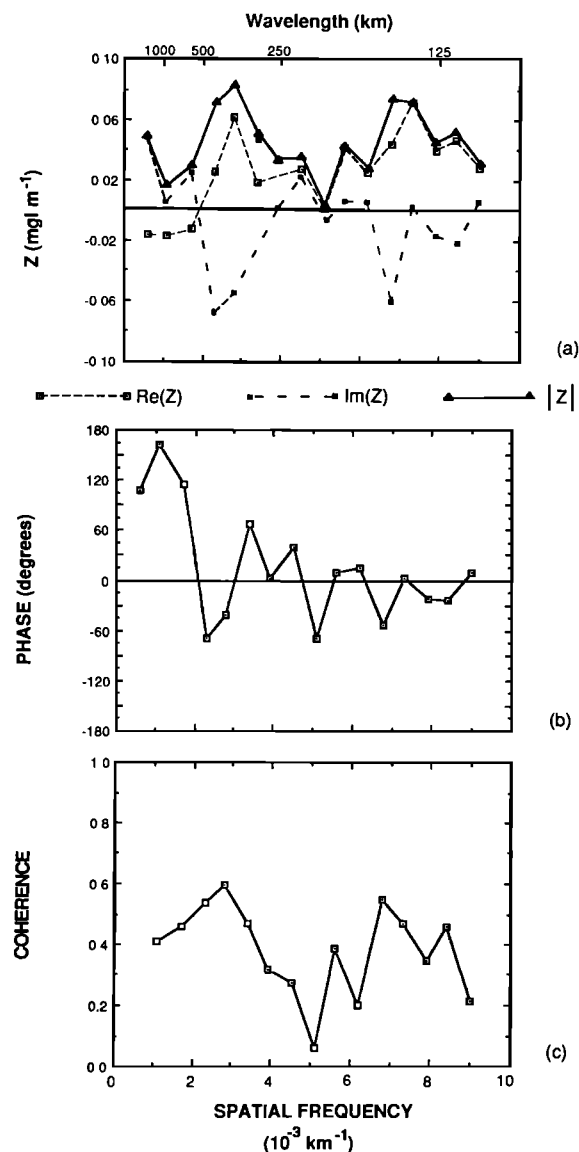


Fig. 39. Spectrum of the free-air gravity versus bathymetry admittance function: (a) real part (open squares), imaginary part (solid squares), and magnitude (triangles); (b) phase; (c) coherence.

correspondingly ranged from 1 to 24. Mean values were subtracted from both the gravity anomalies and the bathymetry, so smaller water depths and less negative anomalies were transformed into positive numbers. The real part, imaginary part, and magnitude of $A(f)$ are plotted in Figure 39a, its phase is plotted in Figure 39b, and the coherence is plotted in Figure 39c.

For very high spatial frequencies, i.e., topographic wavelengths short enough not to be isostatically compensated, one would expect a high coherence

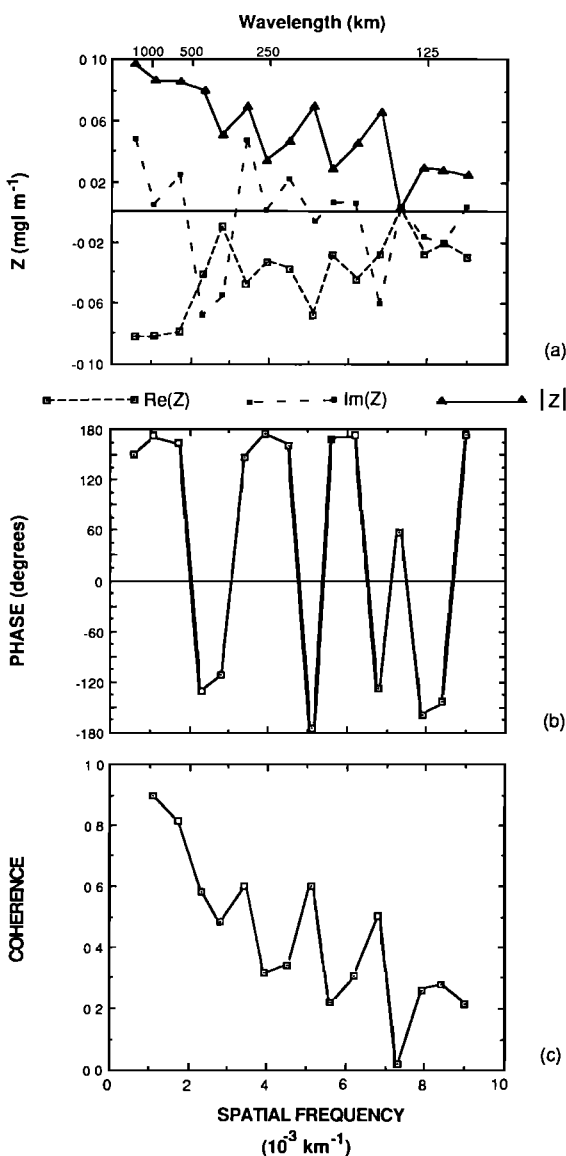


Fig. 40. Spectrum of the Bouguer gravity versus bathymetry admittance function: (a) real part (open squares), imaginary part (solid squares), and magnitude (triangles); (b) phase; (c) coherence.

between the free air anomaly and the bathymetry, and the magnitude of Z should approximate the submarine Bouguer correction: 0.07 mGal m⁻¹. If topography and compensation were the only effects, $|Z|$ should then diminish toward zero at the wavelength limit. In the presence of additional sources of gravity anomalies unrelated to the topography, the coherence would also diminish with increasing wavelength.

The representation of the Ross embayment (Figure 39) is far different. The admittance and the coherence both show strong maxima around wavelengths of 150

km and 350 km and a minimum around 200 km; at both maxima, $|Z|$ equals or even exceeds the expected value for totally uncompensated topography. Clearly, these maxima must reflect structure beneath the seafloor. Since the phase of Z is about 0° (Figure 39b), there must be at least the same thickness of relatively low density rocks beneath the topographic troughs as beneath the ridges. The existence of two maxima suggests that there are two characteristic wavelengths to the structure, a feature that is not readily apparent from the spatial or spectral maps themselves. The large amplitude at 350 km makes it unlikely that this peak is simply a subharmonic, or modulation, of the 150-km peak. This evidence of deep structure correlated with the ridge-trough topography is further support for the concept of the Ross embayment as a rift zone.

At the longest wavelengths, $|Z|$ again becomes large, but with a phase that is closer to 180° than to 0° . This we interpret to reflect incomplete isostatic recovery after retreat of a more extended late Pleistocene grounded ice sheet. The phase reversal arises because of the decrease in water depth grid westward beneath the ice shelf, a decrease that is unrelated to, and in fact masks, the remnant glacio-isostatic depression (see the next section).

The decrease in free-air gravity grid westward across the embayment combined with the decrease in water depth leads to the pronounced Bouguer gravity gradient seen in Figure 42. That combination appears also in the Bouguer gravity admittance and coherence functions (Figure 40) as the large magnitude, reversed phase, and high coherence at long wavelengths. The disappearance of the peaks around 150 km and 350 km shows that the free-air anomalies at these wavelengths are caused principally by the submarine topography, a fact upon which we already commented in noting that the corresponding values of $|Z|$ for the free-air anomalies were about 0.07.

The strong nonisostatic signal in the Ross embayment precludes the modeling of the computed admittance in terms of the isostatic response of the Earth's crust and upper mantle.

Speculations on Glaciological Implications of Isostatic Gravity

To search for the imprint of isostasy, we have filtered the gravimetric and bathymetric maps at 870 km (Figures 41–43). A pronounced inverse correlation between bathymetry and Bouguer anomalies, which indicates that the large-scale features are isostatically compensated, is apparent in Figures 42 and 43. The ratio of gravity difference to bed elevation difference between the relatively shallow water around Iselin Bank in the grid southern Ross Sea and

the deep water along the Transantarctic Mountain front beneath the grid eastern Ross Ice Shelf is about $-0.07 \text{ mGal m}^{-1}$, which is the value expected for oceanic compensation. However, the same ratio computed for the grid eastern to the grid northwestern Ross Ice Shelf is about $-0.10 \text{ mGal m}^{-1}$, which is 50% greater (numerically) than the value expected for oceanic compensation and is associated with a pronounced gradient in the free-air anomaly (Figure 41). We believe that this extra 50% is due to glacio-isostatic imbalance.

If part of the regional free-air anomaly field in the Ross embayment does indeed arise from remnant crustal depression caused by ice loading during late Wisconsin/Holocene time, then it reflects the former extent of the Antarctic ice sheet in this area, the degree of isostatic equilibrium attained by this ice sheet, and its retreat history. We will attempt first to separate the glacio-isostatic signal from other gravity effects.

Free-air gravity anomalies from Goddard Earth Model (GEM) 10B computed through degree and order 4 (Figure 44) should represent deep-seated mantle effects [Bentley *et al.*, 1982]. Gravity anomalies on our low-passed free-air anomaly map (Figure 41) are more negative than the low-order satellite-derived gravity field and have a different trend: the latter increase grid northward from -14 mGal to -11 mGal across the Ross embayment, whereas the former decrease from greater than -20 mGal to less than -28 mGal grid northwestward across the ice shelf.

There is little doubt that during late Wisconsin time the grounded portion of the West Antarctic ice sheet extended farther seaward into the Ross embayment than at present, but the amount and duration of the grounding line advance are a matter of some dispute. The "maximum" reconstruction of Denton *et al.* [1989] for the late Wisconsin maximum (Figure 45) indicates that the West Antarctic ice sheet was then approximately 1000 m thick near the present grounding line and that the grounded margin was near the edge of the continental shelf. Evidence from Ross Sea cores also suggests that grounded ice reached the continental shelf margin during the late Pleistocene [Kellogg *et al.*, 1979]. Geologic data in McMurdo Sound and the dry valley areas yield minimum ages of ice retreat ranging from 3000 to 10,000 years B.P. [Denton *et al.*, 1970] and have further been interpreted as showing that the grounding of the ice sheet occurred more than 47,000 years B.P. [Denton and Borsig, 1974], long enough ago for isostatic compensation to have become virtually complete.

Not all investigators accept this model. Some analyses of marine and glacial geologic evidence indicate only minor expansions of the grounded ice

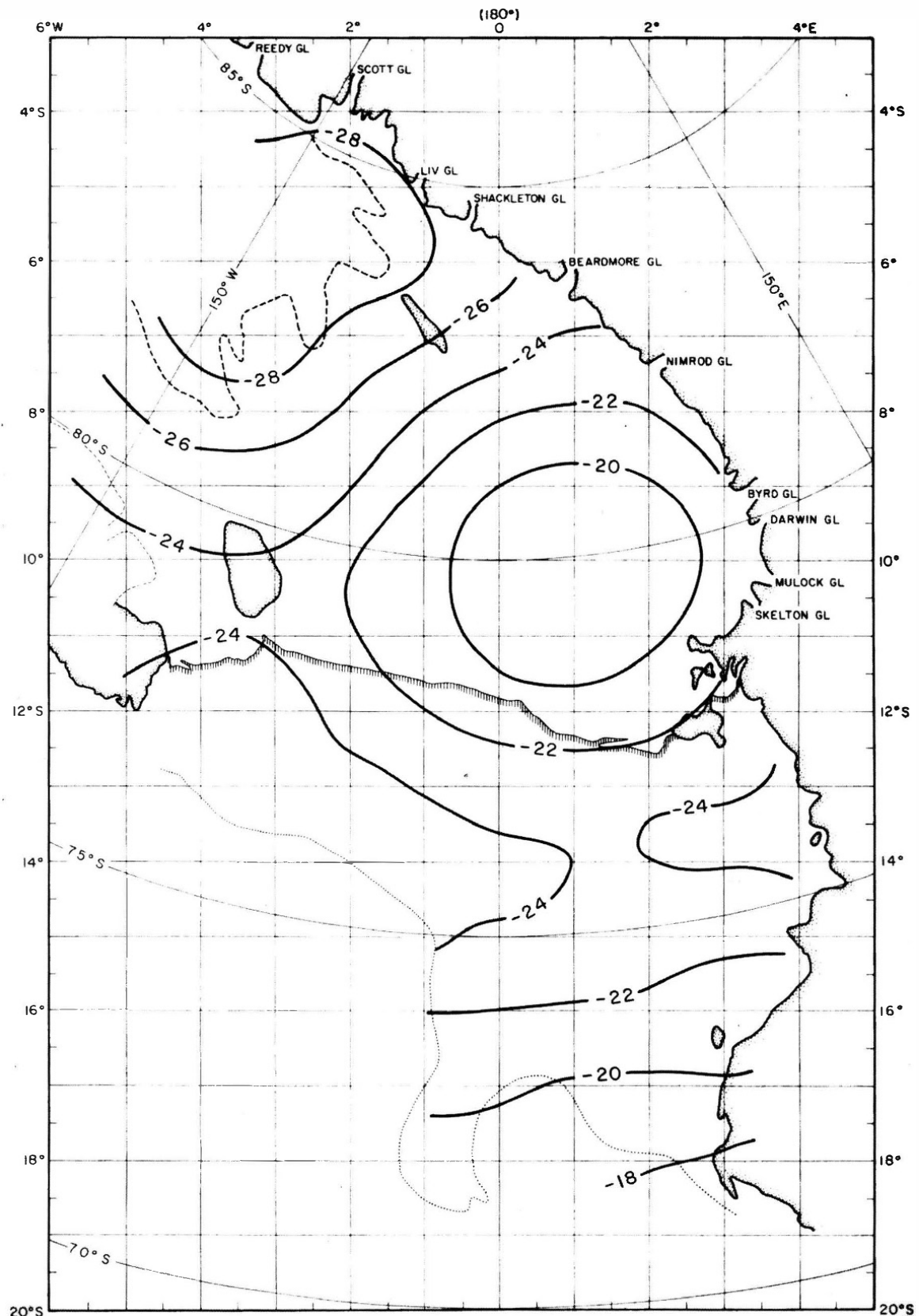


Fig. 41. Map of free-air anomalies in the Ross embayment, filtered to remove wavelengths less than 870 km. The contour interval is 10 mGal.

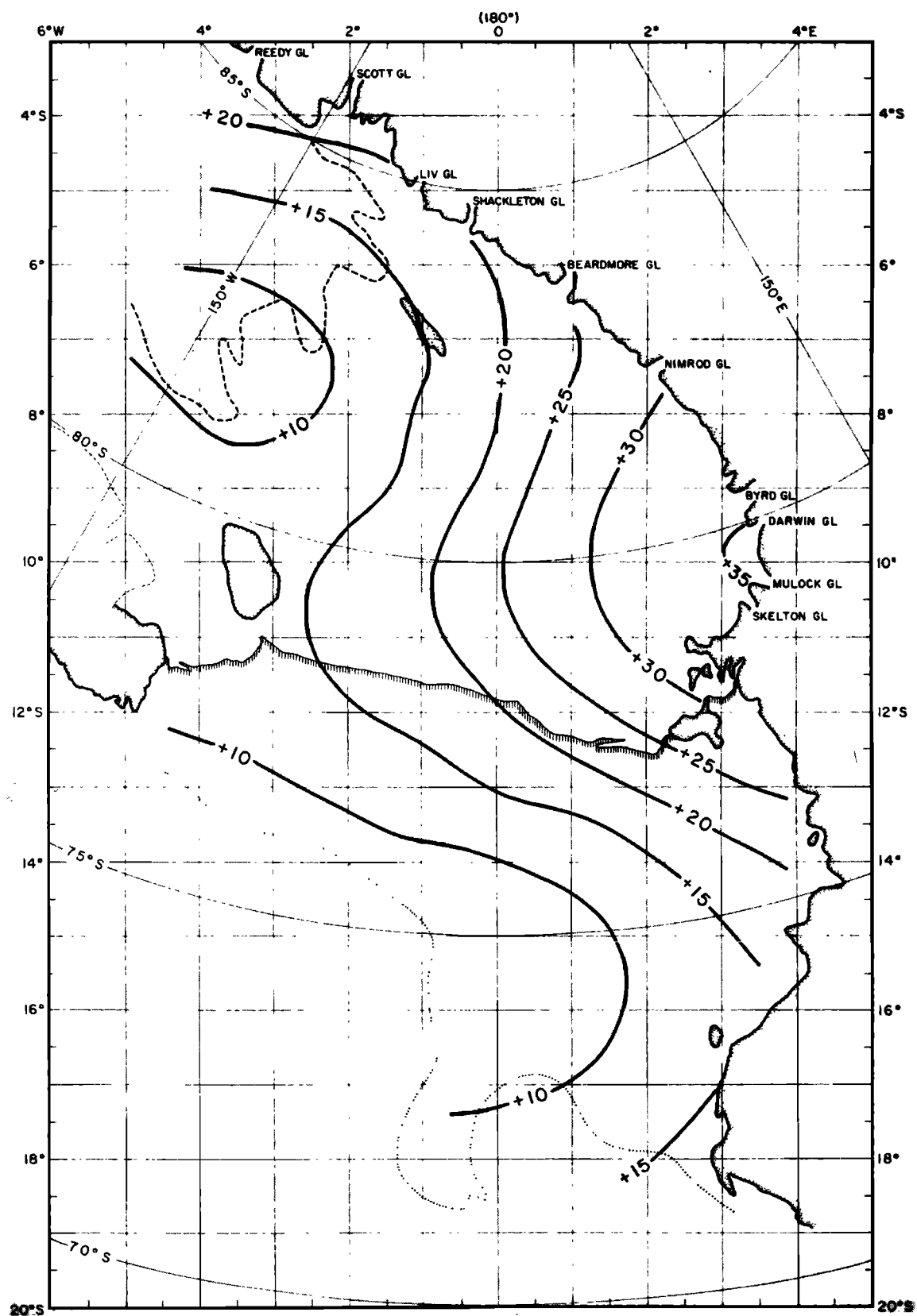


Fig. 42. Map of Bouguer anomalies in the Ross embayment, filtered to remove wavelengths of less than 870 km. The contour interval is 10 mGal.

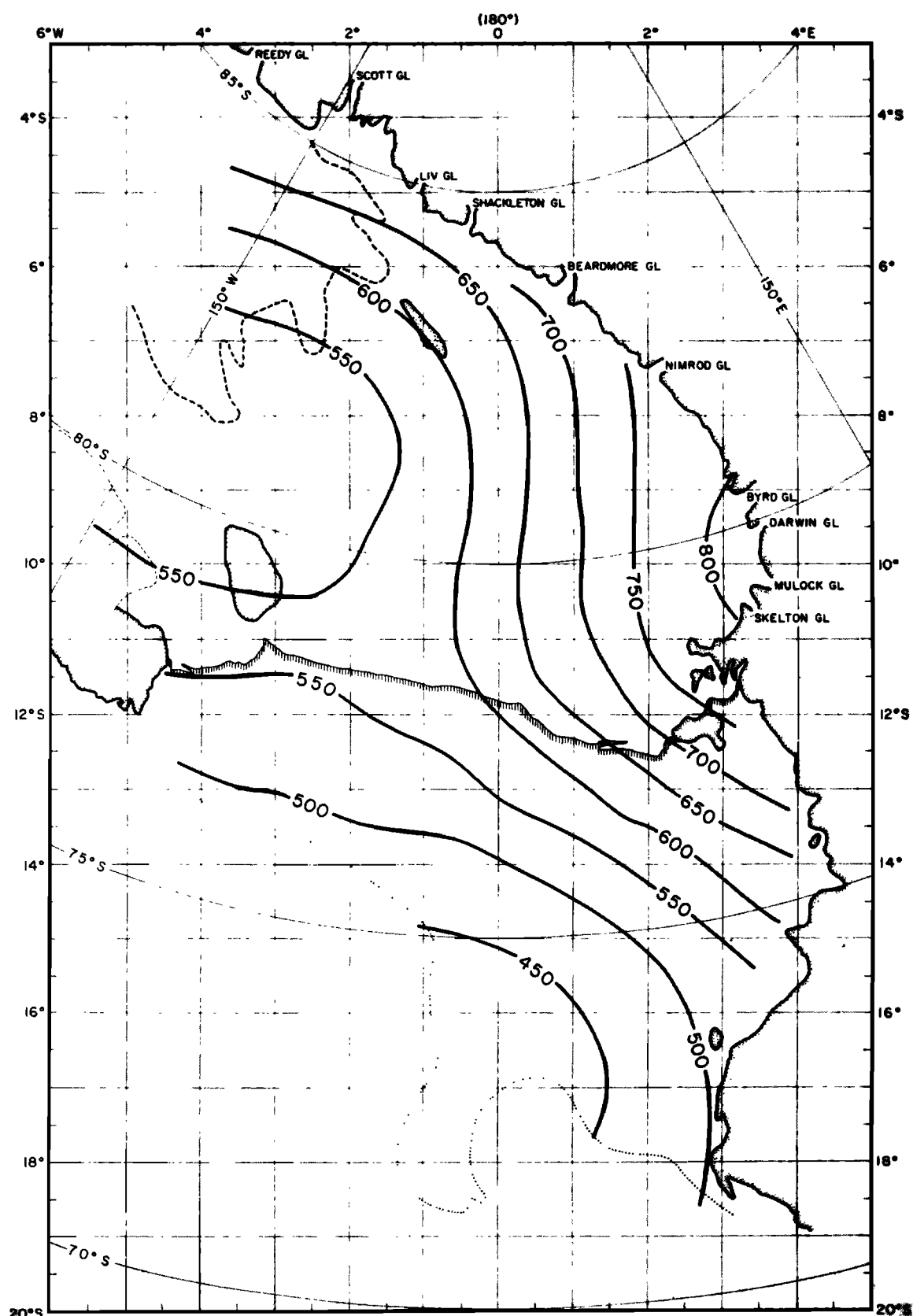


Fig. 43. Map of submarine topography anomalies in the Ross embayment, filtered to remove wavelengths of less than 870 km. The contour interval is 50 m.

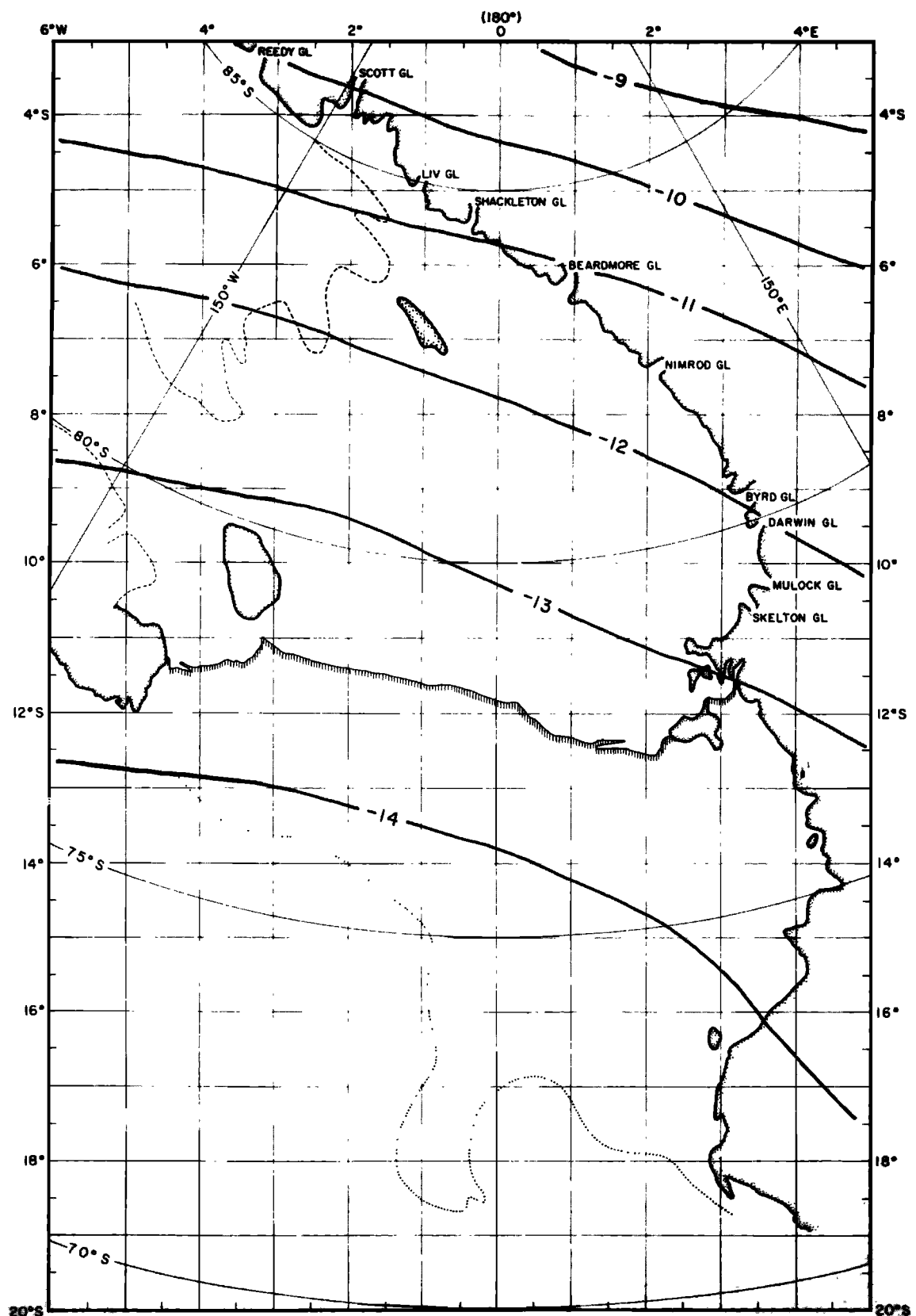


Fig. 44. Free-air gravity contours in the Ross embayment from gravity model GEM 10B, spherical harmonics through degree and order 4. The contour interval is 1 mGal.

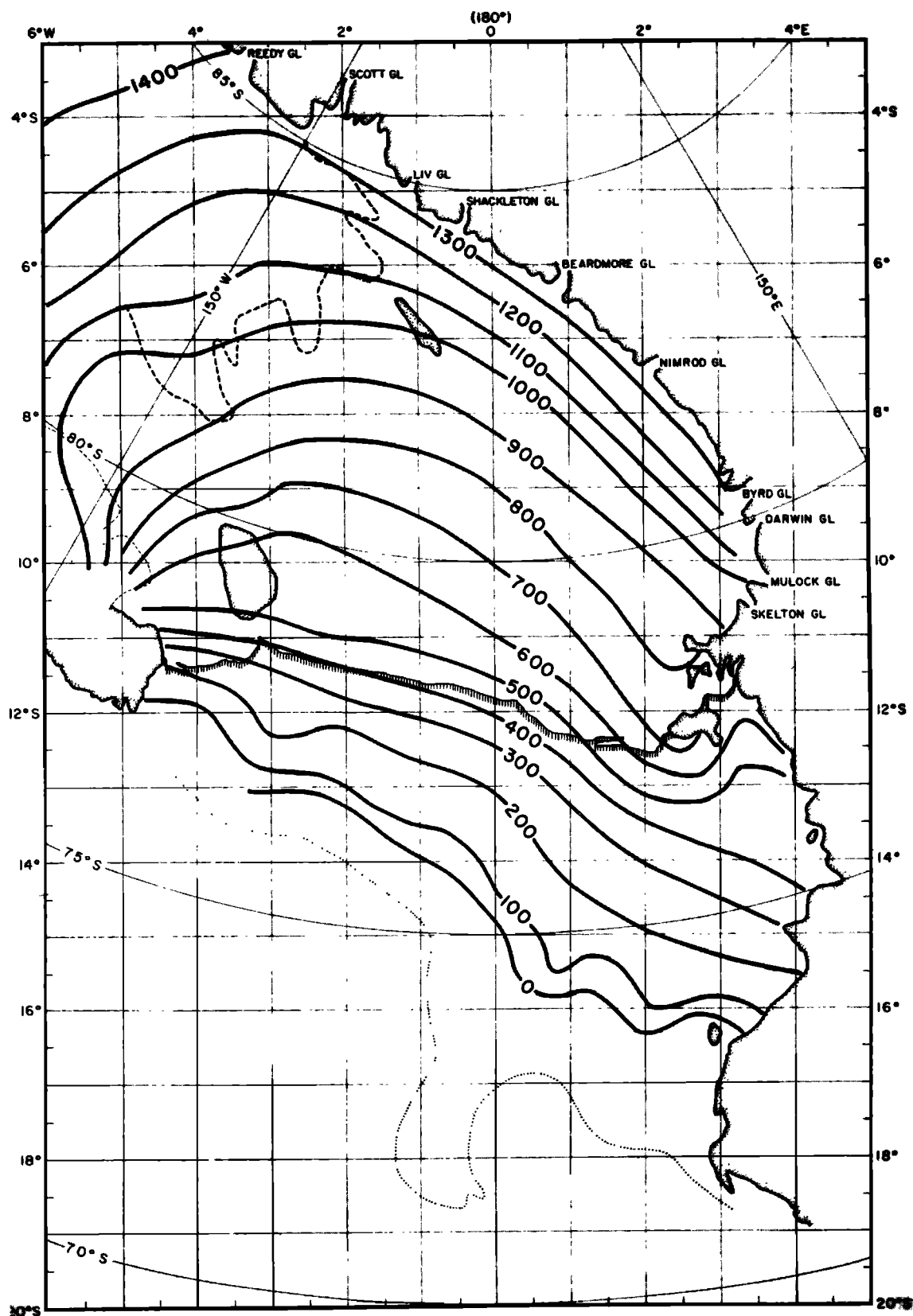


Fig. 45. Map of grounded ice thickness in the Ross embayment during the late Pleistocene glacial maximum, according to the "maximum" reconstruction of Denton *et al.* [1989]. The contour interval is 100 m.

during the Quaternary [Fillon, 1975; Drewry, 1979; Mayewski and Goldthwait, 1985]. Drewry's [1979] reconstruction shows grounding line advance approximately to a line extending from Roosevelt Island to Beardmore Glacier with isolated grounding on shoals in the Ross Sea and around Ross Island. The minimum reconstruction of Denton et al. [1989] is similar to Drewry's with the addition of extensive grounding in the grid eastern Ross embayment.

"Minimum" models for the advance of grounded ice leave the margin approximately in the middle of the gradient in regional gravity, so that the grid southeastern portion of the gravity gradient would have to be attributed to sources other than glacial isostasy. But regional gravity gradients of 10 mGal per thousand kilometers are uncommon in regions away from lithospheric plate boundaries. Furthermore, the gravity gradient on the Ross Ice Shelf is primarily parallel rather than normal to the Transantarctic Mountains. Thus we will assume that the regional gravity gradient reflects incomplete recovery of the lithosphere from former ice loading. We will adopt the "maximum" model of Denton et al. [1989] for the purpose of modeling.

The anomaly gradient can be interpreted qualitatively as implying that the ice sheet retreated from grid east to grid west. To model this retreat, we assume that crustal uplift following "instantaneous" unloading can be adequately described by a simple exponential equation [Heiskanen and Vening Meinesz, 1958; Andrews, 1968; Walcott, 1969; Cathles, 1975] and take the Denton et al. [1989] maximum ice sheet model. The lithospheric depression remaining at present, Z_p , is given by

$$Z_p = Z_0 \exp(-t/t_r) \quad (7)$$

where Z_0 is the original lithospheric depression, t is time since unloading, and t_r is a time constant that depends upon the size of the rebounding area. Cathles [1975] plotted t_r versus linear dimension from values measured in the northern hemisphere and predicted by model studies. Figure 46, adapted from Cathles [1975], shows that for the linear dimension of the Ross embayment (~1000 km) t_r is approximately 4400 years and is relatively independent of both the linear dimension of the load and the crustal rigidity.

From equation (7) the time since unloading is

$$t(\text{years}) = 4400 \ln(Z_0/Z_p) \quad (8)$$

Z_p can be estimated from Δg , the difference between the regional free-air gravity anomaly and the reference field (GEM 10B) using the flat plate approximation

$$Z_p = \frac{\Delta g}{0.042\Delta\rho} \text{ m}$$

where $\Delta\rho = 2.27 \text{ Mg m}^{-3}$, the density contrast between seawater and mantle material, and Δg is in milligals. Bennett [1964] derived an equation for Z_0 in terms of former ice thickness, T (taken from Denton et al. [1989] "maximum" reconstruction Figure 45), and the present average depth of the seafloor, \bar{D} (≈ 650 m):

$$Z_0 = \frac{\rho_i}{\rho_m} T - \frac{\rho_w}{\rho_m} (\bar{D} - Z_p)$$

where ρ_i , ρ_w , and ρ_m are densities of ice, seawater, and mantle rock, respectively. Equation (8) can now be solved for t , the time since "instantaneous" ice unloading occurred.

Critical to this calculation of t is the choice of Δg . The entire difference between the low-pass-filtered gravity anomaly and the GEM 10B fourth-order model (Figure 47) may not reflect only glacio-isostatic imbalance [Bentley et al., 1982] and, in fact, cannot, if the assumed "maximum" ice sheet configuration is approximately correct, because negative anomalies of 4 to 10 mGal lie beyond the edge of that ice sheet (Figure 45).

Consequently, we assume that those negative values of Δg represent a uniform bias for the entire Ross embayment. The mean of Δg in the northern Ross Sea is about -5 mGal; so we increase Δg (decrease Δg numerically) everywhere by 5 mGal. This does not entirely solve the problem, as the isostatic gravity minimum in the southern Ross Sea is in some places still numerically too large to represent even no recovery at all after retreat of the extended ice sheet. Nevertheless, we proceed to model the retreat over the ice shelf itself to see what sort of a model is implied if glacio-isostatic imbalance is, as we believe,

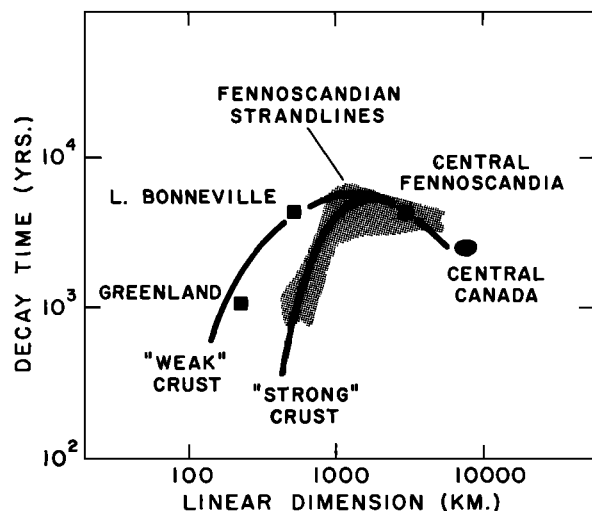


Fig. 46. Decay time constant for isostatic rebound versus linear dimension of areas relieved of loads of ice (Canada, Greenland, Fennoscandia) or water (Lake Bonneville). Adapted from Cathles [1975].

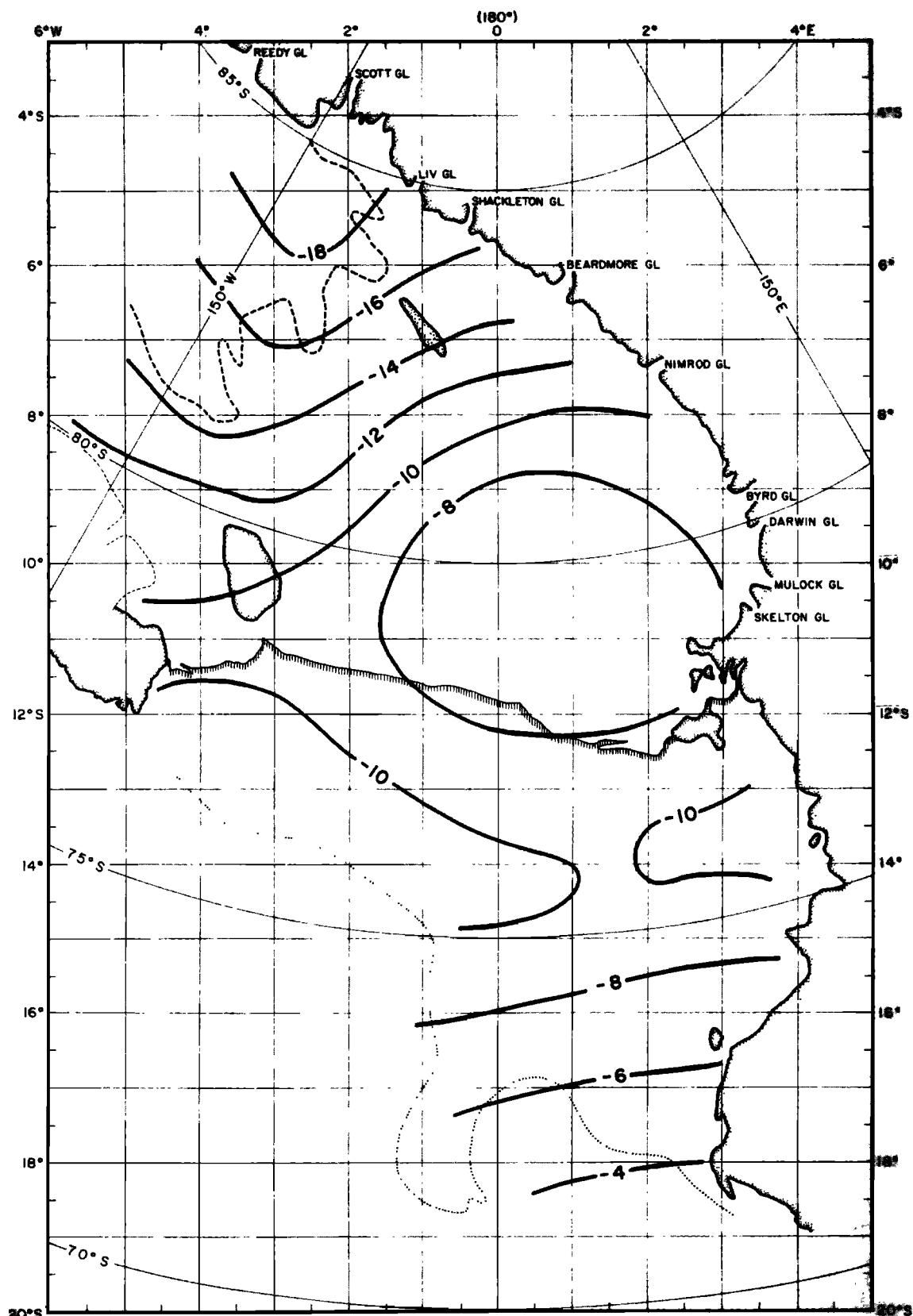


Fig. 47. Map of Δg , the difference between the free-air anomaly fields mapped in Figures 41 and 44, in the Ross embayment. The contour interval is 2 mGal.

the principal source of the observed isostatic anomaly pattern. The resulting map (Figure 48) shows progressive unloading across the ice shelf from more than 10,000 (actually ~12,000) to 4000 years ago. This retreat history is generally similar in timing and configuration to those of *Thomas and Bentley* [1978], *Stuiver et al.* [1981], *Fastook* [1984], and *Lingle* [1984]. Despite the uncertainties about the non-glacio-isostatic component of the isostatic anomalies, we take this agreement as supportive of a model like the maximum reconstruction of *Denton et al.* [1989] rather than a model that involves only a minor advance of the grounding line in the Ross embayment during the late Pleistocene. (The gravity anomalies are also consistent with an ice sheet model [*Stuiver et al.*, 1981] that implies grounding across the entire continental shelf [Greischar, 1982]; however, such a model appears to be incompatible with glacial geological evidence along the East Antarctic margin of the embayment [*Denton et al.*, 1989].)

Isostatic Equilibrium Grounding Line Between the West Antarctic Inland Ice Sheet and the Ross Ice Shelf

Greischar and Bentley [1980] showed how the grounding line might advance if rebound continues and ice dynamic effects do not predominate. Their minimum advance line would have to be moved farther into the ice shelf in light of recent discoveries about the current position of the grounding line; the maximum advance line would not be affected. However, recent knowledge of the dynamic non-steady state of the ice sheet [*Shabtaie et al.*, 1988; *Bindschadler et al.*, 1989] and likely subglacial/submarine sedimentation [*Alley et al.*, 1989] makes it unlikely that isostatic rebound effects will dominate grounding line movement.

SUMMARY

By Antarctic standards the RIGGS gravity survey is remarkably good, both for its areal coverage and for the accuracy of observations. The Ross Ice Shelf, with an area of 560,000 km², was covered by a grid of stations spaced approximately 55 km apart. Since most of the gravity observations were made on floating ice, where accurate elevations could be computed from ice thicknesses, the effect of the commonly principal source of error in calculating gravity anomalies in Antarctica was greatly diminished.

Free-air, Bouguer, and Airy isostatic anomaly maps of the Ross embayment reveal long linear anomalies paralleling the Transantarctic Mountains that are a dominant feature on all of the maps. A likely tectonic

source for these anomalies is block faulting due to extension between East Antarctica and West Antarctica. Deep structural control of gravity lineations implies deep structural control of sea bottom topographic lineations since the two sets of lineations are close to parallel. The control obviously predates the current episode of glaciation in West Antarctica, which suggests that long-standing geologic conditions have determined such glaciological phenomena as the present courses of ice streams. The topography of the ocean bottom below the ice shelf is not fundamentally determined by the ice streams themselves.

The regional data are too widely spaced to determine whether the transition between the gravity highs and lows is steep, indicative of faulting, or gradual, indicative of folding. However, four out of five gravity surveys, at four widely scattered sites (base camps RI, Q13, and C-16 and station J9DC), indicated faults approximately paralleling the Transantarctic Mountains. Faulting also was indicated at the fifth (base camp BC), although there the direction parallels a secondary grid northeast-southwest trend running through Crary Ice Rise. The correspondence of the strikes of these locally modeled structures to regional trends suggests that they are the result of regional tectonic activity.

Spectra were calculated for the free-air anomaly, Bouguer anomaly, and bathymetric maps of the Ross embayment, and an admittance function relating bathymetry to free-air anomaly was calculated to investigate the gravitational response to topographic loading. This technique revealed a long-wavelength signal that we interpret to reflect incomplete isostatic recovery from the load of a more extended late Pleistocene ice sheet. Admittance maxima at shorter wavelengths (150 km and 350 km) we believe to be related to tectonically produced troughs and ridges with trends parallel to the Transantarctic Mountains.

There is little doubt that during late Wisconsin/Holocene time the grounded portion of the West Antarctic ice sheet extended farther seaward than at present. The fact that the low-passed ($\gamma \geq 870$ km) free-air gravity anomalies are even more negative than the low-order satellite-derived gravity field in the Ross embayment suggests recent grounding of the West Antarctic ice sheet out to, or nearly to, the edge of the continental shelf in the Ross Sea. Using the "maximum model" of *Denton et al.* [1989] as a reconstruction of the Antarctic ice sheet during the late Wisconsin glacial maximum and a simple exponential model of crustal rebound, isochrons of grounding line retreat have been mapped in the Ross embayment. The general aspects of this retreat are similar to those calculated from ice dynamical models.

The water layer beneath the Ross Ice Shelf is thin enough near the present grounding line that isostatic

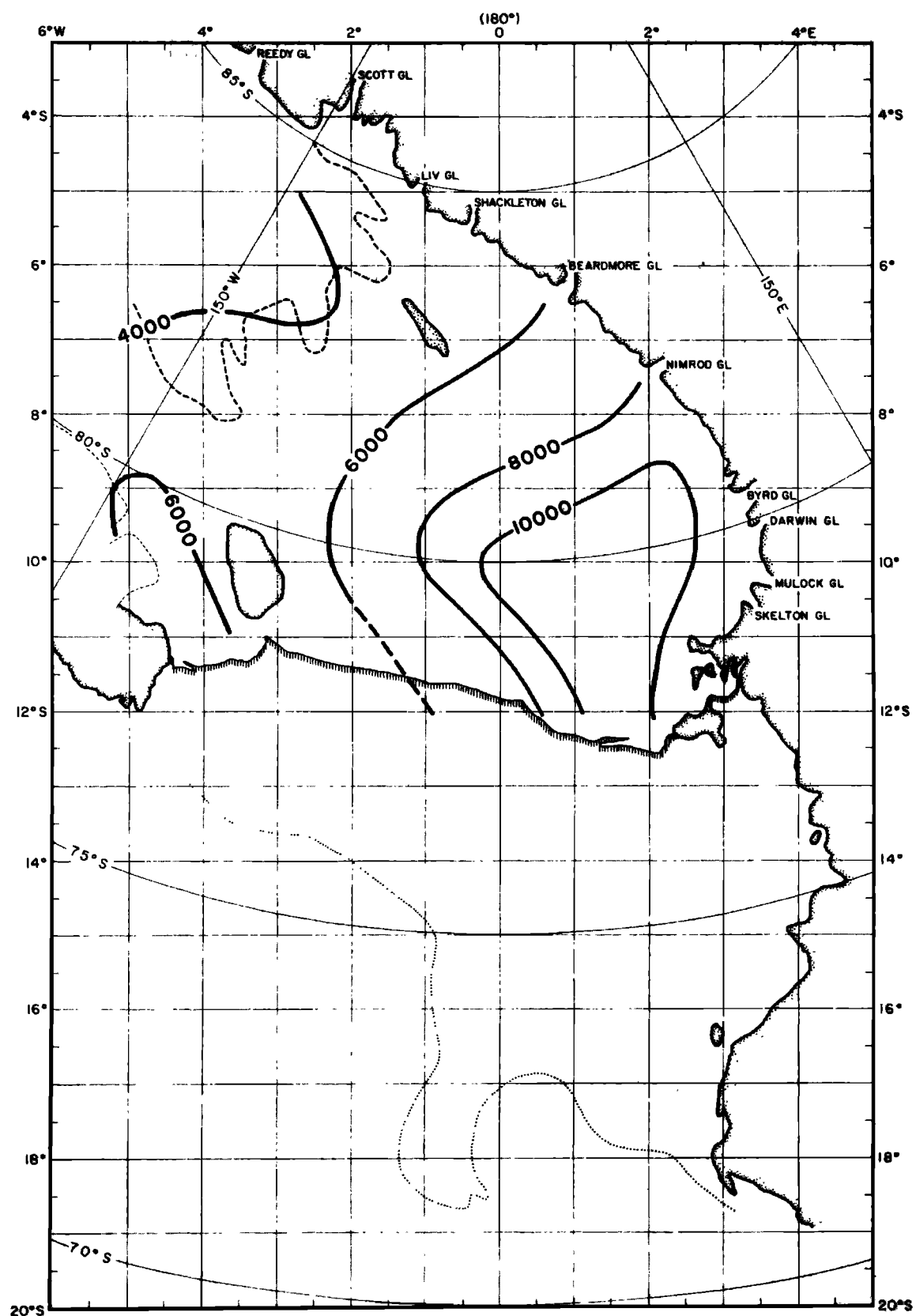


Fig. 48. Map of Holocene retreat of grounded ice from the Ross Ice Shelf modeled on the assumption that $\Delta g + 5$ mGal represents the glacio-isostatic imbalance. The contour interval is 2000 years B.P.

rebound could lead to a kilometer of grounding line advance for each meter of uplift. If the West Antarctic ice sheet were approximately in steady state, an advance of the grounding line into the Ross Ice Shelf would be expected. However, it is probable that ice dynamic effects will swamp isostatic rebound effects in this highly non-steady state system.

APPENDIX

The principal facts for all the RIGGS gravity stations and all other gravity stations on the Ross Ice Shelf are listed in Tables A1-A6 (on microfiche, enclosed in a pocket inside the back cover of this book). An explanation of the columns and column headings follows.

Stn, station.

Numerals in the left column under Code refer to the year of measurement. I: 1973-1974; II: 1974-1975; III: 1976-1977; IV: 1977-1978; letters in the right column refer to the kind of position measurement. G: geoceiver; GR: geoceiver-real time only; I: aircraft inertial navigation system; S: sunshots; L: sighting on landmarks.

GLAT, grid latitude, degrees south.

GLON, grid longitude, degrees.

T_i , ice thickness, meters.

T_w , water layer thickness, meters.

G obs, observed gravity.

Elev, elevation of the ice surface, calculated from the ice thickness except where otherwise indicated by superscripts: 1, from elevation map [Shabtaie and Bentley, 1987]; 2, geoceiver measurement; 3, altimeter measurement.

Depth, depth to the sea floor, meters below sea level.

FAA, free-air anomaly, milligals.

BA, Bouguer anomaly, milligals.

IA, isostatic anomaly, milligals.

Table A7 gives the magnitudes and direction of local gravity gradients at RIGGS stations.

Tables A8-A12 contain the free-air gravity anomalies in the five extensive local surveys, at base camp BC, station J9DC, and base camps RI, Q13, and C-16.

Note. This paper was written as a contribution to Antarctic Research Series volume 42, *The Ross Ice Shelf: Glaciology and Geophysics*, but is published here instead for technical reasons. It should be thought of as paper 6 of that series.

Acknowledgments. We would like to thank especially the many other members of the RIGGS field parties for their capable assistance in collecting the data presented here. Particular thanks go to Tom Kolich for the many hours

spent taking gravity readings. The logistic support of Holmes and Narver, Inc., United States Naval Support Force, Antarctica, and Antarctic Development Squadron Six is gratefully acknowledged. Discussions with J. W. Clough, J. D. Robertson, and C. S. Lingle were helpful during the early stages of writing. Consultation with C. S. Clay substantially improved the section on admittance functions. Comments by U. S. ten Brink and an anonymous referee led to substantial improvements in the paper. This work was supported by National Science Foundation grants GV-36963 and DPP79-20736. This is contribution 511 of the Geophysical and Polar Research Center, University of Wisconsin, Madison.

REFERENCES

- Albert, D. G., and C. R. Bentley, Seismic studies on the grid eastern half of the Ross Ice Shelf, Antarctica: RIGGS III and RIGGS IV, in *The Ross Ice Shelf: Glaciology and Geophysics, Antarct. Res. Ser.*, vol. 42, edited by C. R. Bentley and D. E. Hayes, pp. 87-108, Washington, D.C., 1990.
- Albert, D. G., C. R. Bentley, and L. L. Greischar, 1978, Submarine topography of the Ross embayment from the continental shelf to the Byrd Subglacial Basin, paper presented at the 1978 AGU Spring Meeting, Miami Beach, Fl., April 17-21, 1978.
- Alley, R. B., D. D. Blankenship, S. T. Rooney, and C. R. Bentley, Sedimentation beneath ice shelves—The view from Ice Stream B, *Mar. Geol.*, 85, 101-120, 1989.
- Andrews, J. T., The pattern and interpretation of restrained postglacial and residual rebound in the area of Hudson Bay, in *Earth Science Symposium on Hudson Bay*, edited by P. J. Hood, pp. 49-62, Geological Survey of Canada, Ottawa, Ont., 1968.
- Behrendt, J. C., Gravity increase at the south pole, *Science*, 155, 1015-1017, 1967.
- Behrendt, J. C., W. E. LeMasurier, A. K. Cooper, E. Tessensohn, A. Treku, and D. Damaske, The West Antarctic rift system: A review of geophysical investigations, in *Contributions to Antarctic Research II, Antarct. Res. Ser.*, vol. 53, edited by D. H. Elliot, pp. 67-112, AGU, Washington, D.C., 1991.
- Bennett, H. F., A gravity and magnetic survey of the Ross Ice Shelf area, Antarctica, *Res. Rep.* 64-3, Geophys. and Polar Res. Center, Univ. of Wis., Madison, 1964.
- Bentley, C. R. The structure of Antarctica and its ice cover, in *Research in Geophysics, Solid Earth and Interface Phenomena*, vol. 2, edited by H. Odishaw, pp. 335-389, Massachusetts Institute of Technology, Cambridge, 1964.
- Bentley, C. R., Secular increase of gravity at South Pole Station, in *Antarctic Snow and Ice Studies II, Antarct. Res. Ser.*, vol. 16, edited by A. P. Crary, pp. 191-198, AGU, Washington, D.C., 1971.
- Bentley, C. R., Crustal structure of Antarctica, *Tectonophysics*, 20(1-4), 229-240, 1973.
- Bentley, C. R., The Ross Ice Shelf geophysical and glaciological survey (RIGGS): Introduction and summary of measurements performed, in *The Ross Ice Shelf: Glaciology and Geophysics, Antarct. Res. Ser.*, vol. 42, edited by C. R. Bentley and D. E. Hayes, pp. 1-20, AGU, Washington, D.C., 1984.

- Bentley, C. R., and J. D. Robertson, Isostatic gravity anomalies in West Antarctica, in *Antarctic Geoscience*, edited by C. Craddock, pp. 949–954, University of Wisconsin Press, Madison, 1982.
- Bentley, C. R., J. D. Robertson, and L. L. Greischar, Isostatic gravity anomalies on the Ross Ice Shelf, Antarctica, in *Antarctic Geoscience*, edited by C. Craddock, pp. 1077–1081, University of Wisconsin Press, Madison, 1982.
- Bindschadler, R. A., E. P. Roberts, and D. R. MacAyeal, Distribution of net balance in the vicinity of Crary Ice Rise, Antarctica, *J. Glaciol.*, 35, 370–377, 1989.
- Cathles, L. M., *The Viscosity of the Earth's Mantle*, Princeton University Press, Princeton, N. J., 1975.
- Chiang, E., and C. C. Langway, Antarctic ice core recovery, *Antarct. J. U. S.*, 13, 59–61, 1978.
- Clough, J. W., and B. L. Hansen, The Ross Ice Shelf project, *Science*, 203, 433–434, 1979.
- Cooper, A. K., and F. J. Davey (Eds.), *The Antarctic Continental Margin: Geology and Geophysics of the Western Ross Sea*, *Earth Sci. Ser.*, vol. 5B, Circum-Pacific Council for Energy and Mineral Resources, Houston, Tex., 1987.
- Cooper, A. K., F. J. Davey, and J. C. Behrendt, Seismic stratigraphy and structure of the Victoria Land basin, western Ross Sea, Antarctica, in *The Antarctic Continental Margin: Geology and Geophysics of the Western Ross Sea*, *Earth Sci. Ser.*, vol. 5B, edited by A. K. Cooper and F. J. Davey, pp. 27–76, Circum-Pacific Council for Energy and Mineral Resources, Houston, Tex., 1987.
- Cooper, A. K., F. J. Davey, and K. Hinz, Crustal extension and origin of sedimentary basins beneath the Ross Sea and Ross Ice Shelf, Antarctica, in *Geological Evolution of Antarctica*, edited by M. R. A. Thomson, J. A. Crame, and J. W. Thomson, pp. 285–291, Cambridge University Press, New York, 1991.
- Crary, A. P., Glaciological studies at Little America Station, Antarctica, 1957 and 1958, *IGY Glaciol. Rep.* 5, Int. Geophys. Year World Data Center A, Glaciol. Am. Geogr. Soc., New York, 1961a.
- Crary, A. P., Marine sediment thickness in the eastern Ross Sea area, Antarctica, *Geol. Soc. Am. Bull.*, 72, 787–790, 1961b.
- Crary, A. P., E. S. Robinson, H. F. Bennett, and W. W. Boyd, Glaciological studies of the Ross Ice Shelf, Antarctica, 1957–60, *IGY Glaciol. Rep.* 6, Int. Geophys. Year World Data Center A, Glaciol. Am. Geogr. Soc., New York, 1962.
- Davey, F. J., Geology and structure of the Ross Sea region, in *The Antarctic Continental Margin: Geology and Geophysics of the Western Ross Sea*, *Earth Sci. Ser.*, vol. 5B, edited by A. K. Cooper and F. J. Davey, pp. 1–15, Circum-Pacific Council for Energy and Mineral Resources, Houston, Tex., 1987.
- Davey, F. J., and A. K. Cooper, Gravity studies of the Victoria Land basin and Iselin Bank, in *The Antarctic Continental Margin: Geology and Geophysics of the Western Ross Sea*, *Earth Sci. Ser.*, edited by A. K. Cooper and F. J. Davey, pp. 119–137, Circum-Pacific Council for Energy and Mineral Resources, Houston, Tex., 1987.
- Denton, G. H., and H. W. Borns, Former grounded ice sheets in the Ross Sea, *Antarct. J. U. S.*, 9, 167, 1974.
- Denton, G. H., R. L. Armstrong, and M. Stuiver, Late Cenozoic glaciation in Antarctica: The record in the McMurdo Sound region, *Antarct. J. U. S.*, 5, 15–21, 1970.
- Denton, G. H., J. G. Bockheim, S. C. Wilson, and M. Stuiver, Late Wisconsin and early Holocene glacial history, inner Ross embayment, Antarctica, *Quat. Res.*, 31, 151–182, 1989.
- Drewry, D. J., Late Wisconsin reconstruction for the Ross Sea region, Antarctica, *J. Glaciol.*, 24, 231–244, 1979.
- Elliot, D. H., The Transantarctic Mountain front and the Ross embayment, *Eos Trans. AGU*, 61, 1194, 1980.
- Fastook, J. L., West Antarctica: The sea level controlled marine instability: Past and future, in *Climate Processes and Climate Sensitivity, Geophys. Monogr. Ser.*, vol. 29, edited by J. E. Hansen and T. Takahashi, pp. 275–287, AGU, Washington, D. C., 1984.
- Fillon, R. H., Late Cenozoic paleo-oceanography of the Ross Sea, Antarctica, *Geol. Soc. Am. Bull.*, 86, 839–845, 1975.
- Giovinetto, M. B., E. S. Robinson, and C. W. Swithinbank, The regime of the western part of the Ross Ice Shelf drainage system, *J. Glaciol.*, 6, 55–68, 1966.
- Gow, A. J., The inner structure of the Ross Ice Shelf at Little America V, Antarctica, as revealed by deep core drilling, *IAHS Publ.* 61, 272–284, 1963.
- Grieschar, L. L., An analysis of gravity measurements on the Ross Ice Shelf, Antarctica, Ph.D. thesis, 210 pp., Univ. of Wis., Madison, 1982.
- Grieschar, L. L., and C. R. Bentley, Isostatic equilibrium grounding line between the West Antarctic ice sheet and the Ross Ice Shelf, *Nature*, 283, 651–654, 1980.
- Grieschar, L. L., S. Shabtaie, D. G. Albert, and C. R. Bentley, Ross Ice Shelf geophysical survey, 1977–1978, *Antarct. J. U. S.*, 13, 56–59, 1978.
- Hammond, J. A., and R. L. Iliff, The AFGL gravity program, in *Proceedings of the Ninth Geodesy/Solid Earth and Ocean Physics (GEOP) Research Conference*, edited by I. Mueller, Department of Geodetic Science and Surveying, Ohio State University, Columbus, 1978.
- Harrison, J. C., and L. J. LaCoste, The measurement of surface gravity, in *Proceedings of the Ninth Geodesy/Solid Earth and Ocean Physics (GEOP) Research Conference*, edited by I. Mueller, Department of Geodetic Science and Surveying, Ohio State University, Columbus, 1978.
- Hayes, D. E., and F. J. Davey, A geophysical study of the Ross Sea, Antarctica, *Initial Rep. Deep Sea Drill. Proj.*, 28, 887–907, 1975.
- Hayes, D. E., M. Talwani, R. Houtz, and W. C. Pitman III, Preliminary report of volume 22 U.S.N.S. *Eltanin* cruises 28–32 March 1967–March 1968, *Tech. Rep. CU-1-72*, Lamont-Doherty Geol. Observ. of Columbia Univ., Palisades, N. Y., 1972.
- Hayes, D. E., J. Weissel, T. Aitken, R. Houtz, M. Talwani, R. A. Shearer, and A. B. Watts, Preliminary report of volume 26 U.S.N.S. *Eltanin* cruises 51–55A January 1972–December 1972, *Tech. Rep. CU-1-78*, Lamont-Doherty Geol. Observ. of Columbia Univ., Palisades, N. Y., 1978.
- Heiskanen, W. A., and F. A. Vening Meinesz, *The Earth and Its Gravity Field*, McGraw-Hill, New York, 1958.

- Houtz, R., and F. J. Davey, Seismic profiler and sonobuoy measurements in the Ross Sea, Antarctica, *J. Geophys. Res.*, **78**, 3448–3468, 1973.
- Kellogg, T. B., R. S. Truesdale, and L. E. Osterman, Late Quaternary extent of West Antarctic ice sheet: New evidence from Ross Sea cores, *Geology*, **7**, 249–253, 1979.
- Kirchner, J. F., and C. R. Bentley, RIGGS III: Seismic short-refraction studies using an analytical curve-fitting technique, in *The Ross Ice Shelf: Glaciology and Geophysics, Antarct. Res. Ser.*, vol. 42, edited by C. R. Bentley and D. E. Hayes, pp. 109–126, AGU, Washington, D. C., 1990.
- Kososki, B. A., A gravity study of West Antarctica, M. S. thesis, 78 pp., Univ. of Wis., Madison, 1972.
- Lambeck, K., *Geophysical Geodesy: The Slow Deformations of the Earth*, 718 pp., Oxford University Press, New York, 1988.
- Langway, C. C., Jr., Antarctic ice core studies, *Antarct. J. U. S.*, **10**, 152–153, 1975.
- Lingle, C. S., A numerical model of interactions between a polar ice stream and the ocean: Application to ice stream E, West Antarctica, *J. Geophys. Res.*, **89**, 3523–3549, 1984.
- Mayewski, P., and R. P. Goldthwait, Glacial events in the Transantarctic Mountains: A record of the East Antarctic ice sheet, in *Geology of the Central Transantarctic Mountains, Antarct. Res. Ser.*, vol. 36, edited by M. D. Turner and J. F. Splettstoesser, pp. 275–324, AGU, Washington, D. C., 1985.
- McKenzie, D. P., and C. Bowin, The relationship between bathymetry and gravity in the Atlantic Ocean, *J. Geophys. Res.*, **81**, 1903–1915, 1976.
- Morelli, C., *Geodetic Reference System 1971, Spec. Publ. 3*, 116 pp., Bureau Central de L'Association International de Géodésie, Paris, 1971.
- Nettleton, L. L., *Gravity and Magnetics in Oil Prospecting*, 464 pp., McGraw-Hill, New York, 1976.
- Robertson, J. D., Geophysical studies on the Ross Ice Shelf, Antarctica, Ph.D. thesis, 214 pp., Univ. of Wis., Madison, 1975.
- Robertson, J. D., and C. R. Bentley, Seismic studies on the grid western half of the Ross Ice Shelf: RIGGS I and RIGGS II, in *The Ross Ice Shelf: Glaciology and Geophysics, Antarct. Res. Ser.*, vol. 42, edited by C. R. Bentley and D. E. Hayes, pp. 55–86, AGU, Washington, D. C., 1990.
- Robertson, J. D., C. R. Bentley, J. W. Clough, and L. L. Greischar, Sea bottom topography and crustal structure below the Ross Ice Shelf, Antarctica, in *Antarctic Geoscience*, edited by C. Craddock, pp. 1083–1090, University of Wisconsin Press, Madison, 1982.
- Shabtaie, S., and C. R. Bentley, Tabular icebergs: Implications from geophysical studies of ice shelves, *J. Glaciol.*, **29**, 413–430, 1982.
- Shabtaie, S., and C. R. Bentley, West Antarctic ice streams draining into the Ross Ice Shelf: Configuration and mass balance, *J. Geophys. Res.*, **92**, 1311–1336, 1987.
- Shabtaie, S., C. R. Bentley, R. A. Bindschadler, and D. R. MacAyeal, Mass balance studies of ice streams A, B, and C and possible surging behavior of Ice Stream B, *Ann. Glaciol.*, **11**, 129–136, 1988.
- Simpson, R. W., R. C. Jachens, and R. J. Blakely, A new residual map of the conterminous United States with a discussion on the significance of isostatic residual anomalies, *J. Geophys. Res.*, **91**, 8348–8372, 1986.
- Stern, T. A., and U. S. ten Brink, Flexural uplift of the Transantarctic Mountains, *J. Geophys. Res.*, **94**, 10,315–10,330, 1989.
- Stuiver, M., G. H. Denton, T. J. Hughes, and J. L. Fastook, The history of the marine ice sheet in West Antarctica during the last glaciation: A working hypothesis, in *The Last Great Ice Sheets*, edited by G. H. Denton and T. J. Hughes, pp. 319–436, Wiley-Interscience, New York, 1981.
- Talwani, M., and M. Ewing, Rapid computation of gravitational attraction of three-dimensional bodies of any shape, *Geophysics*, **25**, 203–225, 1960.
- Talwani, M., J. Lamar, and M. Landisman, Rapid gravity computations for two-dimensional bodies with application to the Mendocino Submarine Fracture Zone, *J. Geophys. Res.*, **64**, 49–59, 1969.
- Tessensohn, F., and G. Wörner, The Ross Sea rift system, Antarctica: Structure, evolution and analogues, in *Geological Evolution of Antarctica*, edited by M. R. A. Thomson, J. A. Crame, and J. W. Thomson, pp. 273–277, Cambridge University Press, New York, 1991.
- Thomas, R. H., and C. R. Bentley, The equilibrium state of the eastern half of the Ross Ice Shelf, *J. Glaciol.*, **20**, 509–518, 1978.
- Thomas, R. H., D. R. MacAyeal, D. H. Eilers, and D. R. Gaylor, Glaciological studies on the Ross Ice Shelf, Antarctica, 1973–1978, in *The Ross Ice Shelf: Glaciology and Geophysics, Antarct. Res. Ser.*, vol. 42, edited by C. R. Bentley and D. E. Hayes, pp. 21–53, AGU, Washington, D. C., 1984.
- Walcott, R. I., Isostatic response to loading of the crust in Canada, *Can. J. Earth sci.*, **7**, 716–734, 1969.
- Williams, R. T., and S. Robinson, The ocean tide in the southern Ross Sea, *J. Geophys. Res.*, **85**, 6689–6696, 1980.
- Woollard, G. P., The new gravity system—Changes in international gravity base values and anomaly values, *Geophysics*, **44**, 1352–1366, 1979.

(Received April 3, 1992;
accepted July 27, 1992.)